Université de Strasbourg

École Doctorale des Sciences Chimiques — ED 222
UMR 7006

THÈSE

présentée par

Vineesha SRIVASTAVA

soutenue le **9 Décembre 2024**

pour obtenir le grade de **Docteur de l'Université de Strasbourg**
Discipline/Spécialité: **Physique**

Entanglement Generation and Quantum Gates with Quantum Emitters in a Cavity

Thèse dirigée par

Pr. PUPILLO Guido	Professeur, Université de Strasbourg
Dr. SCHACHENMAYER Johannes	Chargé de recherche, CNRS

Rapporteurs

Pr. SUGNY Dominique	Professeur, Université de Bourgogne-Franche Comté
Pr. SAYRIN Clément	Maître de conférences, Sorbonne Université

Autres membres du jury

Pr. ERCOLESSI Elisa	Professeur, Università di Bologna
Dr. LONG Romain	Maître de conférences, Sorbonne Université

Université de Strasbourg

École Doctorale des Sciences Chimiques

Vineesha SRIVASTAVA

Entanglement Generation and Quantum Gates with Quantum Emitters in a Cavity

Résumé

La génération d'intrication et les opérations de portes quantiques sont fondamentales pour le traitement de l'information quantique. Cette thèse présente des protocoles novateurs pour les portes quantiques multi-qubits non locales et la génération d'intrication dans des systèmes où plusieurs émetteurs quantiques interagissent avec un mode bosonique partagé, offrant une large applicabilité dans les configurations de l'électrodynamique quantique en cavité. Les protocoles clés comprennent la Porte de Phase Géométrique et la Porte de Phase Adiabatique, développées avec des expressions sous forme fermée pour l'échelle d'infidélité en fonction du nombre de qubits et de la coopérativité. Appliqués aux deux qubits, ces protocoles forment un ensemble universel de portes pour le calcul quantique, tandis que dans les systèmes multi-qubits, ils fournissent une famille de portes quantiques déterministes avec des applications dans les simulations quantiques numériques, la métrologie et la correction d'erreurs quantiques. Une contribution significative de cette thèse est un protocole de détection amélioré par l'intrication qui atteint une haute précision de mesure grâce à des méthodes de contrôle optimal, démontrant une versatilité au-delà des opérations de portes conventionnelles. De plus, la thèse étudie un mécanisme de blocage des polaritons en cavité pour réaliser des états W multi-atomiques non locaux et des portes multi-qubits. Toutes les opérations multi-qubits déterministes présentées ne nécessitent que des excitations classiques de la cavité et, dans certains cas, des impulsions globales sur les qubits, établissant ainsi une base évolutive pour le calcul quantique, la détection, et le futur internet quantique en intégrant des opérations multi-qubits efficaces à travers les plateformes expérimentales, particulièrement celles basées sur des systèmes d'atomes neutres.

Mots-clés: Informatique quantique, QED de cavité, génération d'intrication, portes quantiques multi-qubits, méthodes de contrôle optimal, atomes neutres

Abstract

Entanglement generation and quantum gate operations are fundamental to quantum information processing. This thesis presents novel protocols for non-local multi-qubit quantum gates and entanglement generation in systems where multiple quantum emitters interact with a shared bosonic mode, offering broad applicability across cavity QED setups. Key protocols include the Geometric Phase Gate and Adiabatic Phase Gate, developed with closed-form expressions for infidelity scaling with qubit number and cooperativity. When applied to two-qubits, these protocols form a universal gate set for quantum computation, while in multi-qubit systems, they provide a family of deterministic quantum gates with applications in digital quantum simulations, metrology, and quantum error correction. A significant contribution of this thesis is an entanglement-enhanced sensing protocol that achieves high measurement precision through optimal control methods, demonstrating versatility beyond conventional gate operations. Additionally, the thesis investigates a cavity polariton blockade mechanism to realize non-local multi-atom W-states and multi-qubit gates. All of the presented deterministic multi-qubit operations require only classical cavity drives and, in some cases, global qubit pulses, establishing a scalable foundation for quantum computing, sensing, and the future quantum internet by integrating efficient multi-qubit operations across experimental platforms, particularly those based on neutral atom systems.

Keywords: Quantum Computing, Cavity QED, Entanglement generation, Multi-qubit Quantum Gates, Optimal Control Methods, Neutral Atoms

Acknowledgements

First and foremost, I would like to express my deepest gratitude to my advisor, Prof. Guido Pupillo. His unwavering belief in my abilities and his insightful guidance have been the cornerstone of this journey. His mentorship, encouragement, and dedication to academic excellence have been instrumental to my growth as a researcher. Working under his guidance has been a privilege, and his support has been invaluable at every step.

I would like to express my sincere gratitude to Prof. Gavin Brennen, whose expertise and knowledge in the field have significantly enriched this research. His willingness to engage in detailed scientific discussions, and the numerous opportunities I had to learn from his insights, have been invaluable to this work. My sincere appreciation goes to my co-supervisor, Dr. Johannes Schachenmayer, whose thoughtful insights and constructive feedback have been instrumental throughout this journey.

I would like to express my heartfelt gratitude to the esteemed members of my jury, Prof. Dominique Sugny, Prof. Clément Sayrin, Prof. Elisa Ercolessi, and Dr. Romain Long, for dedicating their time, expertise, and thoughtful feedback in evaluating this PhD thesis. I extend my gratitude to the members of my comité de suivi - Prof. Elisa Ercolessi, Prof. Cyriaque Genet, and Prof. Giovanni Manfredi. Their expertise and constructive feedback during our annual meetings have been invaluable in shaping the direction of this research.

I have been fortunate to work alongside exceptional colleagues in the Quantum Matter theory group at CESQ: Dr. Sven Jandura, Dr. Francesco Mattioti, Dr. David Wellnitz, Laura Pecorari, Tatiana Bespalova, Tanul Gupta, Matteo Bergonzoni, Ruben Daraban, Dr. Hugo Perrin, Dr. David Hagenmüller, Dr. Jérôme Dubail, Dr. Camille Le Colennec, Dr. Guillermo Preisser, Federico Astolfi, Réka Schwengelbeck, and Francesco Guerci. The intellectual vibrancy of our group has been a constant source of inspiration. The vibrant research environment at CESQ provided me with valuable opportunities to interact with experimentalists. I thank Prof. Shannon Whitlock for his insights and feedback, and I am grateful to Dr. Manuel Morgado, Dr. Chang Li, Dr. Anuja Padhye, Swayangdipta Bera, Clément Gradziel, Amar Bellahsene, Shuzhe Yang, Maximilian Müllenbach, Dr. Tom Bienaimé and Dr. Stanimir Kondov for enriching discussions.

My secondment at QPerfect was a transformative experience. I am grateful to Dr. Asier Piñeiro Orioli, Dr. Guido Masella, Dr. Vase Moeini, Dr. Anna Leonteva, and Maxime Outteryck for their mentorship and for sharing their expertise so generously.

The administrative team, project managers and institute heads at CESQ and ISIS deserve special recognition - Annia Bertrand, Anna Guyon, Youma Mucret, Michel Wagner, Souhila Demmouche, Ana Helman, Biljana Zasova, Muzet Muriel and Veronique Debord Lazaro have provided exceptional support, ensuring the smooth progression of my research work.

This research was made possible through the support of QUSTEC and Eucor, with funding from the Marie Skłodowska-Curie Actions (MSCA) COFUND scheme. The cross-border, interdisciplinary environment they fostered has been instrumental in my development as a researcher. I thank Nataliia Voievoda, Janosch Nieden, Bernd Finger, Svitlana Semak and Johanne Martinez for their dedicated support of the program. I would also like to extend my gratitude to all QUSTEC fellows and supervisors for their support and time shared at annual summer schools.

My heartfelt thanks go to my landlords, Erika and Gunther Berl, for their considerate support, kindness and encouragement during my research years in Strasbourg. The friendship of my Strasbourg community has been invaluable - Deeksha, Aleena, Satakshi, Ankita, Ann, Sayali, Yamini, Azra, Anjana, Shubhradip, Gyandeep, José, Tanushree, Arvind, Jinu, and Krishna have enriched my life in Strasbourg. A special note of gratitude goes to Anamika aunty, whose kindness and home-cooked meals brought comfort and familiarity, making Strasbourg feel less distant from home.

Special thanks to Ankita and Yashwanth, friends from my earlier academic years, whose continued mentorship and friendship have been invaluable to my growth and progress. I am also grateful to Vibha and Roshni for their steadfast friendship that predates this journey and has provided a constant source of encouragement.

Finally, my deepest gratitude goes to my family - my parents, Vineet and Usha, and my sister, Naveesha. Their unconditional love, unwavering support, and belief in my abilities have been my foundation throughout this journey. Their pride and joy in my accomplishments has made each step of this journey all the more meaningful.

I perceive this opportunity of carrying out my PhD thesis work as a significant milestone in my career development. The knowledge and experiences gained during these years have laid a strong foundation and instilled in me a deeper appreciation for scientific research. Moving forward, I will strive to build upon these experiences and utilize the gained knowledge in the best possible way. As I look forward to future scientific endeavors, I carry with me the valuable lessons, relationships, and experiences gained during these years, committed to continuing this journey with the same enthusiasm and dedication that marked its beginning.

Résumé de la Thèse en Français

I. Introduction

L'intrication et les opérations de portes quantiques sont au cœur du traitement de l'information quantique, stimulant des avancées révolutionnaires en calcul et en communication. L'intrication, caractéristique fondamentale de la mécanique quantique, la distingue de la physique classique en mettant en évidence la nature spécifique du domaine quantique. Elle illustre l'interdépendance des résultats de mesure entre les particules, rendant inadéquate la description individuelle des particules. D'abord considérée comme une curiosité théorique visant à sonder d'éventuelles lacunes de la mécanique quantique [1], puis comme base des tests comparant la mécanique quantique au réalisme local [2–4], l'intrication est aujourd'hui une pierre angulaire de la technologie quantique, essentielle pour la cryptographie quantique, la détection et le calcul. Le succès de ces technologies quantiques repose sur la manipulation haute fidélité des états intriqués, souvent composés de nombreux qubits. Des progrès considérables ont été réalisés ces dernières décennies dans le contrôle des systèmes à plusieurs corps [5–11].

En calcul quantique, la mise en œuvre de portes multi-qubits de haute fidélité est essentielle pour réduire le nombre d'opérations et permettre des schémas de calcul tolérants aux fautes adaptés à des plateformes spécifiques [12–14]. De même, en métrologie quantique, les états intriqués multipartites permettent d'améliorer la sensibilité des mesures au-delà de la limite quantique standard [15–21].

Cependant, un défi majeur réside dans le contrôle des systèmes à N corps et la nature fragile des superpositions quantiques macroscopiques. En calcul quantique, de nombreux systèmes physiques, y compris ceux basés sur des atomes neutres, ne permettent pas intrinsèquement des opérations globales ou non locales. La mise en œuvre d'opérations multi-qubits nécessite des décompositions complexes en séquences d'opérations locales à un ou deux qubits, tandis que les opérations non locales peuvent être réalisées via le transport de qubits [22, 23], bien que ces processus soient coûteux. De plus, la préparation et le contrôle des états intriqués à N particules sont extrêmement sensibles à la décohérence induite par l'interaction avec l'environnement [24–27].

Dans ce contexte, le développement de protocoles efficaces pour la génération d'intrication et les opérations de calcul quantique multi-qubits, ainsi que la compréhension et la quantification des effets de décohérence, sont d'une importance capitale.

L'électrodynamique quantique en cavité (cavity QED) constitue une alternative prometteuse [28, 29]. Dans ces systèmes, des émetteurs quantiques interagissent avec un champ à l'intérieur d'une cavité aux parois hautement réfléchissantes. Ce champ, quantifié, se comporte comme un ensemble d'oscillateurs harmoniques, dont l'un est en résonance ou quasi-résonance avec une transition à deux niveaux d'un émetteur quantique, formant ainsi la base de la cavity QED.

L'objectif principal de cette thèse est d'examiner ces aspects dans le cadre des systèmes de cavity QED en régime de couplage fort. Dans ce régime, l'intensité du couplage entre les émetteurs quantiques et le mode de la cavité dépasse la largeur de raie des émetteurs et celle de la cavité. Plusieurs émetteurs peuvent ainsi se coupler à un même mode de cavité, établissant une connectivité globale à travers l'échange de bosons, facilitant ainsi les opérations non locales.

Depuis les travaux pionniers de *Pellizzari et al.* [30], de nombreux protocoles de génération d'intrication et de portes quantiques ont été proposés ou réalisés avec des atomes neutres ou des ions [31–34]. Cependant, peu de protocoles peuvent être étendus aux opérations multi-qubits [35–37].

Dans cette thèse, nous explorons une approche différente consistant à piloter directement le mode de la cavité avec un champ classique modulé temporellement, sans excitation externe des qubits. Cette méthode permet de mettre en œuvre de nouveaux protocoles de portes quantiques multi-qubits déterministes, notamment une porte de phase géométrique et une porte de phase adiabatique. Nous démontrons que ces protocoles présentent des taux d'erreur proportionnels à $N/\sqrt{C}$ en présence de pertes, avec C la coopérativité des particules individuelles.

Nous proposons également une génération d'intrication multi-qubits via un blocage de polaritons de cavité, avec une excitation globale supplémentaire agissant sur les qubits [38, 39]. Nous réalisons une analyse complète du système et caractérisons analytiquement l'erreur de préparation d'un état W, ainsi que la mise en œuvre optimale de portes CZ et $\mathrm{C_2Z}$.

La deuxième partie principale de cette thèse étudie la création d'états intriqués multiparticules robustes et préparés de manière optimale, conçus pour des applications de détection quantique même dans des environnements bruyants. Bien que les états comprimés offrent une résilience contre la décohérence, la compression seule n'est pas une condition préalable à l'obtention d'un enchevêtrement significatif pour les applications de détection. Dans notre travail, nous nous concentrons sur la préparation d'états intriqués pouvant atteindre la limite de Heisenberg pour la détection quantique dans des conditions idéales (sans bruit). Nous exploitons l'utilité de nos protocoles de porte de phase géométrique déterministes en employant des techniques de contrôle optimal, ce qui rend notre protocole de détection *influencé par le bruit* et donc optimalement robuste aux environnements bruyants dans les expériences de détection.

L'installation que nous avons en tête est illustrée à la Fig. 1. Elle se compose de N systèmes à trois niveaux avec des états de base computationnels $|0\rangle$ et $|1\rangle$, ainsi qu'un état excité $|e\rangle$ avec des fréquences de transition ω_0 et ω_1 entre $|1\rangle$ et $|0\rangle$ et entre $|e\rangle$ et $|1\rangle$, respectivement. Un mode de cavité avec des opérateurs d'annihilation (création) $\hat{a}$ ($\hat{a}^\dagger$) et une fréquence ω_c couple les états $|1\rangle$ et $|e\rangle$ avec une force de couplage g. Ce mode de cavité est excité par un champ classique (complexe) de force $\eta(t)$ selon $H_{\text{drive}} = 2|\eta(t)|\sin(\omega_L t - \arg(\eta(t)))(\hat{a}^\dagger + \hat{a})$. Ce champ classique est désaccordé par rapport à la cavité et à la transition $|1\rangle \leftrightarrow |e\rangle$ de $\delta = \omega_c - \omega_L$ et $\Delta = \omega_e - \omega_L$, respectivement.

L'Hamiltonien dans l'approximation des ondes tournantes et dans le référentiel tournant défini par $\hat{U}_r(t) = \exp\left[it(\omega_L(\hat{a}^\dagger\hat{a} + \hat{n}_e) + \sum_j \omega_0 \,|0_j\rangle\,\langle 0_j|)\right]$ s'écrit ($\hbar = 1$)

$$\hat{H}(t) = \delta\hat{a}^\dagger\hat{a} + (\Delta - i\gamma/2)\hat{n}_e + [(g\hat{S}^- + i\eta(t))\hat{a}^\dagger + \text{h.c.}], \tag{1}$$

avec $\hat{n}_e = \sum_j |e_j\rangle\langle e_j|$, $\hat{S}^+ = \sum_j |e_j\rangle\langle|1_j|$, $\hat{S}^- = \left(\hat{S}^+\right)^\dagger$ et $1/\gamma$ la durée de vie de $|e\rangle$.

Nous modélisons l'évolution du système quantique ouvert à l'aide de l'équation maîtresse de Lindblad $\dot{\rho} = -iH\rho + i\rho H^\dagger + L\rho L^\dagger - \{L^\dagger L, \rho\}/2$ avec l'opérateur de saut $L = \sqrt{\kappa}\hat{a}$ et $1/\kappa$ la durée de vie des excitations dans le mode de cavité. La décroissance de $|e\rangle$ est traitée comme une fuite de population, décrite par un terme non-hermitien dans $\hat{H}$. Pour tous les protocoles, une impulsion temporelle $\eta(t)$ de durée T avec $\eta(0) = \eta(T) = 0$ est appliquée, tandis que g, δ et Δ sont maintenus constants dans le temps.

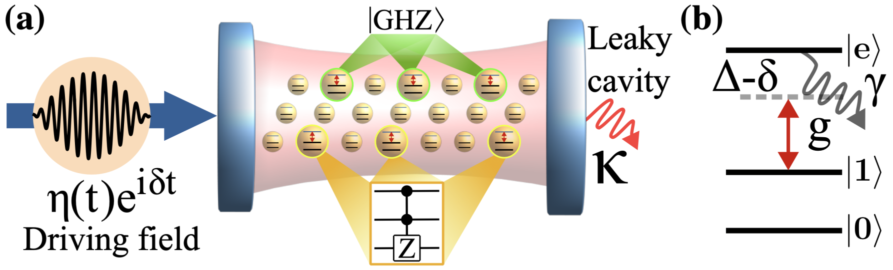

FIGURE 1: (a) Un registre de qubits est couplé à une cavité commune avec un taux de décroissance κ. En excitant simplement la cavité avec un champ classique unique $\eta(t)$ décalé de δ par rapport à la fréquence de résonance de la cavité, un état entrelacé non local comme $|\text{GHZ}\rangle$ est généré, ou, avec une séquence d'excitations, des portes non locales comme une C_2Z sont implémentées. (b) Schéma de niveaux pour chaque qubit composé des états de base computationnelle $|0\rangle$ et $|1\rangle$ (avec une durée de vie infinie), et un état excité auxiliaire $|e\rangle$ (avec une durée de vie $1/\gamma$). La transition $|1\rangle \leftrightarrow |e\rangle$ est couplée à la cavité avec une force de couplage g et décalée de la résonance de la cavité par $\Delta - \delta$.

II. Résultats et discussions

1. Nonlocal multiqubit quantum gates via a driven cavity

Dans ce travail, nous présentons deux protocoles pour réaliser des portes quantiques multi-qubits non locales et déterministes sur des qubits couplés à un mode de cavité commun. Les protocoles reposent uniquement sur une excitation classique du mode de cavité, sans nécessiter de commande externe des qubits. Appliqués à seulement deux qubits, les deux protocoles fournissent un ensemble de portes universelles pour l'informatique quantique, ainsi que des portes à un qubit. Dans le premier protocole, l'état de la cavité suit une trajectoire fermée dans l'espace des phases et accumule une phase géométrique dépendant de l'état des qubits. Cette porte de phase géométrique peut être utilisée avec des portes globales à un qubit pour générer des états GHZ de haute fidélité. Le second protocole utilise une évolution adiabatique du système combiné qubit-cavité pour accumuler une phase dynamique. Des applications répétées de ce protocole permettent de réaliser une famille de portes de phase avec des phases arbitraires, par exemple, des portes de rotation de phase et des portes multi-contrôlées-Z. Pour les deux protocoles, nous fournissons des solutions analytiques pour les taux d'erreur, qui évoluent comme $\sim N/\sqrt{C}$ en présence de pertes pertinentes, où C est la coopérativité et N est le nombre de qubits. Nos protocoles sont applicables à une variété de systèmes et peuvent être généralisés en remplaçant la cavité par un mode bosonique différent, comme un mode phononique. Nous fournissons des estimations des fidélités et durées des portes pour les qubits atomiques et moléculaires ainsi que pour les qubits superconducteurs fluxonium couplés à des cavités optiques ou micro-ondes et décrivons les implications pour la correction d'erreurs quantiques.

Le premier protocole de Porte de Phase Géométrique (protocole GPG) fonctionne dans la limite d'une excitation forte. Il implémente une porte de phase géométrique non locale multi-qubits $\exp\{(i\theta\hat{n}_1^2)\}$, avec $\hat{n}_1 = \sum_{j=1}^{N} |1_j\rangle\langle 1_j|$ l'opérateur nombre pour les qubits dans l'état $|1_j\rangle$. Pour $N = 2$, le protocole GPG forme un ensemble de portes universelles pour le calcul quantique — avec les portes à un seul qubit —, tandis que pour un N arbitraire, il peut être utilisé pour générer des états GHZ.

Le protocole GPG est opéré dans la limite $\Delta/g, \eta/g \to \infty$, avec $\Delta = \mathcal{O}(\eta)$ et $= \mathcal{O}(g)$. Dans cette limite, la dynamique du système peut être efficacement décrite par l'Hamiltonien qui est analogue à l'Hamiltonien géométrique de Molmer-Sorensen [32]. L'Hamiltonien de Molmer-Sorensen (MS) a révolutionné le domaine du traitement de l'information quantique des ions piégés, et avec ce protocole GPG, nous fournissons une réalisation généralisée de l'Hamiltonien MS pour un système général avec des systèmes à trois niveaux couplés à un mode bosonique commun, et ainsi nous l'étendons aux systèmes atome-cavité et molécule-cavité. L'Hamiltonien effectif $\hat{H}_{\text{eff}}$ est obtenu comme suit :

$$\hat{H}_{\text{eff}} = \delta\hat{a}^\dagger\hat{a} + \left(-i\frac{\gamma_1}{2} + \zeta\hat{a}^\dagger + \zeta^*\hat{a}\right)\hat{n}. \tag{2}$$

où $\zeta = g^2\alpha/\sqrt{4g^2|\alpha|^2 + \Delta^2}$, $\dot{\alpha} = -\eta - (i\delta + \kappa/2)\alpha$, $(\alpha(t = 0) = 0)$, et $\gamma_1 = \frac{\gamma}{2}(1 - \sqrt{1 - 4|\zeta|^2/g^2})$. Nous obtenons l'Hamiltonien effectif dans l'Éq.(2) à partir de l'Éq.(1) en effectuant deux transformations de base respectant les deux limites $\Delta/g \to \infty$ et $\eta/g \to \infty$.

Implémentation de portes quantiques : Nous choisissons ζ dans l'Hamiltonien effectif de l'Éq. (2) de manière telle que $\text{Re}(\zeta(t)) = -2\delta\sqrt{(2\theta/(3\delta t))}\sin^2(\pi t/T)$ et $\text{Im}(\zeta(t)) = (2\pi/T)\sqrt{(2\theta/(3\delta t))}\sin(2\pi t/T)$. Ce choix de pulse ζ, appliqué pendant une durée T, implémente l'évolution unitaire effective en l'absence de pertes ($\gamma = \kappa = 0$) donnée par $\hat{U}(T) = \exp\bigl(i\theta\hat{n}_1^2\bigr)$.

Expression analytique de la fidélité de la porte en présence de pertes : Pour évaluer les performances de la porte en présence de pertes, nous calculons la fidélité moyenne de la porte F, particulièrement dans la limite de $T \to \infty$ et $\kappa, \gamma \gg g, \delta$, où $1 - F$ est évalué analytiquement comme

$$1 - F = N\theta/\sqrt{2(1 + 2^{-N})C}, \tag{3}$$

où $C = g^2/(\kappa\gamma)$ désigne la coopérativité de la particule unique. À notre connaissance, il s'agit de la première solution analytique de $1 - F$ pour des Hamiltoniens du type de l'Éq. (2) en présence des pertes pertinentes.

Le protocole GPG peut être utilisé pour implémenter une porte CZ en choisissant $N = 2$ et $\theta = \pi/2$. L'infidélité $1 - F$ est montrée dans la Fig. 2 (a) en fonction de la durée de la pulse gT pour plusieurs valeurs de C et de rapports γ/κ. L'infidélité dans la limite $\Delta \to \infty$ (lignes pleines) atteint sa valeur asymptotique $1.99/\sqrt{C}$ déjà pour des T de l'ordre de quelques dizaines de g^{-1} et diminue le plus rapidement pour $\gamma/\kappa = 1$. Le panneau (a) montre également l'infidélité pour Δ fini (points), choisi pour une intensité de conduite maximale $\max_t|\eta(t)| = 30g$. Cette dernière est suffisante pour garantir des écarts négligeables entre les infidélités pour Δ fini et $\Delta/g \to \infty$. Le panneau (b) compare les résultats numériques (cercles) avec les résultats analytiques (ligne pointillée) pour $1 - F$ en fonction de C dans la limite $T, \Delta \to \infty$, montrant une bonne concordance pour tous les rapports γ/κ.

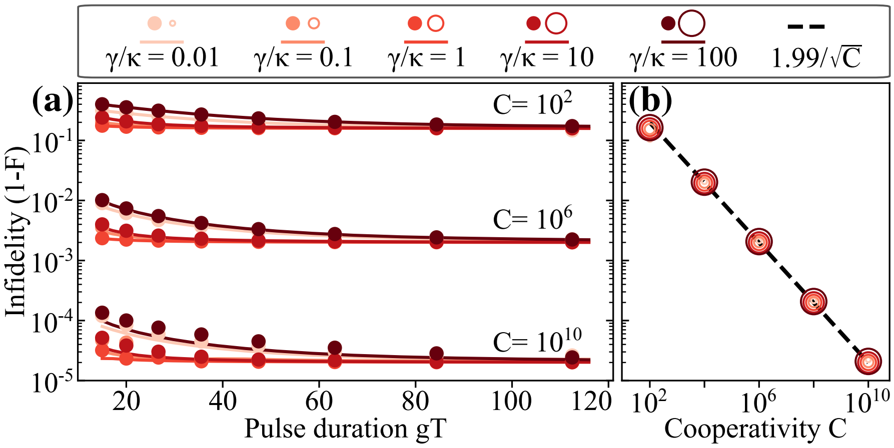

FIGURE 2: Protocole GPG : (a) Infidélité d'une porte CZ en fonction de la durée de la pulse T pour différentes valeurs de C et γ/κ. Les lignes pleines montrent l'infidélité (résultat analytique) dans la limite $\Delta/g \to \infty$, les cercles montrent l'infidélité (calcul numérique) pour une valeur finie de Δ, choisie de sorte que $\max_t |\eta(t)| = 30g$. Pour chaque T, C et γ/κ, δ est optimisé pour obtenir la valeur minimale de 1-F. (b) Valeur numérique (cercles) et analytique (ligne pointillée) de l'infidélité en fonction de C dans la limite $\Delta, T \to \infty$ pour différentes valeurs de γ/κ.

Le deuxième protocole de Porte de Phase Adiabatique (protocole APG) fonctionne dans la limite d'une excitation faible et donc dans la limite opposée à celle du protocole GPG. Il utilise une évolution adiabatique du système conjoint cavité-qubit pour implémenter une porte de phase $\exp(i\varphi(\hat{n}))$, avec $\varphi(\hat{n}) = c_1/(c_2 - \hat{n})$ pour des constantes dépendant des paramètres de l'excitation. Des applications répétées du protocole GPG, chacune avec des paramètres d'excitation différents, peuvent être utilisées pour implémenter des portes de phase avec des phases arbitraires $\varphi(\hat{n})$. Nous discutons explicitement de l'implémentation de portes de rotation de phase et de portes multi-contrôlées-Z en utilisant cette approche et montrons que leurs fidélités surpassent celles des décompositions standard de portes à un et deux qubits pour $N > 2$.

Le protocole APG utilise le même Hamiltonien que dans l'Éq. (1) que le protocole GPG, mais fonctionne pour des valeurs finies de Δ et pour $\eta \to \infty$. Nous montrons qu'une seule pulse $\eta(t)$ appliquée adiabatiquement peut être utilisée pour implémenter des portes de phase avec des phases $\varphi(\hat{n}) = -I/(\delta - \hat{n}g^2/\Delta)$, avec $I = \int_0^T |\eta(t)|^2 \mathrm{d}t$ l'énergie de la pulse.

Une combinaison de plusieurs pulses avec des décalages δ et Δ différents peut alors être utilisée pour implémenter des portes de phase avec des phases arbitraires, par exemple, des portes de rotation de phase ou des portes multi-contrôlées-Z.

Pour implémenter une porte CZ ($N = 2$), jusqu'aux portes à un qubit, I doit être choisi de manière à ce que $|\varphi_2 - 2\varphi_1 + \varphi_0| = \pi$. Étant donné ce choix, les valeurs de δ et Δ qui maximisent F peuvent être trouvées numériquement, ce qui donne $1 - F = 1.79/\sqrt{C}$. La

Fig. 3(a) montre l'infidélité en fonction de T pour une porte CZ en utilisant le protocole APG pour différentes valeurs de C et γ/κ. Pour atteindre l'adiabaticité, $\eta(t)$ est choisi pour atteindre son maximum avec des bords en forme de $\sin^2$ d'une durée $T_0 \leq T/2$. Nous trouvons que $1-F$ atteint sa valeur asymptotique $1.79/\sqrt{C}$ pour des durées de pulse $T \sim 10^2 - 10^3 g^{-1}$, tandis que pour des T plus petits, elle augmente en raison des erreurs diabatiques.

En appliquant le protocole APG $N-1$ fois avec des décalages de pulse $\delta_1, \cdots \delta_{N-1}$ et $\Delta_1, \cdots \Delta_{N-1}$ et des énergies $I_1, \cdots I_{N-1}$, tout ensemble de phases $\varphi(n)$ souhaité peut être implémenté. Nous illustrons cette procédure pour deux classes de portes multi-qubits : les portes de rotation de phase $\exp(-i\alpha Z_1 \otimes \cdots \otimes Z_n)$ – correspondant aux phases $\varphi_n = -\alpha(-1)^n$ – et les portes multi-contrôlées-Z N-qubits (portes CZ), c'est-à-dire des portes de phase avec $\varphi(N) = \pi$ et $\varphi(n) = 0$ pour $n < N$.

L'infidélité pour les deux portes multi-qubits en fonction de N est montrée dans la Fig. 3(b-c) pour différentes valeurs de γ/κ. Nous obtenons que notre protocole surpasse les implémentations utilisant des décompositions en portes CZ individuelles et en portes à un qubit (parfaites) dans les deux cas pour tout $N > 2$.

Estimations réalistes des erreurs de porte et durées des portes : Les protocoles GPG et APG peuvent être appliqués à différentes plateformes de calcul quantique. Par exemple, les états $|1\rangle$ et $|e\rangle$ peuvent être des états Rydberg couplés via un résonateur micro-ondes supraconducteur, par exemple $|1\rangle = |90^2P_{3/2}\rangle$ et $|e\rangle = |90^2S_{1/2}\rangle$ dans le Cs, avec des durées de vie de 2 ms et 820 μs, respectivement, $\omega_e \approx 2\pi \times 5$ GHz et $g \approx 2\pi \times 4$ MHz[42]. Des facteurs de qualité $Q > 3 \times 10^8$ ont été rapportés pour des résonateurs à ligne micro-ondes[43], ce qui donne $\kappa = \omega_e/Q \approx 2\pi \times 17$ Hz, $C = 5 \times 10^9$, et $\gamma/\kappa \simeq 12$. En incluant la décroissance de $|1\rangle$, l'infidélité est $1-F = 3 \times 10^{-3}$ pour une durée de pulse $T = 20/g \approx 800\,\mathrm{ns}$ pour le protocole GPG (à $\Delta = 250g$), et $1-F = 5 \times 10^{-3}$ à $T = 200/g \approx 8\,\mu$s pour le protocole APG. En utilisant les niveaux rotationnels dans l'état fondamental électronique des molécules polaires (par exemple Ca^{79}Br) au lieu des états Rydberg, des fidélités encore plus faibles peuvent être obtenues au prix d'un temps de porte plus long $T \approx 80-400, \mu$s. Des portes très rapides avec $T = 10-100$ ns et des infidélités de quelques pourcents peuvent être obtenues en utilisant des qubits atomiques dans l'état fondamental piégés dans des cavités Fabry-Perot en fibre [44–46] avec un C raisonnable ≈ 1500.

2. Entanglement-enhanced quantum sensing via optimal global control

Dans ce travail, nous étendons l'application de notre protocole de cavité GPG avec des rotations globales supplémentaires de qubits uniques et en utilisant des techniques de

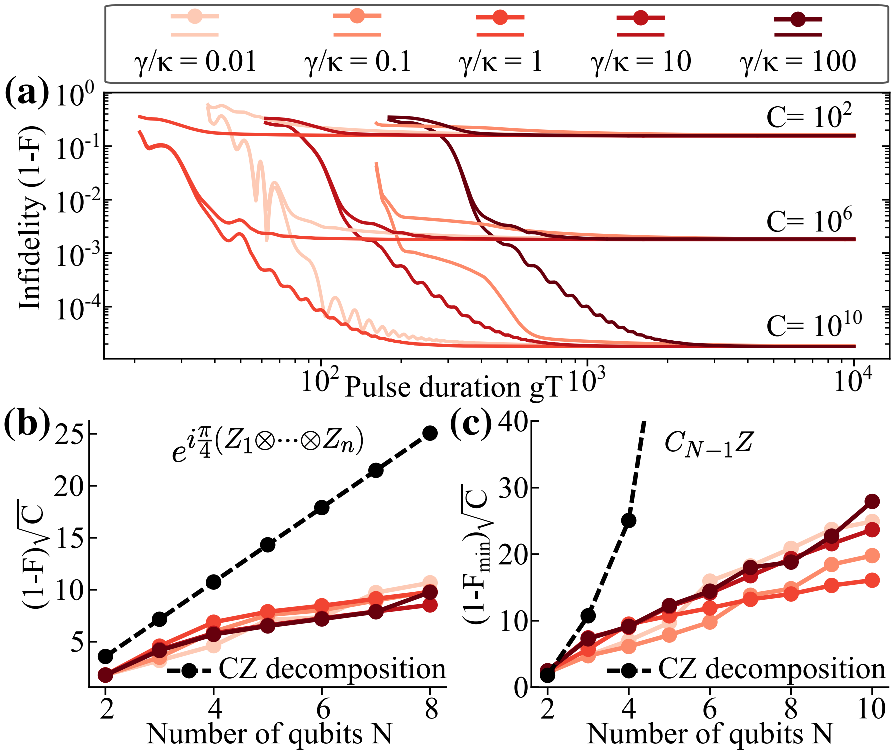

FIGURE 3: Protocole APG : (a) Infidélité (calcul numérique) pour une porte CZ en fonction de la durée de la pulse T pour différentes valeurs de C et de γ/κ. (b) Infidélité d'une porte de rotation de phase avec $\alpha = \pi/4$ dans la limite $T \to \infty$ en fonction de N. L'infidélité de la même porte est également montrée, implémentée en utilisant une décomposition en portes CZ et portes à un qubit selon le circuit de la Réf. [40]. (c) Infidélité d'une porte $\mathrm{C}_{N-1}\mathrm{Z}$ en fonction de N lorsqu'elle est implémentée en utilisant le protocole APG et par décomposition en portes CZ et portes à un qubit à l'aide d'un code Gray sans ancilla [41].

contrôle optimal pour montrer la préparation d'un état arbitraire dans le sous-espace symétrique de Dicke. Nous nous concentrons spécifiquement sur la préparation d'un état intriqué qui est métrologiquement utile pour les mesures de champ. Nous considérons un champ le long de la direction $\vec{n}$ qui est couplé aux N qubits de spin avec l'Hamiltonien d'interaction $\hat{H}_{\vec{n}} = J\hat{J}_{\vec{n}}$, avec J la force de couplage. $\hat{H}_{\vec{n}}$ est appliqué pendant un temps t tel qu'un état de sonde donné ρ soit tourné le long de l'axe du champ d'un angle $\beta = Jt$. L'objectif de l'expérience de détection de champ est d'estimer l'angle de rotation β de manière aussi précise que possible en effectuant des mesures sur les spins en utilisant un observable $\hat{M}$. Pour tout $\hat{M}$ donné (estimateur non biaisé), β peut être estimé avec une variance

$$(\Delta\beta)^2 = (\Delta\hat{M}(\beta))^2 / \left|\partial_\beta \langle \hat{M}(\beta)\rangle\right|^2 . \tag{4}$$

Le problème sur lequel nous nous concentrons est de trouver l'état de sonde *optimal* ρ_{opt} qui peut être préparé en présence de bruit pour un $\hat{H}_{\vec{n}}$ donné et un $\hat{M}$ accessible dans les expériences, c'est-à-dire un état qui minimise $(\Delta\beta)^2$. L'opération de préparation de l'état sur un état initial ρ_0 est donnée par $\rho_0 \to \mathcal{E}(\rho_0)$, avec une séquence de P étapes notée $\mathcal{E}_q = \mathcal{E}_P \cdot \mathcal{E}_{P-1} \cdots \mathcal{E}_1$, où $\mathcal{E}_j = \hat{\mathcal{U}}_j \cdot (\mathcal{E}_{gpg})_j$. Ici $(\mathcal{E}_{gpg})_j$ désigne l'application du protocole GPG en présence de pertes, $\hat{\mathcal{U}}_j = e^{-i\theta^{\alpha}j\hat{J}_z} e^{-i\theta^{\beta}j\hat{J}_y} e^{-i\theta^{\gamma}j\hat{J}_z}$ est défini comme les rotations globales de spin appliquées à l'étape j. Dans ce travail, nous commençons avec un état initial ρ_0 obtenu sous la forme $\rho_0 = \hat{\mathcal{U}}_0 \cdot \rho\mathrm{in}$ avec $\rho\mathrm{in} = |00\ldots0\rangle\langle00\ldots0|$. Nous notons l'état final obtenu par la carte d'opération comme $\rho_f = \mathcal{E}(\rho_0)$. En particulier, nous discutons des résultats de l'erreur de préparation d'état en présence de pertes dues à la cooperativité finie C lors de l'application du protocole de cavité A. Les angles optimaux $\theta_j^{(\alpha,\beta,\gamma)}$ pour $j = 1, 2, \ldots P$ ainsi que les paramètres θ_j et δ_j utilisés dans le Protocole GPG sont obtenus en utilisant la méthode d'optimisation *Broyden–Fletcher–Goldfarb–Shanno* [47, 48] avec la variance d'estimation de paramètres $(\Delta\beta)^2$ comme fonction de coût.

Nous illustrons le protocole en choisissant deux observables différentes $\hat{M}$ d'importance expérimentale : (I) la parité le long de l'axe x $\hat{M} = \bigotimes_{i=1}^{N} \hat{\sigma}_x^{(i)}$ [49, 50], et (II) le carré de l'observable de spin collectif $\hat{M} = \hat{J}_z^2$ le long de $\hat{z}$ [51]. Les choix (I) et (II) correspondent aux observables qui, pour $\kappa = \gamma = 0$, sont théoriquement connus pour saturer l'inégalité de Cramer-Rao quantique avec des états de sonde idéaux GHZ et Dicke $\left|\mathcal{D}_{N/2}^{N}\right\rangle$ pour les champs le long des directions $\vec{n} = \hat{z}$ et $\hat{y}$, respectivement [52, 53].

La figure 4 résume nos résultats pour l'optimal $(\Delta\beta)^2$ en fonction du nombre de qubits N, pour différentes cooperativités C et rapports de largeur de ligne γ/κ, calculés dans la limite $gT \to \infty$. Pour chaque N, C et γ/κ, l'optimisation est réalisée $\mathcal{O}(N)$ fois avec des paramètres initialisés de manière aléatoire et la meilleure valeur est tracée. Pour le cas (I), les états de sonde optimaux préparés avec le protocole informé par le bruit surpassent la SQL avec une variance $(\Delta\beta)^2_{\mathrm{GHZ}}$ qui évolue avec N comme $\sim N^{-1.24}$ pour des cooperativités aussi faibles que $C = 25$, comme $\sim N^{-1.52}$ pour $C = 100$, et s'approchant de la limite de Heisenberg pour $C \gtrsim 10^4$, avec une échelle $\Delta\beta^2 \sim N^{-\alpha}$ et $\alpha > 1.93$. Pour le cas (II), l'optimal $(\Delta\beta)^2_{N/2} \sim N^{-\alpha}$ évolue avec $\alpha \approx 1.4$ pour $C = 25$, $\alpha \approx 1.5$ pour $C = 10^2, 10^4$ et $\alpha \approx 1.6$ pour $C = 10^6$, montrant une amélioration considérable par rapport à la SQL pour toutes les valeurs de C. Dans tous les cas, les résultats optimaux sont essentiellement indépendants du rapport γ/κ.

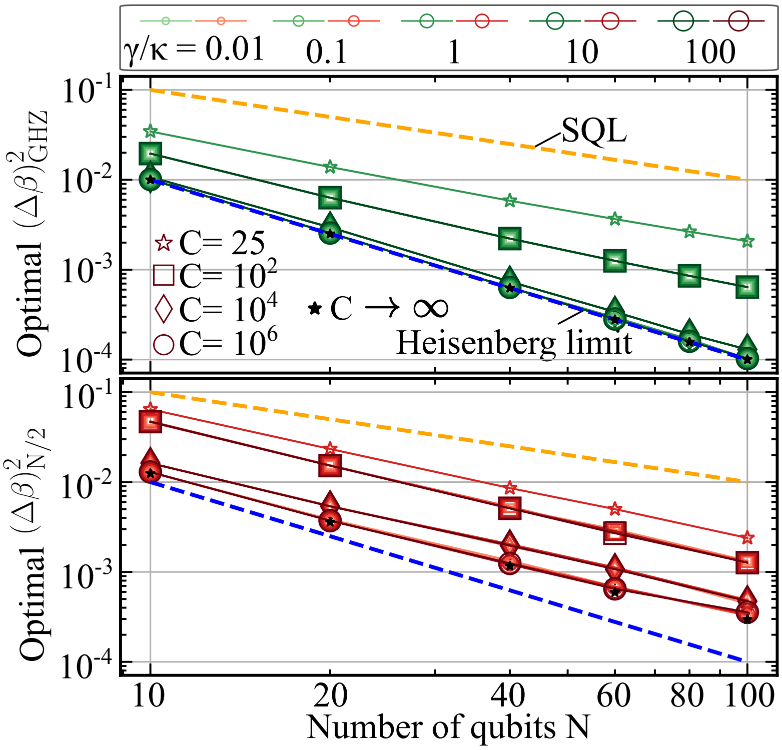

Figure 4: (Panneau supérieur) Optimal $(\Delta\beta)^2_{\mathrm{GHZ}}$ pour $P = 1$ et (panneau inférieur) $(\Delta\beta)^2_{N/2}$ pour $P = 3$, obtenus en fonction du nombre de qubits N, tracés pour des cooperativités spin-cavity $C = 25$ avec $\gamma/\kappa = 1$, et $C = 10^2, 10^4, 10^6$ avec différents rapports $\gamma/\kappa = 0.01, 0.1, 1, 10, 100$, obtenus pour le cas où $gT \to \infty$. Les états optimaux préparés en présence de C fini surpassent avec succès la SQL pour des valeurs aussi petites que $C = 25$.

3. Cavity polariton blockade for non-local entangling gates with trapped atoms

Dans ce travail, nous proposons un schéma pour réaliser des états intriqués multi-qubits de type W et des portes non-locales CZ et C_2Z via un mécanisme de blocage de polaritons dans un système de qubits atomiques couplés à un mode de cavité commun. Le blocage de polaritons est obtenu en ajustant le système, un registre de N qubits, de manière à ce qu'aucun deux atomes ne soient simultanément excités dans l'état excité du qubit, et qu'il n'y ait un couplage effectif qu'entre l'état fondamental et un état W de qubit singulièrement excité. L'étape de contrôle nécessite seulement une excitation externe du mode de cavité et une impulsion globale sur les qubits, sans besoin de traiter individuellement chaque qubit. Nous obtenons analytiquement l'erreur de préparation d'état pour un état W de N qubits, qui évolue comme $\sqrt{(1-1/N)}/\sqrt{C}$, où C est la coopérativité pour une particule. Nous montrons également l'application du mécanisme de blocage de polaritons pour réaliser une porte non-locale CZ et C_2Z en utilisant un ensemble différent d'états de qubits computationnels, et caractérisons les erreurs de porte qui évoluent comme $\sim 1/\sqrt{C}$.

III. Conclusion générale

Dans cette thèse, nous avons introduit une série de protocoles novateurs conçus pour mettre en œuvre un large éventail de portes quantiques multi-qubits non-locales et de génération d'entrelacement dans des systèmes où plusieurs émetteurs quantiques sont couplés à un mode bosonique partagé, rendant ainsi notre approche largement applicable aux configurations générales de QED de cavité. Les deux premiers protocoles clés sont le protocole de Porte de Phase Géométrique (GPG) et le protocole de Porte de Phase Adiabatique (APG)[54], pour lesquels nous avons dérivé des expressions analytiques pour les infidélités d'opération évoluant comme $\sim N/\sqrt{C}$ – en fonction du nombre de qubits N et de la coopérativité C – un paramètre clé caractérisant tout système de QED de cavité en présence de pertes dues à la fois des émetteurs et des photons de cavité vers l'environnement. Ces solutions exactes sont les premières de leur genre, et grâce à elles, nous avons démontré l'efficacité d'une classe de ces protocoles en atteignant un renforcement de l'entrelacement pour la détection quantique. En particulier, nous avons développé un protocole de préparation d'état informé par le bruit pour optimiser les états de sonde intriqués pour la détection quantique dans des environnements bruyants. Nous avons également présenté un protocole de blocage de polaritons de cavité qui facilite la génération d'entrelacement de type état W et offre des perspectives pour la réalisation de portes CZ et C_2Z optimales en temps dans les cadres de QED de cavité. Tous les protocoles reposent sur des excitations classiques simples appliquées au mode de cavité, certains utilisant également des impulsions globales sur les qubits, éliminant ainsi le besoin d'excitation individuelle des qubits. Ces approches sont conçues pour une mise en œuvre immédiate dans des expériences de pointe, en particulier celles utilisant des atomes froids dans des réseaux de pinces dans des cavités[55]. Il est important de noter que la polyvalence de nos protocoles étend leur applicabilité à une gamme de systèmes quantiques, y compris les atomes de Rydberg, les chaînes d'ions piégés, les molécules polaires et les qubits supraconducteurs, ainsi qu'à divers modèles de bruit dans notre protocole de détection informée par le bruit.

Les avancées présentées dans cette thèse non seulement jettent les bases du progrès de l'informatique quantique et de la détection renforcée par l'entrelacement sur diverses plateformes expérimentales, mais mettent également en évidence le potentiel des principales architectures de calcul quantique basées sur des systèmes d'atomes neutres, en proposant l'intégration transparente de nos protocoles simples pour des opérations multi-qubits. Plus important encore, ce travail établit les bases pour la réalisation d'applications évolutives et fiables en informatique quantique, y compris la correction d'erreurs quantiques, et prépare le terrain pour l'avenir de l'internet quantique.

Contents

List of Figures

Dedicated to my parents and sister

Chapter 1

Introduction

Entanglement generation and quantum gate operations lie at the very core of quantum information processing, driving revolutionary advances in computing and communication. From being regarded as a purely theoretical curiosity aimed at probing potential gaps in quantum mechanics [1], and later as the basis for tests comparing quantum mechanics with local realism [2–4], entanglement has now become a cornerstone of quantum technology, crucial for applications in quantum cryptography, sensing, and computation. The success of these quantum technologies relies on high-fidelity manipulation of entangled states often comprising numerous qubits, and tremendous progress has been made in the last decades in achieving control of many-body systems [5–11]. In quantum computing, achieving high-fidelity multi-qubit quantum gates is pivotal for reducing gate count and enabling fault-tolerant computation schemes tailored to specific platforms [12–14]. Similarly, in quantum sensing, multi-partite entangled states have the potential to push measurement sensitivities beyond the standard quantum limit [15–21].

However, a major challenge in realizing such capabilities lies in the challenging control of N-body systems and the fragile nature of macroscopic quantum superpositions. In quantum computing, many physical systems, including neutral atom-based setups, do not inherently support many-body or non-local operations. To realize multi-qubit operations, complex decompositions into sequences of local single- and two-qubit operations are required, and non-local operations can be realized through qubit shuttling (which has been demonstrated, for example, in neutral atom setups [22, 23]), though these are costly operations. Moreover, the preparation and control of N-particle entangled states are highly susceptible to decoherence due to interactions with the surrounding environment [24–27]. Consequently, it is of significant importance to (i) develop novel, efficient protocols for entanglement generation and multi-qubit quantum computing operations,

(ii) gain a clear understanding and quantification of decoherence effects on specific computational or sensing tasks, and (iii) devise methods to mitigate and suppress quantum noise in realistic settings.

In the context of the native availability of non-local interactions, the emergence of cavity quantum electrodynamics (cavity QED) systems offers a powerful alternative [28, 29]. In cavity QED, quantum emitters interact with the field inside a cavity with highly reflective walls. The field is quantized within the cavity, which behaves as a collection of harmonic oscillators with different frequencies, one of which is resonant or nearly resonant with a two-level transition in the quantum emitter, which behaves as a spin-like system. The coherent interactions of these spins with the field bosons of the cavity mode form the basis of cavity QED.

An interesting regime of cavity QED is the strong coupling regime, where the coupling strength between the individual quantum emitters and the cavity mode surpasses both the emitter transition linewidth and the cavity resonance linewidth. In this strong coupling regime of cavity QED, multiple emitters can couple to a single cavity mode, establishing all-to-all connectivity through boson exchange within the shared cavity mode and thus facilitating non-local operations. Since the pioneering work of *Pellizzari et al.* [30], many ideas have been proposed to harness cavity QED to perform quantum gates, but only a few can be generalised to more than two qubits. The primary objective of this thesis is to address points (i) to (iii) above within the framework of strongly coupled cavity QED systems.

Cavity QED systems in strong coupling regime for applications in quantum technologies can be realized with a range of quantum emitters interacting with corresponding resonant or near-resonant bosonic field modes, where the emitter's transition frequency is close to the field mode frequency. Atomic, molecular, and optical (AMO) systems are among the most promising candidates, offering well-controlled excitations and benefiting from significant advancements in atom cooling, trapping, and manipulation due to rapid developments in laser and computational technologies. Some of the earliest AMO systems used in cavity QED experiments involved neutral atoms excited to Rydberg states (high principal quantum number states), including circular Rydberg states (high principal quantum number and high angular momentum states) interacting with microwave photons [42, 65–75]. Another widely used platform today consists of neutral atoms with ground hyperfine energy levels interacting with optical cavity photons, which continues to make substantial progress [44–46, 50, 55, 76–79]. Polar molecules with rotational states coupled to microwave stripline coplanar waveguide cavities present another promising cavity QED setup [80–82].

Cavity QED physics can be emulated on alternative platforms that provide distinct physical settings yet exhibit similar underlying behaviour and dynamics. One such alternative is the trapped-ion systems, where the internal states of ionic quantum emitters interact with the phononic motional modes of an ion chain [6, 31, 32, 83]. In solid-state systems, superconducting qubits with microwave couplers are promising candidates for realizing cavity QED physics [84–91], and so are other quantum emitters such as nitrogen-vacancy centers in diamond [92] and emitters based on 2D materials [93, 94]. In the conceptual descriptions that follow, I primarily use the framework of neutral atom quantum emitters interacting with optical cavities.

In the remainder of this introduction, I provide a brief overview of the general topics addressed in this thesis. Section 1.1 contains a brief introduction to cavity QED, with the description of the state-of-the art fiber based fabry perot cavities. Section 1.2 discusses quantum computing protocols and entanglement-enhanced quantum sensing protocols with cavity QED systems from the literature. Lastly section 1.3 discusses the contribution of this thesis and provides an overview of the chapters.

1.1 Cavity QED: from perturbative to strong coupling era

Cavity QED started in the so called "perturbative era of cavity QED" which was based on modification of the spontaneous emission rate of an excited atomic state in the presence of boundaries as discovered by Edward Purcell[95, 96]. Purcell invoked the Fermi Golden Rule to explain that the modifications in the density of final field states available for an atom radiating near a metallic structure proportionally also modified the spontaneous emission rate by a factor of $\eta = (3/(4\pi^2))Q\lambda^3/V_c$, where Q is the cavity quality factor - a measure of how underdamped a cavity resonator is i.e which quantifies the cavity's ability to store energy relative to its rate of energy loss, V_c is the cavity mode's volume - the effective spatial region within the cavity where the electromagnetic field is confined, and λ the wavelength of the transition (same effect expected for an atom in an optical cavity). Although the η factor increases with increase in the cavity quality factor and decreasing mode volume, Purcell effect only applies in the damped cavity limit, which is limit where the cavity mode is highly lossy i.e. has a broad resonance linewidth κ, and is considered as a continuum. For even higher quality factors, the perturbative cavity QED approach no longer holds true and the atom-cavity or emitter-cavity dynamics qualitatively change and the system enters the strong coupling regime.

In the strong coupling regime of cavity QED, the quality factor Q of the cavities is pushed to the point that the photon lifetime in the cavity $1/\kappa$ would become larger than that of the excited atom in the presence of boundaries- which decreases as $(V_cQ)^{-1}$. To reach the strong coupling regime, it is hence essential to build cavities with large Q but also very small mode volume V_c such that the field per photon $\mathcal{E}_c = (\hbar\omega_c/2\epsilon_0 V_c)^{1/2}$ is as large as possible. Let the parameter measuring the coupling strength between the atom and the cavity mode be denoted by g which is proportional to $d\mathcal{E}_c$(in the units of $\hbar$), where d is the electric dipole matrix element of the atomic transition. Then the strong coupling regime is defined by the conditions $g > \kappa$ and $g > \gamma$, where γ is the spontaneous emission rate of the excited atomic state in free space.

1.1.1 Signature of strong coupling and obtaining g in experiments

The first observation of the spectacular manifestation of strong-coupling dates back to an experiment reported in 1992 [56]. In this experiment, thermal Cs atoms were passed through a cavity tuned to the atomic resonance with maximal electric field intensity at the cavity center, and the transmission of a weak probe cavity field was recorded. Let us assume that the atom has 'spin-like' internal structure with two levels $|e\rangle$ and $|g\rangle$. When no atom is coupled to the cavity, the probe spectrum is a single lorentzian peaked at the cavity frequency. In the presence of strong coupling with a single atom, the probe couples $|g, 0\rangle$ state (atom in state $|g\rangle$ and cavity in vacuum) with the dressed states $|0, +\rangle$ and $|0, -\rangle$ (hybrid atom - cavity states which are superpositions of states $|g, 1\rangle$ and $|e, 0\rangle$), and these two transitions are split by an amount $\hbar g$, known as the "vacuum Rabi splitting". The appearance of two peaks in the probe transmission spectra hence indicates the formation of the atom-photon dressed states and is a signal of strong-coupling indicating resonant energy exchanges between the atom and the cavity photons- possible when g is greater than the atomic and the cavity decay rates. Figure 1.1(a) shows the experimental probe transmission spectra reported from the 1992 experiment, and Figure 1.1(b) shows a similar spectrum obtained in a latest experiment from 2024. The stark difference between the magnitude of the vacuum Rabi splitting, which directly measures the coupling strength g of the cavity QED systems, is a positive indication of the immense technological progress made in the field over the past decades.

In the early days, experiments on cavity QED with atoms were driven by a significant fundamental interest which later on also led to their development for atom-counting technology. A probe laser beam tuned at cavity resonance is fully transmitted when the cavity is empty, and when an atom crosses the mode, the cavity response is dramatically modified. In fact, in this latter case, the laser frequency falls midway between the two Rabi peaks and the light transmission drops sharply. The laser beam is then reflected back on the entrance cavity mirror instead of being transmitted. A few years later, detection method allowed for counting of single atoms in coherent atomic waves extracted from Bose Einstein condensates with a very high efficiency [57], see Figs. 1.2(a)-1.2(b).

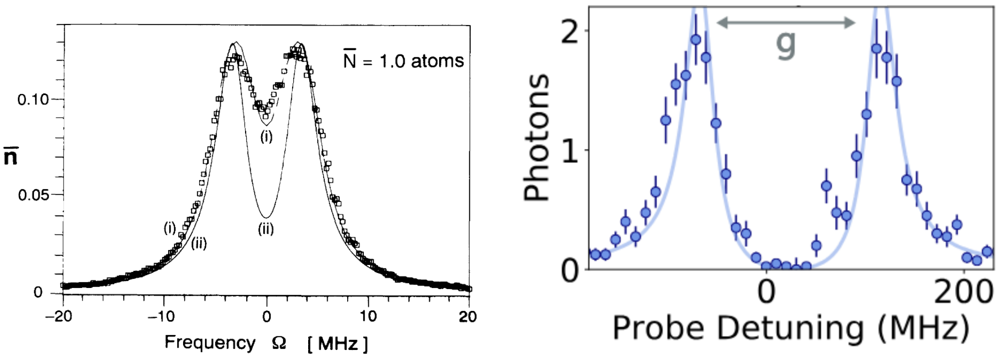

(a) (b)

FIGURE 1.1: First and the latest observation of the vacuum Rabi splitting (a)Intracavity photon number $\bar{n}$ as a function of the probe frequency Ω. The numerical points are from the experiment, curve (i) is a theoretical fit accounting for fluctuations in atom position and number, curve (ii) is the theoretical curve predicted when the atom couples to the cavity mode at the origin with maximal coupling strength g. Plot from Ref. [56], measured $g = 20.1(13)$ MHz. (b) Photon count spectra (similar to (a)) as a function of the detuning of a weak incident probe for a single atom trapped in an optical tweezer placed at a point of maximal coupling strength g with the cavity mode. Plot from Ref.[55], measured $g = 100.0(8)$ MHz.

Today, it is used to perform non-destructive qubit readout of trapped qubits interacting with cavity mode to accelerate quantum error correction schemes [39, 55, 97, 98], see Figs. 1.2(c)-1.2(d).

The coupling strength g as well as the cavity resonance linewidth are obtained by theoretical fits to the transmission spectra as shown in Fig. 1.1. The theoretical fits of the average photon number are obtained as the steady state solution of the open system dynamics in the limit of a weak probe cavity drive.

1.1.2 Fabry-Perot cavity: the simplest cavity and how they evolved

The experiments referenced above are all performed with one of the most fundamental and widely used optical cavity designs called the Fabry-Perot cavity. It consists of two mirrors, with each mirror having specific reflection and transmission properties. From a classical perspective, light bounces back and forth between these two mirrors, creating a resonant cavity where certain wavelengths constructively interfere, depending on the mirror separation and the wavelengths of the light.

The performance of a Fabry-Perot cavity is often characterized by a property known as *finesse*, which is a measure of how effectively the cavity confines light. Given the physical cavity parameters - radii of curvatures at the mirrors, reflectivities etc., the cavity finesse F depends on the cavity mirror coating reflectivity properties and is obtained as the

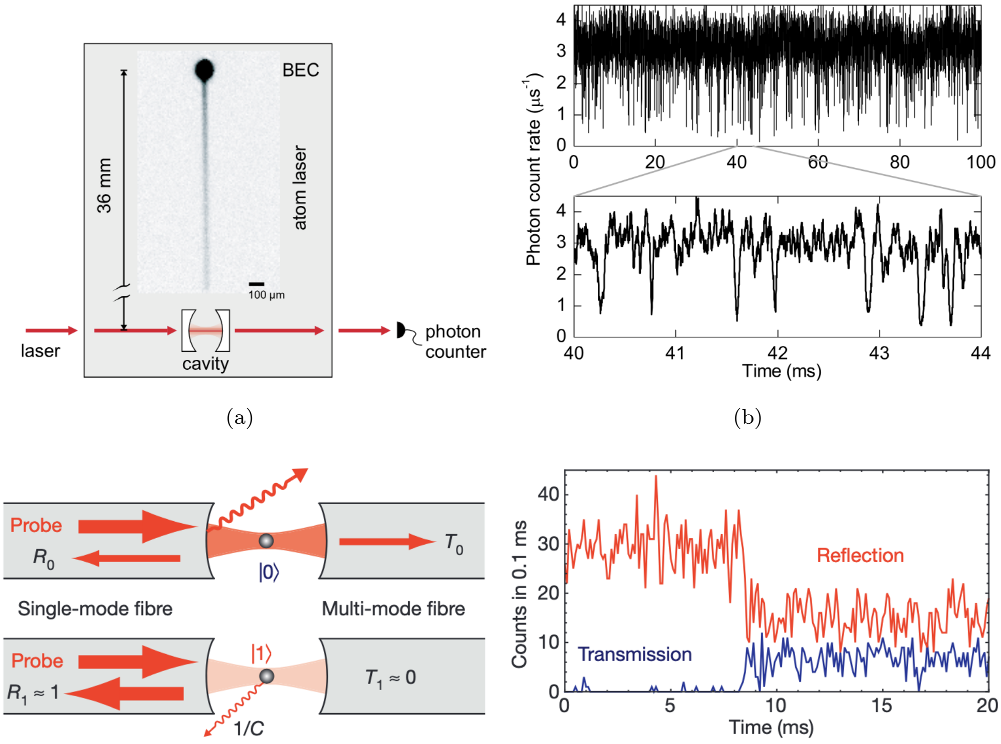

(a) (b)

(c) (d)

FIGURE 1.2: Utility advancements of cavity QED setups- from atom counting to non-destructive qubit readout. (a) Schematic of experimental setup for atom-counting experiment from Ref. [57]. An atom laser beam is released from a BEC and passed through a high finesse cavity center which is probed by a weak laser.(b) Light transmission spectrum of the cavity during the passage of the atom beam, the dips in the transmission spectrum count the single atom transits. (c) Schematic for cavity-assisted detection of atomic qubit from Ref. [39]. When the qubit is in state $|0\rangle$, the cavity probe light is mostly transmitted and when in $|1\rangle$, the incident photons are mostly reflected. (d) Photon count signal for (c) showing the cavity transmission(blue) and reflection(red) for an atom initially in $|1\rangle$ decaying to $|0\rangle$ over time.

ratio of free spectral range (frequency separation between the different cavity modes) given by $c/(2L)$ where L is the cavity length and the width of the cavity resonances κ, usually expressed as the full width at half maxima (FWHM): $\mathcal{F} = \frac{c}{2L\kappa}$, and hence can be quantitatively seen as a measure of how narrow the cavity resonances are with respect to their frequency separation. A higher finesse indicates lower scattering losses and greater light confinement, which is highly desirable in experiments.

Advances in cavity design have led to the development of fiber-based Fabry-Perot cavities. These modern cavities maintain the fundamental principles of the traditional Fabry-Perot setup but are designed with mirrors integrated into optical fibers, significantly reducing the physical size of the cavity and improving its performance. One of the primary advantages of fiber-based cavities is their ability to achieve small radii of curvature (ROC) and small cavity lengths at the same time, which leads to exceptionally small mode waists (typically in the range of $1 - 2\,\mu$m) and mode volumes V_c around λ^3, where λ is the wavelength of the light. These compact mode volumes allow for high single-mode coupling efficiencies with any quantum emitter inside the cavity making fiber-based Fabry-Perot cavities highly effective in cavity QED experiments, especially when precise control and coupling of photons are required.

In pioneering works on fiber-based Fabry-Perot cavities, high finesse values of $F = 37000 \pm 5000$ is achieved in these compact cavities [44]. These large values of F are crucial for advancing cavity QED applications, as fiber-based cavities can achieve both high finesse and tunability while maintaining stable coupling to single-mode optical fibers.

Table 1.1 illustrates the advancements in cavity technology between 2005 and 2024, showing how improvements in cavity mode coupling strength (by decreasing mode waists while maintaining high finesse) reflect the continuous progress in cavity engineering, enabling ever-greater precision and performance in state-of-the-art cavity QED experiments.

Year	atoms	L	ROC	ω_r	V_c	g	Finesse
2005 [57]	1	$178\,\mu$m	77.5 mm	$26\,\mu$m	$2\times10^5\lambda^3$	65.4 MHz	300 000
2024 [55]	20	$100\,\mu$m	$145 - 165\,\mu$m	$4.28\,\mu$m	$3000\ \lambda^3$	100.0(8)MHz	25 904

Table 1.1: Advancements in optical cavity technology between 2005 and 2024, illustrating improvements in atom trapping capabilities in terms of sytem size, cavity length L, radii of curvatures (ROC) of cavity mirrors, mode waist ω_r, mode volume V_c for $\lambda = 780\,$nm, coupling strength g with ^{87}Rb $F = 2 \rightarrow F' = 3$ D_2 transition line and cavity finesse. Note that the state of the art experiments based on fiber based Fabry-perot cavities can trap ~ 20 atoms while maintaining very small mode volume.

1.1.3 Technical progress in microwave based cavities

Substantial technical advancements have been made in the development of microwave-based cavities in recent years. One prominent category includes chip-based coplanar waveguide (CPW) microwave resonators [66, 99], with state-of-the-art CPW resonators now achieving quality factors exceeding $Q > 3 \times 10^8$ [43]. Significant efforts are also focused on the construction of 3D microwave cavities for quantum information processing. Initially developed as superconducting photon boxes [5, 100], these 3D microwave cavities have benefited from considerable technical advancements, resulting in ultra-high-quality factors in modern implementations [101–106].

1.2 Quantum information processing and quantum sensing with cavity QED systems

In this section, we discuss the existing results from literature on various applications of cavity QED systems in the context of quantum computing and quantum sensing. In section 1.2.1, we discuss the various cavity-mediated gate protocols and their performances from the literature. In section 1.2.2, we motivate quantum sensing applications with multi-partite entangled states and discuss the success of cavity QED systems in achieving a quantum advantage in sensing.

1.2.1 Cavity-mediated non-local quantum gates

The implementation of quantum gates between qubits in a cavity QED architecture is fundamentally motivated by the inherent all-to-all connectivity among qubits, which facilitates the realization of non-local quantum gates involving two or more qubits. This all-to-all connectivity can significantly reduce the circuit depth of typical quantum circuits when compared to geometrically local connectivity [58]. Fig. 1.3 demonstrates the drastic reduction in circuit depths as a function of problem size with increasingly connected architechtures. Moreover, the capacity to perform non-local multi-qubit gates may enhance the applicability of quantum error correction (QEC) codes with non-local stabilizers, such as with recently proposed low-density parity-check (LDPC) codes [107–111], which offer substantially lower overhead than the conventional surface codes for QEC [112].

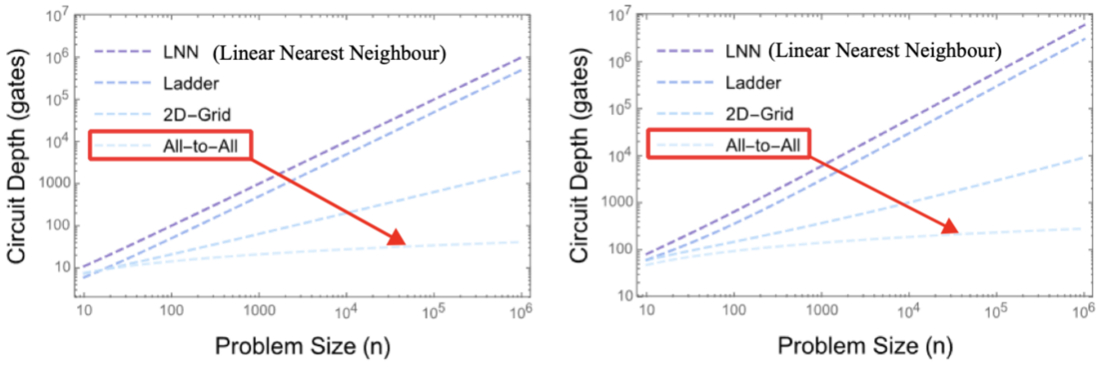

Jordan-Wigner String Grover's Diffusion Operator

FIGURE 1.3: Impact of qubit connectivity on quantum algorithm performance of important quantum algorithms. Figure from Ref. [58]

The basic idea of a two-qubit cavity-mediated quantum gate can be imagined with the proposed setup of Ref. [30] shown in Figure 1.4, which assumes atomic qubits with individual atom control, and is as follows: a laser directed at an atom can manipulate its state, thereby controlling the photon emission from the atom into the cavity mode. The emitted photon depends on the atom's state and can be absorbed by another atom coupled to the same cavity mode, conditional on the state of both the second atom and the photon. This cavity-mediated state-dependent exchange of photons results in an entangling two-qubit operation between the two atoms. The latter can be then used to generate two-qubit gates between any pair of atoms in the cavity.

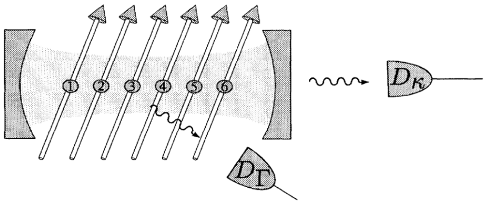

FIGURE 1.4: Schematic of setup for quantum computer based on atomic qubits communicating via interaction with a single quantized cavity mode. Figure from Ref. [30]

After the first proposal a non-local gate in cavity QED by *Pellizzari et al.* [30], many other proposals of non-local gates in cavity QED architechtures have been proposed or realized with neutral atoms or ions by mediating interactions between qubits via a quantized bosonic mode, using motional modes of trapped ions [31–34] or optical cavity modes for neutral atom spin qubits [30, 35, 37, 59, 113–116]. Below, I present a comprehensive list of proposals involving atoms and optical cavities from prior work.

Before proceeding, I introduce here cooperativity C which is a key parameter to characterise qubit-cavity mode coupling strength g relative to photon loss rate κ and spontaneous emission of the qubit γ, and is given by $C \sim g^2/(\kappa\gamma)$. It is hence used to also characterise the performance of any quantum operation involving coherent exchange between the qubit emmitters and cavity mode. The term used for this is the gate operation *fidelity* F, which is the measure of how accurately the gate performs its intended transformation, generally quantified as the overlap between the desired output state and the actual output state. Higher fidelity indicates less deviation from the ideal operation. For examples stated below, the fidelity of a quantum gate or entangling operation is expressed in terms of cooperativity.

- **Measurement-induced probabilistic entanglement generation**

  Many early protocols for non-local entanglement-generation with atoms in optical cavities setups are probabilistic and are based on *measurement induced entanglement* which necessarily require high efficiency photon detectors for high fidelity [36, 117–119].

  For example, the protocol in Ref. [117] for entangling two two-level atoms (labelled a and b, with levels $|0\rangle$ and $|1\rangle$) in the cavity is based on simply understanding the eigenstates of the two-atom plus cavity system - among the three dressed states, one is a stationary state $|\lambda_0\rangle$ which has a zero eigenvalue, whereas the other two, where the cavity is populated, decay in time (the cavity decay channel is assumed much stronger than the atomic decay channel). The stationary state here is in fact a tensor product state of the cavity in vacuum and the maximally entangled atomic state: $|\lambda\rangle = |0\rangle_{\text{cav}} \frac{|0\rangle_a|1\rangle_b - |1\rangle_a|0\rangle_b}{\sqrt{2}}$, and one hence needs a mechanism that destroys population in the cavity mode, which is done by using a leaky cavity and detecting all photons coming out through the mirrors. The protocol starts by preparing the system in the state $|0\rangle_{\text{cav}}|1\rangle_a|0\rangle_b$ (assuming individual laser addressing of atoms) and relies on the efficient detection of a single photon leaking out of the cavity : if a photon is detected, the system is in the ground state $|0\rangle_{\text{cav}}|0\rangle_a|0\rangle_b$ and the experiment has to be repeated, but if not, the system goes into a state which cannot decay - that is the atoms should end up in the entangled state. This protocol was further extended to propose *teleportation* of the state of an atom trapped in a cavity to a second atom trapped in a distant cavity, in Ref. [118]. Note that here the success probablity of the protocol is 50 %, owing to the fact that the overlap of the initial state with $|\lambda_0\rangle$ is precisely 1/2.

In a later work (Ref. [119]), an improved protocol was proposed, incorporating three energy levels in each atom arranged in a Λ configuration. In this setup, the transition $|L\rangle \leftrightarrow |e\rangle$ is coupled to left-circularly polarized light, while $|R\rangle \leftrightarrow |e\rangle$ is coupled to right-circularly polarized light. Both atoms are symmetrically prepared in the same state, and a left-circularly polarized photon is injected into the cavity. This photon can be absorbed by either atom, and detection of a right-circularly polarized photon leaking from the cavity confirms an entangled state, an equal superposition of states with one atom in $|L\rangle$ and the other in $|R\rangle$. Unlike the previous protocol, this approach does not require an initially antisymmetric atomic state and allows the experiment to be repeated by simply reinjecting another photon, a feature absent in the prior proposal. However, it requires a reliable source of single left-circularly polarized photons and efficient single-photon detection. Like the previous approach, it is probabilistic, with an estimated success probability of $p \approxeq 0.45$. Yet, since the experiment can be easily looped by connecting the left-circularly polarisation photon path back to the cavity, and since the failure probability $(1-p)^n$ exponentially decreases with number of trials n, the protocol is also termed as quasi-deterministic.

These and similar protocols inspired efforts to entangle large macroscopic atomic ensembles [120, 121] using similar measurement-based probabilistic protocols, where high fidelity is achieved only through repeated trials.

Finally, Ref. [36] proposes an efficient scheme for multi-atom entanglement using four-level atomic systems without requiring individual atom addressing, though it also relies on detecting cavity decay through single-photon detectors, with a success probability of $p = 1/2$ in the ideal case of unit-efficiency detectors.

In all these proposals, since the protocols depend on detecting cavity decay events, the cavity decay channel is assumed to be significantly stronger than atomic decay, allowing for rapid detection, while spontaneous emission from the atoms is considered small or negligible.

- **Deterministic entanglement generation and quantum gate operation between two atoms**

  For measurement-induced but deterministic entanglement generation the fidelity scales as $\sim (1/C)\log(C)$ and for deterministic two-qubit gates, prior art finds the fidelity error as $\mathcal{O}(C^{-1})$ [115].

  I first describe here the entanglement generation protocol in Ref. [115] which is also measurement-induced but deterministic. This protocol uses a three-level atomic system with two stable ground levels, $|g\rangle$ and $|f\rangle$, and an excited level $|e\rangle$. The protocol starts with an equal superposition state of the two ground states for both atoms. The two-atom state is written as $|\psi\rangle = (|gg\rangle + |gf\rangle + |fg\rangle + |ff\rangle)/2$. By performing an atom-counting measurement or a quantum nondemolition (QND) measurement (similar to those discussed in Section 1.1.1), which measures the number of atoms N in state $|f\rangle$, the state vector is projected into the maximally entangled state $|\psi_{\text{EPR}}\rangle = (|gf\rangle + |fg\rangle)/\sqrt{2}$, provided $N = 1$ is measured. . This was one of the first works to report the scaling of the entanglement generation fidelity F with the cavity QED parameters, including the spontaneous emission rate of the atoms. The fidelity here is expressed as F= $\langle\psi_{\text{EPR}}|\rho|\psi_{\text{EPR}}\rangle$, where ρ is the atomic density matrix, and the error scaling is obtained as $1 - F \sim (1/C)\log(C)$, valid up to a success rate of $p = 50\,\%$. Unlike previous protocols, this approach uses only coherent light sources and homodyne detection, making it more efficient and allowing for deterministic entanglement generation with two measurements on average. Furthermore, using this deterministic entanglement generation protocol, a two-qubit *controlled-NOT* gate protocol is proposed, which requires additional levels and a similar homodyne detection of light. This achieves a similar error scaling as above for entanglement generation.

  Another strategy for quantum gates in optical cavities in this category is based on constructing controlled interactions between the atoms and the cavity field [30, 113, 122] (including the pioneering work from 1995). These are based on the basic idea that we discussed earlier, assuming individual control of atoms: controlled emission of a photon from an atom, which can be absorbed by another atom. For these deterministic gate protocols, the error scales as $1-\mathrm{F} \sim \mathcal{O}(C^{-1/2})$ [115].

I briefly present here the protocol from Ref. [113], which realizes a controlled-NOT (CNOT) operation between two three-level atoms in a cavity QED setup. First, an entangling operation is realized between the atoms using just two levels in each: let $|g_j\rangle$ and $|e_j\rangle, (j = 1, 2)$ denote the ground and excited states of the jth atom. Assuming a dispersive interaction between $|g_j\rangle \leftrightarrow |e_j\rangle$ and the cavity mode with a detuning Δ between the atomic transition and cavity mode frequencies, a Hamiltonian is obtained with photon-number-dependent Stark shifts on the levels $|g_j\rangle, |e_j\rangle$ and a direct dipole coupling term between the two atoms induced by the cavity mode. All these terms in the Hamiltonian scale with $\lambda = g^2/\Delta$. Further assuming the cavity starts in vacuum, the following interaction Hamiltonian is realized:

$$\hat{H}_{\text{int}} = \lambda \left[\sum_{j=1,2} |e_j\rangle\langle e_j| + (\hat{\sigma}_1^+ \hat{\sigma}_2^- + \hat{\sigma}_1^- \hat{\sigma}_2^+) \right], \tag{1.1}$$

where $\hat{\sigma}_j^+ = |e_j\rangle\langle g_j|$. With this interaction Hamiltonian, the following state evolution is realized for an initial state $|e_1\rangle|g_2\rangle$ for the two-atom system:

$$|e_1\rangle|g_2\rangle \to e^{-i\lambda t}[\cos(\lambda t)|e_1\rangle|g_2\rangle - i\sin(\lambda t)|g_1\rangle|e_2\rangle]. \tag{1.2}$$

For an evolution time of $t = \pi/(4\lambda)$, the final state obtained is the maximally entangled Bell state: $|\psi\rangle = (|e_1\rangle|g_2\rangle - i|g_1\rangle|e_2\rangle)/\sqrt{2}$. Now, to realize a CNOT gate, three levels are assumed in a ladder configuration with an extra level denoted by $|i_j\rangle$ such that the $|e_j\rangle \leftrightarrow |i_j\rangle$ transition is highly detuned from the cavity mode and is not affected by it. Let atom 1 be the control atom and atom 2 the target atom. Assuming two individual classical drives on atom 2 in free space tuned to the transitions $|g_2\rangle \leftrightarrow |e_2\rangle$ and $|e_2\rangle \leftrightarrow |i_2\rangle$, the computational states in atom 2 can be made to evolve as follows (with appropriate amplitudes, phases, and times of the classical drive):

$$\begin{aligned} |e_2\rangle &\to \frac{1}{\sqrt{2}}(|e_2\rangle + |g_2\rangle) \to \frac{1}{\sqrt{2}}(|i_2\rangle + |g_2\rangle) \\ |g_2\rangle &\to \frac{1}{\sqrt{2}}(|g_2\rangle - |e_2\rangle) \to \frac{1}{\sqrt{2}}(|g_2\rangle - |i_2\rangle). \end{aligned} \tag{1.3}$$

Now, both atoms are made to interact with the cavity (by moving them simultaneously inside the cavity). The interaction Hamiltonian does not cause any cavity-induced dynamics for the states $|g_1\rangle|g_2\rangle$ and $|g_1\rangle|i_2\rangle$, but the state $|e_1\rangle|i_2\rangle$ acquires a phase of $e^{-i\lambda t}$, while the state $|e_1\rangle|g_2\rangle$ undergoes evolution according to

Eq. (1.2). After an interaction time of π/λ, the following operations are realized:

$$\begin{aligned} |e_1\rangle|i_2\rangle &\rightarrow -|e_1\rangle|i_2\rangle \\ |e_1\rangle|g_2\rangle &\rightarrow |e_1\rangle|g_2\rangle. \end{aligned} \tag{1.4}$$

Now, two classical drives are applied again on atom 2, which are tuned to $|e_2\rangle \rightarrow |i_2\rangle$ and $|g_2\rangle \rightarrow |e_2\rangle$ transitions, respectively. Choosing appropriate amplitudes and phases, one obtains

$$\begin{aligned} |g_2\rangle &\rightarrow \frac{1}{\sqrt{2}}(|g_2\rangle + |e_2\rangle) \\ |i_2\rangle &\rightarrow |e_2\rangle \rightarrow \frac{1}{\sqrt{2}}(|e_2\rangle - |g_2\rangle). \end{aligned} \tag{1.5}$$

Overall, the two-atom computational states undergo the transformation:

$$\begin{aligned} |g_1\rangle|g_2\rangle &\rightarrow |g_1\rangle|g_2\rangle, \\ |g_1\rangle|e_2\rangle &\rightarrow |g_1\rangle|e_2\rangle, \\ |e_1\rangle|g_2\rangle &\rightarrow |e_1\rangle|e_2\rangle, \\ |e_1\rangle|e_2\rangle &\rightarrow |e_1\rangle|g_2\rangle. \end{aligned} \tag{1.6}$$

This transformation corresponds to the CNOT gate operation, in which, if and only if the control atom (atom 1) is in state $|e\rangle$, the target atom (atom 2) flips its state. Note that in all these proposals for realizing deterministic two-qubit quantum gates, individual qubit control with classical laser fields selectively addressing a qubit is required.

- **Heralding entanglement generation**

  Another class of relatively recent proposals is based on *heralding* [35, 37, 59] — where successful cavity-mediated single-photon transfers are indicated by the detection of an auxiliary particle or signal (often a photon). This detected signal serves as a "herald" or a sign that an expected quantum operation has occurred successfully without disturbing the system's primary quantum state. These protocols also require additional detector resources, where non-local gates are achievable with error $\mathcal{O}(C^{-1})$ but with a failure probability of $\mathcal{O}(C^{-1/2})$ [35]. A recent scheme using heralded photon transfers has an improved success probability but places stringent requirements on the level structure of the qubits so that all scattering and photon loss events are detectable [59].

  In Ref. [59], the authors propose a cavity QED architecture with local nodes consisting of a memory qubit and a communication qubit, where the communication qubits can be non-locally connected via cavity-mediated interactions, see

Fig. 1.5(a). Figure 1.5(c) summarizes the protocol for realizing a non-local CNOT gate between distant memory qubits at nodes A and B by first generating cavity-mediated non-local entanglement between the communication qubits at A and B, and then applying local CNOT gates and single qubit operations at each node. Figure 1.5(b) shows the level scheme for the communication qubits showing the cavity coupled and laser coupled transitions with strength g_i and Rabi frequency Ω_i, respectively, where i denotes the node index. The entanglement generation protocol starts with the communication qubit at A in an equal superposition of $|r_0\rangle$ and $|r_1\rangle$, the qubit at B in $|0\rangle$, while all other communication qubits are stored in $|1\rangle$, which do not couple to the cavity, and the environment E of modes external to the cavity is in the vacuum state. A photon is transferred from A to B, conditioned on A being in $|r_0\rangle_A$ using a resonant stimulated Raman adiabatic passage (STIRAP) by ramping up Ω_A while ramping down Ω_B. During this transfer, the photon may also leak out of the cavity or scatter off $|e\rangle$ states to $|0\rangle$ or $|1\rangle$ states in the ground manifold, hence resulting in the state

$$|\psi\rangle = \frac{1}{\sqrt{2}}(\alpha|0\rangle_A|r_0\rangle_B|\mathrm{vac}\rangle_E + \beta|\mathrm{Loss}\rangle) + \frac{1}{\sqrt{2}}|r_1\rangle_A|0\rangle_B|\mathrm{vac}\rangle_E, \tag{1.7}$$

where $|\mathrm{Loss}\rangle$ is a generic state where the photon has scattered into a mode outside the cavity and atoms A and B are left in a collection of ground states. Following this, local swap operations are performed on A and B to swap the states $|r_0\rangle$ and $|r_1\rangle$, and also the two ground states in A, resulting in (note that these operations map the $|\mathrm{Loss}\rangle$ state into itself, as the atoms A and B cannot evolve out of their ground states in this operation):

$$|\psi\rangle = \frac{1}{\sqrt{2}}(\alpha|1\rangle_A|r_1\rangle_B|\mathrm{vac}\rangle_E + \beta|\mathrm{Loss}\rangle) + \frac{1}{\sqrt{2}}|r_0\rangle_A|0\rangle_B|\mathrm{vac}\rangle_E, \tag{1.8}$$

Now a second STIRAP sequence is applied which affects only the last term, giving:

$$|\psi\rangle = \frac{1}{\sqrt{2}}(\alpha|1\rangle_A|r_1\rangle_B|\mathrm{vac}\rangle_E + |0\rangle_A|r_0\rangle_B|\mathrm{vac}\rangle_E) + \beta\frac{1}{\sqrt{2}}(|\mathrm{Loss}\rangle + |\mathrm{Loss}'\rangle), \tag{1.9}$$

where $|\mathrm{Loss}'\rangle$ is the photon scatterred state in the second STIRAP. An entangled state is hence achieved within the α component of $|\psi\rangle$. Measuring whether or not atom B occupies a ground state projects $|\psi\rangle$ into either the entangled state or the loss state, hence heralding the generation of the entangled state upon obtaining an empty B ground state.

State-of-the-art two-qubit quantum gates, which have been realized with a neutral atom-based cavity QED setup [55], propose a protocol that heralds success based on atomic state, without needing additional photon detection.

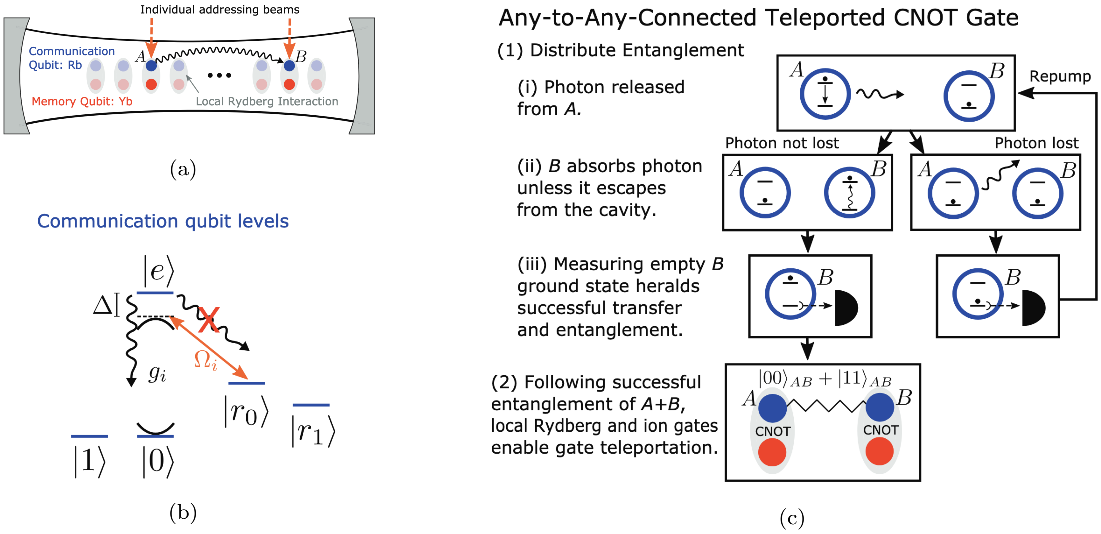

(a)

(b)

(c)

FIGURE 1.5: (a) Proposed architecture for cavity-mediated quantum gate between any two qubits from Ref. [59]. (b) Atomic level scheme for communication qubits. Excited state $|e\rangle$ decays to $|r_0\rangle$ and $|r_1\rangle$ are suppressed. (c) Entanglement generation scheme between distant communication qubits (in blue). Subsequent high-fidelity local operations enable a teleported quantum gate between distant memory qubits (in red). Figure from Ref. [59].

- **Entangled fixed points**

  In contrast, non-local entangled states can be prepared as fixed points of dissipative maps with an $\mathcal{O}(C^{-1})$ fidelity error [123], though a fixed phase relation must be maintained between the fields addressing the qubits.

While some of the proposals above can be extended to N-qubit Toffoli gates [35–37], for large scale digital quantum simulations and computing a unified approach that provides native implementations of larger families of multi-qubit gates would be highly desirable.

1.2.2 Cavity-mediated entanglement generation for quantum sensing

Quantum sensing leverages the principles of quantum mechanics to achieve measurement precision beyond the capabilities of classical sensors. While classical sensors are limited by the standard quantum limit (SQL), which sets a bound on their precision, quantum-enhanced sensors utilize entangled states or those with nonclassical correlations, to overcome these limitations. By exploiting multi-partite entanglement, quantum sensors can achieve measurement precision that scales more efficiently than classical systems, reaching the Heisenberg limit. At this limit, the precision improves from the $1/\sqrt{N}$ scaling of the SQL to $1/N$, which represents the fundamental limit for quantum measurements. The ultimate goal of quantum sensing is to harness entanglement-enhanced techniques to reach this fundamental limit, making entanglement-enhanced sensing the "Holy Grail" of quantum-powered sensing applications.

However, typically the entangled probe states are fragile to errors, posing challenges to quantum sensors that need to be simultaneously sensitive to the unknown field strength they are measuring but insensitive to noise. There are even limits, at least asymptotically, to the improvement quantum error correction can provide to remedy errors [124, 125] (although see [126]). Indeed, experiments have so far relied on preparing simpler, spin squeezed states that are somewhat robust to noise, but that achieve measurement uncertainties scaling only moderately better than the SQL [50, 76–79, 127].

Many proposals for quantum-enhanced sensors, similar to gate proposals using atom-light interactions in cavity QED systems, have concentrated on creating entangled atomic states via processes where the optical electromagnetic field primarily serves as a mediator of interactions between atoms [128–134]. In the microwave domain, however, atom-light interactions have often been used more directly, such as in experiments with Rydberg atoms [133, 134].

Overall, cavity QED serves as a powerful platform for advancing quantum sensing, allowing for the precise manipulation of atom-light interactions essential for achieving entangled states necessary for measurements approaching the Heisenberg limit.

1.3 Contribution of this thesis

In nearly all gate proposals referenced in Sec. 1.2.1, entangling quantum gates are realized by a direct drive of the qubits via a free space mode, e.g. a laser, to turn the interaction between the qubits on or off. In this thesis, we propose and explore a different approach based on simply driving the cavity mode directly with a classical field that is modulated time-dependently, without requiring an external drive of the qubits. We find that this approach enables entirely new protocols for the implementation of large families of deterministic non-local multi-qubit quantum gates - namely a new geometric phase gate protocol and new adiabatic phase gate protocol. Applied to just two qubits, the protocols provide, together with single qubit gates, a universal gate set for quantum computing. For both protocols, we provide analytic solutions for the error rates, which scale as $\sim N/\sqrt{C}$ in the presence of relevant losses, with C the cooperativity and N the qubit number. To our knowledge, these are the first of its kind exact analytic solutions of protocol fidelities. This error scaling of $\mathcal{O}(C^{-1/2})$ is similar to the protocols driving the qubits directly. Applied to more than two qubits, however, each protocol provides a family of deterministic, multi-qubit non-local gates requiring minimal control, showing a unique combination of desirable features such as versatility in gate design, speed, and robustness. Our protocols are applicable to a variety of systems and can be generalized by replacing the cavity by a different bosonic mode, such as a phononic mode. We provide estimates of gate fidelities and durations for atomic and molecular qubits as well as superconducting fluxonium qubits coupled to optical or microwave cavities.

Additionally, with close relation with recent experimental efforts employing quantum zeno dynamics based deterministic entanglement generation [38, 39], we propose deterministic multi-qubit entanglement generation via a non-local cavity polariton blockade with an additional global drive acting on the qubits. In this work, we perform a full quantum-mechanical treatment of the system and characterise analytically the state preparation error of a so-called W state, and also demonstrate the possibility to realize time-optimal CZ and C_2Z gates for two and three qubits, using a new cavity blockade interaction method, for all of which the errors scale as $\mathcal{O}(C^{-1/2})$.

The second major part of this thesis investigates the creation of robust, optimally prepared multi-particle entangled states designed for quantum sensing applications even in noisy environments. While squeezed states do offer resilience against decoherence, squeezing alone is not a prerequisite for achieving significant entanglement for sensing applications. In our work, we focus on preparing entangled states that can attain the Heisenberg limit for quantum sensing under ideal (noise-free) conditions. In this work, we leverage the utility of our determistic geometric-phase-gate protocols by employing optimal control techniques, which make our sensing protocol *noise-informed* and hence optimally robust to noisy environment in sensing experiments.

Below, I provide an overview of the chapters in this thesis, also describing the contribution of each.

Chapter 2 provides a theoretical background of all concepts and calculations used in this thesis. This includes introductory quantum optics, open quantum systems, and optimal control methods.

Chapter 3 discusses the cavity QED model Hamiltonain and components used throughout in this thesis. Some precise example systems where the model has already been realised or can poetntially be realised are presented.

Chapter 4, discusses the geometric phase gate (GPG) protocol proposed with the cavity QED setup described in chapter 3. The GPG protocol operates in the limit of a strong drive on the cavity. It implements a family of geometric phase gates $\hat{U}_A = \exp\big(i\theta\hat{n}^2\big)$, where $\hat{n}$ is the number operator of qubits in state $|1\rangle$, by displacing the state of cavity in a closed loop in phase space. We provide analytic solutions for the error rates, which scale as $\sim N/\sqrt{C}$ with C the cooperativity and N the qubit number, show how a multi-qubit GHZ state can be generated with the GPG protocol and discuss the gate performance for the case of inhomogeneous cavity coupling stengths. Lastly, estimates of gate fidelities and durations for atomic and molecular qubits coupled to optical or microwave cavities are provided, and applications for quantum error correction are suggested.

Chapter 5, presents a deterministic protocol for the preparation of arbitrary entangled states in the symmetric Dicke subspace of N spins coupled to a common cavity mode. By combining the geometric phase gate (GPG) protocol, its analytic solution of the noisy quantum channel dynamics and optimal control methods, the protocol prepares entangled states that are useful for quantum sensing, achieving a precision significantly better than the standard quantum limit in the presence of photon cavity loss, spontaneous emission and dephasing. This work opens the way to entanglement-enhanced sensing with cold trapped atoms in cavities and is also directly relevant for experiments with trapped ions.

In Chapter 6, a second protocol - namely the adiabatic phase gate (APG) protocol is discussed. The APG protocol operates in the limit of a weak drive and thus in the opposite limit of the GPG protocol. It makes use of an adiabatic evolution of the joint cavity-qubit system to implement a family of phase gates $\hat{U}_B = \exp[ic_1/(c_2\hat{n})]$, where c_1 and c_2 are parameters depending on the intensity, duration and detuning of the applied drive. Repeated applications of this protocol allow for the realization of a family of phase gates with arbitrary phases, e.g. phase-rotation gates and multi-controlled-Z gates. An analytic solution of the gate error rate scaling as $\sim N/\sqrt{C}$, similarly as for the GPG protocol is obtained.

Chapter 7, discusses a cavity polariton blockade based approach, again in the limit of a weak cavity drive, and an additional free-space coupling between the qubit computational states. The polariton blockade is achieved by tuning the system, an $N-$qubit register, such that no two atoms are simultaneously excited to the qubit excited state, and there is an effective coupling only between the ground state and a singly-excited W state of the qubit register. The state preparation error is analytically obtained for an $N-$qubit W state which scales as $\sqrt{(1-1/N)}/\sqrt{C}$ where C is the cooperativity. We additionally show the application of the polariton blockade mechanism in realising a non-local CZ and C_2Z gate by using a different set of computational qubit states, and characterise the gate errors which scale as $1/\sqrt{C}$.

Chapter 8 presents the conclusion and outlook.

List of manuscripts submitted in peer-reviewed journals

1. Jandura, Sven, Vineesha Srivastava, Laura Pecorari, Gavin K. Brennen, and Guido Pupillo. "Nonlocal multiqubit quantum gates via a driven cavity." Physical Review A 110, no. 6 (2024).

2. Srivastava Vineesha, Sven Jandura, Gavin K. Brennen, and Guido Pupillo. "Entanglement-enhanced quantum sensing via optimal global control." arXiv preprint : 2409.12932 (2024).

3. Srivastava Vineesha, Sven Jandura, Gavin K. Brennen, and Guido Pupillo. "Cavity polariton blockade for non-local entangling gates with trapped atoms." arXiv preprint : 2502.14781 (2025).

A note on work contribution I have had the privilege of contributing extensively to the three manuscripts included in this thesis, each representing significant advancements in multi-qubit quantum gates and entanglement generation for both quantum computing and quantum sensing.

In the first paper, titled "Non-Local Multi-Qubit Quantum Gates via a Driven Cavity", I collaborated closely with my colleague Sven Jandura to develop the conceptual frameworks for both the geometric and adiabatic phase gates. I was deeply involved from the project's inception through its completion, rigorously testing, verifying, and refining all calculations and gate protocols Sven proposed.

For the second manuscript, titled “Entanglement-Enhanced Quantum Sensing via Optimal Global Control”, I led the project as the first author, significantly contributing to the conceptual development of the protocol, and performing all numerical computations, including the implementation of optimal control techniques essential to the work.

In the third manuscript titled “Cavity polariton blockade for non-local entangling gates with trapped atoms”, I also served as the lead author, expanding on the original concept for generation of W states, leading the development of Cz and C_2Z gates (with Sven Jandura), and producing all numerical results. This manuscript was conceptualized alongside the adiabatic phase gate protocol and showcases our joint efforts in pioneering innovative techniques for multi-qubit control.

Chapter 2

Theory background

2.1 Quantum optics

The description of light, like everything in nature[1], must be framed in the context of quantum mechanics. This was not quite obvious until 1970s when light was still treated classically and quantum mechanics was primarily needed to quantize matter, such as atoms. This semi-classical approach of light-matter interaction was sufficient to describe many optical phenomena including propagation, interference, absorption stimulated emission, and also laser physics. Then why quantize light? In the pursuit of strengthening the theoretical foundations of laser physics, it soon became clear that the semiclassical approach was insufficient, particularly when it came to explaining spontaneous emission.

Although the quantum theory of light existed since its development by Dirac in the early 1930s, quantum optics theory in its modern sense started when Roy J. Glauber developed, in the early 1960s, a clear quantum formalism to describe optics. Glauber introduced the notion of quasi-classical or coherent states of light, a theoretical tool that allowed physicists to understand why all available sources of light, including lasers, delivered light whose properties could be totally explained in the framework of the semi-classical approach. Glauber's formalism revolutionized the field, earning him half of the 2005 Nobel Prize in Physics for his contributions to the quantum theory of optical coherence. This theoretical breakthrough paved the way for discovery of even newer phenomena that could be understood only through the quantization of light. These include the prediction and realization of single photons, as well as squeezed and entangled photons. Such discoveries have had profound implications, not only leading to several more Nobel Prizes- which include the 2012 Nobel prize in Physics awarded

---

[1] maybe except gravity

to Serge Haroche, David Wineland for ground-breaking experimental methods that enable measuring and manipulation of individual quantum systems and the 2022 Nobel Prize in Physics awarded to Alain Aspect, John F. Clauser, and Anton Zeilinger for their groundbreaking experiments with entangled photons, which enabled fundamental tests of quantum mechanics- but also giving rise to entirely new fields -namely quantum information science and quantum metrology.

2.1.1 Field modes in a cavity and interesting photon states

The notion of a photon and other non-classical behaviour of light is obtained by quantizing the free electromagnetic field, far from sources. In this section let us consider the case with field inside a cavity defined by two parallel mirrors. When the electromagnetic field solutions obtained in a coulomb gauge are quantised in the presence of boundary conditions set by the cavity mirrors, we obtain field modes in a cavity acting as one-dimensional oscillators- similar to harmonic oscillator modes for a set of independent mechanical oscillators. The cavity field Hamiltonian is given by

$$\hat{H}_{\mathrm{c}} = \sum_l \hbar\omega_l \left(\hat{a}_l^\dagger \hat{a}_l + \frac{1}{2}\right), \tag{2.1}$$

where $\hat{a}_l$ and $\hat{a}_l^\dagger$ are the single photon annihilation and creation operators in the mode l which satisfy the commutation relations $[\hat{a}_l, \hat{a}_{l'}^\dagger] = \delta_{ll'}$. This Hamiltonian is diagonalised by the so called Fock states or the photon number states $|n_l\rangle$, such that $\hat{H}|n_l\rangle = \hbar\omega_l(n_l + 1/2)|n_l\rangle$. The electric field operator at point $\mathbf{r}$ corresponding to the cavity field modes with each mode l characterised by its wavevector $\mathbf{k}_l$ and polarization $\vec{\epsilon}_l$ is given by [135, 136]

$$\hat{\mathbf{E}}(\mathbf{r}) \quad = \quad \sum_l \mathcal{E}_l \left[\mathbf{f}_l(\mathbf{r})\hat{a}_l + \mathbf{f}_l(\mathbf{r})^* \hat{a}_l^\dagger\right],$$

where $\mathcal{E}_l$ are the normalisation factors with dimension of an electric field, and the vector function $\mathbf{f}_l = f_l(\mathbf{r})\vec{\epsilon}_l$ describes the spatial structure of the field mode l. Equating the electronagnetic energy in the photon state $|n_l\rangle$ given by $\langle n_l| \int \epsilon_0^2 |\hat{\mathbf{E}}(\mathbf{r})|^2 d^3\mathbf{r} |n_l\rangle$ (where ϵ_0 is the vacuum permittivity) with $\hbar\omega_l(n_l + 1/2)$, one obtains

$$\mathcal{E}_l = \sqrt{\hbar\omega_l/(2\epsilon_0 V_l)}, \tag{2.2}$$

where $V_l = \int |\mathbf{f}_l(\mathbf{r})|^2 d^3\mathbf{r}$ denotes the effective mode volume of the cavity. The value $\mathcal{E}_l$ is often expressed as the electric field per photon.

In this thesis and in the context of cavity quantum electrodynamics discussed from now on, we consider only one mode of the cavity field and label the selected mode with $l = c$, with ω_c hence denoting the single cavity mode frequency. The single mode cavity Electric field operator is simply described as (dropping the subscript for creation and annihilation operators and spatial mode function for mode c)

$$\hat{\mathbf{E}}_c = \mathcal{E}_c \mathbf{f}(\mathbf{r})(\hat{a} + \hat{a}^\dagger), \tag{2.3}$$

with $\max|\mathbf{f}|^2 = 1$ and $\nabla \cdot \mathbf{f} = 0$. Throughout, we also consider the energy of the cavity field to be shifted by the amount $\hbar\omega_c/2$ and work with the shifted Hamiltonian which reads

$$\hat{H}_\mathrm{c} = \hbar\omega_c \hat{a}^\dagger \hat{a}, \tag{2.4}$$

which is now again diagonalised by the Fock states $|n\rangle$ with energies $n\hbar\omega_c$. The field evoltion of the single mode can be obtained by using the Heisenberg picture dynamics $\dot{\hat{a}} = -\frac{i}{\hbar}[\hat{H}_\mathrm{c}, \hat{a}]$ and we obtain

$$\hat{a}(t) = \hat{a}(0)e^{-i\omega_c t}. \tag{2.5}$$

2.1.1.1 Coherent states and displacement operator

We introduced above the energy eigenstates of the cavity mode Hamiltonian, which are photon number states denoted by $|n\rangle$. As can be checked, these states correspond to a zero average electric field, that is, $\langle n|\hat{E}_c|n\rangle = 0$ irrespective of the photon number n. In this section, we introduce another important class of states which have a non-zero electric field average, these are termed as the coherent states or Glauber states [137]. A coherent state is denoted as $|\alpha\rangle$, where α is a complex number, and are the eigenstates of the field annihilation operator:

$$\hat{a}|\alpha\rangle = \alpha|\alpha\rangle. \tag{2.6}$$

The states $\langle\alpha|$ then become the left eigenstates of $\hat{a}^\dagger$ with eigenvalue α^*: $\langle\alpha|\hat{a}^\dagger = \alpha^*\langle\alpha|$.

In terms of the number states $|n\rangle$, $|\alpha\rangle$ is expanded as

$$|\alpha\rangle = e^{-\frac{1}{2}|\alpha|^2} \sum_{n=0}^{\infty} \frac{\alpha^n}{\sqrt{n!}} |n\rangle. \tag{2.7}$$

The expectation value of the electric field operator is proportional to $|\alpha|\mathcal{E}_c$, where $\mathcal{E}_c$ is the field amplitude and is similar to the classical field expression.

A coherent state $|\alpha\rangle$ can be created from a vacuum state $|0\rangle$ by the application of a displacement operator which reads [137]

$$\hat{D}(\alpha) = e^{\alpha\hat{a}^{\dagger} - \alpha^{*}\hat{a}}, \tag{2.8}$$

such that

$$\hat{D}(\alpha)|0\rangle = |\alpha\rangle. \tag{2.9}$$

2.1.2 Quantum optical phase space

Similar to the quadrature position and momentum operators for a quantum mechanical harmonic oscillator, we can define the quadradure operators for the quantised field of the cavity mode as

$$\hat{X}_1 = \frac{(\hat{a} + \hat{a}^{\dagger})}{2} \tag{2.10}$$

$$\hat{X}_2 = \frac{(\hat{a} - \hat{a}^{\dagger})}{2i}. \tag{2.11}$$

A coherent state α has the expectation values of the quadrature operators as $\langle\alpha|\hat{X}_1|\alpha\rangle = \mathrm{Re}(\alpha)$ and $\langle\alpha|\hat{X}_2|\alpha\rangle = \mathrm{Im}(\alpha)$. The state $|\alpha\rangle$ can hence be representated as a point on the quantum optical phase space formed by the complex plane of α.

2.2 Cavity QED models

2.2.1 Single quantum emitter coupled to single cavity mode

Jaynes and Cummings in their seminal work in 1963 introduced the fully quantized model describing the simple one atom- one cavity mode interaction [138]. The Hamiltonian is expanded as

$$\hat{H}_{JC} = \hat{H}_a + \hat{H}_c + \hat{H}_{ac}, \tag{2.12}$$

with $\hat{H}_a$, $\hat{H}_c$ and $\hat{H}_{ac}$ denoting the atomic Hamiltonian, the cavity mode Hmailtonian and the atom-cavity mode interaction Hamiltonian terms respectively. We consider the 'spin-like' atom describe above with levels $|e\rangle$ and $|g\rangle$ with an electric-dipole transition at frequency ω_a, which correspond also to the eigen states of the Pauli $\hat{\sigma}^z$ operator with eigen values $+1$ and -1 respectively. The atomic Hamiltonian hence has the form $\hat{H}_a = \frac{\hbar\omega_a}{2}\hat{\sigma}^z$. The atomic dipole- field coupling is given by $-\mathbf{D}\cdot\mathbf{E}_c$ where $\mathbf{D}$ is the atomic dipole operator and $\hat{\mathbf{E}}_c(\mathbf{r})$ is the electric field operator for the cavity mode at the atomic location

$\mathbf{r}$ (see Eq. (2.2)). The atomic dipole operator is expanded as $\mathbf{D} = -\mathbf{d}(\hat{\sigma}^- + \hat{\sigma}_+)$, where $\mathbf{d} = d\vec{\epsilon}_a$ is the atomic transition dipole vector with the atomic transition polarisation $\vec{\epsilon}_a$ and we have defined the atomic raising and lowering operators given by $\hat{\sigma}^+ = |e\rangle\langle g|$ and $\hat{\sigma}^- = |g\rangle\langle e|$, respectively. The atom-cavity interaction Hamiltonian is expressed as

$$\hat{H}_{ac} = \mathbf{d}[\hat{\sigma}^- + \hat{\sigma}^+] \cdot \mathcal{E}_c \mathbf{f}(\mathbf{r})[\hat{a} + \hat{a}^\dagger]. \tag{2.13}$$

In the product above, we have two terms proportional to $\hat{\sigma}^+\hat{a}$ and its conjugate $\hat{\sigma}^-\hat{a}^\dagger$ corresponding to resonant processes when $\omega_{eg} \approx \omega_c$; and other two terms proportional to $\hat{\sigma}^+\hat{a}^\dagger$ and $\hat{\sigma}^-\hat{a}$ which are highly non-resonant. We saw that the field operators evolve with time as $\hat{a}(t) = \hat{a}(0)e^{-i\omega_c t}$, $\hat{a}^\dagger(0) = e^{-i\omega_c t}$(see Eq. (2.5)), similarly the spin operators evolve according to $\dot{\hat{\sigma}}_\pm = -\frac{i}{\hbar}[\hat{H}_a, \hat{\sigma}_\pm]$ as $\hat{\sigma}^\pm(t) = \hat{\sigma}^\pm(0)e^{\pm i\omega_{eg}t}$ and we obtain the time-dependencies of the resonant and non-resonant terms in $\hat{H}_{ac}$ given by

$$\begin{aligned}
\hat{\sigma}^+\hat{a} &\sim e^{i(\omega_{eg}-\omega_c)t} && (2.14)\\
\hat{\sigma}^-\hat{a}^\dagger &\sim e^{-i(\omega_{eg}-\omega_c)t} && (2.15)\\
\hat{\sigma}^+\hat{a}^\dagger &\sim e^{i(\omega_{eg}+\omega_c)t} && (2.16)\\
\hat{\sigma}^-\hat{a} &\sim e^{-i(\omega_{eg}+\omega_c)t}. && (2.17)
\end{aligned}$$

We see that for $\omega_{eg} \approx \omega_c$, the last two terms oscillate very rapidly as compared to the first two. Now we make the rotating wave approximation and drop the fast rotating terms which have a very negligible effect on the dynamics of the system. The interaction Hamiltonian is then reduced to the well known Jaynes-Cummings interaction Hamiltonian which reads

$$\hat{H}_{ac} = \hbar g[\hat{\sigma}^+\hat{a} + \hat{\sigma}^-\hat{a}^\dagger], \tag{2.18}$$

where

$$g = \mathcal{E}_c \frac{\mathbf{d} \cdot \mathbf{f}(\mathbf{r})}{\hbar} = \sqrt{\frac{|\mathbf{d} \cdot \mathbf{f}(\mathbf{r})|^2 \omega_c}{2\hbar_0 V_c}}. \tag{2.19}$$

The Jaynes-Cummings Hamiltonain of the single atom- single mode then reads

$$\hat{H}_{JC} = \frac{\hbar\omega_a}{2}\hat{\sigma}^z_j + \hbar\omega_c \hat{a}^\dagger\hat{a} + \hbar g(\hat{\sigma}^+\hat{a} + \hat{\sigma}^-\hat{a}^\dagger). \tag{2.20}$$

The Hamiltonian conserves the total number of excitations in the system, that is $\left[\hat{H}_{JC}, |e\rangle\langle e| + \hat{a}^\dagger\hat{a}\right] = 0$, and $\hat{H}_{ac}$ only couples states of the type

$$|e\rangle_a|n\rangle_c \leftrightarrow |g\rangle_a|n+1\rangle_c, \tag{2.21}$$

where $|.\rangle_a$ denotes an atomic bare state and $|n\rangle_c$ denotes a bare state of the cavity mode with n photons.

The Jaynes-cummings Hamiltonian can hence be diagonalised in the basis of these bare-state doublets $\{|e\rangle_a|n\rangle_c, |g\rangle_a|n+1\rangle_c\}$, which leads to eigenstates which have both atomic and photonic components. These states are termed as dressed states of the atom-cavity system and for a given n are given by

$$\begin{aligned} |+,n\rangle &= \cos(\theta_n/2)|e,n\rangle + \sin(\theta_n/2)|g,n+1\rangle, && (2.22)\\ |-,n\rangle &= -\sin(\theta_n/2)|e,n\rangle + \cos(\theta_n/2)|g,n+1\rangle, && (2.23) \end{aligned}$$

where $\theta_n = \tan^{-1}(2g/\Delta_{ac})$ with the atom-cavity detuning $\Delta_{ac} = \omega_a - \omega_c$. The energies of these states are

$$E_n^{\pm} = \left(n + \frac{1}{2}\right)\hbar\omega_c \pm \frac{\hbar}{2}\sqrt{\Delta_{ac}^2 + 4g^2(n+1)}. \tag{2.24}$$

Fig. 2.1 schematically describes the Jaynes-Cummings coupling and the eigen spectrum.

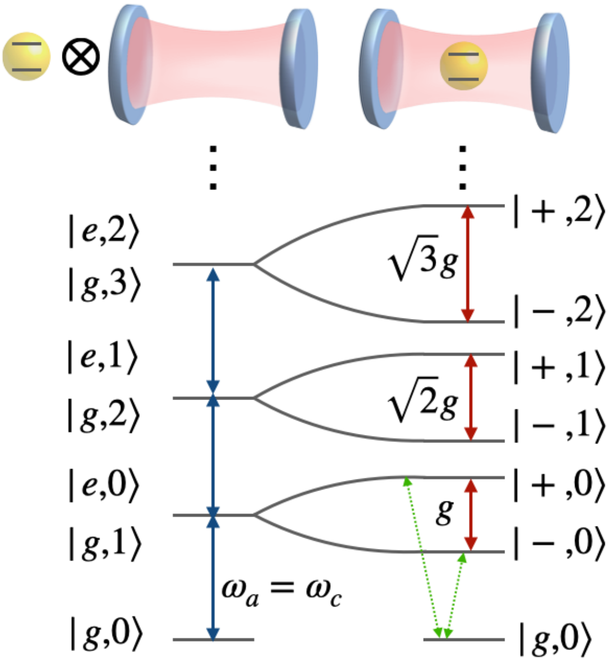

FIGURE 2.1: (Left)Bare energy states of the atom and the cavity mode when the cavity mode is resonant with the atomic transition ($\omega_c = \omega_a$) and (Right) the energy eigenstates of the Jaynes Cummings interaction Hamiltonian with atom-cavity mode coupling strength g ($\hbar = 1$). We have used the shorthand $|e,n\rangle$ for $|e\rangle_a|n\rangle_c$. The green dashed arrows indicate the transitions which are coupled when a weak external probe drives the system, resulting in observation of vacuum Rabi splitting peaks in the probe transmisison spectrum (see Sec. 1.1.1, Fig. 1.1).

2.2.2 Many quantum emitters coupled to a single cavity mode

The Tavis Cummings Hamiltonain is a straightforward generalisation of the Jaynes Cummings Hamiltonian describing the coupling of N identical quantum emitters to a single cavity mode, rather than a single emitter [139]. The Tavis-Cummings Hamiltonian reads ($\hbar = 1$)

$$\hat{H}_{TC} = \sum_{j=1}^{N} \Big(\frac{\omega_a}{2} \hat{\sigma}_j^z + g_j (\hat{\sigma}_j^+ \hat{a} + \hat{\sigma}_j^- \hat{a}^\dagger) \Big) + \omega_c \hat{a} \hat{a}^\dagger, \tag{2.25}$$

where $\hat{\sigma}_j^z = |e_j\rangle\langle e_j| - |g_j\rangle\langle g_j|$ is the Pauli-z operator for the quantum emitter labelled with index j, and similarly $\hat{\sigma}_j^+ = |e_j\rangle\langle g_j|$, $\hat{\sigma}_j^- = |g_j\rangle\langle e_j|$ are the emitter excitation and de-excitation operators for the jth emitter.

2.2.2.1 Symmetric Dicke subspace

To better understand the system of N quantum emitters, we can represent it using the formalism of N spin-$\frac{1}{2}$ particles($|\uparrow\rangle \equiv |e\rangle$, $|\downarrow\rangle \equiv |g\rangle$). We utilize a collective spin basis, which is formed by the simultaneous eigenstates of the collective spin operators, defined as $\hat{S}^2 = \hat{S}_x^2 + \hat{S}_y^2 + \hat{S}_z^2$ and $\hat{S}_z$. Here, the operators $\hat{S}_\alpha$ for $\alpha \in \{x, y, z\}$ are given by $\hat{S}_\alpha = \sum_j \hat{\sigma}_j^\alpha$. The basis states are represented as

$$\{|J, M\rangle\}, \quad \text{where} \quad 0 \leq J \leq N/2, \quad -J \leq M \leq J. \tag{2.26}$$

The respective eigenvalues of $\hat{S}^2$ and $\hat{S}_z$ correspond to $J(J+1)$ and M, respectively. The system of N quantum emitters can hence be seen as a spin J, with the ground state $|g, g \cdots g\rangle = |N/2, -N/2\rangle$. This collective basis is called the generalised Dicke basis, named after the person who introduced the formalism to describe collective supperradiance phenomenon of atomic ensembles when confined in a volume smaller than the wavelength [140].

We now define a useful subspace of this generalised Dicke basis, called the permutation invariant or the symmetric Dicke subspace given by

$$|\mathcal{D}_{n_1}^N\rangle \equiv |n_1\rangle \equiv |J = N/2, M = n_1 - N/2\rangle. \tag{2.27}$$

We now define the collective spin raising and lowering operators given by $\hat{S}^+ = \sum_j \hat{\sigma}_j^+$ and $\hat{S}^- = \sum_j \hat{\sigma}_j^-$, respectively. With this and assuming each quantum emitter couples identically to the single-mode cavity with strength g, the Tavis -Cummings Hamiltonian can be re-written as

$$\hat{H}_{TC} = \frac{\omega_a}{2}\hat{S}^z + \omega_s \hat{a}^\dagger \hat{a} + g(\hat{S}^+\hat{a} + \hat{S}^-\hat{a}^\dagger). \tag{2.28}$$

We will use this model to describe our cavity QED setup in the following chapter 2. Note however that each quantum emitter is assumed to be strongly coupled with the single mode in the cavity with maximal coupling strength g, and with the emitters placed with enough spacing between them such that collective effects are neglected.

2.2.3 Representation of symmetric states on collective bloch sphere

To visualize quantum states in the symmetric Dicke subspace, we can use the Husimi Q distribution. This representation offers a way to map the state's structure onto the collective Bloch sphere, providing an intuitive view of its orientation and coherence properties. For a given quantum state ρ in this subspace, the Husimi Q function is defined as:

$$Q(\Omega) = \frac{1}{\pi}\langle\Omega|\rho|\Omega\rangle, \tag{2.29}$$

where $|\Omega\rangle$ denotes a coherent spin state specified by the angles θ (polar angle) and ϕ (aximuthal angle) on the Bloch sphere. This distribution effectively projects the density of ρ onto the sphere, revealing how the quantum state is "spread" or concentrated in particular directions.

In the symmetric Dicke subspace, where states are characterized by collective spin alignments, the Q function highlights features such as phase coherence, population imbalance, and entanglement structure by showing the probability-like distribution across the Bloch sphere. This visualization provides a powerful tool for interpreting the spatial and phase properties of symmetric Dicke states in quantum sensing and metrology tasks, as we will see in Chapter 5.

2.3 Open Quantum Systems

In quantum mechanics, the concept of an open quantum system is fundamental to understanding real-world quantum dynamics. Unlike idealized closed systems, which evolve in isolation, open quantum systems interact with their surrounding environment. These interactions can result in energy exchange, loss of coherence, or dephasing within the system. Essentially, any quantum system that we attempt to measure or manipulate unavoidably interacts with its environment, making perfect isolation impractical in experimental and natural scenarios.

Interactions between a quantum system and its environment can lead to phenomena such as energy dissipation or dephasing. For instance, an atom in an excited state might undergo spontaneous emission, losing energy as it decays to a lower state, or a photon within a cavity could escape, leading to a loss of information from the system. On the other hand, certain types of environmental interactions—such as indirect measurements—can induce dephasing, where the coherence between different quantum states is lost without an accompanying energy loss. These interactions lead to entanglement between the system and its environment, resulting in complex, non-unitary dynamics that require specialized models to describe accurately.

2.3.1 Markovian Lindblad Master Equation

In practical applications, particularly in quantum optics, open quantum systems provide a framework to analyze and predict the dynamics of quantum states interacting with a continuous environment, such as the electromagnetic field [28, 141, 142]. This framework is essential in understanding phenomena where the environment acts as a bath, continually influencing the system's behavior. Often, the environmental influence can be modeled as a Markovian bath [142] (memoryless), meaning that the environment responds instantaneously and independently to each state of the system, significantly simplifying the analysis [141, 142].

The Lindblad master equation is a powerful tool for describing the dynamics of Markovian open quantum systems [143]. This equation models the time evolution of the system's density matrix while incorporating the effects of the environment in a mathematically consistent manner. For a system with density matrix ρ [142], the Lindblad equation takes the form:

$$\frac{d\rho}{dt} = -\frac{i}{\hbar}[\hat{H}, \rho] + \sum_j \left(\hat{L}_j \rho \hat{L}_j^\dagger - \frac{1}{2}\{\hat{L}_j^\dagger \hat{L}_j, \rho\} \right) \tag{2.30}$$

where $\hat{H}$ represents the system's Hamiltonian, governing its intrinsic dynamics, and $\hat{L}_j$ are Lindblad operators representing the interactions with the environment. These operators capture different dissipative processes, such as energy decay or dephasing, and can vary based on the specific nature of the system-environment interaction.

The Lindblad equation is particularly valuable because it preserves the physical properties of the density matrix, such as its trace and positivity, which are essential for ensuring a valid quantum description. Under the Markovian approximation, we assume that the environment does not have memory effects; the system's evolution depends solely on its present state and not on its history. This simplifies the modeling process, as we can treat the environmental influences as stationary, allowing for a steady-state solution where time evolution is only dependent on the current system properties.

The Markovian Lindblad framework finds applications across a broad range of quantum technologies, including quantum computing, quantum optics, and quantum thermodynamics. Its use in simulating energy losses and decoherence mechanisms allows for a detailed understanding of system behaviors under realistic conditions, such as photon loss in optical cavities or spin relaxation in magnetic environments.

2.3.2 Non-Hermitian Terms in the Hamiltonian

An alternative approach to modeling open quantum systems is by incorporating non-Hermitian terms in the Hamiltonian. Traditionally, the Hamiltonian of a closed quantum system is Hermitian, ensuring real eigenvalues that correspond to observable energy levels. However, when a system interacts with an environment, effective non-Hermitian terms can be introduced to represent dissipative dynamics directly within the Hamiltonian framework.

In this approach, the system Hamiltonian $\hat{H}$ is modified to include a non-Hermitian component $\hat{H}' = \hat{H} - i\Gamma$, where Γ is a term representing decay rates or losses. This term effectively introduces complex eigenvalues in the Hamiltonian, with the imaginary part indicating the rate of energy dissipation or decay. For instance, in a quantum optical cavity with photon leakage, Γ can represent the rate at which photons are lost to the environment, causing a gradual reduction in the photon population over time.

Non-Hermitian dynamics are often used to represent the conditional evolution of a quantum system under the assumption that no quantum jumps (or losses) have occurred. This conditional evolution approach is closely related to the quantum trajectories method, which is a popular framework for simulating the dynamics of open quantum systems.

In the quantum trajectories approach, a system interacting with its environment can be described by a stochastic series of quantum jumps interspersed with deterministic evolution governed by a non-Hermitian Hamiltonian. The non-Hermitian term represents the conditional evolution of the system between jumps, assuming that no measurement or interaction with the environment has taken place. As such, the probability of a jump occurring over a small time interval is proportional to the loss rate encoded by the imaginary part of the non-Hermitian term. If a jump does not occur, the system continues to evolve according to this non-Hermitian Hamiltonian, causing a gradual decay in population. This decay reflects the likelihood of losing a particle or energy to the environment at each infinitesimal time step.

Using non-Hermitian dynamics to represent conditional evolution is efficient for calculating state evolution under the assumption of no losses, which allows insight into the dynamics of a "pure" trajectory. However, it does not account for the stochastic nature of environmental interactions, where decay or decoherence events could occur. The full open quantum system dynamics, averaged over many such trajectories (including jump events), are captured more comprehensively in the Lindblad master equation formalism discussed in Sec. 2.3.1, where both no-jump evolution and jump events are treated within the same framework.

For the example of an atom undergoing spontaneous emission treated with a non-Hermitian term, the Hamiltonian may be modified as: $\hat{H}' = \hat{H} - i\frac{\gamma}{2}|e\rangle\langle e|$, where $|e\rangle$ is the excited atom state and γ is its rate of spontaneous emission. This term introduces an imaginary component to the energy associated with the excited state, resulting in a decay of the population in $|e\rangle$. Physically, this is equivalent to assuming that once the atom decays, it leaves the system's Hilbert space, rather than transitioning to another state within the system (such as a ground state).

This approach captures the decay out of the Hilbert space but neglects internal transitions within the system, meaning that it does not model the atom's state after decay or any back-action from this transition. In situations where the decay product remains accessible within the system, such as in a quantum gate where fidelity is critical, this non-Hermitian method could lead to computing of lower bounds on gate fidelities. The decay out of the system reduces fidelity since information about decay events is lost.

To validate results from non-Hermitian simulations, one strategy is to include an ancillary state within the Hilbert space and model the decay as a transition to this ancillary state. This allows us to track the population that has "left" the primary system states and observe its effect without assuming an irreversible loss of information.

2.4 Quantum Optimal Control Methods

Quantum optimal control methods are essential for tuning quantum dynamics to achieve precise outcomes by optimizing classical control parameters that affect a quantum system's Hamiltonian. These techniques, both analytical and numerical, enable steering of quantum systems along specific trajectories or toward desired states, thus enhancing performance in various quantum technologies. Quantum optimal control has proven especially valuable in domains like quantum computing, where it facilitates tasks such as state preparation, error correction, and gate optimization across platforms including superconducting qubits, trapped ions, and neutral atoms [144, 145]. For instance, the Gradient Ascent Pulse Engineering (GRAPE) method was initially developed for nuclear magnetic resonance (NMR) spectroscopy but has since been widely applied in quantum control to design time-continuous pulse sequences [146]. These pulse sequences allow smooth, precise control over quantum state evolution by continuously modulating the parameters that influence the system's Hamiltonian.

However, not all quantum control problems necessitate continuous pulses. In many cases, especially when optimizing discrete control variables rather than time-dependent fields, simpler parameter tuning techniques can achieve the desired objectives without the need for complex pulse design, which is the case in this thesis where optimal control methods are utilised in Chapter 5. In this work, we utilise the quasi-Newton optimization methods named as the Broyden–Fletcher–Goldfarb–Shanno (BFGS) algorithm. The BFGS method is computationally efficient as it approximates the Hessian matrix, avoiding the direct calculation of second derivatives. This approach makes BFGS particularly advantageous in high-dimensional optimization problems, common in quantum control tasks where one seeks to optimize a finite set of parameters.

The BFGS algorithm is an iterative, quasi-Newton method for solving unconstrained nonlinear optimization problems. By leveraging an approximation of the Hessian matrix, it balances computational efficiency with rapid convergence, a crucial aspect in large-scale optimization problems. Unlike Newton's method, which requires costly Hessian calculations, BFGS constructs an inverse Hessian approximation that updates at each step using available gradient information, thereby offering a practical trade-off between precision and speed.

To apply BFGS, a differentiable cost function $f(x)$ is defined over the control parameters x. BFGS seeks the x that minimizes $f(x)$ by iteratively refining both the parameter vector x and an approximation of the inverse Hessian matrix. The method begins with an initial guess x_0 and an initial positive-definite matrix B_0 that approximates the inverse Hessian.

Access to analytic gradients $\nabla f(x)$ significantly enhances BFGS performance, enabling precise gradient calculations. When analytic gradients are unavailable, numerical approximations can be used, though they may reduce the accuracy and computational efficiency of the optimization.

The BFGS update rule for control variables x_k at each iteration is:

$$x_{k+1} = x_k - \alpha_k B_k^{-1} \nabla f(x_k),$$

where B_k is the current approximation of the inverse Hessian matrix and α_k is a step size determined through line search. This update allows x_k to approach the minimum of $f(x)$ by balancing convergence speed and stability.

The BFGS algorithm updates the inverse Hessian approximation B_k through:

$$B_{k+1} = B_k + \frac{\Delta y_k \Delta y_k^T}{\Delta y_k^T \Delta s_k} - \frac{B_k \Delta s_k \Delta s_k^T B_k}{\Delta s_k^T B_k \Delta s_k},$$

where $\Delta s_k = x_{k+1} - x_k$ and $\Delta y_k = \nabla f(x_{k+1}) - \nabla f(x_k)$. This approach integrates information about changes in x and $\nabla f(x)$, constructing a quasi-Newton approximation without explicit second-derivative calculations.

BFGS offers several advantages:

- **Fast Convergence**: BFGS achieves superlinear convergence, making it suitable for complex, high-dimensional optimization problems.
- **Efficiency with Quasi-Newton Approach**: The quasi-Newton approximation of the Hessian enables BFGS to deliver high convergence rates without the burden of full Hessian calculations.
- **Stability with Analytic Gradients**: When analytic gradients are available, BFGS performs exceptionally well by leveraging accurate gradient information, improving descent direction accuracy in high-dimensional spaces and minimizing potential errors.

Despite its strengths, BFGS has limitations:

- **Sensitivity to Local Minima**: Like many gradient-based methods, BFGS may converge to local minima in non-convex landscapes.
- **Dependency on Differentiability**: BFGS requires a continuously differentiable cost function, limiting its application in scenarios where gradient calculations are infeasible or noisy.

In Chapter 5, we employ the BFGS optimisation method to find the classical parameters of a protocol that is designed for the state preparation of an optimal probe state for a defined quantum sensing task. Moreover, the protocol is such that it allows analytic computation of the gradients with respect to the optimisation parameters, making the optimisation highly effective.

2.5 From Symmetric subspace to a collective Hilbert space

We saw in Sec. 2.2.2.1, the description of a permutation invariant or the symmetric Dicke subspace for a system of N spin-1/2 particles, which is formed by the states $\{|J, M\rangle\}$ for $J = N/2$. The Dicke states for $J < N/2$ can be constructed iteratively and each state $|J, M\rangle$ has a degeneracy [60, 147]

$$d_N^J = (2J+1)\frac{N!}{(N/2+J+1)!(N/2-J)!}, \tag{2.31}$$

meaning there are d_N^J number of ways to combine N spin-1/2 particles to obtain an total angular momentum J. We will see below that this degeneracy is not lifted when describing collective and local homogeneous processes on the system of N spin-1/2 particles.

All collective decay mechanisms and local-homogeneous decay mechanisms in a system of N spin-1/2 particles can be described using the Lindblad master equation,

$$\begin{aligned} \dot{\rho} \;\; = \;\; & -\frac{i}{\hbar}[\hat{H}, \rho] + \frac{\gamma_{\Downarrow}}{2}\mathcal{L}_{J_-}[\rho] + \frac{\gamma_{\Phi}}{2}\mathcal{L}_{J_z}[\rho] + \frac{\gamma_{\Uparrow}}{2}\mathcal{L}_{J_+}[\rho] \\ & + \sum_{n=1}^{N}\left(\frac{\gamma_{\downarrow}}{2}\mathcal{L}_{J_{-,n}}[\rho] + \frac{\gamma_{\phi}}{2}\mathcal{L}_{J_{z,n}}[\rho] + \frac{\gamma_{\uparrow}}{2}\mathcal{L}_{J_{+,n}}[\rho]\right), \end{aligned} \tag{2.32}$$

where ρ is the density matrix of the full system and $\hat{H}$ is the N spin$-1/2$ ensemble Hamiltonian, which we assume to be constructed only with the collective operators $J_\alpha = \sum_n^N J_{\alpha,n}$, where $J_{\alpha,n} = \sigma_{\alpha,n}/2$ for $\alpha = \{x, y, z\}$, and $J_{\pm,n} = J_{x,n} + iJ_{y,n}$. The $\mathcal{L}_A[\rho]$ are the Lindblad superoperators which are defimed by $\mathcal{L}_A[\rho] = 2A\rho A^\dagger - A^\dagger A\rho - \rho A^\dagger A$, and γ_i terms are rates corresponding to emission, dephasing, and pumping, corresponding to local and collective processes acting on the spins. Fig. 2.2(a) from Ref. [60] schematically describes these processes. The states in the Dicke ladders for $J < N/2$ become relevant for the processes described in Eq. (2.32), which do not limit their action in the $(N+1)-$dimensional symmetric Dicke subspace. But the good news is that, for an initial state prepared with permutation symmetric collective operators, all the terms in Eq. 2.32 still preserve the permutational symmetry of the system, that is Eq. 2.32 does not create coherences between (elements with $M \neq M'$) Dicke states with $J \neq J'$. So the relevant Hilbert space for any density matrix of the N spin-1/2 particles is spanned by the states $\{|J, M\rangle\}$ for J varying from $\mathrm{J}_{\min}$ to $J = N/2$ and $-J \leq M \leq J$. We term this Hilbert space as the *collective* Hilbert space $\mathcal{H}_c$. Any system density matrix in this collective Hilbert space is written as

$$\rho = \sum_{J,M,M'} p_{JMM'} |J, M\rangle\langle J, M'|, \tag{2.33}$$

with $p_{JMM'} = \langle J, M|\rho|J, M'\rangle$. Note that Eq. (2.33) is a block-diagonal density matrix, with each block corresponding to a J value of dimension $2J + 1$. The dimension of this collective Hilbert space is thus $\mathrm{dim}\mathcal{H}_c = \sum_{J=J_{\min}}^{N/2}(2J + 1) = (N + 3)(N + 1)/4$ if N is odd ($J_{\min} = 1/2$) or $(N + 2)^2/4$ if N is even ($J_{\min} = 0$). This formalism is extensively used in Chapter 5 for evaluating the effect of local homogeneous dephasing processes acting on spins in the context of quantum sensing.

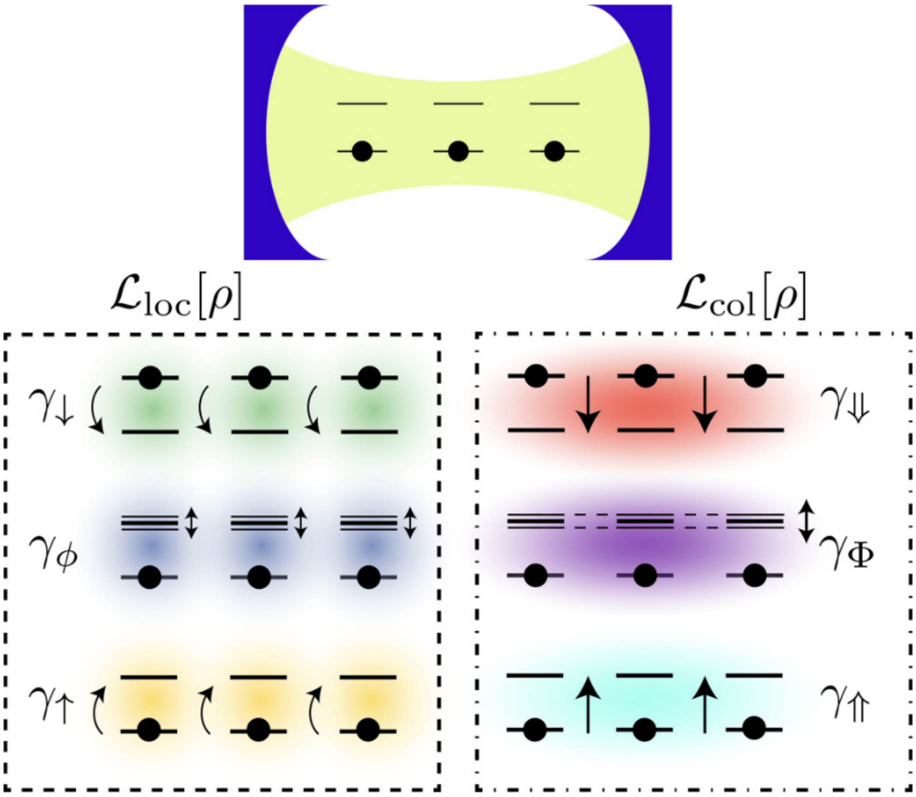

FIGURE 2.2: Schemmatic of open system dynamics for an ensemble of N spin-1/2 particles interacting with a shared bosonic mode through coherent dynamics. The action of dissipative processes on the two-level system dynamics is quantified by different rates for homogeneous local (dashed box) and collective processes (dot-dashed box), given by $\mathcal{L}_{\rm loc}[\rho]$ and $\mathcal{L}_{\rm col}[\rho]$, respectively: local and collective emission, set by $\gamma_{\downarrow}$ and $\gamma_{\Downarrow}$, local and collective dephasing, set by γ_{ϕ} and γ_{Φ}, and local and collective pumping, set by $\gamma_{\uparrow}$ and $\gamma_{\Uparrow}$ (see Eq. (2.32)). Figure from Ref. [60].

Chapter 3

Cavity QED Setup and Model

In this chapter, we discuss the cavity QED setup, Hamiltonian and the open system model describing its dynamics. In Section. 3.1, we describe all the components of the setup and write down the system Hamiltonian. In Sec. 3.2, we discuss the model used to describe the system dynamics. In Sec. 3.4,, we describe shortly several physical platforms where such a setup has been or can be realised, and hence demostrating the generality of the protocols described in the following chapters.

3.1 Setup and Hamiltonain

The setup we work with is rather general and is shown in Fig. 3.1. It consists of N atomic systems with three relevant energy levels - two the computational basis states $|0\rangle$ and $|1\rangle$ and an excited state $|e\rangle$, with energies ($\hbar = 1$) ω_0', ω_1' and ω_e' respectively. A cavity mode with annihilation (creation) operators $\hat{a}(\hat{a}^\dagger)$ and frequency ω_c couples the states $|1\rangle$ and $|e\rangle$ with coupling strength g. We assume that all individual systems couple with the identical coupling strength g to the cavity mode. Additionally, the cavity mode is driven by a (complex) classical field of strength $\eta(t)$ and frequency ω_L. The full Hamiltonian of the system reads

$$\hat{H}_f = \hat{H}_a + \hat{H}_c + \hat{H}_{ac} + \hat{H}_{\text{drive}}, \tag{3.1}$$

where $\hat{H}_a$, $\hat{H}_c$, $\hat{H}_{ac}$ and $\hat{H}_{\text{drive}}$ denote respectively the Hamiltonian terms for the atomic systems, the cavity, the atoms-cavity interaction and the cavity drive. We have ($\hbar = 1$)

$$\begin{aligned} \hat{H}_a &= \sum_{j=1}^{N} \left(\omega_0' |0_j\rangle\langle 0_j| + \omega_1' |1_j\rangle\langle 1_j| + \omega_e' |e_j\rangle\langle e_j| \right), && (3.2) \\ \hat{H}_c &= \omega_c \hat{a}^\dagger \hat{a}. && (3.3) \end{aligned}$$

The interaction Hamiltonian $\hat{H}_{ac}$ of the atoms with the single cavity mode is obtained as the $N-$body generalisation of the Jaynes-Cummings Hamiltonian, known as the Tavis-Cummings Hamiltonian which was first delevoped and exactly solved in Ref. [139]. It reads

$$\hat{H}_{ac} = g\left(\sum_{j=1}^{N}|e_j\rangle\langle 1_j|\hat{a} + \text{h.c.}\right). \tag{3.4}$$

Finally, we describe the cavity mode drive described by a classical field with frequency ω_L, which can for example be passed through an optical fibre coupled to one of the cavity mirrors. This drive term reads

$$\hat{H}_{\text{drive}} = 2|\eta(t)|\sin(\omega_L t - \arg(\eta(t)))(\hat{a}^\dagger + \hat{a}). \tag{3.5}$$

We now set the zero energy at the energy of $|1\rangle$ state, i.e set $\omega_1' = 0$, and define the transition frequencies $\omega_0 = -\omega_0'$ for the $|1\rangle \leftrightarrow |0\rangle$ and $\omega_e = \omega_e'$ for the $|1\rangle \leftrightarrow |e\rangle$ transition. We define the number operators $\hat{n}_0 = \sum_j |0_j\rangle\langle 0_j|$, $\hat{n}_1 = \sum_j |1_j\rangle\langle 1_j|$ and $\hat{n}_e = \sum_j |e_j\rangle\langle e_j|$, and the collective raising and lowering operators as $\hat{S}^+ = \sum_j |e_j\rangle\langle 1_j|$, $\hat{S}^- = (\hat{S}^+)^\dagger$ respectively. The full Hamiltonian is re-written as

$$\hat{H}_f = -\omega_0\hat{n}_0 + \omega_e\hat{n}_e + \omega_c\hat{a}^\dagger\hat{a} + g\left(\hat{S}^+\hat{a} + \hat{S}^-\hat{a}^\dagger\right) + 2|\eta(t)|\sin(\omega_L t - \arg(\eta(t)))(\hat{a}^\dagger + \hat{a}). \tag{3.6}$$

We now move into a rotating frame defined by

$$\hat{U}_r(t) = \exp\left[it(\omega_L(\hat{a}^\dagger\hat{a} + \hat{n}_e) - \omega_0\hat{n}_0)\right]. \tag{3.7}$$

The rotated Hamiltonian is obtained as

$$\begin{aligned}\hat{H} &= \hat{U}_r\hat{H}_f\hat{U}_r^\dagger + i\left(\partial_t\hat{U}_r\right)\hat{U}_r^\dagger && (3.8)\\ & && (3.9)\end{aligned}$$

Defininig $\hat{O} = \omega_L(\hat{a}^\dagger\hat{a} + \hat{n}_e) - \omega_0\hat{n}_0$, then each of the Hamiltonian terms in $\hat{H}_f$ is transformed under $\hat{U}_r = e^{it\hat{O}}$ as $e^{it\hat{O}}\hat{H}_f e^{-it\hat{O}}$ into

$$\begin{aligned} e^{it\hat{O}}\hat{n}_0 e^{-it\hat{O}} &= \hat{n}_0,\ e^{it\hat{O}}\hat{n}_e e^{-it\hat{O}} = \hat{n}_e && (3.10)\\ e^{it\hat{O}}\hat{a}e^{-it\hat{O}} &= e^{-i\omega_L t}\hat{a},\ e^{it\hat{O}}\hat{a}^\dagger e^{-it\hat{O}} = e^{i\omega_L t}\hat{a}^\dagger, && (3.11)\\ e^{it\hat{O}}\hat{S}^+ e^{-it\hat{O}} &= e^{i\omega_L t}\hat{S}^+,\ e^{it\hat{O}}\hat{S}^- e^{-it\hat{O}} = e^{-i\omega_L t}\hat{S}^-. && (3.12)\end{aligned}$$

In writing the above results, we make use of the Baker–Campbell–Hausdorff formula and the commutation relations $[\hat{a}, \hat{a}^\dagger] = 1$ and $[\hat{n}_e, \hat{S}^+] = \hat{S}^+$. With $i\left(\partial_t\hat{U}_r\right)\hat{U}_r^\dagger = -\hat{O}$,

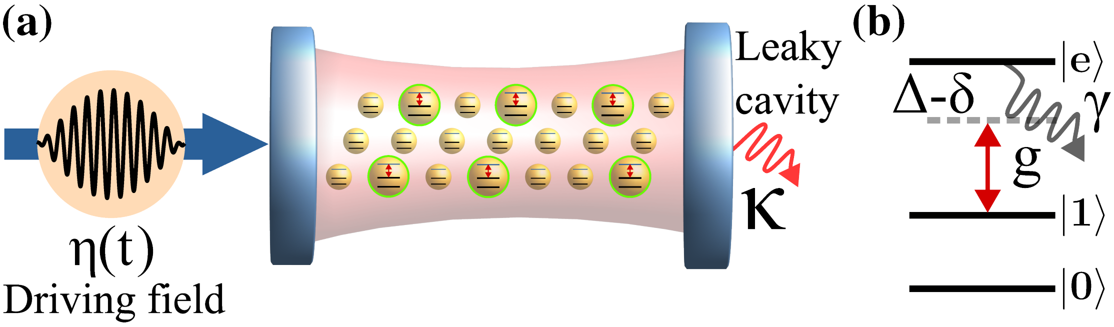

FIGURE 3.1: (a) A register of qubits is coupled to a common cavity with decay rate κ. The cavity mode is externally driven with a single classical field $\eta(t)$ detuned by δ from the resonance frequency of the cavity. (b) Level scheme for each atomic system consisting of the computational basis states $|0\rangle$ and $|1\rangle$ (with infinite lifetime), and an ancillary excited state $|e\rangle$ (with lifetime $1/\gamma$). The $|1\rangle \leftrightarrow |e\rangle$ transition is coupled to the cavity with coupling strength g and detuned from the cavity resonance by $\Delta - \delta$.

the Hamiltonian in the rotating frame then reads

$$\begin{aligned}\hat{H}(t) &= (\omega_e - \omega_L)\hat{n}_e + (\omega_c - \omega_L)\hat{a}^\dagger\hat{a} + g\left(\hat{S}^+\hat{a} + \hat{S}^-\hat{a}^\dagger\right) \\ &\quad -i(\eta(t)^* e^{i\omega_L t} - \eta(t)e^{-i\omega_L t})(\hat{a}^\dagger e^{i\omega_L t} + \hat{a}e^{-i\omega_L t}).\end{aligned} \tag{3.13}$$

We apply now the rotating wave approximation defined by the limit $\omega_L \gg |\eta(t)|$, which leads to discarding the fast rotating terms with frequency $2\omega_L$. We define the detunings of the classical field from the cavity and the $|1\rangle \leftrightarrow |e\rangle$ transition by $\delta = \omega_c - \omega_L$ and $\Delta = \omega_e - \omega_L$, respectively. The Hamiltonian in the rotating frame and with the rotating wave approximation then reads

$$\hat{H}(t) = \delta\hat{a}^\dagger\hat{a} + \Delta\hat{n}_e + [(g\hat{S}^- + i\eta(t))\hat{a}^\dagger + \text{h.c.}]. \tag{3.14}$$

3.1.1 Free-space laser coupling of computational states

In addition to the cavity drive, global or local free-space laser drives (acting on the atoms from side) coupling the atomic computational states can be added allowing for more control knobs of the atomic system. The free space laser-atom coupling is described by

$$\hat{H}_\Omega = \sum_j \left(\frac{\Omega_j(t)}{2}|1_j\rangle\langle 0_j| + \text{h.c.}\right), \tag{3.15}$$

where Ω_j is the laser Rabi frequency driving the $|0\rangle \leftrightarrow |1\rangle$ transition in atom j. In this thesis, we consider $\Omega_j = \Omega \ \ \forall j$ whenever $\hat{H}_\Omega$ is added.

3.2 Open System Dynamics

We generally consider two loss mechanisms in our model - the finite lifetime of the excited state $|e\rangle$ with a spontaneous emission rate γ, and the finite lifetime of a photon in a cavity, which decays at a rate κ. Throughout this thesis, unless stated otherwise, the decay of $|e\rangle$ is treated as a population loss, represented by a non-Hermitian term in $\hat{H}$. Consequently, all analytic derivations and results obtained with this model will be exact if none of the decay channels from $|e\rangle$ can repopulate $|0\rangle$ or $|1\rangle$. In cases where repopulation is possible, our results may provide, for instance, a lower bound on operation fidelities.

To address the decay of the cavity mode, we employ the master equation approach within the framework of the Markovian approximation. This approximation is particularly useful, as it allows us to simplify the dynamics by assuming that the system has negligible memory effects. In this approach, we assume the system's interactions with the environment are instantaneous, effectively disregarding any history of past interactions. This leads to a tractable equation for the system's density matrix, facilitating analysis of the time evolution of the system states while incorporating decay processes in a manageable form.

The Markovian approximation is widely applicable to atomic systems interacting with electromagnetic fields, particularly when the coupling to the environment (such as a photonic bath – here, the modes outside the cavity) is weak, and the bath correlation time is much shorter than the system's intrinsic dynamical timescales. Under these conditions, memory effects are minimal, making the Markovian approximation a reliable approach for describing decay mechanisms.

In this model, to address the cavity mode decay specifically, we examine the system's evolution using the Lindblad master equation, with the jump operator given by $\hat{L} = \sqrt{\kappa}\hat{a}$. The system Hamiltonian and the master equation reads

$$\begin{aligned} \hat{H}(t) &= \delta\hat{a}^\dagger\hat{a} + (\Delta - i\gamma/2)\hat{n}_e + [(g\hat{S}^- + i\eta(t))\hat{a}^\dagger + \text{h.c.}], && (3.16)\\ \dot{\rho} &= -iH\rho + i\rho H^\dagger + L\rho L^\dagger - \{L^\dagger L, \rho\}/2, && (3.17)\end{aligned}$$

where ρ is the joint atoms-cavity density operator. We define here the single-atom of cooperativity C which characterises the coupling regime of any cavity QED system, as

$$C = \frac{g^2}{\kappa\gamma}. \tag{3.18}$$

Throughout this work, we work in the strong-coupling regime of cavity QED, which is defined as $g > (\kappa, \gamma)$ implying $C > 1$.

In Table, 3.1 we list and define all the parameters characterising our setup.

$\vert 0\rangle$, $\vert 1\rangle$	long-lived computational levels
$\vert e\rangle$	finite-lifetime excited energy level
ω_0	$\vert 0\rangle \leftrightarrow \vert 1\rangle$ transition frequency
ω_e	$\vert 1\rangle \leftrightarrow \vert e\rangle$ transition frequency
g	single atom ($\vert 1\rangle \leftrightarrow \vert e\rangle$ transition) - cavity mode coupling strength
$\eta(t)$	$\vert\eta(t)\vert e^{i(\arg\eta(t))t}$, strength of classical drive on cavity mode
Ω	Rabi frequency of free-space laser coupling between $\vert 0\rangle \leftrightarrow \vert 1\rangle$
δ	detuning between the cavity mode frequency and the classical drive frequency
Δ	detuning between $\vert 1\rangle \leftrightarrow \vert e\rangle$ transition frequency and the classical drive frequency
κ	empty cavity resonance linewidth (FWHM)
γ	$\vert 1\rangle \leftrightarrow \vert e\rangle$ transition atomic linewidth (FWHM)
C	$g^2/(\kappa\gamma)$, single atom-cavity cooperativity

TABLE 3.1: Cavity QED setup and model parameter definitions.

3.3 Initialisation and qubit addressability

In the following chapters, we present several protocols for entanglement generation, quantum computing, and quantum sensing that can be implemented using the setup described above. In experiments, to restrict our gates to address only a subset of qubits in a register (for example, to implement a quantum gate between spatially separated atoms in a cavity), the $|1\rangle$ state of spectator qubits can be transferred to an ancillary atomic state $|a\rangle$ that does not couple to the bosonic mode. This isolation can occur either because the frequency of the $|a\rangle \leftrightarrow |e\rangle$ transition is far off-resonant with the cavity mode frequency or due to selection rules that forbid direct coupling between $|a\rangle$ to $|e\rangle$. Alternatively, a spatially addressable off-resonant laser beam can be used in experiments to apply an ac-Stark shift to the qubits, shifting the $|1\rangle \leftrightarrow |e\rangle$ transition far enough out of resonance with the cavity to neglect the coupling [148, 149]. Another approach in neutral atom cavity QED experimental setups is using optical tweezers to trap and move selectively atoms in and out of the cavity (see example setup in Sec. 3.4.1).

3.4 Existing and proposed physical platforms for our setup

In this section, we review the state-of-the-art for experimental setups in which our model is realized or could potentially be implemented. We also provide the achieved or estimated coupling strengths for these systems.

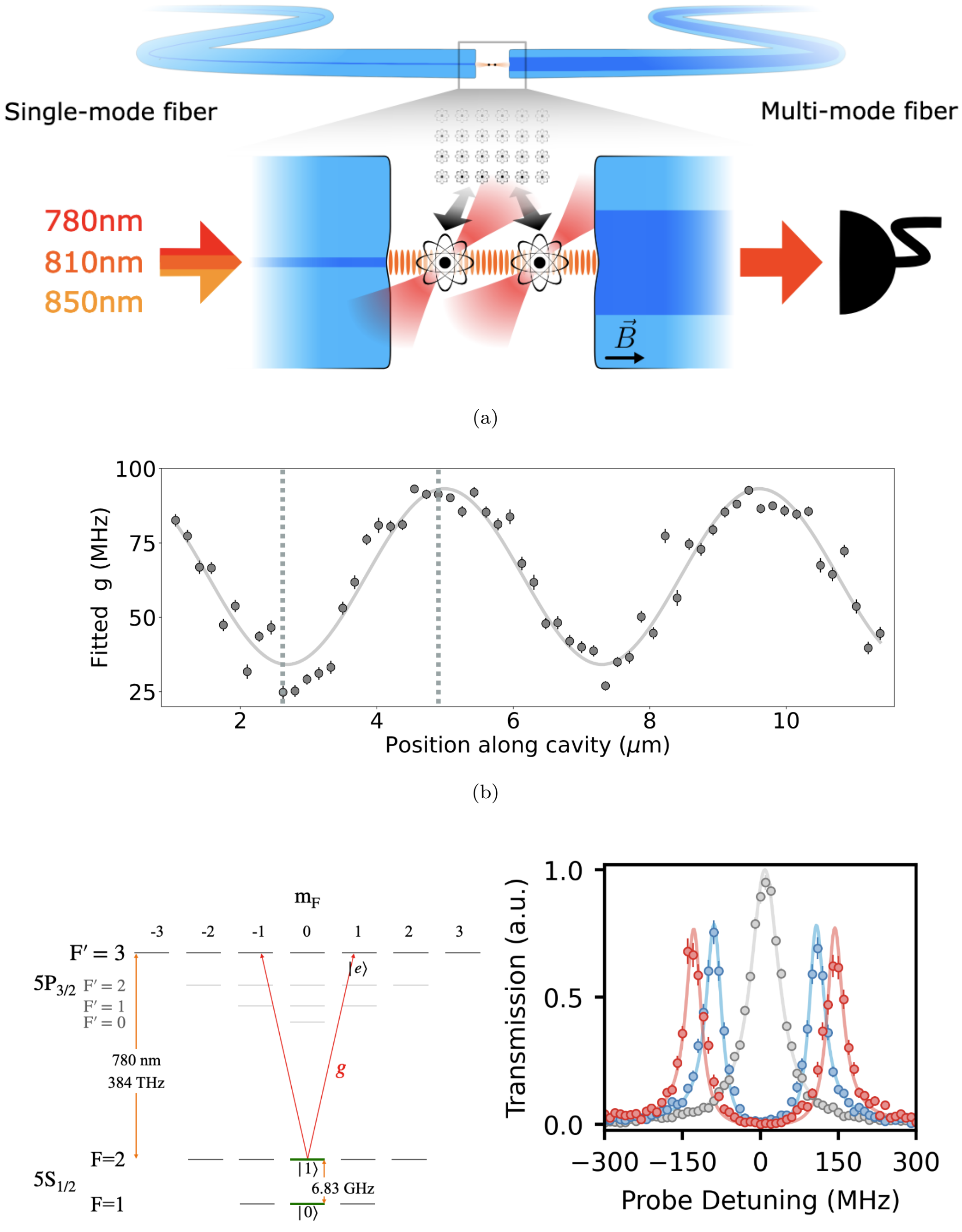

(a)

(b)

(c)

(d)

FIGURE 3.2: (a) Schematic of experimental setup from Ref. [55]. Atoms are loaded in optical tweezers above a Fabry-Perot fiber cavity(FPFC) and are transported in the cavity mode. (b) Fit of atom-cavity coupling strength g as a function of position along the cavity of experiment in Ref. [55]. The atom tweezers are positioned at the regions of maximal g. (c) Energy level diagram of ^{87}Rb. The 780 nm cavity mode of the FPFC couples the D_2 $2 \leftrightarrow 3'$ transition of *Rb*. (d) Resonant probe transmission spectra of the bare cavity(gray), one atom(blue) and two atoms(red) coupled to the cavity mode. The spectra are fitted with theoretical curves, yielding $g = 100.0(8)$ MHz and $\kappa = 65(1)$ MHz. Plot from Ref. [55].

3.4.1 Fiber based Fabry-Perot cavity with atomic tweezer traps

Fiber based Fabry-Perot cavities (FFPC) are microcavities with low scattring losses, which allow achieving high cooperativity. We recall from section 1.1.2 the definition of an important characterising property of such cavities called the *finesse*, which is a measure of how narrow the cavity resonances are with respect to their frequency separation. It depends on the cavity mirror coating reflectivity properties and is given by the ratio of the free spectral range $c/(2L)$ and the resonance linewidth κ: $\mathcal{F} = \frac{c}{2L\kappa}$, where L is the cavity length. The quality factor Q of the cavity is a measure of how underdamped the resonator is and is defined by the ratio of cavity's centre frequency c/λ (where λ is the wavelength of the trapped light) to its linewidth : $Q = (2L\mathcal{F})/\lambda$. A very recent experiment demonstrates a fiber Fabry-Perot cavity of length $L = 100\,\mu$m with coating reflectivities $> 99.993\%$ centered around $\lambda = 780\,$nm obtaining a resonance linewidth of $\kappa = 57.9\,$MHz and hence achieving a finesse of $\mathcal{F} = 25904$, and quality factor $Q = 6.6 \times 10^6$ [55].

Such Fiber based cavities also provide access for optical tweezers, such that the atoms interact with the cavity mode while being trapped in optical tweezers placed at the antinodes of the cavity mode (with maximal coupling strength g), see Fig. 3.2(a)-(c). For the state-of-the-art example with Rubidium atoms shown in Fig. 3.2(c), an additional optical lattice formed with 850 nm light is overlapped with 780 nm cavity mode forming a beat note with a period of $4.7\,\mu$m, and a cavity of $100\,\mu$m can hence accommodate 20 atoms trapped at the regions of maximal overlap or maximal g. In each atom, the computational states can be chosen for example, as the hyperfine levels of ^{87}Rb which are $|0\rangle = |5S_{1/2}, F = 1, m_F = 0\rangle$ and $|1\rangle = |5S_{1/2}, F = 2, m_F = 0\rangle$, while $|e\rangle$ can be chosen as the electronically excited state $|e\rangle = |5P_{3/2}, F' = 3, m_F = 1\rangle$ (see Fig. 3.2(d)). The effective two level system coupled to the cavity mode is hence realised by the $|1\rangle \leftrightarrow |e\rangle$ transition which has a natural linewidth of $\gamma = 2\pi \times 6\,$MHz. The cavity drive is realised through a single mode input port, which is also used for the atom-cavity system characterisation and non-destructive qubit readout schemes. The transmission spectrum (see Fig. 1(e)) of the atom-cavity system reveals coupling strength $g = 100.0(8)\,$MHz and cavity resonance linewidth $\kappa = 65(1)\,$MHz hence achieving a cooperativity $C \approx 25$ [55].

3.4.1.1 Future implementations of FFPCs with large cavity lengths

In the pioneering work realising the first FFPC, a maximal finesse of $F \approx 130\,000$ is envisioned for a cavity made from two fibre mirrors with identical coatings [44] and $F \approx 170\,000$ if the transmission of one mirror is suppressed. With further technical advancements, a finesse of $F = 2 \times 10^5$ should be achievable in near future. Defining the cavity waist size ω_r (which is a function of cavity length L, radius of curvature R of cavity mirrors and wavelength λ), the cavity cooperativity can be written as $C = 3\lambda^2 F/(2\pi^3\omega_r^2)$. Combining the maximal finesse of $F = 130000$ with a realistic cavity waist size of $\omega_r = 1.3\,\mu$m at $\lambda = 780\,$nm (and $L = 2\,\mu$m), a maximal cooperativity of $C = 2280$ is thus projected.

Note however that for trapping two or more atoms with a spacing of $\approx 4.7\,\mu$m as described above, we must consider longer FFPCs. Similar to Ref. [55], let us then consider a cavity length of $L = 100\,\mu$m which can trap $N \approx 20$ atoms. We consider radii of curvature of FFPC mirrors as $R = 55\,\mu$m in accordance with the recent fabrication limits of $R = 50\,\mu$m. With these, we obtain the cavity waist size at $\lambda = 780\,$nm as [44].

$$\omega_r = \sqrt{\frac{\lambda}{2\pi}}\,(L(2R-L))^{1/4} = 1.98\,\mu m. \tag{3.19}$$

Combining this with a maximal optimistic finesse of $F = 200\,000$, we obtain a projected cooperativity value of $C \approx 1500$. Similarly, $g = \sqrt{3\lambda^2 c\gamma/(2\pi^2 w_r^2 L)} \approx 2\pi \times 260$ MHz and $\kappa = \pi c/(LF) \approx 2\pi \times 7.5\,$MHz. With the atomic resonance linewidth for the D_2 transition in ^{87}Rb given by $\gamma = 2\pi \times 6\,$Mz, we have $\gamma/\kappa \approx 0.8$.

3.4.2 Rydberg atoms coupled to a superconducting microwave cavity

Choosing the microwave domain for cavities would ideally provide very long photon lifetimes $1/\kappa = Q/\omega_c$, as very high quality factors Q can be achieved at relatively low frequencies. Consequently, one would require a quantum emitter with a strong dipole transition in the microwave domain. A natural choice for this is atoms in highly excited atomic Rydberg states with high principal quantum number n. These atoms have large electric dipole moments associated with transitions in the microwave regime between Rydberg states, which is $> 1000ea_0$ for $n \gtrsim 30$ [150] (scaling roughly as $\sim n^2 ea_0$ [151]) , where e is the electron charge and a_0 the Bohr radius, and is strong enough to realise the strong-coupling regime of cavity QED with extremely high single atom-cavity cooperativity. Additionally, the lifetime of Rydberg states increases with n and scales approximately as n^3 (a typical lifetime for $n = 50$ is of $\sim 100\,\mu$s [151]), which supports the use of high-n Rydberg states to enhance coherence times in such systems.

One recent type of microwave cavities are realised as superconducting microwave stripline resonators known as *coplanar waveguide(CPW) resonators* which achieve quality factors $Q > 3 \times 10^8$ [43], yielding $\kappa = \omega_e/Q \approx 2\pi \times 17\,$Hz. We consider here the example from Ref. [42]. In order to couple the CPW resonators with Rydberg atoms, the atoms are trapped just above the electric field antinode of the CPW as shown in Fig. 3.3(a).

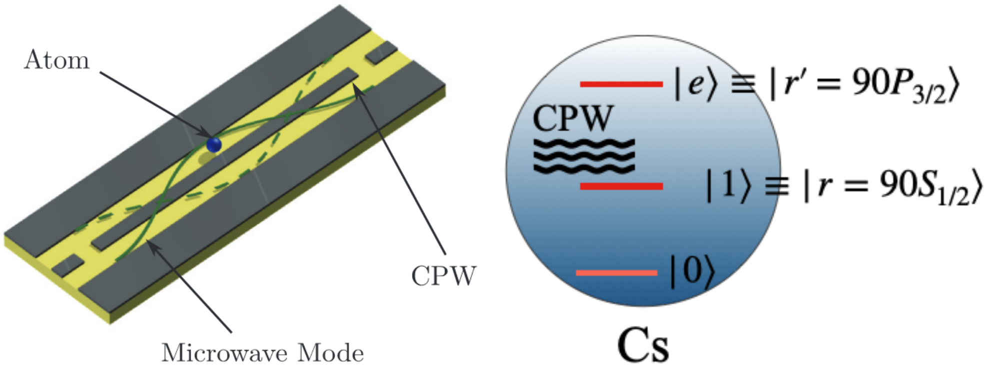

(a) (b)

FIGURE 3.3: (a) Schematic of atom trapped above the electric field antinode of superconducting coplanar waveguide resonator [42] (b) Proposed level scheme for Cs atom coupled to microwave coplanar waveguide resonator.

The cavity coupled states $|1\rangle$ and $|e\rangle$ are chosen as the Rydberg states $|1\rangle = |90\ ^2P_{3/2}\rangle$ and $|e\rangle = |90\ ^2S_{1/2}\rangle$ in Cs with lifetime 2 ms and 820 μs, respectively, see Fig. 3.3(b), while $|0\rangle$ is chosen as a long-lived state in the ground manifold of the atoms. In this case, the $|1\rangle \leftrightarrow |e\rangle$ transition has the frequency $\omega_e \approx 2\pi \times 5$ GHz, and is thus in the microwave regime. The states $|1\rangle$ and $|r\rangle$ may be coupled via a superconducting microwave resonator with reasonable coupling strength $g \approx 2\pi \times 4$ MHz and thus a cooperativity $C = 5 \times 10^9$, with $\gamma/\kappa \simeq 12$.

When using this system, we must be careful to include the decay of the state $|1\rangle$ in our analysis, which is important as the latter is now a Rydberg state with a lifetime comparable to that of $|e\rangle$.

Additionally this platform may pose other challenges:

- **Sensitivity to electric fields and stray field effects**: Rydberg states are highly hensitive to electric fields due to their large polarizability with static polarizability scaling as $\sim n^7$. This makes them vulnerable to stray electric fields, field noise, and fluctuations, which can lead to dephasing, particularly in the presence of unintended electric fields near the cavity or in the trapping environment.

- **Dipole-dipole interactions and unwanted blockade effects** : A natural consequence of the large dipole moments of Rydberg atoms is strong interactions between them. This can induce energy shifts and lead to unintended interactions in protocols that require isolated qubit states in a multi-atom setting. For example, Rydberg blockade can occur, where an excited Rydberg state in one atom suppresses excitation of nearby atoms..

- **Thermal and blackbody radiation effects** : Radiative and blackbody-induced transitions reduce the coherence times of low angular momentum Rydberg states, effectively shortening the lifetimes of the Rydberg states $|1\rangle$ and $|e\rangle$ [152].
- **Challenges with atom positioning and stability** : Precisely positioning Rydberg atoms to interact with microwave fields can be challenging, especially in strong-coupling regimes..

3.4.3 Circular Rydberg atoms coupled to a superconducting microwave cavity

Among the many available states in the Rydberg manifold, the large angular momentum states are an ideal choice, as they are insensitive to optically coupled decay channels. These states are called the *circular Rydberg states* [153]. These states have longer lifetimes, reaching approximately 10 ms at cryogenic temperatures (owing to only a single microwave-frequency radiative decay channel to next highest circular state). Pioneering experiments with circular Rydberg atoms and superconducting microwave *photon boxes* were realized and improved in the years 1984-2007 [65, 67–75]. These systems, in fact, were among the first to realize cavity QED setups.

Researchers currently working with circular Rydberg atoms aim to bridge the technical gap in preparing these states and are focused towards trapping these large circular atoms in optical tweezers [154, 155]. Specifically, it is very difficult to excite atoms to the circular Rydberg states with high fidelity [156], and the highest reported fidelity to date is 96 % [157, 158]. Recently, there are proposals which sidestep this challenge by using multiple circular Rydberg states to encode qubits, in the context of quantum computing [154] and quantum simulation [159] applications.

Given that Rydberg-atom arrays are a leading platform for quantum computing and simulation due to their strong interactions, high coherence, and flexible geometries, current efforts with circular Rydberg states are focused on extending these capabilities to potentially overcome current limitations in fidelity, which are often due to finite Rydberg-state lifetimes and technical imperfections, such as atomic motion.

3.4.4 Polar molecules coupled to a stripline microwave cavity

Ultracold polar molecules coupled to a microwave resonator [80–82] provide yet another prospective candidates for quantum emitters interacting with microwave photons. They have very large coherence times of transitions between rotational states with fairly large

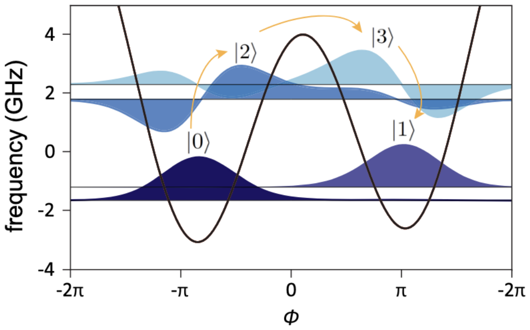

Figure 3.4: First four fluxonium wave functions from Ref. [61].

electric dipole moments. Following Ref. [80], one can assume Ca^{79}Br molecules [160] trapped electrostatically in the vicinity of a superconducting microwave stripline resonator. The computational basis states can be chosen as $|0\rangle = |N = 1, m_N = 0, F = 1, m_F = 0\rangle$, $|1\rangle = |N = 1, m_N = 0, F = 2, m_F = 1\rangle$, which are different hyperfine levels of the first excited rotational manifold of the molecule, where N is the rotational quantum number. The state $|e\rangle$ is then chosen in the second excited rotational level, $|e\rangle = |N = 2, m_N = 0, F = 2, m_F = 1\rangle$. These states are chosen to ensure that $|0\rangle, |1\rangle$ and $|e\rangle$ are simultaneously trappable [80].

For this choice of states the frequency of the $|1\rangle \leftrightarrow |e\rangle$ transition is given by $\omega_e = 2\pi \times 11$ GHz and is thus in the microwave regime. Coupling strengths up to $g = 2\pi \times 400$ kHz can be achieved with realistic experimental parameters [80]. Assuming $Q = 3 \times 10^8$ (as in Sec. 3.4.2) yields $\kappa = \omega_e/Q \approx 2\pi \times 37$ Hz, while the decay from $|e\rangle$ is $\gamma \lesssim 10^{-2}$Hz [161] and can be neglected.

3.4.5 Superconducting fluxonium qubits in circuit QED architechture

Our cavity QED model can also be realised in a setup with superconducting qubits coupled via a driven microwave resonator. For our purposes, we consider fluxonium qubits [86] which have a level structure compatible with our protocols.

Considering the experimental parameters from [61] at an external flux of $\Phi_{\mathrm{ext}} = 0.49\Phi_0$ (near, but not at the so-called sweet spot of $0.5\Phi_0$), we obtain the ground state $|0\rangle$ and the long lived state $|1\rangle$ (T_1 in the millisecond regime [162]) separated by $\sim 2\pi \times 100$MHz, while the next higher excited state $|e\rangle$ is separated by $2\pi \times 3.5$GHz from $|0\rangle$ [163, 164], see Fig. 3.4.

We note that the dominant error in this regime is a finite dephasing time $T_2^* \approx 20\mu$s of the $|0\rangle \leftrightarrow |1\rangle$ transition [165], which is in fact not included in the error analysis of the protocols described in the following chapters (dephasing effects are analysed numerically in Chapter 5 for quantum sensing protocol). One must hence estimate the effect of these errors as an additional T/T_2^* contribution to the operation infidelities.

A coupling strength of $g = 2\pi \times 10\text{MHz}$ (much smaller than the spacing between $|0\rangle$ and $|1\rangle$) can be assumed to selectively couple the $|0\rangle \leftrightarrow |e\rangle$ transition to the microwave resonator. This transition is chosen instead of the $|1\rangle \leftrightarrow |e\rangle$ transition and roles of $|0\rangle$ and $|1\rangle$ are flipped since the coupling of the $|1\rangle \leftrightarrow |e\rangle$ transition to the cavity is weaker than the coupling of $|0\rangle \leftrightarrow |e\rangle$, further suppressing the unwanted coupling of $|1\rangle \leftrightarrow |e\rangle$ to the cavity. Further, we can take $1/\gamma = 5\,\mu\text{s}$ including decay *and* dephasing of $|e\rangle$, and $Q = 3 \times 10^8$.

Chapter 4

Geometric Phase Gate Protocol

The current chapter is an adaptation of *Protocol A* from the publication "Non-Local Multi-Qubit Quantum Gates via a Driven Cavity" [54]. In this chapter, we refer to Protocol A as the geometric phase gate(GPG) protocol, and describe its working with our setup and model discussed in Chapter 2. For number of qubits $N = 2$, the geometric phase gate forms a universal gate set for quantum computation together with single qubit gates; while for arbitrary N it can be used to generate GHZ states. The geometric phase gate protocol operates in the limit of a large detuning Δ[1] between the cavity and the $|1\rangle \leftrightarrow |e\rangle$ transition (coupled to cavity mode with strength g) and of the cavity driving strength η of the same order (i.e., $\Delta/g, \eta/g \to \infty$ and $\Delta = \mathcal{O}(\eta)$). We take δ (the detuning between the cavity mode and the cavity drive field) to be of order $\mathcal{O}(g)$ and choose the pulse duration T to be of the order of $\mathcal{O}(g^{-1})$, such that it does not diverge in the limit $\Delta/g, \eta/g \to \infty$.

Geometric phase gates were first introduced in the context of trapped-ion quantum computing schemes [31, 32]. Here, we present the first protocol for implementing these gates in general cavity QED setups. We provide the solution of its dynamics in the presence of losses due to atomic spontaneous emission and photon leakage from the cavity mode, which we believe is being done for the first time.

The GPG protocol implements a family of geometric phase gates $\hat{U}_A = \exp\big(i\theta\hat{n}_1^2\big)$, where $\hat{n}_1 = \sum_{j=1}^{N} |1_j\rangle\langle 1_j|$ is the number operator of qubits in state $|1\rangle$, by displacing the state of the cavity in a closed loop in phase space. Any angle θ can be achieved by choosing an appropriate drive $\eta(t)$ of the cavity mode. One distinguishing feature of the GPG protocol is its speed: In many previous proposals, the cavity is far detuned from the

---

[1] Strictly speaking, the detuning between the cavity and the $|1\rangle \leftrightarrow |e\rangle$ transition is $\Delta - \delta$, which is proportional to Δ. Here, hence we loosely refer the limit of large detuning between the cavity and atom transition as $\Delta/g \to \infty$, given that $\delta = \mathcal{O}(g)$

qubit frequency to avoid a large number of photons in the cavity and thus a large error through photon losses. This comes at the cost of a long gate duration of the order Δ/g^2, where Δ is the detuning of the cavity and g is the coupling between the qubits and the cavity. In the GPG protocol, the cavity is also far detuned, but a driving strength which is of the order of Δ and adapted to the photon loss rate allows for gate durations of order g^{-1}. An additional advantage of the GPG protocol is its robustness: Similar to the Mølmer-Sørensen gate for trapped ions [32], $\hat{U}_A$ is independent of the initial state of the cavity mode, which is of particular importance if the cavity mode is in the microwave regime and may exhibit significant thermal population. Furthermore, the protocol is inherently robust against pulse imperfections in the drive of the cavity, since only the area enclosed and not the exact trajectory in phase space determines $\hat{U}_A$.

In Sec. 4.1, we begin by discussing the derivation of an effective Hamiltonian, valid in the limits defined above. We start by applying a time-dependent basis transformation on the cavity in Sec. 4.1.1, followed by a time-dependent basis transformation on the qubits in Sec. 4.1.2 to eliminate the state $|e\rangle$. The resulting effective Hamiltonian resembles that of a Mølmer-Sorensen gate for trapped ions [32] and is then used in Sec. 4.2 to derive a family of geometric phase gates $\hat{U}_A = \exp\big(i\theta\hat{n}^2\big)$. This section also discusses how $\hat{U}_A$ can be used, together with global single-qubit gates, to generate an N-qubit GHZ state.

The fidelity of the gate for arbitrary N is calculated analytically in Sec. 4.3 as a function of the finite qubit transition linewidth γ and cavity linewidth κ. This fidelity scales as $\sim N/\sqrt{C}$, where $C = g^2/(\kappa\gamma)$ is the cooperativity. This calculation is the first of its kind, obtained by exactly solving the quantum open-system dynamics for non-zero γ and κ. Section 4.4 verifies these analytical results against numerical simulations of the full Lindblad dynamics for a CZ gate using the GPG protocol, showing excellent agreement. Finally, Sec. 4.5 provides estimates of CZ gate fidelities and durations for atomic qubits coupled to an optical cavity, as well as molecular qubits, and superconducting fluxonium qubits coupled to a microwave cavity, and Sec. 4.6 presents the chapter conclusion and outlook.

4.1 Derivation of an Effective Hamiltonian for implementing a geometric phase gate

In this section, we show a detailed derivation of an effective Hamiltonian $\hat{H}_{\text{eff}}$ derived in the limits $\Delta/g \to \infty$ and $\eta/g \to \infty$ starting from the full Hamiltonian $\hat{H}(t)$. We recall here the full Hamiltonain from Eq. (3.16) which reads (described in detail chapter 3)

$$\hat{H}(t) = \delta \hat{a}^\dagger \hat{a} + (\Delta - i\gamma/2)\hat{n}_e + [(g\hat{S}^- + i\eta(t))\hat{a}^\dagger + \text{h.c.}]. \tag{4.1}$$

4.1.1 Basis Transformation on the Cavity

To motivate the first basis transformation, acting on the cavity, we note that due to the limit $\eta/g \to \infty$ the cavity typically contains many photons. To see this quantitatively, we look first at the average number of photons in the cavity because of drive η when no qubits are coupled to the cavity mode. We discuss below the exact solution of the cavity state at any time t when $n_1 = 0$ at $t = 0$, that is when no qubits are coupled to the cavity mode at time $t = 0$. The state of the cavity evolves independently under

$$\dot{\rho}_{\text{cav}} = -i[\hat{H}_{\text{cav}}, \rho_{\text{cav}}] + \hat{L}\rho_{\text{cav}}\hat{L}^\dagger - \{\hat{L}^\dagger \hat{L}, \rho_{\text{cav}}\}/2, \tag{4.2}$$

with $\hat{H}_{\text{cav}} = \delta \hat{a}^\dagger \hat{a} + (i\eta \hat{a}^\dagger + \text{h.c.})$. Note that for an initial pure state, the cavity remains in a pure state at all times, even if it undergoes decay. Hence we use the Ansatz for $\rho_{\text{cav}}(t)$ given by

$$\rho_{\text{cav}}(t) = |-\alpha(t)\rangle\langle -\alpha(t)|, \tag{4.3}$$

Now on substituting the Ansatz from Eq. (4.3) in the Lindblad equation in Eq. (4.2), we obtain on the left side

$$\text{L.H.S} = \dot{\rho}_{\text{cav}} = -\dot{\alpha}\hat{a}^\dagger \rho_{\text{cav}} - \dot{\alpha}^* \rho_{\text{cav}} \hat{a} - \frac{d|\alpha|^2}{dt}\rho_{\text{cav}}, \tag{4.4}$$

where we have used the property of the coherent state that is $\frac{\mathrm{d}}{\mathrm{d}t}|\alpha(t)\rangle = \dot{\alpha}\hat{a}^\dagger |\alpha\rangle - \frac{1}{2}\frac{\mathrm{d}|\alpha|^2}{\mathrm{d}t}|\alpha\rangle$. The right side of the equation is similarly obtained as

$$\begin{aligned} \text{R.H.S} &= \Big((\eta + (i\delta + \kappa/2)\alpha)\hat{a}^\dagger \rho_{\text{cav}} + \text{h.c.}\Big) \\ &+ (\eta^* \alpha + \eta \alpha^* + \kappa |\alpha|^2)\rho_{\text{cav}}. \end{aligned} \tag{4.5}$$

On equating the above two equations, we hence obtain the solution given by

$$\dot{\alpha} = -\eta - (i\delta + \kappa/2)\alpha. \tag{4.6}$$

Note also that the state $\rho_{\text{cav}}(t)$ can be rewritten as being created using a time-dependent displacement operator $D(\alpha(t)) = \exp\big(\alpha(t)\hat{a}^\dagger - \alpha^*(t)\hat{a}\big)$ (see Sec. 2.1.1.1), giving $\rho_{\text{cav}}(t) = \hat{D}(-\alpha(t))\rho_{\text{cav}}(0)(\hat{D}(-\alpha(t)))^\dagger$.

In the steady state we have $\dot{\alpha} = 0$, so that Eq. (4.6) yields an average number of photons of

$$|\alpha|^2 = \frac{|\eta|^2}{\delta^2(1+\kappa^2/(4\delta^2))} \approx \frac{|\eta|^2}{\delta^2} \tag{4.7}$$

We see that the cavity contains photons $\sim \eta^2/\delta^2$, which diverge in the limit $\eta/g \to \infty$, $\delta = \mathcal{O}(g)$. It is thus useful to switch into a time-dependent frame of the cavity which reduces the number of photons. Since due to the simultaneous limit $\Delta/g \to \infty$ the number of photons only weakly depends on n_1 (i.e the number of qubits in state $|1\rangle$), we choose a frame which is given by the evolution that the cavity would undergo if it were not coupled to the qubits. We find this frame above, which is given by the simple displacement $\hat{D}(\alpha)$ where $\alpha(t)$ is the solution of Eq. (4.6) for $\alpha(t=0)=0$.

Now if $n_1 = 0$, a cavity starting in the empty state $|0\rangle$ will be in the coherent state $|\psi_{\text{cav}}(t)\rangle = |{-\alpha(t)}\rangle$ at time t, so that for a cavity state $|\psi_{\text{cav}}(t)\rangle$, $\hat{D}(\alpha)\,|\psi_{\text{cav}}(t)\rangle = |0\rangle$.

Given the evolution of ρ for $n = 0$, we now treat the evolution of the joint cavity-qubit system for a general n. For this, we now proceed with the basis transformation $\tilde{\rho}(t) = \hat{D}(\alpha(t))\rho(t)\hat{D}(\alpha(t))^\dagger$. For general n_1, the evolution of $\tilde{\rho}$ is then given by (see Appendix A.1)

$$\tilde{\hat{H}} = \delta\hat{a}^\dagger\hat{a} + (\Delta - i\gamma/2)\hat{n}_e + g[(\hat{a}^\dagger - \alpha^*)\hat{S}^- + \text{h.c.}] \tag{4.8}$$

and $\tilde{\hat{L}} = \hat{L} = \sqrt{\kappa}\hat{a}$. Hence, the drive of the cavity mode is converted into an effective drive of the qubits with strength $-ig\alpha$. Because the decay in the original frame is compensated by a κ-dependent choice of α, in this new frame there are no excitations in the cavity mode and no decay events if $n_1 = 0$ – even if in the original frame there may be many excitations and decay events.

4.1.2 Basis Transformation on the Qubits

In order to derive an effective Hamiltonian on the computational states $|0\rangle, |1\rangle$, and the cavity and to eliminate the state $|e\rangle$, we now use the limit $\Delta/g \to \infty$. For this, we consider $\tilde{\hat{H}}^{(0)} = \Delta\hat{n}_e - (g\alpha^* S^- + \text{h.c.})$, which is the part of $\tilde{\hat{H}}$ which scales with Δ. (Recall that as $\Delta/g \to \infty$ we also consider the limit $\eta/g \to \infty$, and thus $|\alpha| \to \infty$). We perform a time-dependent basis transformation on the qubits so that the new basis states are the instantaneous eigenvectors of $\tilde{\hat{H}}^{(0)}$. Such a basis transformation is given by (see Appendix A.2)

$$\hat{U} = \exp\left[\frac{\lambda}{2}\left(-e^{i\mu}\hat{S}^+ + e^{-i\mu}\hat{S}^-\right)\right] \tag{4.9}$$

with $\cos\lambda = \Delta/\sqrt{4g^2|\alpha|^2+\Delta^2}$ and $\mu = \arg(\alpha)$. In this new basis, the Hamiltonian is given by $\bar{\tilde{H}} = \hat{U}\tilde{H}\hat{U}^\dagger + i\dot{\hat{U}}\hat{U}^\dagger$. The inertial term is of the form $i\dot{\hat{U}}\hat{U}^\dagger = \mathcal{O}(1)S^+ + \text{h.c.}$, where $\mathcal{O}(g)$ denotes a term which does not diverge as $\Delta/g \to \infty$. Crucially, since the gap between the eigenstates of $\hat{H}^{(0)}$ diverges as $\Delta/g \to \infty$ and we consider a pulse duration T independent of Δ, the inertial term can be neglected as $\Delta/g \to \infty$, leaving $\bar{\tilde{H}} = \hat{U}\tilde{H}\hat{U}^\dagger$.

A direct calculation (see Appendix A.2) now shows

$$\begin{aligned}\bar{\tilde{H}} &= \delta\hat{a}^\dagger\hat{a} + \left(\varepsilon_1 - i\frac{\gamma_1}{2}\right)\hat{n}_1 + \left(\varepsilon_e - i\frac{\gamma_e}{2}\right)\hat{n}_e \\ &+ (\zeta\hat{a}^\dagger + \zeta^*\hat{a})(\hat{n} - \hat{n}_e)\end{aligned} \tag{4.10}$$

where

$$\varepsilon_{e/1} = (\Delta \pm \sqrt{\Delta^2 + 4g^2|\alpha|^2})/2 + \mathcal{O}(1) \tag{4.11}$$

$$\zeta = \frac{g^2\alpha}{\sqrt{4g^2|\alpha|^2+\Delta^2}} \tag{4.12}$$

$$\gamma_{e/1} = \frac{\gamma}{2}\left(1 \pm \sqrt{1 - 4|\zeta|^2/g^2}\right) \tag{4.13}$$

where the expressions above are evaluated with the + sign for ε_e and γ_e and the − sign for ε_1 and γ_1. We note that Eqs. (4.11)–(4.13) are time-dependent. In Sec. 4.2 below we use the time-dependency of ζ to implement the desired quantum gate.

If we assume that none of the qubits start in state $|e\rangle$, the terms in Eq. (4.10) proportional to $\hat{n}_e$ can be neglected. Furthermore, the $\varepsilon_1\hat{n}_1$ term just corresponds to a frequency shift of the qubits, which can be compensated for either by single qubit z-rotation at the end of the gate, or by a change of reference frame. We are thus left with the effective Hamiltonian

$$\hat{H}_{\text{eff}} = \delta\hat{a}^\dagger\hat{a} + \left(-i\frac{\gamma_1}{2} + \zeta\hat{a}^\dagger + \zeta^*\hat{a}\right)\hat{n}_1. \tag{4.14}$$

This effective Hamiltonian simply describes a driven cavity, where the driving strength $\zeta\hat{n}$ depends on the number n of qubits in state $|1\rangle$. It is thus analogous to the Hamiltonian for a Mølmer-Sørensen gate [32].

The finite lifetime γ of the state $|e\rangle$ leads to an effective error rate $\gamma_1\hat{n}_1$. Note that since the basis transformation in this section only affected the space of the qubits, the Lindblad operator $\hat{L}_{\text{eff}} = \hat{L} = \sqrt{\kappa}\hat{a}$ is unchanged. We discuss the influence of these error sources in Sec. 4.3 below.

4.2 Implementation of the Geometric Phase Gate: Decay-free case

In this section we use the effective Hamiltonian (4.14) to derive a shape of $\zeta(t)$ which implements a quantum gate $\hat{U}_A = \exp\bigl(i\theta\hat{n}_1^2\bigr)$ on the qubits only and leaves the system in a state with no entanglement between the photons and the qubits. We first consider the loss free case $\gamma = \kappa = 0$, while the infidelity for finite values of γ and κ is calculated in the next section.

We show that if $\zeta(t)$ is chosen of the form $\zeta(t) = -\delta f(t) + i\dot{f}(t)$, the effective Hamiltonian (4.14) implements the quantum gate $\hat{U}_A = \exp\bigl(i\theta\hat{n}_1^2\bigr)$ with

$$\theta = \delta \int_0^T \mathrm{d}t f(t)^2. \tag{4.15}$$

We note that here f can be any *real* function satisfying $f(0) = f(T) = 0$, $\dot{f}(0) = \dot{f}(T) = 0$, and $\delta^2 f(t)^2 + \dot{f}(t)^2 < g^2/4$ for all t. These constraints follow from the two points below:

(i) To find a pulse $\eta(t)$ in the original Hamiltonian (4.1) which leads to the desired $\zeta(t)$ in the effective Hamiltonian (4.14), Eqs. (4.12) and (4.6) have to be inverted to first find $\alpha(t)$ and then $\eta(t)$. Equation (4.12) is only invertible if $|\zeta(t)| < g/2$, which imposes the constraint $\delta^2 f(t)^2 + \dot{f}(t)^2 < g^2/4$ on the choice of f, while Eq. (4.6) can be solved for $\eta(t)$ for any differentiable $\alpha(t)$.

(ii) However, we require $\alpha(0) = \alpha(T) = 0$, so that the new frame introduced in Sec. 4.1.2 coincides with the lab frame at $t = 0$ and $t = T$. This is guaranteed by $f(0) = f(T) = 0$ and $\dot{f}(0) = \dot{f}(T) = 0$.

Now we show that the choice $\zeta(t) = -\delta f(t) + i\dot{f}(t)$ indeed leads to the implementation of $\hat{U}_A$ with the phase θ given by Eq. (4.15). While this derivation is analogous to that of a Mølmer-Sorensen gate [32], we rederive it here in a way which allows for the easy addition of the effects of finite γ and κ in the next section.

We first assume that the qubits start in a computational basis state $|q\rangle$ ($q \in \{0,1\}^N$) with exactly $n_1 = \sum_{j=1}^N q_j$ qubits in state $|1\rangle$ (i.e. $\hat{n}_1 |q\rangle = n_1 |q\rangle$). Additionally, we assume that the cavity starts in a coherent state $|\beta(0)\rangle$. Since any initial state of the joint cavity-qubit system can be written as a superposition of states of the form $|\psi(0)\rangle = |\beta(0)\rangle \otimes |q\rangle$, those states suffice to uniquely determine the dynamics of the system under $\hat{H}_{\text{eff}}$ for any initial state.

We now make the Ansatz $|\psi(t)\rangle = e^{i\varphi_{n_1}(t)}|\beta_{n_1}(t)\rangle \otimes |q\rangle$, which indeed satisfies the Schrödinger equation for $\hat{H}_{\text{eff}}$ if

$$\begin{aligned} \dot{\beta}_{n_1} &= -i\delta\beta_n - in_1\zeta & (4.16)\\ \dot{\varphi}_{n_1} &= -n_1\mathrm{Re}(\zeta^*\beta_{n_1}) & (4.17) \end{aligned}$$

Making the choice $\zeta(t) = -\delta f(t) + i\dot{f}(t)$, the solution to Eq. (4.16) is given by

$$\beta_{n_1}(t) = \beta(0)e^{-i\delta t} + n_1 f(t) \tag{4.18}$$

Plugging this into Eq. (4.17) yields

$$\begin{aligned} \varphi_{n_1}(T) &= -n_1\mathrm{Re}\left[\int_0^T \mathrm{d}t(-\delta f(t) - i\dot{f}(t))\left(\beta(0)e^{-i\delta t} + n_1 f(t)\right)\right]\\ &= -n_1\mathrm{Re}\left[\int_0^T \mathrm{d}t\left(-n_1\delta f(t)^2 + \dot{h}(t)\right)\right], & (4.19) \end{aligned}$$

where

$$h(t) = -i\left(\beta(0)f(t)e^{-i\delta t} + \frac{1}{2}n_1 f(t)^2\right). \tag{4.20}$$

Using that $h(0) = h(T) = 0$, we obtain $\varphi_n(T) = n_1^2\theta$.

Thus, the final state at time $t = T$ is $|\psi(T)\rangle = e^{i\theta n_1^2}\left|\beta(0)e^{-i\delta T}\right\rangle \otimes |q\rangle = \left|\beta(0)e^{-i\delta T}\right\rangle \otimes (\hat{U}_A|q\rangle)$. Since the final state of the cavity is independent of n, there is no entanglement between the qubits and the cavity at time T. Furthermore, since $\hat{U}_A$ is *independent* of $\beta(0)$, and any arbitrary initial state of the cavity can be written as a superposition of different coherent states $|\beta(0)\rangle$, the implemented unitary is in fact independent of the initial state of the cavity.

4.2.1 Generation of GHZ states

The unitary $\hat{U}_A$ can be used together with global single qubit gates to generate the GHZ state [166, 167]

$$|\mathrm{GHZ}\rangle = (|0...0\rangle + |1...1\rangle)/\sqrt{2} \tag{4.21}$$

on N qubits as follows: Start by preparing the system in $|+\rangle^{\otimes N}$, where $|+\rangle = (|0\rangle + |1\rangle)/\sqrt{2}$. Then apply $\hat{U}_A$ for $\theta = \pi/2$, followed by the single qubit gate $\hat{U}_{sq} = \hat{U}_3\hat{U}_2\hat{U}_1$ on each qubit, where $\hat{U}_1 = \exp(i\pi\sigma_z/4)$, $\hat{U}_2 = (\sigma_x + \sigma_z)/\sqrt{2}$ and $\hat{U}_3 = \exp(i\pi(N+1)\sigma_z/(4N))$. For convenience, we restate the proof of this known result in Appendix A.5.

4.3 Geometric Phase Gate Performance in the presence of losses

In this section we calculate the gate fidelity for the implementation of $\hat{U}_A$ in the presence of losses. In contrast to the previous section we restrict ourselves to an initial state $|0\rangle$ of the cavity. We start by solving the Lindblad equation with the effective Hamiltonian $\hat{H}_{\text{eff}}$ and the jump operator $\hat{L}$. This allows us to find the quantum channel $\mathcal{E}$ acting on the qubits which is obtained if the cavity is traced out after the gate. Given $\mathcal{E}$, we then find an expression for the infidelity. In the limit $\gamma, \kappa \to 0$ and $T \to \infty$, the infidelity is found analytically to be

$$1 - F = \left(\frac{\kappa}{4(1+2^{-N})\delta} + \frac{\gamma\delta}{2g^2} \right) N\theta. \tag{4.22}$$

To our knowledge this is the first analytical solution of $1 - F$ for Hamiltonians of the type of Eq. (4.14) in the presence of the relevant losses.

4.3.1 Solution of the Lindblad Equation

In this section, we present the solution of the Lindblad equation for $\hat{H}_{\text{eff}}$ of Eq. (4.14) and $\hat{L}$, which is to our knowledge has never been done before for a Hamiltonain of the form $\hat{H}_{\text{eff}}$. We proceed analogously to Sec. 4.2 by first providing an Ansatz for the density matrix of the joint cavity-qubit system and then verifying that this Ansatz provides the correct solution of the time-dependent Lindblad equation.

To determine $\mathcal{E}$, it is sufficient to consider initial operator of the form $\rho(0) = |0\rangle\langle 0| \otimes |q\rangle\langle q'|$ of the joint cavity-qubit system, where $|q\rangle$ and $|q'\rangle$ ($q, q' \in \{0,1\}^N$) are computational basis states with exactly $n = \sum_j q_j$ and $m = \sum_j q'_j$ qubits in state $|1\rangle$.

We now make the Ansatz

$$\rho(t) = e^{i\varphi_{nm}} |\beta_n\rangle\langle\beta_m| \otimes |q\rangle\langle q'| / \langle\beta_n|\beta_m\rangle. \tag{4.23}$$

In Appendix A.3 we show that this Ansatz solves the Lindblad equation if

$$\begin{aligned} \dot{\beta}_n &= -(i\delta + \kappa/2)\beta_n - in\zeta && (4.24) \\ \dot{\varphi}_{nm} &= (m-n)(\zeta\beta_m + \zeta^*\beta_n) + i(m+n)\gamma_1/2 && (4.25) \end{aligned}$$

The quantum operation on the Hilbert space of the qubits is given by

$$\mathcal{E}(|q\rangle\langle q'|) = \text{tr}_{\text{cav}}(\rho(T)) = e^{i\varphi_{nm}(T)} |q\rangle\langle q'|. \tag{4.26}$$

This latter expression for $\mathcal{E}$ is used in the next subsection to determine the fidelity F.

4.3.2 Analytic calculation of the fidelity for γ, $\kappa \neq 0$

With Eq. (4.26), the averaged gate fidelity can be computed as

$$\begin{aligned} F &= \int \mathrm{d}\psi \, \langle\psi| \, e^{-i\theta\hat{n}_1^2} \mathcal{E}(|\psi\rangle \langle\psi|) e^{i\theta\hat{n}_1^2} \, |\psi\rangle \\ &= \frac{\sum_{n=0}^{N} \binom{N}{n} e^{i\varphi_{nn}} + \sum_{n,m=0}^{N} \binom{N}{n} \binom{N}{m} e^{i\varphi_{nm} - i(n^2-m^2)\theta}}{2^N(2^N+1)}, \end{aligned} \tag{4.27}$$

where the integral is taken over the whole computational subspace, and the second expression follows from [168].

Equation (4.27) now allows us to calculate the gate fidelity for arbitrary values of δ, T, γ and κ by inserting the solutions of Eqs. (4.24) and (4.25), given by

$$\beta_n(t) = -in \int_0^t \mathrm{d}t' \zeta(t') e^{-(i\delta+\kappa/2)(t-t')} \tag{4.28}$$

and

$$\begin{aligned} \varphi_{nm}(T) = \int_0^T & \Big[\; (m-n)(\zeta(t)\beta_m(t)^* + \zeta(t)^*\beta_n(t)) \\ & + \; i(m+n)\gamma_-(t)/2 \Big] \mathrm{d}t, \end{aligned} \tag{4.29}$$

respectively. In the limit $\gamma, \kappa \to 0$ and $T \to \infty$ this can be evaluated to Eq. (4.22), see Appendix. A.3.1. From Eq. (4.22) we observe that δ can be used to trade between the infidelity arising from the decay of photons in the cavity (proportional to κ) and decay of the ancillary state $|e\rangle$ (proportional to γ). The infidelity is minimized for $\delta = \sqrt{\kappa/[2(1+2^{-N})\gamma]}g$, which gives

$$1 - F = N\theta/\sqrt{2(1+2^{-N})C}, \tag{4.30}$$

where $C = g^2/(\gamma\kappa)$ denotes the cooperativity.

4.4 CZ gate: Numerical Results

In the following, we confirm our analysis above and find the infidelity of the $\hat{U}_A$ gate away from the limit $\Delta/g, \eta/g \to \infty$ via a numerical simulation of the full Lindblad equation for the specific case of the CZ gate ($N = 2$). The latter is implemented, up to single qubit gates, for $\theta = \pi/2$, see Fig. 4.2. To achieve this, we choose $f(t) = \sqrt{4\pi/(3\delta T)}\sin^2(\pi t/T)$,

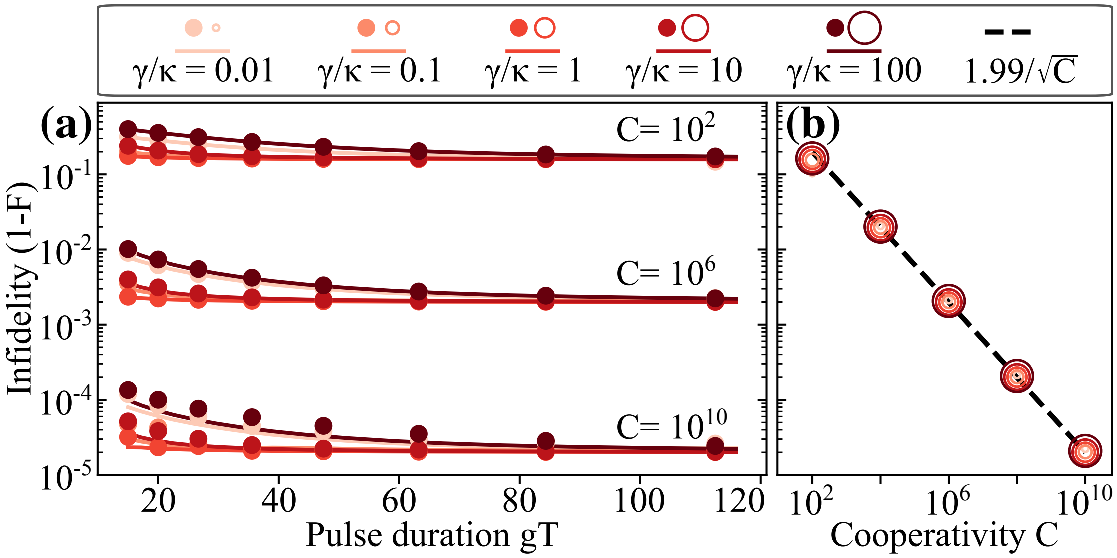

FIGURE 4.1: Numerical verification of CZ gate with geometric phase gate protocol: (a) Infidelity of a CZ gate vs pulse duration T for different values of C and γ/κ. Solid lines show the infidelity (analytic result) in the $\Delta \to \infty$ limit, circles show the infidelity (numerical calculation) at a finite value of Δ, chosen such that $\max_t |\eta(t)| = 30g$. For each T, C and γ/κ, δ is optimized to obtain the minimal 1-F. (b) Numerical (circles) and analytical (dashed line) value of the infidelity vs C in the $\Delta, T \to \infty$ limit for different values of γ/κ.

which satisfies the requirement $\delta \int_0^T f(t)^2 \mathrm{d}t = \pi/2$ (see Eq. (4.15)). We numerically verify that there is a δ with $|\zeta(t)| < g/2$ for all t as long as $gT \geq 8.3$. Fig. 4.3 shows the ideal evolution of the cavity state $|\beta_{n_1}\rangle$ in the quantum optical phase space, in the effective frame, for different two-qubit computational basis states. We see that the cavity evolution always forms a closed loop in the phase space, and the the loop is scaled with n_1, the number or qubits in the the $|1\rangle$ state along each axes, hence giving an area under the loop proportional to n_1^2, which also corresponds to the phase aquired by the computational qubit states.

$$|0\rangle_{\mathrm{cav}} \otimes \begin{bmatrix} |00\rangle \\ |01\rangle \\ |10\rangle \\ |11\rangle \end{bmatrix} \xrightarrow{\hat{U}_A} |0\rangle_{\mathrm{cav}} \otimes \begin{bmatrix} |00\rangle \\ e^{i\theta}|01\rangle \\ e^{i\theta}|10\rangle \\ e^{i4\theta}|11\rangle \end{bmatrix}$$

FIGURE 4.2: Action of ideal geometric phase gate unitary $\hat{U}_A$ on the computational qubit states for a system of $N = 2$ qubits. The choice of $\theta = \pi/2$ implements a CZ gate.

For the chosen f, the infidelity $1 - F$ is shown in Fig. 4.1(a) as a function of the pulse duration T for several values of the cooperativity C and ratios γ/κ. The solid lines

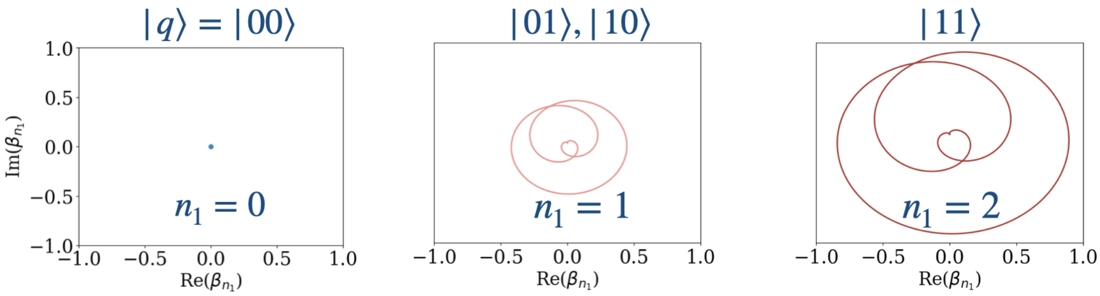

FIGURE 4.3: Ideal CZ gate dynamics: ideal dynamics of the cavity state $|\beta_{n_1}\rangle$ in the quantum optical phase space during the application of $\hat{U}_A = e^{i(\pi/2)\hat{n}_1^2}$. The cavity undergoes no evolution when no qubit is coupled to the cavity. For one qubit coupled to the cavity, i.e when one qubit starts in state $|1\rangle$, the cavity performs a closed loop evolution. For $n_1 = 2$, the cavity performs a similar phase space evolution but with area scaling with n_1^2.

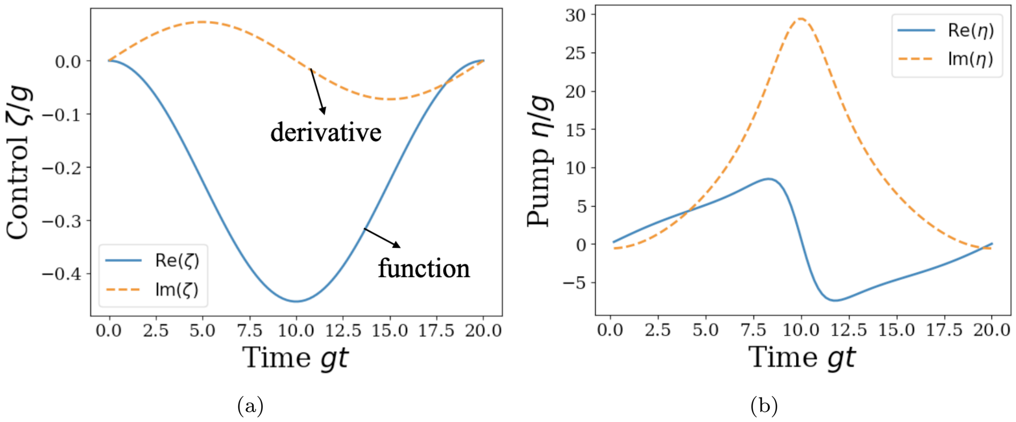

(a)

(b)

FIGURE 4.4: Example cavity drive pulses implementing CZ gate (a) in the effective frame and (b) in the original frame for .for $\max_t|\eta(t)| = 30g$, $\delta = 0.98g$, $\Delta = 26.67g$, $\kappa = 0.05g$ and $\gamma = 0.015g$. The pulse $\zeta(t)$ in the effective frame is given by $\zeta(t) = -\delta f(t) + i\dot{f}(t)$ (imaginary part goes as the derivative of the real part) for $f(t) = \sqrt{4\pi/(3\delta T)}\sin^2(\pi t/T)$ such that $\theta = \pi/2$. The pulse in the original frame is obtained by inverting ζ using Eqs. (4.12) and (4.6).

show the infidelity in the limit $\Delta/g \to \infty$ calculated analytically using Eqs. (4.27)-(4.29). The choice of δ has been optimized to achieve the best fidelity at each value of the pulse duration T. As $T \to \infty$ the infidelity approaches its asymptotic value, which is as predicted by Eq. (4.22) independent of γ/κ and only depends on the cooperativity C. For shorter pulse durations, there is a slight dependency on γ/κ, with the best infidelity always being achieved at $\gamma/\kappa \sim 1$. Note that the asymptotic value of the infidelity as $T \to \infty$ is often already closely approached for durations $T \sim 20g^{-1}$, underlining the fast speed of the gate protocol.

The dots in Fig. 4.1(a) show the infidelity which is achieved at a finite value of Δ, chosen such that $\max_t \eta(t) = 30g$. These values were found through a numerical integration of the Lindblad equation given by $\hat{H}$ [Eq. (4.1)] and the jump operator $\hat{L}$. Only small deviations between the numerical and the analytical results can be observed, showing that a maximum driving strength of $30g$ is sufficient to implement the GPG protocol with high fidelity. Fig. 4.4(b)-(c) shows example cavity drive pulses $\zeta(t)$ and the corresponding $\eta(t)$ in the original frame for $\max_t|\eta(t)| = 30g$, $\delta = 0.98g$, $\Delta = 26.67g$, $\kappa = 0.05g$ and $\gamma = 0.015g$, achieving $\theta = \pi/2$.

Finally, Fig. 4.1(b) compares the asymptotic value of the infidelity from Fig. 4.1(a) with its analytical prediction $1 - F = 1.99/\sqrt{C}$ from Eq. (4.30). A good agreement is observed for all values of C and γ/κ.

4.5 Fidelity estimates in realistic systems

In this section we provide estimates for the achievable gate fidelity and pulse duration for CZ gate with the geometric phase gate protocol for different physical systems. The systems are described in detail in section3.4. Table 4.1 summarises the results. We discuss atoms coupled to an optical cavity in Sec. 4.5.1, Rydberg atoms coupled to a microwave cavity in Sec. 4.5.2, polar molecules coupled to a microwave cavity in Sec. 4.5.3, and superconducting fluxonium qubits coupled to a microwave cavity in Sec. 4.5.4.

4.5.1 Neutral atoms coupled to an optical cavity

We consider neutral ^{87}Rb atoms trapped in optical tweezers and coupled to a fiber Fabry-Perot cavity as described in section 3.4.1. As qubit states, we choose the electronic groundstates $|0\rangle = \big|5\,^2S_{1/2}\,F = 1\,m_F = 0\big\rangle$ and $|1\rangle = \big|5\,^2S_{1/2}\,F = 2\,m_F = 0\big\rangle$, while the ancillary state $|e\rangle$ is the electronically excited state $|e\rangle = \big|5\,^2P_{3/2}\,F = 3\,m_F = 0\big\rangle$. The linewidth of the $|1\rangle \leftrightarrow |e\rangle$ transition ($\lambda = 780$ nm) is $\gamma = 2\pi \times 6$ MHz (FWHM).

For the cavity we assume a finesse $\mathcal{F} \approx 2 \times 10^5$, a waist radius $w_r \approx 2\,\mu$m and a length $L \approx 40\,\mu$m resulting in a cooperativity of $C = 3\lambda^2\mathcal{F}/(2\pi^3 w_r^2) \approx 1500$ with a coupling strength of $g \approx 2\pi \times 400$ MHz and $\kappa \approx 2\pi \times 20$ MHz (FWHM), so that $\gamma/\kappa \approx 0.3$.

With the numbers above, a CZ gate on two atoms can be achieved with a fidelity of $1 - F \approx 5.1\%$ in the limit $T, \Delta/g \to \infty$. Finite values for Δ can be chosen as long as $\Delta < \omega_0$, with the latter the energy separation between the states $|0\rangle$ and $|1\rangle$ (which is about 6.8 GHz for the states given above). For example, for a detuning $\Delta = 1$ GHz, the infidelity only slightly increases to $1 - F = 6.4\%$ for a choice of a finite (fast) pulse duration $T = 80$ ns. Other choices of Δ and T are possible [see plot Fig. 4.1(a)].

4.5.2 Rydberg atoms coupled to a microwave cavity

Higher fidelities at the expense of longer gate durations can be achieved by taking both $|1\rangle$ and $|e\rangle$ to be Rydberg states. We take the example described in section 3.4.2 with $|1\rangle = \left|90\ {}^2P_{3/2}\right\rangle$ and $|e\rangle = \left|90\ {}^2S_{1/2}\right\rangle$ in Cs with lifetime 2 ms and 820 μs, respectively , while $|0\rangle$ is chosen as a long-lived state in the ground manifold of the atoms. The states $|1\rangle$ and $|e\rangle$ may be coupled via a superconducting microwave resonator with reasonable coupling strength $g \approx 2\pi \times 4$ MHz [42]. Quality factors $Q > 3 \times 10^8$ have been reported for microwave stripline resonators [43], yielding $\kappa = \omega_e/Q \approx 2\pi \times 17$ Hz, and thus a cooperativity $C = 5 \times 10^9$, with $\gamma/\kappa \simeq 12$.

We include the decay of the state $|1\rangle$ in our analysis, which is important as the latter is now a Rydberg state with a lifetime comparable to that of $|e\rangle$. Therefore, the minimal infidelity is not achieved anymore as $\Delta, T \to \infty$, but at finite values of T. As an example we choose $\Delta = 2\pi \times 400$ MHz, which is much smaller than the spacing of $|1\rangle$ and $|e\rangle$ to adjacent Rydberg states (approximately 5 GHz). The minimal infidelity of $1 - F = 2.3 \times 10^{-4}$ is then achieved at $T = 800$ns. Furthermore, the GPG protocol could be used to generate a GHZ state on 40 qubits with an infidelity below 10^{-2}, in a duration of $T = 800$ ns (the same duration as for a CZ gate).

4.5.3 Polar Molecules coupled to a microwave cavity

We consider ultracold polar molecules coupled to a microwave resonator [80–82]. Following the discussion in section 3.4.4, we chose the computational basis states as$|0\rangle = |N = 1, m_N = 0, F = 1, m_F = 0\rangle$, $|1\rangle = |N = 1, m_N = 0, F = 2, m_F = 1\rangle$ to be different hyperfine levels of the first excited rotational manifold of the CaBr molecule, where N is the rotational quantum number. The ancillary state $|e\rangle$ is chosen in the second excited rotational level, $|e\rangle = |N = 2, m_N = 0, F = 2, m_F = 1\rangle$.

For this choice of states the frequency of the $|1\rangle \leftrightarrow |e\rangle$ transition is given by $\omega_e = 2\pi \times 11$ GHz and is thus in the microwave regime. Coupling strengths up to $g = 2\pi \times 400$ kHz can be achieved with realistic experimental parameters [80]. Assuming $Q = 3 \times 10^8$ (as in Sec. 4.5.2) yields $\kappa = \omega_e/Q \approx 2\pi \times 37$ Hz, while the decay from $|e\rangle$ is $\gamma \lesssim 10^{-2}$Hz [161] and can be neglected. If we assume $\gamma = 0$, arbitrarily low fidelities can be reached if we allow for arbitrarily long gate times. At finite pulse duration, the GPG protocol can achieve an infidelity of $1 - F = 1.0 \times 10^{-5}$ already at a pulse duration of $T = 80\,\mu$s, at $\Delta = 2\pi \times 1.2\,\text{MHz} \gg g$. Again, other choices of T and Δ are possible, see Fig. 4.1(a).

4.5.4 Superconducting Fluxonium qubits

Lastly, we choose the system of fluxonium qubits which have a compaticle level structure for our protocol. Following discussion in section 3.4.5, we choose the ground state $|0\rangle$ and the long lived state $|1\rangle$ (T_1 in the millisecond regime [162]) separated by $\sim 2\pi \times 100$MHz, while the next higher excited state $|e\rangle$ is separated by $2\pi \times 3.5$GHz from $|0\rangle$ [163, 164].

The dominant error in this regime is a finite dephasing time $T_2^* \approx 20\mu$s of the $|0\rangle \leftrightarrow |1\rangle$ transition [165], which is in fact not included in the error analysis in this chapter. We estimate the effect of this errors as an additional T/T_2^* contribution to the infidelity. We assume a coupling strength of $g = 2\pi \times 10$MHz (much smaller than the spacing between $|0\rangle$ and $|1\rangle$) to selectively couple the $|0\rangle \leftrightarrow |e\rangle$ transition to the microwave resonator. We choose this transition instead of the $|1\rangle \leftrightarrow |e\rangle$ transition and flip the roles of $|0\rangle$ and $|1\rangle$ since the coupling of the $|1\rangle \leftrightarrow |e\rangle$ transition to the cavity is weaker than the coupling of $|0\rangle \leftrightarrow |e\rangle$, further suppressing the unwanted coupling of $|1\rangle \leftrightarrow |e\rangle$ to the cavity. Further, we take $1/\gamma = 5\,\mu$s (including decay *and* dephasing of $|e\rangle$) and $Q = 3 \times 10^8$. These values allow for an infidelity of 4.0% for a CZ gate (dominated by the contribution from T_2^* of 3.2%) at $\Delta = 2\pi \times 30$ MHz, $\delta = 2\pi \times 13$ MHz and $T = 640$ ns. The T_2^* contribution could be reduced by using a larger coupling strength g, which would however lead to an increased unwanted coupling of the $|1\rangle \leftrightarrow |e\rangle$ transition to the cavity, the effect of which is beyond the scope of this work.

We note that while this fidelity estimates are lower than that for traditional nearest neighbor two qubit gates on fluxonium qubits [169], the non-local nature of our gate allows to couple distant qubits, which is only possible with several CZ gates – implying a reduced fidelity in systems with only nearest neighbor coupling. We also note that dynamical decoupling schemes have been proposed to extend T_2^* of a fluxonium qubit beyond $100\mu s$ [170], which would reduce the infidelities to 1.5%.

Emitter type	Neutral	Rydberg	Molecules	Fluxonium
Field type	optical	microwave	microwave	microwave
Coupling strength g	400 MHz	4 MHz	400 kHz	10 MHz
Cavity linewidth κ	20 MHz	17 Hz	40 Hz	-
Emitter transition linewidth γ	6 MHz	204 Hz	$< 10^{-2}$ Hz	0.8 MHz
Cooperativity C	1500	5×10^9	$> 10^{11}$	-
Gate infidelity	0.05	3×10^{-3}	6×10^{-5}	0.04
Pulse duration T	8 ns	800 ns	80 μs	640 ns

Table 4.1: GPG protocol in realistic setups: achievable gate fidelity and pulse duration for CZ gate with the geometric phase gate protocol for different physical systems: Neutral ^{87}Rb atoms coupled to a fiber-based Fabry Perot optical cavity, Cs Rydberg atoms coupled via superconducting microwave resonator, Polar Ca^{79}Br molecules coupled to microwave resonator and superconducting fluxonium qubits coupled to microwave resonator.

4.6 Conclusion and outlook

We have demonstrated that by driving the strongly detuned cavity with a strong drive η, the unitary $\hat{U}_A = \exp\bigl(i\theta\hat{n}_1^2\bigr)$ can be implemented through the proper choice of $\eta(t)$. We derived the infidelity of the GPG protocol and showed that it agrees with numerical simulations. Finally, we demonstrated how the GPG protocol can be used together with single qubit gates to generate a GHZ state on N qubits.

We evaluated the fidelity of the protocols in the presence of a finite lifetime of the ancillary state $|e\rangle$ of the qubits and of the photons in the cavity, finding that the infidelity scales as $\mathcal{O}(C^{-1/2})$. For Rydberg atoms or polar molecules coupled via a microwave cavity, we expect that our protocol can achieve infidelities below 10^{-3} with realistic parameters, while for neutral atoms coupled via optical cavities infidelities of the order of a few percent can be reached. We expect that our protocol may significantly benefit from optimization of the time-dependent pulse-shape $\eta(t)$. In particular, while the infidelity for the various gates in the limit $T \to \infty$ is independent of the exact choice of η, we expect that the infidelity at finite T could be improved by applying quantum optimal control techniques to optimize the pulse-shape of $\eta(t)$ [171, 172], making our protocol both achieve higher-fidelity and faster.

In Chapter 5, we demonstrate the utility of the GPG protocol, when combined with optimal control methods, for the preparation of metrologically useful optimal probe states which achieve a significant entanglement-enhanced advantage in quantum sensing beyond the standard quantum limit, in the presence of noise.

Chapter 5

Environment Adaptive Entanglement-Enhanced Quantum Sensing

The current chapter is an adaptation of the manuscript “Environment Adaptive Entanglement Enhanced Quantum Sensing” [173]. We combine the geometric phase gate described in chapter 4 along with its analytic solution of the noisy quantum channel dynamics with optimal control methods to prepare entangled states that are useful for quantum sensing, achieving a precision significantly better than the standard quantum limit in the presence of photon cavity loss, spontaneous emission, and dephasing. This work opens the way to entanglement-enhanced sensing with cold trapped atoms in cavities and is also directly relevant for experiments with trapped ions. The chapter is organised as follows: Sec. 5.1 intoduces entanglement enhanced quantum sensing and describes a basic field-sensing experiment where the designed state-preparation for sensing protocol can be applied. For the protocol, we work with the same cavity QED setup that we describe in chapter 3. Sec 5.2 presents the quantum channel of the geometric phase gate discussed in chapter 4 and recalls the exact solution of the quantum channel dynamics in the presence of losses, here focusing on the dynamics in the symmetric Dicke subspace. In Sec. 5.3, we introduce the state-preparation protocol consisting of sequence of pulses where the geometric phase gate operations are combined with global single-qubit rotations to consecutively steer and squeeze an initial coherent Dicke state for a finite number of steps P. Section 5.4 discusses the preparation of an arbitrary final state in the symmetric Dicke subspace which is optimised for a cost function corresponding to the variance of a desired measurement with an observable $\hat{M}$, where the final state is the probe state in the quantum sensing experiment. Section 5.5 discusses the extensive numerical results obtained by our protocol, including discussion of experimental observability of the performance of the optimally prepared states in the presence of dephasing Sec. 5.5.2, effects of dephasing during the state preparation protocol in Sec. 5.5.5, and insights on results when the spontaneous emission is treated in the Lindblad formalism in Sec. 5.5.6. Finally, Sec. 5.6 provides performance estimates of our state preparation protocol for an example system with neutral atoms and optical cavity and Sec. 5.7 presents the chapter conclusion and outlook.

5.1 Introduction to entanglement-enhanced quantum sensing

In quantum sensing, entanglement-enhanced strategies exploit the properties of entangled quantum states to achieve sensitivities beyond the classical limits, often approaching or even reaching the Heisenberg limit. Such enhancements make quantum sensing particularly powerful for detecting weak fields, measuring time intervals with extreme precision, or probing delicate changes in physical parameters, all of which are important for applications for example in in metrology, and gravitational wave detection.

5.1.1 Sensitivity Limits

For typical system of N spin-1/2 paticles interacting with a field pointing in $\vec{n}$ direction, the Hamiltonian can be described as $\hat{H}_{\vec{n}} = JJ_{\vec{n}}$, where J is spin-field coupling strength and $J_{\vec{n}}$ is the component of the collective spin angular momentum parallel to the field direction. This Hamiltonian generates the dynamics $\hat{U} = e^{-i\beta J_{\vec{n}}}$, where we define

$$\beta = Jt. \tag{5.1}$$

A very general sensing experiment can be designed with the task of estimating this small parameter β by measuring the expectation value of a Hermitian operator $\hat{M}$. For a constant evolution time t, and with the knowledge of the spins' coupling component (eg. electric dipole moment or gyromagnetic ratio), this is equivalent to measuring the field strength. The precision with which we can estimate the parameter β in this quantum field sensing setup is fundamentally constrained by quantum mechanics, which can be associated with the variance in the estimation of β written as

$$(\Delta\beta)^2 = \frac{(\Delta\hat{M}(\beta))^2}{\left|\partial_\beta\langle\hat{M}(\beta)\rangle\right|^2}, \tag{5.2}$$

where $(\Delta\hat{M})^2 = \langle\hat{M}^2\rangle - \langle\hat{M}\rangle^2$. Specifically, this precision of a parameter estimate is bounded by the Quantum Cramér-Rao Bound (QCRB), which gives a minimum variance $(\Delta\beta)^2 \geq 1/(mF_Q[\rho])$, where m is the number of independent measurements, and $F_Q[\rho]$ is the Quantum Fisher Information (QFI) associated with the probe state ρ. The QFI is maximized for entangled states, which provides a mechanism for surpassing the classical shot noise limit that characterizes unentangled, or classical, sensing schemes [52].

For an entangled state, the QFI scales quadratically with the number of particles N, leading to the so-called Heisenberg scaling, where $(\Delta\beta)^2 \propto 1/N^2$. In contrast, for a product (unentangled) state, the scaling is linear in N, known as the standard quantum limit (SQL), where $(\Delta\beta)^2 \propto 1/N$. This distinction underscores the potential for entanglement to dramatically improve sensing precision.

For example, let us consider the case of a Greenberger-Horne-Zeilinger (GHZ) state, which for N spins is defined as

$$|GHZ\rangle = \frac{1}{\sqrt{2}}(|0\rangle^{\otimes N} + |1\rangle^{\otimes N}), \tag{5.3}$$

where $|0\rangle \equiv |+1/2\rangle_z$ and $|1\rangle \equiv |-1/2\rangle_z$. Now consider the dynamics generated by a field along $\vec{z}$ of the form $\hat{U} = e^{-i\beta J_z}$. Under such dynamics, the state is evolved as

$$|GHZ\rangle \sim \frac{1}{\sqrt{2}}(|0\rangle^{\otimes N} + e^{-iN\beta}|1\rangle^{\otimes N}), \tag{5.4}$$

with a difference of phases of the two terms scaling as $\sim N$. Now choosing a measurement operator $\hat{M}$ as the parity along $x-$basis, one obtains for this state $\langle\hat{M}\rangle = \cos(N\theta)$, $(\Delta\hat{M})^2 = \sin^2(N\theta)$ [52]. Hence obtaining

$$(\Delta\beta)^2|_{\beta=0} = \frac{1}{N^2}, \tag{5.5}$$

which means saturating the Heisenberg scaling.

Thus when entangled probe states are used, the effective rotation caused by the interaction Hamiltonian $\hat{H}_{\vec{n}}$ results in a correlated phase evolution across all qubits, amplifying the observable shift induced by a small change in β. This amplification can be exploited by carefully chosen measurements to detect field strengths or other physical parameters with enhanced sensitivity.

5.1.2 Optimal strategies in quantum sensing

In practical terms, achieving the precision promised by the QFI requires selecting an optimal measurement observable $\hat{M}$ that maximizes sensitivity to changes in β [174, 175]. The variance of the estimator for β is minimized by choosing an observable that aligns closely with the dynamics generated by the Hamiltonian $\hat{H}_{\vec{n}} = J\hat{J}_{\vec{n}}$, where $\hat{J}_{\vec{n}}$ is the collective spin operator along the field direction. The optimal measurement observable is generally constructed from components of the spin operator that yield the maximum sensitivity, often involving squeezing or entangling the spin state along specific directions. This process reduces the variance in one quadrature of the spin state at the expense of increased variance in the orthogonal quadrature, an effect characterized by spin squeezing.

However another alternative approach, which we explore in this work, is to fix an operator $\hat{M}$ available in experiments for a defined field sensing task, and find the optimal entangled state that maximizes sensitivity to changes in β.

5.2 Geometric phase gate on symmetric Dicke subspace

We first recall here the setup from chapter 3 consisting of N three-level spin systems with computational *qubit* basis states $|0\rangle$ and $|1\rangle$ and an excited state $|e\rangle$. The levels $|1\rangle$ and $|e\rangle$ are coupled via a cavity mode with annihilation (creation) operators $\hat{a}(\hat{a}^\dagger)$ with coupling strength g (Fig. 5.1(a)). The cavity mode is driven by a complex classical field of strength $\eta(t)$ which is detuned from the cavity and the $|1\rangle \leftrightarrow |e\rangle$ transition by δ and Δ, respectively. The relevant Hamiltonian reads

$$\hat{H} = \delta\hat{a}^\dagger\hat{a} + \left(\Delta - i\frac{\gamma}{2}\right)\hat{n}_e + \left[\left(g\hat{S}^- + i\eta(t)\right)\hat{a}^\dagger + \text{h.c.}\right]$$

with $\hat{n}_e = \sum_j |e_j\rangle\langle e_j|$, $\hat{S}^+ = \sum_j |e_j\rangle\langle 1_j|$, $\hat{S}^- = (\hat{S}^+)^\dagger$, and γ the spontaneous emission rate from $|e\rangle$ state.

In chapter 4, we show that in the limit of strong cavity driving $\eta/g \to \infty$ and large detuning $\Delta/g \to \infty$, and $\delta = \mathcal{O}(g)$, the system dynamics can be reduced to the effective Hamiltonian

$$\hat{H}_{\text{eff}} = \delta\hat{a}^\dagger\hat{a} + \left(-i\frac{\gamma_1}{2} + \zeta\hat{a}^\dagger + \zeta^*\hat{a}\right)\hat{n}_1, \tag{5.6}$$

with $\hat{n}_1 = \sum_j |1_j\rangle\langle 1_j|$, $\gamma_1 = \gamma(1 - \sqrt{1 - 4|\zeta|^2/g^2})/2$, and $\zeta = g^2\alpha/\sqrt{4g^2|\alpha|^2 + \Delta^2}$ where $\dot{\alpha} = -\eta - (i\delta + \kappa/2)\alpha$ with $\alpha(t = 0) = 0$. Here we recall the basic elements of the derivation: Eq. (5.6) is obtained from $\hat{H}$ by first moving into a frame rotating with the cavity by applying a time-dependent displacement operator $\hat{D}(\alpha(t)) = \exp\left(\alpha\hat{a}^\dagger - \alpha^*\hat{a}\right)$,

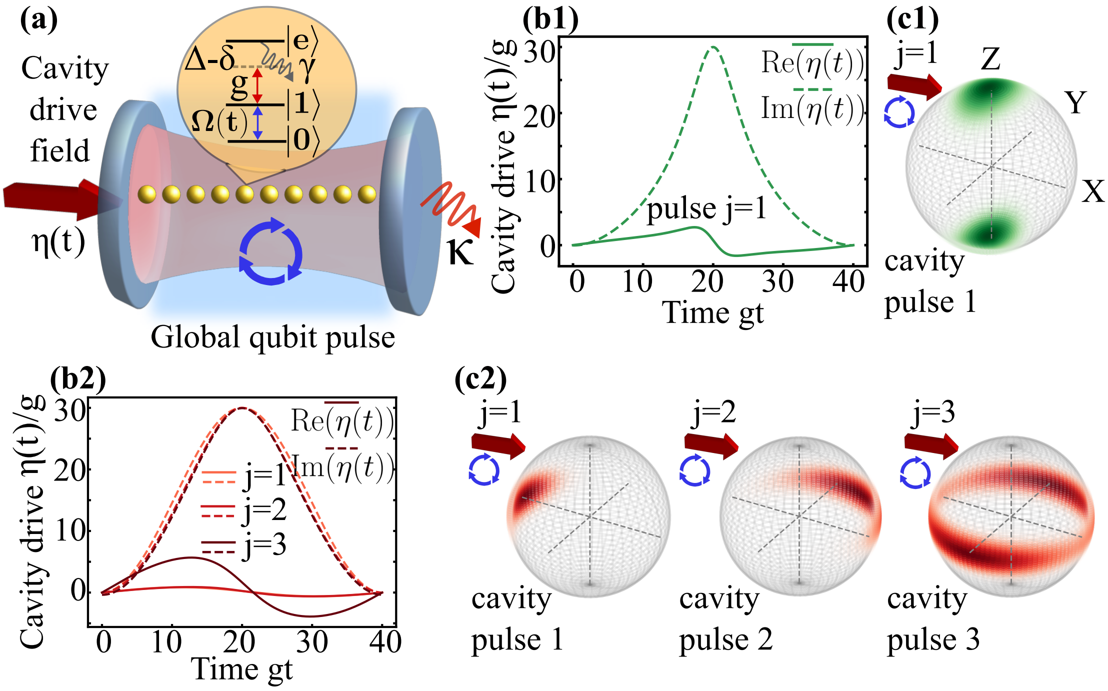

FIGURE 5.1: (a) A register of spins with states $\{|0\rangle, |1\rangle, |e\rangle\}$ is coupled to a cavity mode with coupling strength g addressing the $|1\rangle \leftrightarrow |e\rangle$ transition, with detuning $\Delta - \delta$. The cavity mode is externally driven by a laser with amplitude $|\eta(t)|$, and a global laser pulse is applied on the $|0\rangle \leftrightarrow |1\rangle$ spin transition. Panels (b1,b2): Cavity drive pulses of the optimal state preparation protocol for $N = 40$, $C = 10^4$ and $\gamma/\kappa = 0.01$, for GHZ-like and Dicke-like states, respectively. Throughout, we make a choice of the cavity drive pulse $\zeta(t)$ in the effective frame with $\mathrm{Re}(\zeta(t)) = -2\delta\sqrt{\frac{2\phi}{3\delta T}}\sin^2(\frac{\pi t}{T})$ and $\mathrm{Im}(\zeta(\mathrm{t})) = -\partial_t \mathrm{Re}(\zeta(t))/\delta$ (see [62] and [54]). The obtained minimal measurement precision variances here are $N(\Delta\beta)^2_{\mathrm{GHZ}} = 0.03$ and $N(\Delta\beta)^2_{N/2} = 0.08$. The parameters used in optimal state preparation protocol can be found in tables. 5.1 and 5.2. (c1, c2): State trajectories in Husimi-Q representation of the spin states in the symmetric Dicke subspace after the application of each protocol step $j\,\forall j = 1, \ldots, P$.

with the amplitude $\alpha(t)$. The $\eta, \kappa-$dependent choice of α ensures that in the rotated frame the cavity drive $\eta(t)$ effectively appears as a collective drive of the qubits as $-g(\alpha\hat{S}^+ + \alpha^*\hat{S}^-)$. Further rotating in a frame that diagonalizes the qubit subspace in the limit $\Delta/g \to \infty$ and assuming that $n_e = 0$ at time $t = 0$ leads to Eq. (5.6). Interestingly, Eq. (5.6) is equivalent up to single spin rotations to the Mølmer-Sørensen Hamiltonian [32], originally developed for trapped ions, and can be thus used to generate fast geometric phase gates – albeit now for spin systems coupled to a cavity.

In this chapter as well, we are interested in the open system dynamics determined by Eq. (5.6) containing the non-hermitian contribution of γ and within a Lindblad master equation approach with $\dot{\rho} = -i\hat{H}_{\mathrm{eff}}\rho + i\rho\hat{H}^\dagger_{\mathrm{eff}} + \hat{L}\rho\hat{L}^\dagger - \{\hat{L}^\dagger\hat{L}, \rho\}/2$, with ρ the system density matrix and $\hat{L} = \sqrt{\kappa}\hat{a}$ the jump operator where κ is the the cavity mode decay rate. Later in section 5.5.6 decay from $|e\rangle$ with rate γ is also included as a local-homogeneous collective process in the Lindblad master equation defined in a collective

Hilbert space and results are analysed numerically.

We define the quantum channel of the geometric phase gate (realised with a single cavity drive of duration T) acting on a basis state $|q_n\rangle\langle q_m|$ of the qubit density matrix, where $\hat{n}_1|q_n\rangle = n|q_n\rangle$, ($q_n \in \{0,1\}^N$) as

$$\mathcal{E}_{\text{gpg}}(|q_n\rangle \langle q_m|) = e^{i\varphi_{nm}(T)} |q_n\rangle \langle q_m| \,. \tag{5.7}$$

The channel $\mathcal{E}_{\text{gpg}}$ is obtained after tracing out the cavity from the joint spin-cavity state, which results in phase accumulation as a function of n, m (i.e., the number of qubits in the $|1\rangle$ state).

In the following, we recall the exact solution of the geometric phases $\varphi_{nm}(T)$ in Eq. 5.7. We describe the state of the joint spin-cavity system at any time t as $\rho(t) = \sum_{n,m} \rho_{nm}(t)$, and use an Ansatz for the state components $\rho_{nm}(t)$ given by

$$\rho_{nm}(t) = e^{i\varphi_{nm}(t)} |\beta_n\rangle \langle \beta_m| \otimes |q_n\rangle \langle q_m| / \langle \beta_n|\beta_m\rangle, \tag{5.8}$$

where $\varphi_{nm}(t)$ are the *geometric-phases* acquired by the qubit state component $|q_n\rangle \langle q_m|$, and $|\beta_n\rangle \langle \beta_m|$ is the corresponding state of the cavity mode. With this Ansatz, we exactly solve the open quantum system for $\rho_{nm}(t)$ with $\kappa, \gamma \neq 0$. The latter is described by the Lindbladian master equation given by

$$\dot{\rho}_{nm} \quad = -i\hat{H}^n_{\text{eff}}\rho_{nm} + i\rho_{nm}(\hat{H}^m_{\text{eff}})^\dagger + \hat{L}\rho_{nm}\hat{L}^\dagger - \tfrac{1}{2}\{\hat{L}^\dagger\hat{L}, \rho_{nm}\},$$

with $\hat{H}^n_{\text{eff}} = \delta a^\dagger a + (-i\frac{\gamma_1}{2} + \zeta(t)\hat{a}^\dagger + \zeta(t)^*\hat{a})n$. On substituting the Ansatz for ρ_{nm} in the master equation, we obtain the derivatives for $\beta_n(t)$ and $\varphi_{nm}(t)$ as

$$\dot{\beta}_n \quad = \quad -(i\delta + \kappa/2)\beta_n - in\zeta, \tag{5.9}$$

$$\dot{\varphi}_{nm} \quad = \quad (m-n)(\zeta\beta_m + \zeta^*\beta_n) + i(m+n)\gamma_1/2. \tag{5.10}$$

We now take the initial state of the joint spin-cavity system as $\rho(0) = |\beta_n(0)\rangle \langle \beta_m(0)| \otimes |q_n\rangle \langle q_m|$, which forms the basis for all possible initial states and is hence sufficient to obtain a general solution for the state evolution. The solutions corresponding to $\beta(t)$ and $\psi_{nm}(t)$ are then given by (refer to chapter 4 for details)

$$\beta_n(t) = \beta_n(0)e^{-(i\delta+\kappa/2)t} - in\int_0^t \mathrm{d}t'\zeta(t')e^{-(i\delta+\kappa/2)(t-t')}, \tag{5.11}$$

and

$$\begin{aligned}\varphi_{nm}(t) = \int_0^t \quad \Big[& \quad (m-n)(\zeta(t)\beta_m(t)^* + \zeta(t)^*\beta_n(t)) \\ + & \quad i(m+n)\gamma_1(t)/2\Big]\mathrm{d}t.\end{aligned} \tag{5.12}$$

The cavity drive pulses $\zeta(t)$ in $\hat{H}_{\text{eff}}$ are chosen of duration T such that $\zeta(0) = \zeta(T) = 0$ so that $\beta_n(0) = \beta_n(T)$, ensuring that the cavity mode is decoupled from the spins at the end of the geometric phase gate. One can hence write the corresponding quantum channel of the geometric phase gate on a spin basis state by tracing out the cavity mode as in Eq. (5.7). In the limit $T \to \infty$, a simple analytic solution to Eqs. (5.9) and (5.10) is obtained via an adiabatic approximation and to the first order in κ, γ, by setting $\dot{\beta}_n = 0$ in Eq. (5.9) as

$$\frac{\varphi_{nm}}{\phi} = n^2 - m^2 + (m-n)^2\frac{i\kappa}{2\delta} + (m+n)\frac{i\gamma\delta}{2g^2}, \tag{5.13}$$

where

$$\phi = \delta^{-1}\int_0^T \mathrm{d}t|\zeta(t)|^2, \tag{5.14}$$

is the *geometric phase* corresponding to the unitary evolution $\hat{U}_{\text{gpg}} = e^{i\phi\hat{n}_1^2}$ in the lossless case ($\kappa, \gamma = 0$). To our knowledge, this is the first analytic solution of geometric gate dynamics in the presence of relevant noise.

Recall from section 2.2.2.1 the *symmetric Dicke subspace*, which is the vector space spanned by states

$$|\mathcal{D}_n^N\rangle = \frac{1}{\sqrt{\binom{N}{n}}} \sum_{\{\mathcal{P} \,\mid\, \hat{n}_1|q_n\rangle = n|q_n\rangle\}} \mathcal{P}|q_n\rangle, \tag{5.15}$$

where $\mathcal{P}$ denotes all qubit permutations resulting in computational states $|q_n\rangle$ with a fixed number of spins n in $|1\rangle$. These are the simultaneous eigenstates of the collective spin angular momentum operators $\hat{J}^2 = \hat{J}_x^2 + \hat{J}_y^2 + \hat{J}_z^2$ and $\hat{J}_z$. We note that for a choice of initial state $\left|\mathcal{D}_0^N\right\rangle$ in the symmetric Dicke subspace, the qubit dynamics during a geometric phase gate remains restricted to the symmetric Dicke subspace. The action of the quantum channel $\mathcal{E}_{\text{gpg}}$ on ρ expanded in the Dicke basis then reads

$$\mathcal{E}_{\text{gpg}}(\rho) = \sum_{n,m} e^{i\varphi_{nm}(T)} \left\langle\mathcal{D}_n^N\right| \rho \left|\mathcal{D}_m^N\right\rangle \left|\mathcal{D}_n^N\right\rangle \left\langle\mathcal{D}_m^N\right|, \tag{5.16}$$

see Eq. (5.7).

5.3 State preparation of arbitrary state in symmetric Dicke subspace

The state-preparation protocol for obtaining arbitrary N-particle entangled states within the Dicke subspace is now realized by a pulse sequence with P steps, where each step j consists of the cavity geometric phase gate $(\mathcal{E}_{\text{gpg}})_j$ followed by a global qubit rotation:

$$\hat{\mathcal{U}}_j = e^{-i\theta_j^\alpha \hat{J}_z} e^{-i\theta_j^\beta \hat{J}_y} e^{-i\theta_j^\gamma \hat{J}_z}. \tag{5.17}$$

These global rotations can be realised with a side-drive on the spins.We recall the Hamiltonian for the side drive with Rabi frequency Ω from 3.1.1, written now in terms of the collective spin operators:

$$\begin{aligned} \hat{H}_\Omega &= \frac{\Omega(t)}{2}\hat{J}_+ + \frac{\Omega(t)^*}{2}\hat{J}_- && (5.18)\\ &\equiv |\Omega(t)|(\cos(\arg(\Omega))\hat{J}_x - \sin(\arg(\Omega))\hat{J}_y) && (5.19)\\ e^{-i\hat{H}_\Omega t} &= e^{-i(\pi/2)\hat{J}_z} e^{-i\arg(\Omega(t))\hat{J}_z} e^{-i|\Omega(t)|t\hat{J}_y} && (5.20) \end{aligned}$$

where $\hat{J}_+ = \hat{J}_x + i\hat{J}_y$, $\hat{J}_- = \hat{J}_x - i\hat{J}_y$ and $\Omega(t) = |\Omega(t)|e^{i\arg(\Omega)t}$. In writing the last equation above, we note that in a frame rotating along z with phase $\arg(\Omega) + \pi/2$, the Hamiltonian $\hat{H}_\Omega$ is equivalent to $\hat{H}'_\Omega = |\Omega|\hat{J}_y$ which produces a unitary evolution $e^{-i|\Omega(t)|t\hat{J}_y}$. On transforming back to the original frame, the total unitary evolution is given by Eq. (5.20).

We now define the quantum channel $\mathcal{E}_\text{q}$ which reads

$$\mathcal{E}_\text{q} = \mathcal{E}_P \cdot \mathcal{E}_{P-1} \cdots \mathcal{E}_1 \cdot \hat{\mathcal{U}}_0, \tag{5.21}$$

with $\mathcal{E}_j = \hat{\mathcal{U}}_j \cdot (\mathcal{E}_{\text{gpg}})_j$. In Refs. [176–178], it has been shown that such a sequence with a finite number of steps P combining global spin rotations and squeezing-like geometric phase operations can synthesize any arbitrary state in the symmatric subspace Dicke subspace. However here, we find optimal solutions for open quantum systems.

In the limit $T \to \infty$, $(\mathcal{E}_{\text{gpg}})_j$ is fully characterised by the geometric phase ϕ_j and cavity-drive detuning δ_j for fixed loss rates κ, γ (see Eq. (5.13)). The state-preparation protocol is thus characterised by the set of parameters given by

$$\Theta = \{\theta_0^\alpha, \theta_0^\beta, \theta_0^\gamma, \theta_j^\alpha, \theta_j^\beta, \theta_j^\gamma, \phi_j, \delta_j \ldots ; \forall j = 1, 2 \ldots P\}, \tag{5.22}$$

consisting of the global rotation angles $\theta_j^{\alpha,\beta,\gamma}$, the geometric phases ϕ_js and corresponding δ_js in $\mathcal{E}_q$.

5.4 Optimal probe state preparation for field sensing experiment

In this section, we employ the state-preparation protocol described above to prepare an *optimally robust* probe state for a defined field-sensing experiment. We define a very general field sensing experiment as introduced in section 5.1 by considering a field along the direction $\vec{n}$ that is coupled to the N spin qubits with interaction Hamiltonian $\hat{H}_{\vec{n}} = J\hat{J}_{\vec{n}}$, with J the coupling strength. $\hat{H}_{\vec{n}}$ is applied for a time t such that a given probe state ρ is rotated along the field axis by an angle $\beta = Jt$. The goal of the field-sensing experiment is to estimate the rotation angle β as accurately as possible by performing measurements on the spins using an observable $\hat{M}$. For any given $\hat{M}$ (unbiased estimator), β can be estimated with a variance

$$(\Delta\beta)^2 = \frac{(\Delta\hat{M}(\beta))^2}{\left|\partial_\beta\langle\hat{M}(\beta)\rangle\right|^2}, \tag{5.23}$$

where $\hat{M}(\beta) = e^{-i\hat{H}_{\vec{n}}\beta}\hat{M}e^{i\hat{H}_{\vec{n}}\beta}$ and $(\Delta X)^2 = \langle X^2\rangle - \langle X\rangle^2$. The minimal $(\Delta\beta)^2$ is bound by the quantum Cramer-Rao inequality $(\Delta\beta)^2 \geq 1/\mathcal{F}_Q(\rho, \hat{H}_{\vec{n}})$, where $\mathcal{F}_Q(\rho, \hat{H}_{\vec{n}})$ is the quantum Fisher information, with $\mathcal{F}_Q = N$ and $\mathcal{F}_Q = N^2$ for uncorrelated and maximally entangled N-spin states, respectively [179].

The problem we focus on is finding the *optimal* probe state ρ_{opt} that can be prepared in the presence of noise for given $\hat{H}_{\vec{n}}$ and $\hat{M}$ accessible in experiments. This is achieved by choosing $(\Delta\beta)^2$ in Eq. (5.23) as the *protocol cost function* and minimizing it with respect to Θ in $\mathcal{E}_q$, for the chosen $\hat{M}$, keeping β as an additional free parameter in the optimisation [180]. The latter is performed numerically using the *Broyden–Fletcher–Goldfarb–Shanno* method [47, 48], where gradients of the cost function are computed analytically. Since the optimal parameters Θ_{opt} are found for $\kappa, \gamma \neq 0$, the obtained cavity drive and global qubit pulses are *noise-informed.*

We illustrate below the protocol by choosing two different observables $\hat{M}$ of experimental relevance:(I) parity along the x axis $\hat{M} = \bigotimes_{i=1}^{N}\hat{\sigma}_x^{(i)}$ [49, 50], and (II) square of the collective spin observable $\hat{M} = \hat{J}_z^2$ along $\hat{z}$ [51]. Choices (I) and (II) correspond to the observables that for $\kappa = \gamma = 0$ are theoretically known to saturate the quantum Cramer-Rao inequality with ideal GHZ and Dicke $\left|\mathcal{D}_{N/2}^{N}\right\rangle$ probe states for fields along $\vec{n} = \hat{z}$ and $\hat{y}$ directions, respectively [52, 53].

5.4.1 Analytic gradients of cost function

In this section we provide the derivatives of our protocol cost function $(\Delta\beta)^2$ with respect to all parameters Θ in Eq. (5.22). We first start out by writing the derivatives of the states obtained after each step j in the protocol given by $\mathcal{E}_q$ in Eq. (5.21).

Our protocol starts with the application of $\hat{\mathcal{U}}_0$ on the initial state $\rho_{\text{in}} = |\mathcal{D}_0\rangle$, giving $\rho_0 = \hat{\mathcal{U}}_0\rho_{\text{in}}\hat{\mathcal{U}}_0^\dagger$. The states ρ_j obtained after application of each $\mathcal{E}_j$ for $j = 1, 2 \ldots P$ are obtained as

$$\rho_j \quad = \quad \hat{\mathcal{U}}_j\mathcal{E}_{gpg}(\rho_{j-1})\hat{\mathcal{U}}_j^\dagger. \tag{5.24}$$

It is then straightforward to write the derivatives of ρ_0 and ρ_j $\forall j = 1, 2, \ldots P$ with respect to the parameters Θ, which are obtained as given below

$$\begin{aligned}
\partial_{\theta_0}\rho_0 \quad &= (\partial_{\theta_0}\hat{U}_0)\rho_{\text{in}}\hat{U}_0^\dagger + \hat{U}_0\rho_{\text{in}}(\partial_{\theta_0^\alpha}\hat{U}_0^\dagger), \\
\partial_{\theta_j}\rho_0 \quad &= \partial_{\phi_j}\rho_0 = \partial_{\delta_j}\rho_0 = 0, \\
\partial_{\theta_j}\rho_j \quad &= (\partial_{\theta_j}\hat{U}_j)\mathcal{E}_{gpg}(\rho_{j-1})\hat{U}_j^\dagger + \hat{U}_j\mathcal{E}_{gpg}(\rho_{j-1})(\partial_{\theta_j}\hat{U}_j^\dagger), \\
\partial_{\phi_j}\rho_j \quad &= \hat{U}_j(\sum_{n,m}\partial_{\phi_j}(\varphi_{nm})e^{i\varphi_{nm}}\langle\mathcal{D}_n|\,\rho_j\,|\mathcal{D}_m\rangle\,|\mathcal{D}_n\rangle\,\langle\mathcal{D}_m|)\hat{U}_j^\dagger, \\
\partial_{\delta_j}\rho_j \quad &= \hat{U}_j(\sum_{n,m}\partial_{\delta_j}(\varphi_{nm})e^{i\varphi_{nm}}\langle\mathcal{D}_n|\,\rho_j\,|\mathcal{D}_m\rangle\,|\mathcal{D}_n\rangle\,\langle\mathcal{D}_m|)\hat{U}_j^\dagger \\
\partial_{\Theta_{k<j}}\rho_j \quad &= \mathcal{E}_j\ldots\mathcal{E}_{k+1}(\partial_{\Theta_k}\rho_k), \partial_{\Theta_{k>j}}\rho_j = 0.
\end{aligned}$$

We have used the shorthand θ_j for $\theta_j^\alpha, \theta_j^\beta, \theta_j^\gamma$ and Θ_j refers to all elements in the set $\{\theta_j^\alpha, \theta_j^\beta, \theta_j^\gamma, \phi_j, \delta_j\}$ in the equations above. Note that the derivatives of the state ρ_j are simply obtained by performing similar operations- applying the geometric-phase-gate operation $\mathcal{E}_{\text{gpg}}$ and global spin rotation operations. For example, obtaining $\partial_{\phi_j}\rho_j$ and $\partial_{\delta_j}\rho_j$ are similar to calculating $\mathcal{E}_{\text{gpg}}(\rho_j)$ but with modified phases $e^{i\varphi_{nm}} \to \partial_{\phi_j}(\varphi_{nm})e^{i\varphi_{nm}}$ and $e^{i\varphi_{nm}} \to \partial_{\delta_j}(\varphi_{nm})e^{i\varphi_{nm}}$ respectively. The optimal probe state is prepared after at $j = P$ protocol steps which we denote by $\rho_P = \rho_{\text{opt}}$. With the prescription described above we obtain the exact derivatives corresponding to $\partial_\Theta\rho_{\text{opt}}$, for all parameters Θ. In the following, we obtain the derivatives of the protocol cost function $(\Delta\beta)^2$ for the two choices of the measurement operator $\hat{M}$ corresponding to $(\Delta\beta)^2_{\text{GHZ}}$ and $(\Delta\beta)^2_{N/2}$ for case I and II below respectively.

5.4.1.1 Case I: Choosing $\hat{M} = \hat{\mathcal{P}}_x = \bigotimes_{i=1}^{N} \hat{\sigma}_x^{(i)}$

The operator $\mathcal{P}_x = \bigotimes_{i=1}^{N} \hat{\sigma}_x^{(i)}$ measures the parity of the state along x. Using $e^{i\pi/2\sigma_x} = i\sigma_x$, we rewrite $\hat{M}$ as

$$\hat{M} \;=\; e^{i\pi(\hat{J}_x - N/2)}. \tag{5.25}$$

We choose the field generator corresponding to a field along z for this case as $\hat{H}_{\vec{z}} = J\hat{J}_z$. Let the state obtained after the rotation of the optimal probe state ρ_{opt} by an angle $\beta = Jt$ along the field axis be denoted by $\rho_{\text{opt}}^{\beta}$. We obtain

$$\rho_{\text{opt}}^{\beta} = e^{-i\beta\hat{J}_z}\rho_{\text{opt}}e^{i\beta\hat{J}_z},\; \partial_\beta\rho_{\text{opt}}^{\beta} = i\left[\rho_{\text{opt}}^{\beta}, \hat{J}_z\right], \tag{5.26}$$

$$\partial_\Theta\partial_\beta\rho_{\text{opt}}^{\beta} = i\left[\partial_\Theta\rho_{\text{opt}}^{\beta}, \hat{J}_z\right], \tag{5.27}$$

$$\langle\hat{\mathcal{P}}_x(\beta)\rangle = \text{Tr}(\hat{\mathcal{P}}_x, \rho_{\text{opt}}^{\beta}), \tag{5.28}$$

$$\partial_\Theta\langle\hat{\mathcal{P}}_x(\beta)\rangle = \text{Tr}(\hat{\mathcal{P}}_x, \partial_\Theta\rho_{\text{opt}}^{\beta}), \tag{5.29}$$

where $\partial_\Theta\rho_{\text{opt}}^{\beta} = e^{-i\beta\hat{J}_z}(\partial_\Theta\rho_{\text{opt}})e^{i\beta\hat{J}_z}$. Similarly, $\langle\hat{\mathcal{P}}_x^2(\beta)\rangle = \text{Tr}(\hat{\mathcal{P}}_x^2, \rho_{\text{opt}}^{\beta})$, $\partial_\Theta\langle\hat{\mathcal{P}}_x^2(\beta)\rangle = \text{Tr}(\hat{\mathcal{P}}_x^2, \partial_\Theta\rho_{\text{opt}}^{\beta})$, $\partial_\beta\langle\hat{\mathcal{P}}_x(\beta)\rangle = \text{Tr}(\hat{\mathcal{P}}_x, \partial_\beta\rho_{\text{opt}}^{\beta})$ and $\partial_\Theta\partial_\beta\langle\hat{\mathcal{P}}_x(\beta)\rangle = \text{Tr}(\hat{\mathcal{P}}_x, \partial_\Theta\partial_\beta\rho_{\text{opt}}^{\beta})$.

With these, we obtain the derivatives of $(\Delta\beta)^2_{\text{GHZ}}$ as

$$\begin{aligned}\partial_\Theta(\Delta\beta)^2_{\text{GHZ}} = \Bigg[&\left(\partial_\Theta\langle\hat{\mathcal{P}}_x^2(\beta)\rangle - \partial_\Theta(\langle\hat{\mathcal{P}}_x(\beta)\rangle)^2\right)\left|\partial_\beta\langle\hat{\mathcal{P}}_x(\beta)\rangle\right|^2 \\ &- \left(\langle\hat{\mathcal{P}}_x^2(\beta)\rangle - \langle\hat{\mathcal{P}}_x(\beta)\rangle^2\right)\partial_\Theta\left|\partial_\beta\langle\hat{\mathcal{P}}_x(\beta)\rangle\right|^2\Bigg] / \left|\partial_\beta\langle\hat{\mathcal{P}}_x(\beta)\rangle\right|^4.\end{aligned} \tag{5.30}$$

5.4.1.2 Case II: Choosing $\hat{M} = \hat{J}_z^2$

For this choice of measurement operator $\hat{M}$, we choose the field along y axis corresponding to $\hat{H}_{\vec{y}} = J\hat{J}_y$. The second and the fourth moments for $\hat{M} = \hat{J}_z^2$ after rotation of the probe state ρ_{opt} by angle $\beta = Jt$, written with $\langle\hat{X}\rangle = \text{Tr}(\hat{X}, \rho_{\text{opt}})$ are given by

$$\langle\hat{J}_z^2(\beta)\rangle = \langle\hat{J}_z^2\rangle\cos^2\beta + \langle\hat{J}_x^2\rangle\sin^2\beta - \langle\{\hat{J}_z, \hat{J}_x\}\rangle\sin\beta\cos\beta, \tag{5.31}$$

$$\begin{aligned}\langle\hat{J}_z^4(\beta)\rangle = &\langle\hat{J}_z^4\rangle\cos^4\beta + \langle\hat{J}_x^4\rangle\sin^4\beta \\ &+ (\langle\{\hat{J}_z, \hat{J}_x\}^2\rangle + \langle\{\hat{J}_z^2, \hat{J}_x^2\}\rangle)\cos^2\beta\sin^2\beta \\ &- \langle\hat{A}\rangle\cos^3\beta\sin\beta - \langle\hat{B}\rangle\cos\beta\sin^3\beta,\end{aligned} \tag{5.32}$$

where $\hat{A} = \{\hat{J}_z^2, \{\hat{J}_z, \hat{J}_x\}\}$ and $\hat{B} = \{\hat{J}_x^2, \{\hat{J}_z, \hat{J}_x\}\}$.

The variance of the measurement results is then obtained as $(\Delta \hat{J}_z^2(\beta))^2 = \langle \hat{J}_z^4(\beta)\rangle - \langle \hat{J}_z^2(\beta)\rangle^2$. The derivative term in the denominator of $(\Delta\beta)^2$ is obtained as

$$\begin{aligned}\partial_\beta \langle \hat{J}_z^2(\beta)\rangle = {} & 2(\langle \hat{J}_x^2\rangle - \langle \hat{J}_z^2\rangle)\cos\beta\sin\beta \\ & - \langle\{\hat{J}_z, \hat{J}_x\}\rangle(\cos^2\beta - \sin^2\beta).\end{aligned} \tag{5.33}$$

By writing $\partial_\Theta\langle \hat{X}\rangle = \mathrm{Tr}(\hat{X}, \partial_\Theta \rho_{\mathrm{opt}})$, it is straightforward to obtain $\partial_\Theta(\Delta\beta)^2_{N/2}$ similar to Eq. (5.30).

5.4.2 Protocol optimisation at $gT \to \infty$ and at finite T

For finding the optimal state preparation protocol parameters for the case of $gT \to \infty$, we make use of Eq. (5.13) in the application of $\mathcal{E}_{\mathrm{gpg}}$ where we have $\phi = \frac{1}{\delta}\int_0^T |\zeta(t)|^2$, and hence we must have the same sign for ϕ_j and δ_j in each step j while finding the optimal parameters. We hence perform a boundless optimisation using $\varphi_{nm} = (n^2 - m^2)\phi_j + (m-n)^2 \frac{i\kappa}{2}\left|\frac{\phi_j}{\delta_j}\right| + (m+n)\frac{i\gamma}{2g^2}|\phi_j\delta_j|$, and post adjust the sign of δ_j corresponding to the sign of ϕ_j.

For finding the optimal protocol parameters for a finite cavity pulse duration gT, the quantum channel $\mathcal{E}_{\mathrm{gpg}}$ from Eq. 5.7 is applied using the solution in Eqs.5.11- 5.12 with $\beta_n(0) = 0$, that is assuming the cavity mode starts in vacuum (note that the protocol is independent of the initial cavity state, see chapter 4). The optimisation is partially bounded where the bounds are introduced for the δ_j values arising from the physical constraint of limiting the pulse duration to the finite value of gT while keeping reasonable $\max_t|\eta(t)|$. The constraint can be explicitly written from the transformation from the full Hamiltonian to the effective Hamiltonian in Eq. (5.6), as $|\zeta|^2 < g^2/4$, which sets the bounds $\delta^{(j)} \in \left(\frac{2\pi}{T}, \frac{3g^2T}{32\phi^{(j)}}\right)$. We start the optimisation with the parameters corresponding to the $T \to \infty$ case, with $\delta^{(j)}$s adjusted within the bounds mentioned above.

5.5 Results

We perform extensive numerical simulations in the parameter ranges $10 \le N \le 100$, $25 \le C \le 10^6$, $10^{-2} \le \gamma/\kappa \le 10^2$ for cavity pulse durations $10 \le gT \le 10^2$. For both cases (I) and (II), we find that the noise-informed protocol prepares final probe states resulting in measurement variances $(\Delta\beta)^2$ that scale better with N than the SQL in all cases with $C \gtrsim 20$ and closely approach the Heisenberg scaling $(\Delta\beta)^2 \sim N^{-2}$ for $C \gtrsim 10^3$, independently of the ratio γ/κ. The resulting global control pulses have a smooth, continuous form for all protocol steps P.

Figure 5.1(b1) and (b2) show example results of optimal cavity drive pulses $\eta(t)$ found to minimize $(\Delta\beta)^2$ for observables (I) and (II), respectively, for $N = 40$, $C = 10^4$, $\gamma/\kappa = 0.01$ and $gT = 40$. The plots show a continuous, smooth profile for both real and imaginary parts of $\eta(t)$. The protocol for case (I) requires only $P = 1$ step, identically to the noiseless case [181]. Surprisingly, for case (II), the protocol converges to the asymptotic results in just $P = 3$ steps, instead of the generically expected $P \sim N^4$ [177] for constructive unitary synthesis or $P \sim N$ [176, 178] for state synthesis by search. For each P, panels (c1) and (c2) show the corresponding state trajectories in Husimi-Q representation of qubit state in the symmetric Dicke subspace. As expected, they appear similar, but not identical, to those of GHZ and symmetric Dicke states: asymmetries due to squeezing-like behavior are visible, resulting on only $\sim 57\%$ and $\sim 15\%$ overlap with ideal GHZ and symmetric Dicke states, respectively. Nevertheless, we term them as GHZ-like and $\left|\mathcal{D}^N_{N/2}\right\rangle$-like states.

Fig. 5.2 summarize our results for optimal $(\Delta\beta)^2$ as a function of qubit number N, for different cooperativities C and linewidth ratios γ/κ, computed in the limit $gT \to \infty$. For each N, C and γ/κ, the optimisation is performed $\mathcal{O}(N)$ times with randomly initialised parameters and the best value is plotted. For case (I) [panel (a)], the optimal probe states prepared with the noise-informed protocol surpass the SQL with variance $(\Delta\beta)^2_{\mathrm{GHZ}}$ scaling with N as $\sim N^{-1.24}$ for cooperativities as small as $C = 25$, as $\sim N^{-1.52}$ for $C = 100$, and closely approaching the Heisenberg limit for $C \gtrsim 10^4$, with scaling $\Delta\beta^2 \sim N^{-\alpha}$ and $\alpha > 1.93$. For case (II) [panel (b)], the optimal $(\Delta\beta)^2_{N/2} \sim N^{-\alpha}$ scale with $\alpha \approx 1.4$ for $C = 25$, $\alpha \approx 1.5$ for $C = 10^2, 10^4$ and $\alpha \approx 1.6$ for $C = 10^6$, showing considerable improvement over the SQL for all C. In all cases, optimal results are essentially independent of the ratio γ/κ. While our sensing protocol does not allow for arbitrarily high precision, i.e. arbitrarily large N, as to be expected since no QEC is employed, it provides a simple method using minimal quantum control resources to achieve quantum advantage in the presence of realistic noise.

For each N and γ/κ, $(\Delta\beta)^2$ decreases monotonically with increasing P, reaching the analytic predictions for $C \to \infty$ in just a few steps, Fig. 5.3 shows an example with $N = 10$. We also compare the $(\Delta\beta)^2$ values of the unoptimized protocol—designed for ideal, noise-free conditions—with those of the optimized protocol for case I, as shown in Fig. 5.3(a). The results demonstrate a clear advantage of our noise-informed protocol.

Moreover, pulse durations $gT \lesssim 40$ are sufficient to converge to analytic results obtained in the adiabatic limit $gT \to \infty$ from Eqs. (5.7) and (5.13), in all shown cases. As an example, Fig.5.4 shows the obtained optimal $(\Delta\beta)^2_{\mathrm{GHZ}}$ and $(\Delta\beta)^2_{N/2}$ for $N = 10$ as a function of the cavity pulse duration in each application of $\mathcal{E}_{\mathrm{gpg}}$. The obtained optimal values optimal $(\Delta\beta)^2_{\mathrm{GHZ}}$ and $(\Delta\beta)^2_{N/2}$ show a dependence on γ/κ and is minimal for

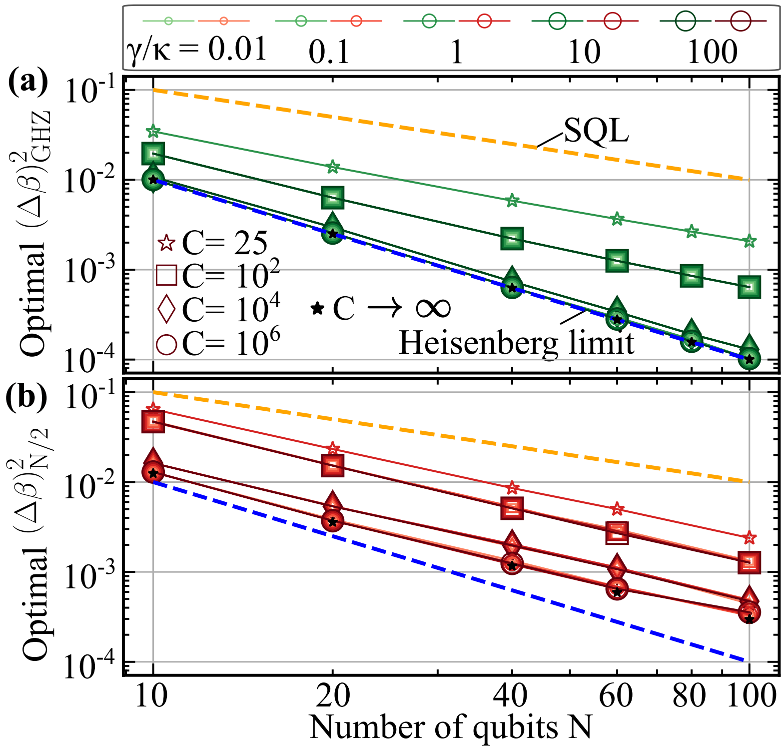

FIGURE 5.2: (a) Optimal $(\Delta\beta)^2_{\mathrm{GHZ}}$ for $P = 1$ and (b) $(\Delta\beta)^2_{N/2}$ for $P = 3$ obtained as a function of number of qubits N, plotted for spin-cavity cooperativities $C = 25$ with $\gamma/\kappa = 1$, and $C = 10^2, 10^4, 10^6$ with different ratios $\gamma/\kappa = 0.01, 0.1, 1, 10, 100$, obtained for the case of $gT \to \infty$. The optimal states prepared in the presence of finite C successfully surpass the SQL for values as small as $C = 25$.

$\gamma = \kappa$. For large cooperativities of $C > 100$, the optimal values converge close to the values corresponding to $gT \to \infty$ case for pulse durations $gT \approx 30 - 40g^{-1}$.

5.5.1 Optimal state preparation protocol parameters

In this section, we tabulate the obtained optimal parameters Θ in $\mathcal{E}_q$ which prepare the optimal probe states ρ_{opt} minimising $(\Delta\beta)^2_{\mathrm{GHZ}}$ and $(\Delta\beta)^2_{N/2}$ in Tables 5.1 and 5.2 respectively.

5.5.2 Experimental observability

In order to explore the experimental observability of the above predictions, in this section we show the performance of the prepared optimal probe states during signal collection in a field-sensing experiment with the field generator $\hat{H}_{\vec{n}}$ where spin qubits are additionally subjected to homogeneous local dephasing with rate γ_ϕ, as originated for example by optical trapping of atoms in independent tweezers [182]. Homogeneous local dephasing can be described as a *collective* process [147], with each N-qubit state

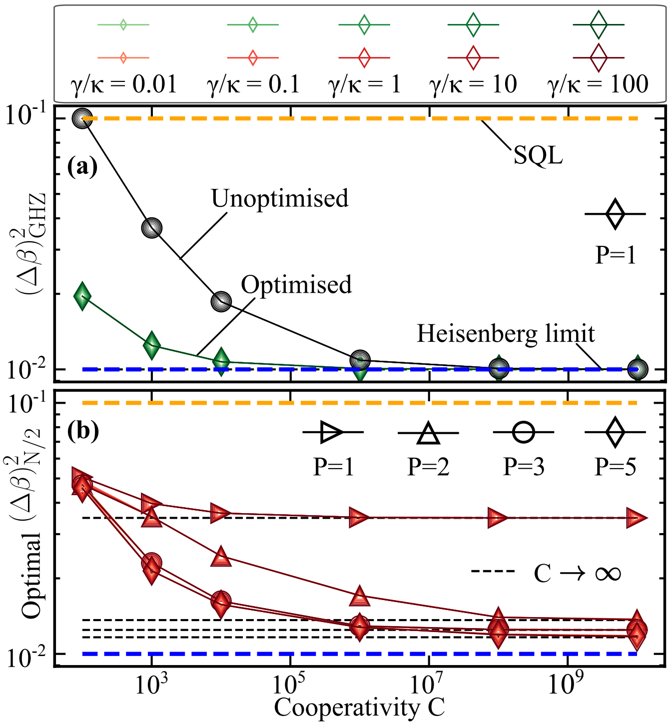

FIGURE 5.3: (a) Optimal $(\Delta\beta)^2_{\mathrm{GHZ}}$ for $P = 1$ step obtained as a function of cooperativity C , plotted for $N = 10$ and different ratios γ/κ. The circle markers correspond to the results obtained with the application of *unoptimised* pulses referring to the pulses which prepare the ideal GHZ state with $(\Delta\beta)^2_{\mathrm{GHZ}} = 1/N^2$ for the case $\kappa = \gamma = 0$. (b) $(\Delta\beta)^2_{N/2}$ for $P = 1, 2, 3, 5$ steps obtained as a function of Cooperativity C , plotted for $N = 10$ and different ratios γ/κ.

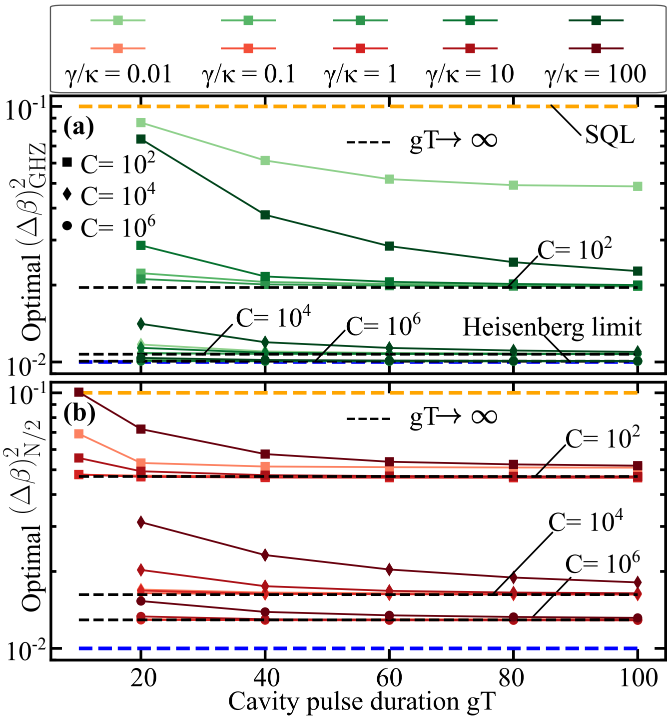

FIGURE 5.4: (a) Optimal $(\Delta\beta)^2_{GHZ}$ for $P = 1$ step and (b) $(\Delta\beta)^2_{N/2}$ for $P = 3$ steps obtained as a function of the cavity drive pulse duration gT, plotted for $N = 10$, cooperativities $C = 10^2, 10^4, 10^6$ and different ratios γ/κ.

N	C	γ/κ	$N(\Delta\beta)^2_{\text{GHZ}}$	$(\theta_0^\alpha, \theta_0^\beta, \theta_0^\gamma)$ $(\phi_1, \delta_1, \theta_1^\alpha, \theta_1^\beta, \theta_1^\gamma)$, Δ_1
10	10^2	0.01	0.61	(0.98, 1.57, 0.88) (0.86, 2.18g, -1.16, 1.57, 0.96), 26g
		1.0	0.20	(1.57, 1.41, 0.34) (1.56, 0.48g, 0, 1.57, 1.36), 237g
	10^4	0.01	0.109	(0, 1.56, 0.50) (1.56, 2.15g, 0, 1.57, -0.04), 9g
		1.0	0.107	(-0.22, 1.55, 0.36) (1.57, 0.44g,0, 1.57, 0.19), 267g
40	10^2	1.0	0.096	(-0.34, 1.14, 0.50) (1.61, 0.30g, 0, 1.57, 0.07), 457g
	10^4	0.01	0.030	(1.51, 1.54, 0.37) (1.57, 2.03g , 0.08, 1.57, 1.58), 12g
		1.0	0.029	(-0.04, 1.53, 0.37) (1.57, 0.28g, 0.08, 1.57,0.02), 497g
100	10^2	0.01	0.15	(1.51, 0.98, 0.69) (1.56, 2.13g, 0, 1.57, 1.32), 10g
		1.0	0.07	(1.47, 0.87, 0.69) (1.64, 0.24g, 0, 1.57, 1.29), 597g
	10^4	0.01	0.013	(1.42, 1.51, 0.22) (1.57, 1.80g, 0.03, 1.57, 1.66), 19g
		1.0	0.013	(1.38, 1.51, 0.22) (1.57, 0.18g, 0.03, 1.57, 1.63), 844g

TABLE 5.1: Optimal state preparation protocol parameters Θ_{opt} minimizing $(\Delta\beta)^2_{\text{GHZ}}$. The listed values correspond to the cavity pulses in the application of geometric phase gate $\mathcal{E}_{\text{gpg}}$ of duration of $T = 40g^{-1}$. The Δ_j values are derived from the optimal ϕ_j, δ_j by inverting the pulse $\zeta(t)$ in Eq. (5.6) to $\eta(t)$ in the full Hamiltonian(see [62], and 4). An extra rotation along $\hat{z}$ direction to set $\beta_{\text{opt}} = 0$ is incorporated in θ_1^α[180].

ρ in the collective Hilbert space $\mathcal{H}_C$ of dimension $\sum_{J=J_{\min}}^{J_{\max}}(2J+1)$, with $J_{\max} = N/2$ and $J_{\min} = (N \bmod 2)/2$. Having the field generator $\hat{H}_{\vec{n}} = J\hat{J}_{\vec{n}}$, where J is the coupling strength of the spins with the field, we describe the homogeneous local dephasing (fluctuations in transition frequency) on the two-level spin with index 'j' using the jump operator $\mathcal{A}^{(j)} = \frac{1}{2}\hat{\sigma}_z^{(j)}$ where $\hat{\sigma}_z^{(j)} = |1_j\rangle\langle 1_j| - |0_j\rangle\langle 0_j|$. The optimal probe state ρ_{opt} evolves according to $\dot{\rho}_{\text{opt}} = -i\left[\hat{H}_{\vec{n}}, \rho_{\text{opt}}\right] + \gamma_\phi \sum_{j=1}^{N} \mathcal{L}^{(j)}[\rho_{\text{opt}}]$, where $\mathcal{L}^{(j)}[\rho_{\text{opt}}] = \mathcal{A}^{(j)}\rho_{\text{opt}}(\mathcal{A}^{(j)})^\dagger - \frac{1}{2}\{(\mathcal{A}^{(j)})^\dagger\mathcal{A}^{(j)}, \rho_{\text{opt}}\}$. We solve the model numerically using *piqs* package [60], using the prepared optimal probe states as initial states at $Jt = 0$.

In Fig. 5.5, we evolve the optimal probe states prepared for $N = 40$, $C = 10^4$ and $\gamma/\kappa = 1.0$ as initial state at $Jt = 0$ under the field with the local homogeneous dephasing acting on the spins. We see that $(\Delta\beta)^2_{\text{GHZ}}$ increases rapidly with time t as $\sim e^{N\gamma_\phi t}$ for any given γ_ϕ/J using GHZ-like probe states. Results for $\left|\mathcal{D}_{N/2}^{N}\right\rangle$ −like states appear instead to be essentially independent of γ_ϕ/J for the shown t.

N	C	γ/κ	$N(\Delta\beta)^2_{N/2}$	$(\theta_0^\alpha, \theta_0^\beta, \theta_0^\gamma)$, θ_{-1}^β $(\phi_1, \delta_1, \theta_1^\alpha, \theta_1^\beta, \theta_1^\gamma)$, Δ_1 $(\phi_2, \delta_2, \theta_2^\alpha, \theta_2^\beta, \theta_2^\gamma)$, Δ_2 $(\phi_3, \delta_3, \theta_3^\alpha, \theta_3^\beta, \theta_3^\gamma)$, Δ_3
10	10^2	0.01	0.51	(1.19, 2.10, 0.66), 2.22 (0, -, -2.11, 1.50, 0.70), - (0.21, 8g, -2.46, 2.15, -1.72), 8g (0.02, 7.06g, -0.96, 2.86, -2.01), 39g
		1.0	0.47	(1.15, -0.97, 0.43), 0.24 (0.08, 1.17g, 0.49, 1.08, 0.92), 323g (-0.14, -0.83g, -0.25, 0.96, 0.92), 393g (0.06, 1.06g, -0.99, -0.59, 0.13), 427g
	10^4	0.01	0.165	(-0.08, -1.57, 0.63), 0.09 (0.10, 7.22g, 0.29, 2.52, -0.48), 17g (0.30, 5.66g, 1.91, 0.18, -0.42), 11g (1.38, 1.86g, 0.92, 0, 1.57), 21g
		1.0	0.163	(-0.34, 1.57, 0.42), 2.09 (0.10, 1.14g, 1.68, 0.61, -0.23), 293g (0.29, 0.67g, 0.49, 0.18, 1.25), 362g (1.38, 0.25g, 3.14, 2.00, 0.79), 611g
40	10^2	0.01	0.21	(0.04, 0, 0.41), -0.03 (0.95, 0.41g, -1.03, 1.51, 0.43), 265g (-0.07, -7.07g, -2.59, 0.63, -0.19), 21g (0.03, 7.07g, 1.82, -0.26,-2.74), 33g
		1.0	0.20	(0.36, -1.51, 0.49), -1.08 (0.06, 0.82g, -0.90, 2.47, 0.45), 600g (-0.04, -0.71g, -0.41, 0.56, -0.84), 900g (0.01, 0.94g, 0.33, 1.16, -0.90), 1200g
	10^4	0.01	0.081	(0.29, 1.57, 0.74), 0.51 (0.05, 6.34g, 1.50, 0.42, -0.02), 32g (0.22, 5.72g, -0.35, 0.09, 0.97), 15g (1.47, 0.89g, 0, 0.48, -0.60), 90g
		1.0	0.086	(0.26, 1.57, 0.74), 0.51 (0.04, 5.30g, 1.28, 0.43, -0.05), 44g (0.21, 0.67g, -0.67, 0.09, 0.75), 400g (1.45, 0.17g, 0, -0.48, -0.92), 900g
100	10^2	0.01	0.133	(0.23, 0, 0.72), 2.16 (0.32, 0.64g, -1.93, -1.58, 0.92), 300g (-0.04, -7.07g, 1.83, -0.34, -1.05), 28g (0.04, 3.26g, -0.11, 0.97, 1.33), 90g
	10^4	0.01	0.045	(-1.17, 1.55, 0.53), 0 (0.02, 15.69g, 0.078, -0.34, -1.07), 11g (0.17, 4.55g, 0.84, 0.10, 0.80), 26g (-0.08, -7.07g, 1.07, 0.04, 0.88), 19g

TABLE 5.2: Optimal state preparation protocol parameters Θ_{opt} minimizing $(\Delta\beta)^2_{N/2}$. The listed values correspond to the cavity pulses in the application of geometric phase gate $\mathcal{E}_{\text{gpg}}$ of duration of $T = 40g^{-1}$.The Δ_j values are derived from the optimal ϕ_j, δ_j by inverting the pulse $\zeta(t)$ in Eq. (5.6) to $\eta(t)$ in the full Hamiltonian(see [62] and chapter 4). The angles θ_{-1}^β refer to the extra rotation along the field axis $\hat{y}$ at the end of the protocol steps to set $\beta_{\text{opt}} = 0$ [180].

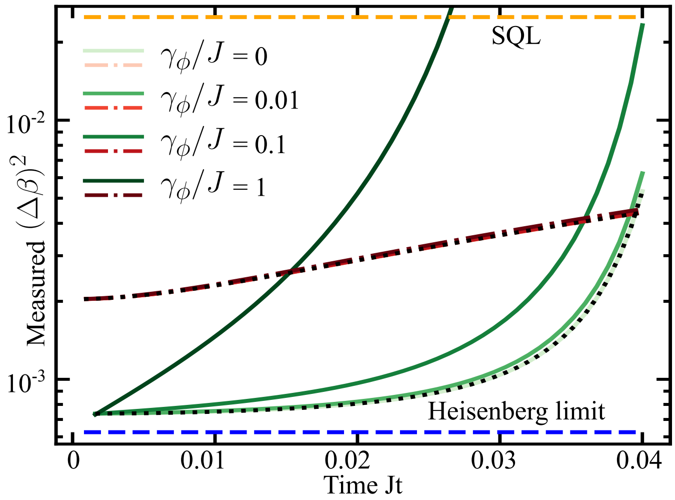

FIGURE 5.5: Measured $(\Delta\beta)^2$ as a function of dimensionless signal acquisition time Jt by evolving the optimal state minimising $(\Delta\beta)^2$ under a field coupled with the spins with coupling strength J with local homogeneous dephasing acting on the spins with rates $\gamma_\phi/J = 0, 0.01, 0.1, 1.0$ for $N = 40$, $C = 10^4$, $\gamma/\kappa = 1.0$. Green solid lines (darker shade for larger γ_ϕ) correspond to GHZ-like states while red dash-dot lines correspond to the $\left|\mathcal{D}^N_{N/2}\right\rangle$-like states. Dotted black curves are the optimal $(\Delta\beta)^2$ obtained with analytic solution of $\mathcal{E}_{\text{gpg}}$ for $\gamma_\phi/J = 0$.

In the following, we first present the analytic expressions for the measured $(\Delta\beta)^2$ with ideal GHZ and $\left|\mathcal{D}^N_{N/2}\right\rangle$ states in the presence of local homogeneous dephasing of the spins as a function of time during signal acquisition in field sensing experiment, and further present the numerical results of the measured $(\Delta\beta)^2$ with the optimal probe states prepared with different N at finite cooperativities. All results are summarized in Fig.5.6.

5.5.3 GHZ-like states undergoing dephasing during signal collection

Analytical results of evolution of an ideal GHZ state acted upon by a field $\hat{H}_{\vec{z}} = J\hat{J}_z$ in the presence of local homogeneous dephasing on the spins are presented in Ref. [183]. We summarize the results here, and write the analytic expression for $(\Delta\beta)^2$ of ideal GHZ states (rotated by $\pi/2N$ along z such that $\beta_{\text{opt}} = 0$).

In accordance with the definition of jump operator $\mathcal{A}_j = \frac{1}{2}\hat{\sigma}_z$ in the master equation dynamics(see main text), the local dephasing map on a single spin is defined as $\mathcal{A}_t(\hat{\sigma}_x \pm i\hat{\sigma}_y) = e^{-i\frac{\gamma_\phi}{2}t}e^{\mp iJt}(\hat{\sigma}_x + i\hat{\sigma}_y)$, and $\mathcal{A}_t(\hat{\sigma}_z) = \hat{\sigma}_z$, $\mathcal{A}_t(\hat{\mathbb{I}}) = \hat{\mathbb{I}}$. This map can be directly applied on the ideal GHZ state expanded as [183]

$$\rho_{GHZ} = \frac{1}{2^{N+1}}\left(\otimes_{j=1}^{N}(\hat{\mathbb{I}} + \hat{\sigma}_{z;j}) + \otimes_{j=1}^{N}(\hat{\mathbb{I}} - \hat{\sigma}_{z;j}) + \otimes_{j=1}^{N}(\hat{\sigma}_{x;j} + i\hat{\sigma}_{y;j}) + \otimes_{j=1}^{N}(\hat{\sigma}_{x;j} - i\hat{\sigma}_{y;j})\right)$$

Now for the GHZ state rotated by $\pi/2N$ along $\hat{z}$ given by $e^{-i(\pi/2N)\hat{J}_z}\rho_{GHZ}e^{i(\pi/2N)\hat{J}_z}$, and under the dephasing map, for $\hat{M} = \mathcal{P}_x$ we obtain

$$\langle\hat{M}\rangle = e^{-N\frac{\gamma_\phi}{2}t}\cos(NJt+\pi/2), \quad (\Delta\hat{M})^2 = 1 - e^{-N\gamma_\phi t}\cos^2(NJt+\pi/2), \tag{5.34}$$

$$(\Delta Jt)^2 = \frac{e^{N\gamma_\phi t}}{N^2}\frac{1 - e^{-N\gamma_\phi t}\cos^2(NJt+\pi/2)}{|\sin(NJt+\pi/2) + (\gamma_\phi/2J)\cos(NJt+\pi/2)|^2}. \tag{5.35}$$

For the obtained noisy GHZ-like optimal probe states, we fit $\langle\hat{M}\rangle$ with

$$\langle\hat{M}\rangle = \sum_{m=N/2}^{1}\alpha_m e^{-m\gamma_\phi t}\cos(2m(Jt+\pi/(2N))) + \alpha_0, \tag{5.36}$$

and expect a similar $\sim \exp\{N\gamma_\phi t\}$ scaling in $(\Delta Jt)^2$. For the case of $\gamma_\phi/J = 0.01$ in Fig.5.5, we obtain non-zero fit parameters $\alpha_{N/2-1} = 0.78$, $\alpha_{N/2-2} = 0.16$, $\alpha_0 = 0.05$.

5.5.4 $\left|\mathcal{D}^N_{N/2}\right\rangle$-like states undergoing dephasing during signal collection

We can perform a similar calculation to evaluate the effect of dephasing during signal accumulation on the $\left|\mathcal{D}^N_{N/2}\right\rangle$ state by a field $\hat{H}_{\vec{y}} = J\hat{J}_y$. In this scenario, the map generated by the signal and that due to dephasing in the $\hat{z}$ basis do not commute. To simplify this calculation, we assume that the input state is a perfect $\left|\mathcal{D}^N_{N/2}\right\rangle$, which then undergoes dephasing at a rate γ_ϕ over a time t, followed by perfect rotation of the system by the unitary $U = e^{-iJt\hat{J}_y}$ without dephasing. This models a field profile where the field strength $J(\tau)$ is near zero until time t where it turns on strongly so that the integrated action angle is $\beta = \int_0^t J(\tau)d\tau = Jt$. The variance of the estimation of β given the measurement operator $\hat{M} = \hat{J}_z^2$ is given by [52]:

$$(\Delta\beta)^2 = \frac{(\Delta\hat{J}_x^2)^2 f(\beta) + 4\langle\hat{J}_x^2\rangle - 3\langle\hat{J}_y^2\rangle - 2\langle\hat{J}_z^2\rangle(1+\langle\hat{J}_x^2\rangle) + 6\langle\hat{J}_z\hat{J}_x^2\hat{J}_z\rangle}{4(\langle\hat{J}_x^2\rangle - \langle\hat{J}_z^2\rangle)^2} \tag{5.37}$$

where

$$f(\beta) = \frac{(\Delta\hat{J}_z^2)^2}{\tan^2(\beta)(\Delta\hat{J}_x^2)^2} + \tan^2(\beta).$$

Now we define the set of n bit strings with Hamming weight w as $\mathcal{B}^n_w = \{\vec{x}|\sum_j x_j = w\}$ and furthermore the distance between two binary strings as $d(\vec{x},\vec{y}) = \sum_j |x_j - y_j|$. The Dicke state can be written

$$\left|\mathcal{D}^N_{N/2}\right\rangle = \sqrt{\frac{1}{\binom{N}{N/2}}}\sum_{\vec{x}\in\mathcal{B}^n_w}|\vec{x}\rangle\otimes\left|\mathcal{D}^{N-n}_{N/2-w}\right\rangle\sqrt{\binom{N-n}{N/2-w}}.$$

Let the output of dephasing map after time t acting on a state ρ be written $S_t(\rho)$. Notice that the expression for the variance in Eq. (5.37) involves second and fourth moments of angular momentum operators. This fact together with the permutation invariance property of the Dicke states, and the local action of the dephasing map, implies that the we can focus on the action of the map on a decomposition of the input state into a partition of the state into a subsystem of the first two or four qubits and the rest. Specifically we have the following decomposition of the output state:

$$\begin{aligned} S_t\Big(\Big|\mathcal{D}^N_{N/2}\Big\rangle\Big\langle\mathcal{D}^N_{N/2}\Big|\Big) &= \tfrac{1}{\binom{N}{N/2}}\textstyle\sum_w\sum_{\vec{x},\vec{y}\in\mathcal{B}^j_w}|\vec{x}\rangle\langle\vec{y}|\,e^{-d(\vec{x},\vec{y})\gamma_\phi t}\otimes S_t\Big(\Big|\mathcal{D}^{N-j}_{N/2-w}\Big\rangle\Big\langle\mathcal{D}^{N-j}_{N/2-w}\Big|\Big)\binom{N-j}{N/2-w} \\ &\quad+\Big(\text{terms having } S_t\Big(\Big|\mathcal{D}^{N-j}_{N/2-w}\Big\rangle\Big\langle\mathcal{D}^{N-j}_{N/2-w'}\Big|\Big)\text{with } w\neq w'\Big). \end{aligned}$$

where we can focus on this decomposition for $j = 2, 4$. The last terms which are off diagonal in the Dicke basis will not contribute to expectation values of weight 2 or 4 Pauli operators, when we take the trace, namely $\langle\hat{O}\rangle = \mathrm{Tr}\Big[\hat{O}S_t\Big(\Big|\mathcal{D}^N_{N/2}\Big\rangle\Big\langle\mathcal{D}^N_{N/2}\Big|\Big)\Big]$. The input state is invariant under rotations about $\hat{z}$ as is the dephasing map so $\langle\hat{J}_x^2\rangle = \langle\hat{J}_y^2\rangle$. Also because there are an equal number of diagonal terms with even and odd Hamming weight we have $\langle\hat{J}_z^2\rangle = \langle\hat{J}_z^4\rangle = 0$. Now we write

$$\hat{J}_x^2 = \frac{1}{4}\sum_{j\neq k}X_jX_k + \frac{N}{4}\mathbf{1}, \quad \hat{J}_x^4 = \frac{1}{16}\sum_{j\neq k, j'\neq k'}X_jX_kX_{j'}X_{k'} + \frac{N}{8}\sum_{j\neq k}X_jX_k + \frac{N^2}{16}\mathbf{1}.$$

For $\langle\hat{J}_x^2\rangle$ the two point expectation value

$$\langle X_jX_k\rangle = \frac{e^{-2\gamma_\phi t}N}{2(N-1)}$$

for $j \neq k$, of which there are $N(N-1)$ terms, and hence

$$\langle\hat{J}_x^2\rangle = \frac{1}{4}\Big(\frac{e^{-2\gamma_\phi t}N^2}{2} + N\Big).$$

For $\langle\hat{J}_x^4\rangle$, the four point expectation value

$$\langle X_jX_kX_\ell X_m\rangle = \frac{e^{-4\gamma_\phi t}3N(N-2)}{8(N-1)(N-3)},$$

for $j \neq k \neq \ell \neq m$, of which there are $N(N-1)(N-2)(N-3)$ terms. The number of terms involving $\langle\mathbf{1}\rangle$ are $3N^2 - 2N$. The remaining terms only involve two point expectation values $\langle X_jX_k\rangle$ with $j \neq k$ and there are $N^4 - N(N-1)(N-2)(N-3) - (3N^2 - 2N)$ of them. Hence

$$\langle\hat{J}_x^4\rangle = \frac{1}{16}\Big((3N^2 - 2N) + e^{-2\gamma_\phi t}(3N^3 - 4N^2) + \frac{e^{-4\gamma_\phi t}3N^2(N-2)^2}{8}\Big).$$

Finally, we find

$$\begin{aligned}\langle \hat{J}_z\hat{J}_x^2\hat{J}_z\rangle &= \mathrm{Tr}\left[\hat{J}_z\hat{J}_x^2\hat{J}_zS_t\Big(\left|\mathcal{D}^N_{N/2}\right\rangle\left\langle\mathcal{D}^N_{N/2}\right|\Big)\right]\\ &= \mathrm{Tr}\left[\hat{J}_x^2\hat{J}_zS_t\Big(\left|\mathcal{D}^N_{N/2}\right\rangle\left\langle\mathcal{D}^N_{N/2}\right|\Big)\hat{J}_z\right]\\ &= \mathrm{Tr}\left[\hat{J}_x^2S_t\Big(\hat{J}_z\left|\mathcal{D}^N_{N/2}\right\rangle\left\langle\mathcal{D}^N_{N/2}\right|\hat{J}_z\Big)\right]\\ &= 0\end{aligned}$$

using the fact that $\hat{J}_z$ commutes with the dephasing channel, and $\hat{J}_z\left|\mathcal{D}^N_{N/2}\right\rangle = 0$. Hence we arrive at for $\beta = Jt$

$$(\Delta Jt)^2 = \frac{16e^{2\gamma_\phi t}(2e^{2\gamma_\phi t}+N)+(16e^{4\gamma_\phi t}(N-1)+16e^{2\gamma_\phi t}N(N-2)+N(12-12N+N^2))\tan^2(Jt)}{8N(2e^{2\gamma_\phi t}+N)^2}. \tag{5.38}$$

Notice as expected, at $t=0$ the variance $(\Delta\beta)^2 = \frac{2}{N(N+2)}$.

In Fig.5.6, we plot the measured $(\Delta\beta)^2 = (\Delta Jt)^2$ as a function of the signal acquisition time Jt for ideal GHZ and $\left|\mathcal{D}^N_{N/2}\right\rangle$ probe states(panel (a)) with local homogeneous dephasing rates $\gamma_\phi/J = 0, 0.01, 0.1, 1.0$ for $N = 10, 40, 60$ and compare their performance in field-sensing experiment against the performance of the optimal probe states(similar to Fig.5.5 but for longer signal collection times) prepared for $C = 10^4$, $\gamma/\kappa = 1.0$(panel (b)) and $C = 10^2$, $\gamma/\kappa = 1.0$(panel (c)). We observe a qualitatively similar behaviour of the optimal probe states prepared at finite cooperativities.

5.5.5 Spins under local homogeneous dephasing during state preparation

In this section, we study the robustness of our state preparation protocol against the local homogeneous dephasing process. We consider the dephasing effects introduced as local homogeneous dephasing processes, which can be described as a *collective* process[147], and we work in the collective Hilbert space $\mathcal{H}_C$ of dimension $\sum_{J=J_{\min}}^{J_{\max}}(2J+1)$ where $J_{\max} = N/2$ and $J_{\min} = (N \bmod 2)/2$. We study primarily the effects of the local homogeneous dephasing process during the application of the geometric phase gate $\mathcal{E}_{\mathrm{gpg}}$ and consider negligible dephasing during the fast global spin rotation operations. We perform the numerical calculations in the collective Hilbert space using the *piqs* solver[60].

In our geometric phase gate protocol implemented during the state preparation protocol, we make use of the cavity mode coupled with the $|1\rangle \leftrightarrow |e\rangle$ transition with strength g, while the state $|0\rangle$ remains uncoupled. To add finite local homogeneous dephasing in the three-level system, we model the three level dephasing with the jump operators $\mathcal{A}^{(j)}_{\gamma^e_\phi} = |e_j\rangle\langle e_j|$ and $\mathcal{A}^{(j)}_{\gamma^1_\phi} = |1_j\rangle\langle 1_j|$ corresponding to dephasing of states $|e\rangle$ and $|1\rangle$ with

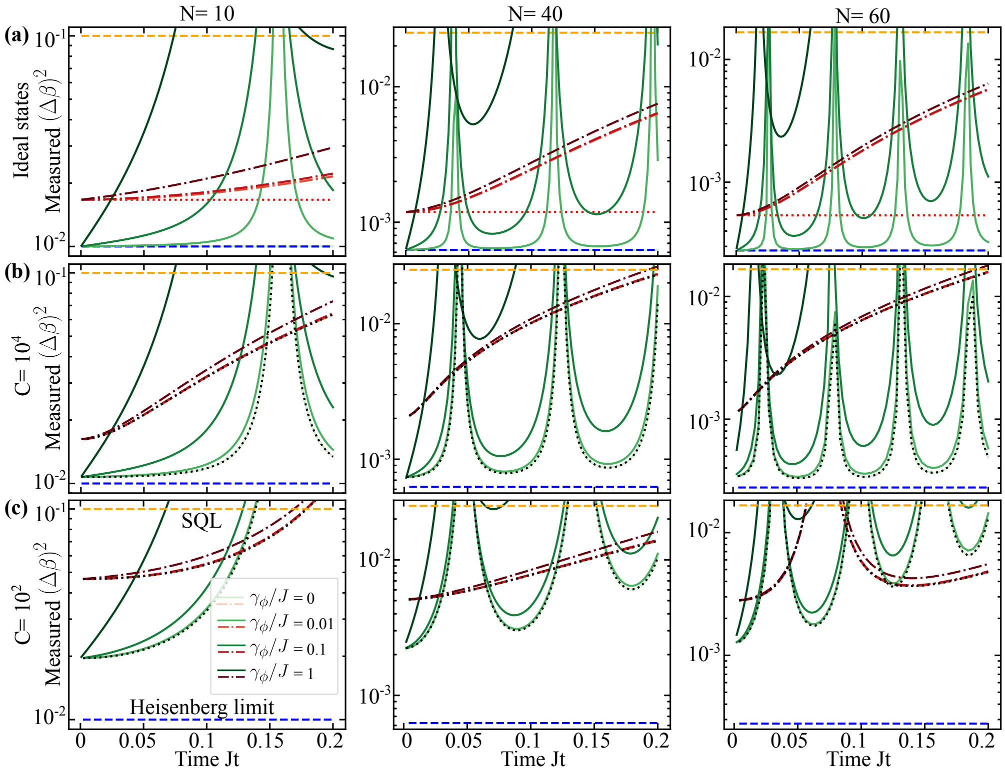

FIGURE 5.6: (a) $(\Delta\beta)^2 = (\Delta Jt)^2$ as a function of dimensionless signal acquisition time Jt for ideal GHZ states and ideal $\left|\mathcal{D}^N_{N/2}\right\rangle$ states evolving under a field coupled with strength J with local homogeneous dephasing acting on spins obtained in Eqs. (5.35) and (5.38) respectively, for dephasing rates $\gamma_\phi/J = 0, 0.01, 0.1, 1.0$ and $N = 10, 40, 60$. The dotted red lines correspond to $(\Delta\beta)^2 = 2/(N(N+2))$. (b) Measured $(\Delta\beta)^2$ as a function of dimensionless signal acquisition time Jt by numerically evolving the optimal probe states prepared at cooperativity $C = 10^4$, $\gamma/\kappa = 1.0$ under a field coupled with spins with coupling strength J, with local dephasing on spins with rates γ_ϕ (for similar values as in panel (a)). Dotted black curves are the optimal $(\Delta\beta)^2$ obtained with analytic solution of $\mathcal{E}_{\text{gpg}}$ for $\gamma_\phi/J = 0$. (c) Similar to panel (b) for optimal states prepared at cooperativity $C = 10^2$, $\gamma/\kappa = 1.0$. The cooperativity C values corresponding to an entire panel (row) and N values corresponding to an entire column are indicated to the left and the top sides respectively. Throughout, green solid lines (darker shades for larger γ_ϕ) correspond to GHZ-like states while red dash-dot lines correspond to $\left|\mathcal{D}^N_{N/2}\right\rangle$ states.

rates γ^e_ϕ and γ^1_ϕ respectively [184]. We include as before the cavity mode decay with rate κ and the corresponding jump operator $\mathcal{A}_\kappa = \hat{a}$. The state ρ in the original frame evolves according to $\dot{\rho} = -i\left[\hat{H}, \rho\right] + \mathbf{L}[\rho]$ where

$$\mathbf{L}[\rho] \quad = \quad \kappa\mathbf{L}_\kappa[\rho] + \sum_{j=1}^{N}\left(\gamma^1_\phi\mathbf{L}^{(j)}_{\gamma^1_\phi}[\rho] + \gamma^e_\phi\mathbf{L}^{(j)}_{\gamma^e_\phi}[\rho]\right), \tag{5.39}$$

with $\mathbf{L}_\alpha[\rho] = \mathcal{A}_\alpha\rho\mathcal{A}^\dagger_\alpha - \frac{1}{2}\{\mathcal{A}^\dagger_\alpha\mathcal{A}, \rho\}$.

We move from the original frame to the effective frame by performing two basis transformations. The first basis transformation acts only on the cavity subspace mapping $\rho \to \rho'$ and $\hat{H} \to \hat{H}'$ with $\mathbf{L}[\rho'] = \mathbf{L}[\rho]$. The second basis transformation defined by $\hat{U} = \exp\left[\frac{\lambda}{2}\hat{O}\right]$ with $\hat{O} = -e^{i\mu}\hat{S}^{+} + e^{-i\mu}\hat{S}^{-}$, where $\mu = \arg(\alpha)$ and λ such that $\cos(\lambda) = \Delta/\sqrt{\Delta^2 + 4g^2|\alpha|^2}$(see 4, section 4.1.2) acts on the qubit subspace alone which maps $\rho' \to \tilde{\rho} = \hat{U}\rho'\hat{U}^{\dagger}$. We hence obtain

$$\begin{aligned} \dot{\tilde{\rho}} &= \left(-i\hat{U}\hat{H}'\hat{U}^{\dagger} + \partial_t((\lambda/2)\hat{O})\right)\tilde{\rho} \\ &+ \tilde{\rho}\left(i\hat{U}\hat{H}'\hat{U}^{\dagger} + \partial_t((\lambda/2)\hat{O}^{\dagger})\right) + \hat{U}\mathbf{L}[\rho]\hat{U}^{\dagger} \\ &\equiv \dot{\rho}_{\text{eff}} = -i\left[\hat{H}_{\text{eff}}, \tilde{\rho}\right] + \mathcal{L}(\rho_{\text{eff}}). \end{aligned} \tag{5.40}$$

In the effective frame, we map $\tilde{\rho} \to \rho_{\text{eff}}$ where we restrict the dynamics only to the computational states $|0\rangle$ and $|1\rangle$, by assuming that we initially always start with a state with $n_e = 0$, neglecting energy terms of the order $\mathcal{O}(\Delta)$, and coupling terms of the order $\mathcal{O}(g)$ between the states with energy difference diverging with $\Delta/g \to \infty$. We use $\hat{U}\hat{H}'\hat{U}^{\dagger} + i\partial_t((\lambda/2)\hat{O} = \hat{H}_{\text{eff}} + \mathcal{O}(g)(\hat{S}^{+}, \hat{S}^{-}) \approx \hat{H}_{\text{eff}}$. We map similarly $\tilde{\mathcal{L}}[\tilde{\rho}] = \hat{U}\mathbf{L}[\rho]\hat{U}^{\dagger} \to \mathcal{L}(\rho_{\text{eff}})$. The transformed jump operators $\tilde{\mathcal{A}^{(j)}} = \hat{U}\mathcal{A}^{(j)}\hat{U}^{\dagger}$ are obtained as

$$\begin{aligned} \tilde{\mathcal{A}}^{(j)}_{\gamma_\phi^1} &= \mathcal{A}^{(j)}_{\gamma_\phi^1}\frac{1}{2}\left(1 + \sqrt{1 - 4|\zeta|^2/g^2}\right) \\ &+\mathcal{A}^{(j)}_{\gamma_\phi^e}\frac{1}{2}\left(1 - \sqrt{1 - 4|\zeta|^2/g^2}\right) \\ &-(e^{i\mu}(\mathcal{A}^{(j)}_{\gamma})^{\dagger} + e^{-i\mu}(\mathcal{A}^{(j)}_{\gamma}))\frac{1}{2}(|\zeta|/g), \end{aligned} \tag{5.41}$$

$$\begin{aligned} \tilde{\mathcal{A}}^{(j)}_{\gamma_\phi^e} &= \mathcal{A}^{(j)}_{\gamma_\phi^e}\frac{1}{2}\left(1 + \sqrt{1 - 4|\zeta|^2/g^2}\right) \\ &+\mathcal{A}^{(j)}_{\gamma_\phi^1}\frac{1}{2}\left(1 - \sqrt{1 - 4|\zeta|^2/g^2}\right) \\ &+(e^{i\mu}(\mathcal{A}^{(j)}_{\gamma})^{\dagger} + e^{-i\mu}(\mathcal{A}^{(j)}_{\gamma}))\frac{1}{2}(|\zeta|/g) \end{aligned} \tag{5.42}$$

The Lindbladian $\mathcal{L}[\rho_{\text{eff}}] =$ is obtained from $\hat{U}\mathbf{L}\hat{U}^\dagger$ after applying similar assumptions described above as in the derivation of $\hat{H}_{\text{eff}}$, given by

$$\begin{aligned}
&\mathcal{L}[\rho_{\text{eff}}] = \kappa\mathcal{L}_\kappa[\rho_{\text{eff}}] + \sum_{j=1}^{N}\left(\gamma_\phi'\mathcal{L}_{\gamma_\phi'}^{(j)}[\rho_{\text{eff}}] + \gamma'\mathcal{L}_{\gamma'}^{(j)}[\rho_{\text{eff}}]\right), \\
&\mathcal{L}_\kappa[\rho_{\text{eff}}] = \mathbf{L}_\kappa[\rho_{\text{eff}}], \\
&\mathcal{L}_{\gamma_\phi'}^{(j)}[\rho_{\text{eff}}] = \mathcal{A}_{\gamma_\phi'}^{(j)}\rho_{\text{eff}}(\mathcal{A}_{\gamma_\phi'}^{(j)})^\dagger - \frac{1}{2}\{(\mathcal{A}_{\gamma_\phi'}^{(j)})^\dagger\mathcal{A}_{\gamma_\phi'}^{(j)}, \rho_{\text{eff}}\}, \\
&\mathcal{L}_{\gamma'}^{(j)}[\rho_{\text{eff}}] = -\frac{1}{2}\{\hat{n}_1^{(j)}, \rho\},
\end{aligned} \tag{5.43}$$

where

$$\begin{aligned}
\gamma_\phi' &= \gamma_\phi^1\frac{(1+\sqrt{(1-4|\zeta|^2/g^2)})^2}{4} + \gamma_\phi^e\frac{(1-\sqrt{(1-4|\zeta|^2/g^2)})^2}{4}, \\
\mathcal{A}_{\gamma_\phi'}^{(j)} &= \frac{1}{2}\sigma_z^{(j)},\ \ \gamma' = (\gamma_\phi^1 + \gamma_\phi^e)\frac{|\zeta|^2}{g^2}.
\end{aligned} \tag{5.44}$$

We combine $\mathcal{L}_{\gamma'}^{(j)}[\rho_{\text{eff}}]$ in the Hamiltonian as non-hermitian contribution resulting in solving the system with

$$\begin{aligned}
\hat{H}_{\text{eff}} &= \delta\hat{a}^\dagger\hat{a} + \left(-i\frac{(\gamma_1+\gamma')}{2} + \zeta\hat{a}^\dagger + \zeta^*\hat{a}\right)\hat{n}_1, \\
\mathcal{L}[\rho_{\text{eff}}] &= \kappa\mathcal{L}_\kappa[\rho_{\text{eff}}] + \gamma_\phi'\sum_{j=1}^{N}\mathcal{L}_{\gamma_\phi'}^{(j)}[\rho_{\text{eff}}]
\end{aligned} \tag{5.45}$$

In Fig. 5.7, $(\Delta\beta)^2_{N/2}$ and $(\Delta\beta)^2_{\text{GHZ}}$ is plotted by simulating the master equation dynamics with the model described above (solid lines) with dephasing rates $\gamma_\phi^1 = \gamma_\phi^e = \gamma_\phi = 0, 10^{-4}\,g, 10^{-3}\,g$ for $N = 10$, $C = 10^2$, $\gamma/\kappa = 1.0$. The results with $\gamma_\phi/g = 0$(circle markers) coincide with the results obtained with analytical solution(dashed lines) in Eqs. (5.11)-(5.12), which validate our state preparation protocol. We see that the optimal probe states remain quite robust against dephasing rates of the order $\gamma_\phi/g < 10^{-4}$.

5.5.6 Local homogeneous spontaneous emission treated as a collective process

In this section, we treat the local homogeneous spontaneous emission rate γ of state $|e\rangle$ in the master equation approach with jump operator $\mathcal{A}_\gamma^{(j)} = |1_j\rangle\langle e_j|$. The transformed jump operator $\tilde{\mathcal{A}}_\gamma^{(j)} = \hat{U}\mathcal{A}_\gamma^{(j)}\hat{U}^\dagger$(similar to qubit basis transformation performed

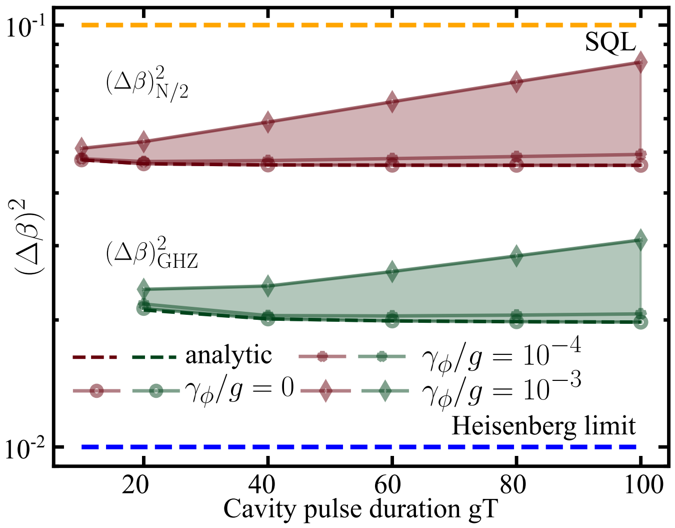

FIGURE 5.7: $(\Delta\beta)^2_{N/2}$ and $(\Delta\beta)^2_{\mathrm{GHZ}}$ obtained with our optimal state preparation protocol when local homogeneous dephasing of states $|1\rangle$ and $|e\rangle$ is added with rates $\gamma^1_\phi = \gamma^e_\phi = \gamma_\phi$, for $N = 10$, $C = 10^2$, $\gamma/\kappa = 1.0$. The markers correspond to numerical results obtained with simulations performed with the effective model derived in Eq. (5.45) in the collective Hilbert space. The dashed lines correspond to the values obtained with analytical solutions in Eqs. (5.11)-(5.12).

in Eqs. (5.41)-(5.42)) is obtained as

$$\begin{aligned}
\tilde{\mathcal{A}_{\gamma}^{(j)}} &= \mathcal{A}_{\gamma}^{(j)}\frac{1}{2}\left(1+\sqrt{1-4|\zeta|^2/g^2}\right) \\
&\quad -(\mathcal{A}_{\gamma^e_\phi}^{(j)} - \mathcal{A}_{\gamma^1_\phi}^{(j)})e^{i\psi}(|\zeta|/g) \\
&\quad -(\mathcal{A}_{\gamma}^{(j)})^\dagger\frac{e^{i2\psi}}{2}\left(1-\sqrt{1-4|\zeta|^2/g^2}\right). \qquad (5.46)
\end{aligned}$$

We obtain a similar effective Lindbladian $\mathcal{L}_{\mathrm{eff}}$ in the same form as in Eqs. (5.43), with

$$\gamma'_\phi = \gamma|\zeta|^2/g^2, \quad \mathcal{A}_{\gamma'_\phi} = \frac{1}{2}\sigma_z^{(j)}, \qquad (5.47)$$

$$\gamma' = \gamma\frac{(1-\sqrt{(1-4|\zeta|^2/g^2)})^2}{4}. \qquad (5.48)$$

The effective model is reduced to

$$\hat{H}_{\mathrm{eff}} = \delta\hat{a}^\dagger\hat{a} + \left(-i\frac{\gamma'}{2} + \zeta\hat{a}^\dagger + \zeta^*\hat{a}\right)\hat{n}_1, \qquad (5.49)$$

$$\mathcal{L}[\rho_{\mathrm{eff}}] = \kappa\mathcal{L}_\kappa[\rho_{\mathrm{eff}}] + \gamma'_\phi\sum_{j=1}^{N}\mathcal{L}^{(j)}_{\gamma'_\phi}[\rho_{\mathrm{eff}}]. \qquad (5.50)$$

In Fig. 5.8, $(\Delta\beta)^2_{N/2}$ and $(\Delta\beta)^2_{\mathrm{GHZ}}$ for $N = 10$, $C = 10^4$, $\gamma/\kappa = 0.01$ is plotted by simulating the master equation dynamics with the model described above (solid lines). It is compared against the values obtained when γ is treated as a non-hermitian contribution (dashed lines, see Eq. (5.6)). We see that the solid lines always lie very close or below

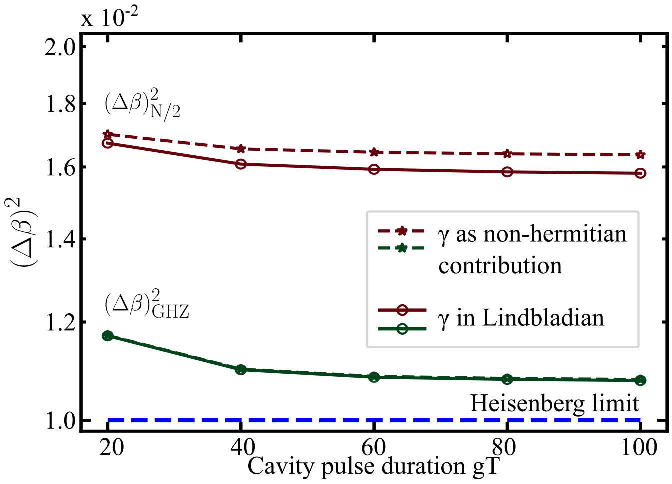

FIGURE 5.8: $(\Delta\beta)^2_{N/2}$ and $(\Delta\beta)^2_{\mathrm{GHZ}}$ obtained with our optimal state preparation protocol for $N = 10$, $C = 10^4$, $\gamma/\kappa = 0.01$ with the spontaneous emission from the $|e\rangle$ state treated as a non-hermitian contribution (dashed lines, star markers) compared with the values obtained when decay is treated as a Lindbladian jump operator in the master equation formalism(solid lines, circle markers).

the dashed lines, hence implying an upper bound on the variance corresponding to the $(\Delta\beta)^2$ values obtained in the main text by treating γ as a non-hermitian contribution.

5.6 Example system

Our results are directly relevant to state-of-the-art experiments with neutral atoms trapped in optical cavities. As an example, we consider ^{87}Rb atoms trapped in optical tweezers and coupled to a fiber Fabry-Perot cavity [44–46]. We choose qubit states $|0\rangle = \left|5^2S_{1/2}, F = 1, m_F = 0\right\rangle$, $|1\rangle = \left|5^2S_{1/2}, F = 2, m_F = 0\right\rangle$, and $|e\rangle = \left|5^2P_{3/2}, F = 3, m_F = 0\right\rangle$, where the linewidth of the $|1\rangle \leftrightarrow |e\rangle$ transition ($\lambda = 780\,\mathrm{nm}$) is $\gamma = 2\pi\times 6\,\mathrm{MHz}$ (FWHM). We assume a cavity finesse $F \approx 2\times10^5$, a waist radius $\omega_r \approx 2\,\mu\mathrm{m}$ and a length $L \approx 40\,\mu\mathrm{m}$ resulting in a cooperativity of $C = 3\lambda^2 F/(2\pi^3\omega_r^2) \approx 1500$ with a coupling strength of $g = \sqrt{3\lambda^2 C\gamma/(2\pi^2\omega_r^2 L)} \approx 2\pi \times 400\,\mathrm{MHz}$ and $\kappa = \pi C/LF \approx 2\pi \times 20\,\mathrm{MHz}$ (FWHM), so that $\gamma/\kappa \approx 0.3$. Our noise-informed state preparation protocol obtains for $N = 10$ atoms a minimal $(\Delta\beta)^2_{N/2} = 0.022$ with $P = 3$ protocol steps and a minimal $(\Delta\beta)^2_{\mathrm{GHZ}} = 0.013$ with $P = 1$ protocol step, where in each step the cavity pulse is applied for a duration $T = 20g^{-1} \approx 8\,\mathrm{ns}$. Tweezer induced dephasing rates on state $|1\rangle$ can be as small as $\gamma_\phi/g = 0.03 \times 10^{-6}$ [185], which we find to be negligible (see Fig. 5.7 for reference).

5.7 Conclusion and outlook

In this chapter, we presented a simple, deterministic protocol to prepare entangled states in the symmetric Dicke subspace of spins that we show for medium sized systems, N up to 100, provide a quantum advantage for sensing and are optimally robust in the presence of a noisy environment. We focused on spins coupled to a common cavity mode in the regime of strong coupling of cavity quantum electrodynamics, as can be realized, for example, with cold atoms trapped in optical cavities. No direct interactions are required between the spins, though that can provide another handle for Dicke state control [186]. When applied to the measurement of the strength of a weak external field, the protocol prepares multi-particle entangled states leading to a scaling with N of the measurement precision characterised by the variance of the estimated field strength that is significantly better than the SQL in the presence of relevant noise, such as photon cavity loss, spontaneous emission and dephasing already for moderately large strengths of light-matter interactions. Surprisingly, the protocol requires only a few global pulses of the cavity mode drive and global rotations, whose parameters we provide. We discussed the performance of different classes of entangled states that can be prepared using the protocol for field signal acquisition in the presence of spin dephasing.

Finally, state-preparation protocol described in this chapter is sufficient to achieve unitary synthesis in the Dicke subspace. The control algebra $\{\hat{J}_z^2, \hat{J}_x, \hat{J}_y, \hat{J}_z\}$ is universal for Dicke state preparation starting from a canonical product state like $\left|D_N^N\right\rangle$ [187] and is efficient [177, 178]. By a simple modification that enables multi-controlled phase gates, our protocol is exactly universal for such unitary synthesis: in chapter 6 we propose a new adiabatic phase gate using the same cavity setup but in the weak drive, long pulse time limit with detunings $\Delta, \delta = O(g)$. There we show that sequential application of N adiabatic gates can generate a multi-controlled phase gate deterministically $V(\phi) = e^{i\phi|D_N^N\rangle\langle D_N^N|}$. Writing an arbitrary unitary in the Dicke subspace in its spectral decomposition, $U = \sum_{j=1}^{N+1} e^{i\lambda_j|\lambda_j\rangle\langle\lambda_j|}$, the following decomposition suffices $U = \prod_{j=1}^{N+1} W(\lambda_j)^\dagger V(\lambda_j) W(\lambda_j)$, where $W(\lambda_j)^\dagger$ is any unitary extension of the state mapping $W(\lambda_j)^\dagger \left|D_N^N\right\rangle = |\lambda_j\rangle$.

While the results presented in this work are directly relevant to state-of-the-art experiments with cold atoms trapped in tweezer arrays in cavities [55], we anticipate that our noise-informed protocols can be generalized to different physical setups and noise models, e.g. for Rydberg atoms and cold ion chains. This will be subject of future work.

Chapter 6

Adiabatic Phase Gate Protocol

This chapter is an adaptation of *Protocol B* from the publication titled "Non-Local Multi-Qubit Quantum Gates via a Driven Cavity" [54]. In this chapter, we refer to Protocol B as the Adiabatic Phase Gate (APG) protocol, and describe its working with our setup and model discussed in Chapter 2. Similar to the geometric phase gate (GPG) protocol from chapter 4, for number of qubits $N = 2$, the APG forms a universal gate set for quantum computation together with single qubit gates. In contrast to the GPG protocol, the APG protocol, as the name suggests is an adiabatic protocol that operates in the limit of a weak cavity drive pulse strength $\eta/g \to 0$, with detunings $\Delta, \delta = \mathcal{O}(g)$, and a pulse duration $T = \mathcal{O}(\eta^{-2})$. It makes use of an adiabatic evolution of the joint cavity-qubit system to implement a family of phase gates $\hat{U}_B = \exp[ic_1/(c_2 - \hat{n})]$, where c_1 and c_2 are parameters depending on the intensity, duration and detuning of the applied drive. Similar to the GPG protocol, here again we obtain a closed-form expression for the operation fidelity of the APG protocol which scales as $\sim 1/\sqrt{C}$, with C the single atom- cavity cooperativity. The distinguishing feature of APG protocol is its versatility: Since $\hat{U}_B$ depends *nonlinearly* on c_2, the repeated application of $\hat{U}_B$ with different values of c_1 and c_2 can be used to synthesise *arbitrary* phase gates $\exp(i\varphi(\hat{n}))$. This can be used to implement phase-rotation gates of the form $\exp\Big(i\alpha\sigma_z^{(1)} \otimes ... \otimes \sigma_z^{(N)}\Big)$ with arbitrary phases α where $\hat{\sigma}_z^{(j)}$ is the pauli z operator acting on qubit j, which appear in many variational quantum algorithms for fermionic systems [40, 188]. It can also be used to implement multi-controlled Z gates, enabling generalized Toffoli gates which are frequently used as primitives in QEC to perform majority voting circuits for syndrome extraction and for measurement free QEC [189–191]. Note that synthesizing multi-controlled Z gates using only single- and two-qubit gates either requires circuits of large depths or additional ancilla qubits [41], both of which can be avoided using the APG protocol.

In Sec. 6.1 we discuss the APG protocol in the absence of losses, followed by the calculation of the infidelity for finite values of γ and κ in Sec. 6.2. We confirm our analysis through a numerical simulation in Sec. 6.3. In Sec. 6.4 we discuss how several repetitions of APG protocol can be used to implement *arbitrary* phase gates. Finally in Sec. 6.5, we summarise the gate times and fidelity estimates for a CZ gate implemented with the APG protocol in realistic example setups, and Sec. 6.6 presents the chapter conclusion and outlook.

6.1 Implementation of the Adiabatic Phase Gate: Decay-free case

We recall here again the Hamiltonian and model for our cavity QED setup from chapter 3:

$$\begin{aligned} \hat{H}(t) &= \delta\hat{a}^\dagger\hat{a} + (\Delta - i\gamma/2)\hat{n}_e + [(g\hat{S}^- + i\eta(t))\hat{a}^\dagger + \text{h.c.}], && (6.1)\\ \dot{\rho} &= -iH\rho + i\rho H^\dagger + L\rho L^\dagger - \{L^\dagger L, \rho\}/2, && (6.2) \end{aligned}$$

We start by assuming $\gamma = \kappa = 0$. We consider an initial state $|\psi(0)\rangle = |0\rangle \otimes |q\rangle$, with the cavity starting in state $|0\rangle$ and the qubits in a computational basis state $|q\rangle$ ($q \in \{0,1\}^N$), with exactly $n = \sum_j q_j$ qubits in state $|1\rangle$. Note that $|\psi(0)\rangle$ is an eigenstate of the Hamiltonian $\hat{H}$ [Eq. (6.1)] for $\eta = 0$. If now η is varied slowly enough, the system will stay in an eigenstate of H and accumulate a dynamical phase. Since at the final time we have again $\eta(T) = 0$, we obtain $|\psi(T)\rangle = e^{i\varphi_n}|0\rangle \otimes |q\rangle$, where the dynamical phase is given by

$$\varphi_n = -\int_0^T \langle\psi_n(t)| H(t) |\psi_n(t)\rangle \, \mathrm{d}t. \tag{6.3}$$

Using second order perturbation theory, one obtains (see Appendix B.1)

$$\varphi_n = -\frac{I}{\delta - ng^2/\Delta}, \tag{6.4}$$

where $I = \int_0^T |\eta(t)|^2 \mathrm{d}t$ is the pulse energy. Thus, the pulse implements a unitary $U_B = \exp\left[-iI/(\delta - \hat{n}g^2/\Delta)\right]$.

6.2 Adiabatic phase gate performance in the presence of losses

For $\gamma, \kappa \neq 0$ the quantum operation on the space of the qubits can be approximated by (see Appendix B.2)

$$\mathcal{E}(|q\rangle \langle q'|) = c_{nm} e^{i(\varphi_n - \varphi_m)} |q\rangle \langle q'| \,. \tag{6.5}$$

Again, $|q\rangle$ and $|q'\rangle$ are computational basis states of the qubits with exactly $n = \sum_j q_j$ and $m = \sum_j q'_j$ qubits in state $|1\rangle$, respectively. The coefficients c_{nm} are given by

$$c_{nm} = 1 - [(\gamma_n + \gamma_m + (s_n - s_m)^2], \tag{6.6}$$

with

$$\gamma_n = \frac{\gamma n g^2}{(\Delta\delta - ng^2)^2} I = -\frac{\gamma}{\Delta} \frac{ng^2}{\Delta\delta - ng^2} \varphi_n \tag{6.7}$$

$$s_n = \frac{\sqrt{\kappa}\Delta}{\Delta\delta - ng^2} \sqrt{I} = \pm \frac{\sqrt{\kappa\Delta}}{\sqrt{|\Delta\delta - ng^2|}} \sqrt{|\varphi_n|}. \tag{6.8}$$

where in the last equality the sign is + if $\Delta/(\Delta\delta - ng^2) > 0$ and − otherwise.

The fidelity can be calculated analogously to Eq. (4.27) as

$$F = \frac{\sum_{n=0}^{N} \binom{N}{n} c_{nn} + \sum_{n,m=0}^{N} \binom{N}{n}\binom{N}{m} c_{nm}}{2^N (2^N + 1)} \tag{6.9}$$

To implement a CZ gate ($N = 2$), up to single qubit gates, I has to be chosen such that $|\varphi_2 - 2\varphi_1 + \varphi_0| = \pi$. Given this choice, the values of δ and Δ that maximize F can be found numerically as $\delta = 0.529\sqrt{\kappa/\gamma}g$, $\Delta = -2.09\sqrt{\gamma/\kappa}g$, which gives $1-F = 1.79/\sqrt{C}$.

The scaling of the optimal δ and Δ with γ and κ can be explained as follows: Inserting the second expressions from Eq. (6.7) and (6.8) into Eq. (6.9) shows that for any given phases $\varphi_0, ..., \varphi_N$, the infidelity is of the form $1-F = \gamma h_1(\delta\Delta)/|\Delta| + \kappa h_2(\delta\Delta)|\Delta|$, where h_1 and h_2 are positive functions independent of γ and κ which only depend on δ and Δ through their product $\delta\Delta$. At a fixed value of $\delta\Delta$, the optimal choice of Δ is thus $|\Delta| = \sqrt{\gamma/\kappa}\sqrt{h_1(\delta\Delta)/h_2(\delta\Delta)}$, and the infidelity is $1 - F = \sqrt{2\gamma\kappa h_1(\delta\Delta)h_2(\delta\Delta)}$. Since h_1 and h_2 are independent of γ and κ, the optimal value of the product $\delta\Delta$ is also independent of γ and κ. Since $\Delta \propto \sqrt{\gamma/\kappa}$ it follows $\delta \propto \sqrt{\kappa/\gamma}$.

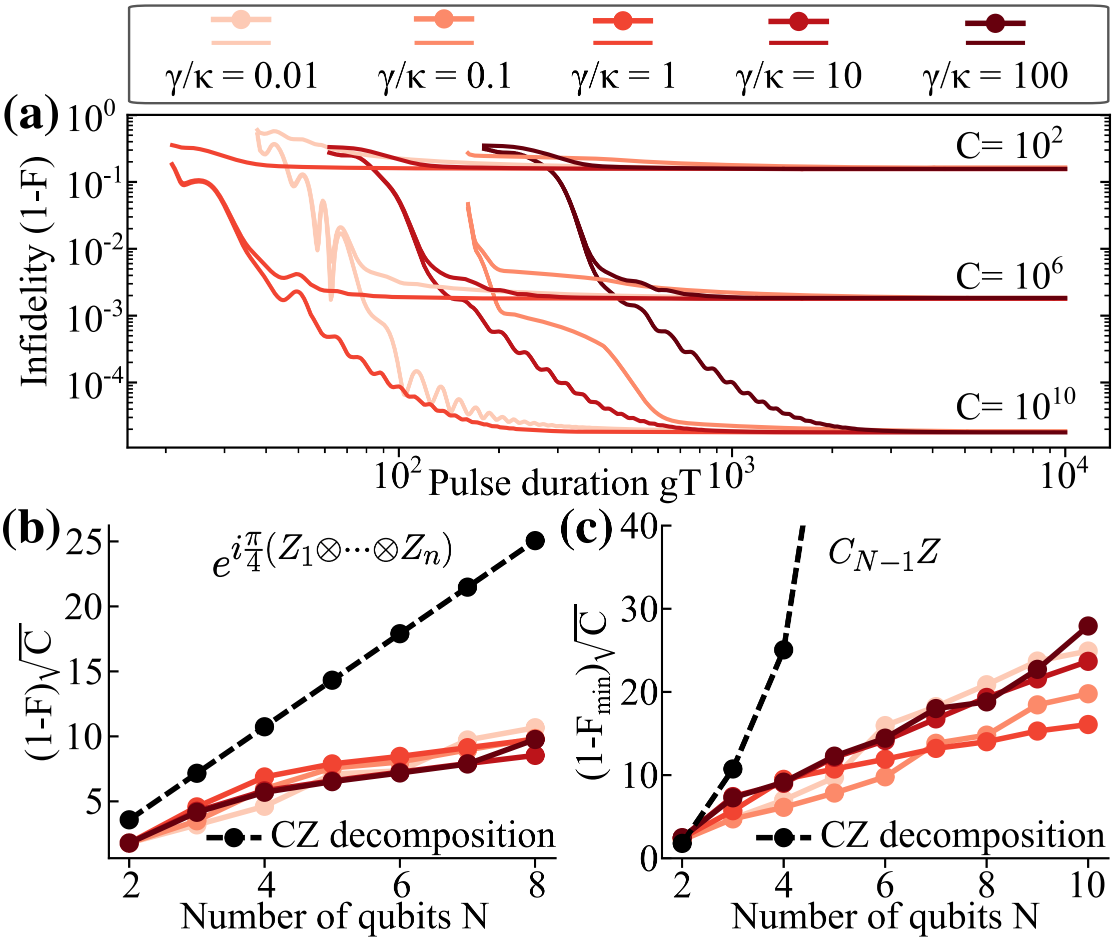

FIGURE 6.1: Numerical results of CZ gate and performance of phase rotation gate and $C_{N-1}Z$ gate with adiabatic phase gate protocol: (a) Infidelity (numerical calculation) for a CZ gate as a function of pulse duration T for different values of C and γ/κ. (b) Infidelity of a phase-rotation gate with $\alpha = \pi/4$ in the $T \to \infty$ limit as a function of N. Also shown is the infidelity of the same gate implemented using a decomposition into CZ and single-qubit gates using the circuit from Ref. [40]. (c) Infidelity of a $C_{N-1}Z$ gate vs N when implemented using APG protocol and by decomposition into CZ and single qubit gates using an ancilla-free Gray-code [41].

6.3 CZ gate: Numerical Results

To confirm our formula for the infidelity and to determine the infididelity for finite pulse durations T, we numerically solve the Lindblad equations for different pulse durations T and different values of γ and κ. To achieve adiabaticity, $\eta(t)$ is chosen as a flat-top pulse, rising to its maximium value $\eta_{\max}$ with a $\sin^2$-shaped flank of duration $T_0 \leq T/2$, staying at $\eta_{\max}$ for a duration $T - 2T_0$, and then falling back to 0 in a $\sin^2$-shaped flank. T_0 and $\eta_{\max}$ are numerically chosen to satisfy $|\varphi_2 - 2\varphi_1 + \varphi_0| = \pi$ with the minimal possible slope $\max_t |\dot{\eta}(t)|$.

Figure 6.1(a) shows the infidelity as a function of T for a CZ gate using APG protocol for different values of C and γ/κ. We find that $1 - F$ approaches its asymptotic value

$1.79/\sqrt{C}$ for pulse durations $10^2 g^{-1} \lesssim T \lesssim 10^3 g^{-1}$, while for smaller T it increases due to diabatic errors. The different behavior for different γ/κ ratios arises due to a nontrivial behavior of $|\varphi_2 - 2\varphi_1 + \varphi_0|$ away from the perturbative approximation made above.

6.4 Implementation of arbitrary phase gates

In the following we show how $N-1$ repetitions of APG protocol can be used to implement an *arbitrary* symmetric phase gate $\exp(i\varphi(\hat{n}))$ for *any* function $\varphi(\hat{n})$, up to single qubit gates and a global phase.

To see this, let us consider applying the APG protocol $N-1$ times, with different detunings $\delta_1, ..., \delta_{N-1}$ and $\Delta_1, ..., \Delta_{N-1}$ and different pulse energies $I_1, ..., I_{N-1}$ in each pulse. We require the that $\Delta_k - \delta_k$ is independent of k, so that the different pulses can be implemented by only changing the amplitude, duration and detuning of the external drive of the cavity, while the detuning between the cavity frequency and the $|1\rangle \leftrightarrow |e\rangle$ transition stays constant. Each of these pulses now implements a phase gate $\exp(i\varphi_k(\hat{n}))$ with $\varphi_k(\hat{n})$ given through Eq. (6.4). Taking all pulses together and adding a global phase θ_g and a single qubit phase θ_s, the implemented phase gate is

$$\varphi(\hat{n}) = \theta_g + \hat{n}\theta_s - \sum_{k=1}^{N-1} \frac{I_k}{\delta_k - \hat{n} g^2 \Delta_k} \tag{6.10}$$

Observe that the $\varphi(\hat{n})$ depend *linearly* on the $N+1$ variables θ_g, θ_s and $I_1, ..., I_{N-1}$. Thus, since there are $N+1$ possible values of n (from 0 to N), Eq. (6.10) has a unique solution of the θ_g, θ_s and $I_1, ..., I_{N-1}$ as a function of $\varphi(\cdot)$ and the δ_k and Δ_k. Hence there are pulse energies $I_1, ..., I_{N-1}$ to implement $\exp(i\varphi(\hat{n}))$ up to single qubit gates and a global phase. Note that such $I_1, ..., I_{N-1}$ can be found for *any* choice of the δ_k and Δ_k. In Appendix B.4 we give a method based on linear programming to find the δ_k and Δ_k which minimize the gate infidelity.

We exemplify the procedure described above for two classes of multi-qubit gates: Phase-rotation gates $\exp(-i\alpha Z_1 \otimes ... \otimes Z_n)$ – corresponding to phases $\varphi_n = -\alpha(-1)^n$ – and N-qubit multi-controlled-Z gates (C$_{N-1}$Z gates), i.e. phase gates with $\varphi_N = \pi$ and $\varphi_n = 0$ for $n < N$. The infidelity for both multi-qubit gates as a function of N is shown in Fig. 6.1(b,c) for different values of γ/κ. Here, we take $\delta_k - \Delta_k = 2.09g/\sqrt{\kappa/\gamma} + 0.529g\sqrt{\kappa/\gamma}$ (the optimal choice for $N=2$), and choose the $\delta_1, ..., \delta_{N-1}$ to maximize the fidelity (See Appendix B.4). Note that for C$_{N-1}$Z gates we consider the minimal fidelity $F_{\min} = \min_{|\psi\rangle} \langle\psi| C_{N-1}Z\mathcal{E}(|\psi\rangle\langle\psi|)C_{N-1}Z |\psi\rangle$ instead of the average gate fidelity for a fair comparison between different N. An approximately linear scaling of the infidelity with N is observed for both gates in Fig. 6.1(b,c). Our protocol outperforms implementations using decompositions into individual CZ and (perfect) single qubit gates in both cases for any $N > 2$. An application of GPG protocol is to perform non-local $\mathrm{C}_{N-1}\mathrm{Z}$ gates, which are locally equivalent to multi-controlled Toffoli gates, for majority voting circuits. These are frequently used e.g. in measurement free quantum error correction [189–191]. Even though for $N > 2$ the gate is not Clifford and our implementation is not fault tolerant, the gate *can* be used for fault tolerant quantum error correction when it involves controls that are ancilla that carry error syndrome data that is classical [189].

6.5 Realistic fidelity estimates

In this section we provide estimates for the achievable gate fidelity and pulse duration for CZ gate with the adiabatic phase gate protocol for different physical systems. The systems are described in detail in section 3.4, and other specificities are described in section 4.5. Table 6.1 summarises the results.

Emitter type	Neutral	Rydberg	Molecules	Fluxonium
Field type	optical	microwave	microwave	microwave
Coupling strength g	400 MHz	4 MHz	400 kHz	10 MHz
Cavity linewidth κ	20 MHz	17 Hz	40 Hz	-
Emitter transition linewidth γ	6 MHz	204 Hz	$< 10^{-2}$ Hz	0.8 MHz
Cooperativity C	1500	5×10^9	$> 10^{11}$	-
Gate infidelity	0.046	5×10^{-3}	6×10^{-4}	0.037
Pulse duration T	120 ns	8 μs	400 μs	640 ns

Table 6.1: APG protocol in realistic setups: achievable gate fidelity and pulse duration for CZ gate with the geometric phase gate protocol for different physical systems: Neutral ^{87}Rb atoms coupled to a fiber-based Fabry Perot optical cavity, Cs Rydberg atoms coupled via superconducting microwave resonator, Polar Ca^{79}Br molecules coupled to microwave resonator and superconducting fluxonium qubits coupled to microwave resonator.

6.6 Conclusion and outlook

In this chapter, we showed that by driving the cavity with a weak and slowly changing pulse $\eta(t)$, a multi-qubit quantum gate can be implemented by adiabatic evolution. Like for the GPG protocol, the infidelity in the limit $T \to \infty$ only depends on the cooperativity and not on the ratio γ/κ. We also showed how $N-1$ repetitions of the protocol with different pulse parameters can be used to implement *any* symmetric phase gate, which has significant implications in digital quantum simulations. Implementation of these native *arbitrary* phase gates without decomposing them into single- and two-qubit gates significantly enhances the prospect of realizing non-local stabilizers and quantum error correction schemes such as LDPC codes [108, 109] with reduced qubit overheads compared to current leading schemes, in particular if our protocols are parallelized in architectures that exploit multiple modes (e.g. frequency, polarization, spatial modes for overlapping cavities) as necessary for parallel operations to support QEC.

Chapter 7

Cavity polariton blockade for non-local entangling gates with trapped atoms

The current chapter is an adaptation of the manuscript “Cavity polariton blockade for non-local entangling gates with trapped atoms” [192]. In the spirit of exploiting *non-locality* and *multi-qubit* interactions with cavity QED setups, in Chapter 4 and Chapter 6, we saw two practical protocols for realising non-local multi-qubit quantum gate operations - of a geometric phase gate and an adiabatic phase gate - mediated by a common cavity mode by solely driving the cavity mode to implement non-local multi-qubit phase gates such that the gate operations are achieved in a single control step. Also in Chapter 5, we have demonstrated the utility of the geometric phase gate, when combined with optimal control methods, for the preparation of metrologically useful optimal probe states which achieve a significant entanglement-enhanced advantage in quantum sensing beyond the standard quantum limit, in the presence of noise [173].

In this chapter, also with close relation with the current experimental efforts [38, 39], we propose deterministic multi-qubit entanglement generation via a non-local excitation blockade with an additional global drive acting on the qubits.

In the pioneering work [193], the authors introduced a deterministic protocol to generate multi-qubit entangled states by employing Quantum Zeno Dynamics (QZD) [194, 195]. This is based on nondestructive measurement [196] in a cavity QED setup with a single-mode cavity that couples to N atomic qubits: Let each atomic qubit be comprised of computational states $|0\rangle$ and $|1\rangle$; All the atoms are initialized in the qubit excited state

$|1\rangle$ and acted upon by a resonant pulse on the qubit transition resulting in a coherent evolution of the system which is combined with a simultaneous and continuous measurement performed by probing the cavity resonantly. The measurement is such that the cavity probe is resonant with the cavity mode when all the atoms are in the qubit state $|0\rangle$, and the measurement effectively probes the ground state of the qubit register $|\mathcal{D}_0\rangle = |0\rangle^{\otimes N}$. The measurement back-action on the state $|\mathcal{D}_0\rangle$ prevents it from being populated, due to Quantum Zeno Dynamics. Instead, states very similar to the so-called W state are prepared, with the latter denoted as $|\mathcal{D}_1\rangle = (1/\sqrt{N})(|10\dots0\rangle + |010\dots0\rangle + \dots + |00\dots1\rangle)$ in the following. These states are robust to particle loss and can be used as a resource for some tasks like distributed sensing [197]. While the results of Ref. [193] constitute a significant breakthrough in the experimental manipulation of many-particle quantum states, it is an interesting open question whether the QZD scheme can be generalized to new protocols ensuring a high-fidelity of preparation of the desired multi-particle state. In addition, it would be highly interesting both theoretically and experimentally whether QZD-like protocols could be devised that allow for performing deterministic multi-qubit quantum operations – including full quantum gates – of use for quantum computing and sensing. Very recent breakthrough experiments with cold neutral atoms trapped in optical tweezers in fiber based Fabry-Perot optical cavity have demonstrated that realizing quantum gates and operations with high-fidelity is becoming possible thanks to the possibility to trap multiple atomic qubits inside an optical cavity in a regime of strong light-matter coupling [198]. These works open the way to non-local entanglement generation using the delocalized photon field and are possible key components of future architectures for distributed quantum computing and sensing [199–201].

In this work, we propose a new protocol that generalizes the idea of QZD-based state preparation to account for the formation of mixed light-matter polariton states for qubits coupled to the cavity mode, and use it to demonstrate theoretically a viable pathway to generating multi-qubit entangled W states as well as two-qubit controlled-Z (CZ) and three-qubit $\mathrm{C_2Z}$ quantum gates. Due to coupling to the delocalized cavity mode, the latter gates can be non-local. Our protocol relies on a new cavity polariton blockade mechanism for multiqubit entanglement generation, which impedes the formation of polariton modes with more than one excitation, due to strong measurement induced excitation blockade. The latter is a combination of Quantum Zeno Dynamics and energy detuning of a selectively probed cavity polariton state from the coherent global qubit drive. Interestingly, the protocol only requires global drives of the cavity for generating a multi-particle entangled state and of the cavity and of a single global laser on the qubit transition to drive the two-qubit and three-qubit quantum gates. We present a full quantum-mechanical treatment of the system dynamics and derive analytical expressions for the W state preparation error, as well as the CZ and C_2Z gate errors. These errors are evaluated while taking fully into account the relevant physical losses in experiments, arising from a finite cavity resonance linewidth κ and atomic linewidth γ, using optimal values for drive strength ratios and detuning parameters. We assume coupling of atoms with the cavity mode with coupling strength g in the strong coupling regime, such that the single-particle cooperativity $C = g^2/(\kappa\gamma) \gg 1$. To our knowledge, this is the first time that a full analytical treatment is carried out in the presence of losses for deterministic quantum gates – with the exception of the protocols in Ref. [54]. This work opens the way to the realization of multi-particle non-local entangled states generation and quantum gates based on a new polariton blockade mechanism. While we provide precise predictions for experiments with neutral atoms trapped in cavities, the present work can be relevant to other physical platforms, such as exciton polaritons in the solid state [202–204], depending on achievable light-matter couplings, intrinsic non-linearities and polariton lifetimes in those systems.

The chapter is organized as follows: In Sec. 7.1, we recall the system Hamiltonian for N atomic spin qubits coupled to a common cavity mode controlled with two laser drives – one acting on the cavity mode and the other acting globally on the qubits. Additionally here we introduce the cavity polariton states which are the eigenstates of the atoms-cavity coupling Hamiltonian.In Sec. 7.2 we first derive an effective Hamiltonian in the regime where the cavity drive and the losses (cavity decay and spontaneous emission) are treated perturbatively with respect to the cavity-qubit coupling. We then establish the *cavity polariton blockade*, where a cavity polariton state becomes resonant to the cavity drive at a specific detuning. The cavity drive then induces dressing of the states it couples to, and can no longer be treated perturbatively in the corresponding subspace formed by the dressed states (blockaded subspace). This creates an energy barrier (blockade-like) or energy leakage (QZD like) in the system depending on whether the strength of detuning of the global drive exceeds the loss rates. By treating the coupling from the global qubit drive between the blockaded subspace with other cavity polariton states perturbatively, one can suppress population in the blockaded subspace. Here, we choose the blockaded subspace such that simultaneous excitation of two qubits to the $|1\rangle$ state is suppressed. The resulting effective Hamiltonian, after tracing out the cavity mode in vacuum and in the absence of losses, is analogous to a driven two-level system with the logical states $|\mathcal{D}_0\rangle$ (all qubits in $|0\rangle$) and the W state $|\mathcal{D}_1\rangle$ (equal superposition of all states with one qubit in $|1\rangle$ state and rest in the $|0\rangle$ state), which we term as the effective blockade Hamiltonian. In Sec. 7.3, we describe the W state preparation in the presence of losses and present an analytical expression for state preparation infidelity. We obtain the W state-preparation error scaling as $\sqrt{1-1/N}/\sqrt{C}$, hence saturating with the total number of atoms N. In Sec. 7.4, we adapt the cavity polariton approach for the implementation of time-optimal CZ and C_2Z gates. By introducing a new computational state $|1'\rangle$, we use $|1\rangle$ state as an auxiliary state to realize a blockade-like interaction, enabling a CZ or C$_2$Z gate with the computational states $|0\rangle$ and $|1'\rangle$. We also semi-analytically present the CZ and C_2Z gate errors, which scale as $1/\sqrt{C}$. This scaling of errors with C for our protocols is consistent with the expected error scaling for deterministic protocols [205].

7.1 Model

In this section we recall our system model and Hamiltonian from chapter 3 mainly in the context of atomic qubits coupled to an optical cavity, and additionally introduce the cavity polariton states. We first describe the various system components and parameters, and write the Hamiltonian of the system in the laboratory frame. Next we apply a rotating wave approximation and further split the Hamiltonian intro three components set by different energy scales which becomes relevant for the derivation of the effective blockade Hamiltonian using perturbation theory in Sec. 7.2. In Sec. 7.1.1, we introduce the cavity polariton states in terms of a convenient symmetric basis for the system Hamiltonian.

We consider a system of N atoms coupled to an optical cavity which supports a single mode with frequency ω_c as shown in Fig. 7.1(a). Each atom is modeled as a three-level system [Fig. 7.1(b)] with two computational qubit states $|0\rangle$ and $|1\rangle$, and an excited state $|e\rangle$ with finite lifetime $1/\gamma$. We define the energies of the states $|0\rangle$, $|1\rangle$ and $|e\rangle$ as ω_0, ω_1 and ω_e respectively ($\hbar = 1$). The cavity mode creation and annihilation operators are $\hat{a}^\dagger$ and $\hat{a}$ respectively, and the cavity excitation has a finite lifetime $1/\kappa$. The atomic levels $|1\rangle$ and $|e\rangle$ are coupled via the cavity mode with coupling strength g. An external cavity probe- a drive laser with frequency ω_L drives the cavity mode with amplitude $\eta(t)$. In addition, there is a free-space coupling between the states $|0\rangle$ and $|1\rangle$ with Rabi-frequency $\Omega(t)$, which can be realized by a global laser pulse on the qubits with frequency ω_{gl}, given by $\Omega(t)\cos(\omega_{\mathrm{gl}}t)|1\rangle\langle 0| + \mathrm{h.c.}$ We define $\hat{n}_s = \sum_{j=1}^{N} |s_j\rangle\langle s_j|$ which denotes the number operator for atoms in state $|s\rangle$ for $s \in \{0, 1, e\}$ and j denotes the atom-index.

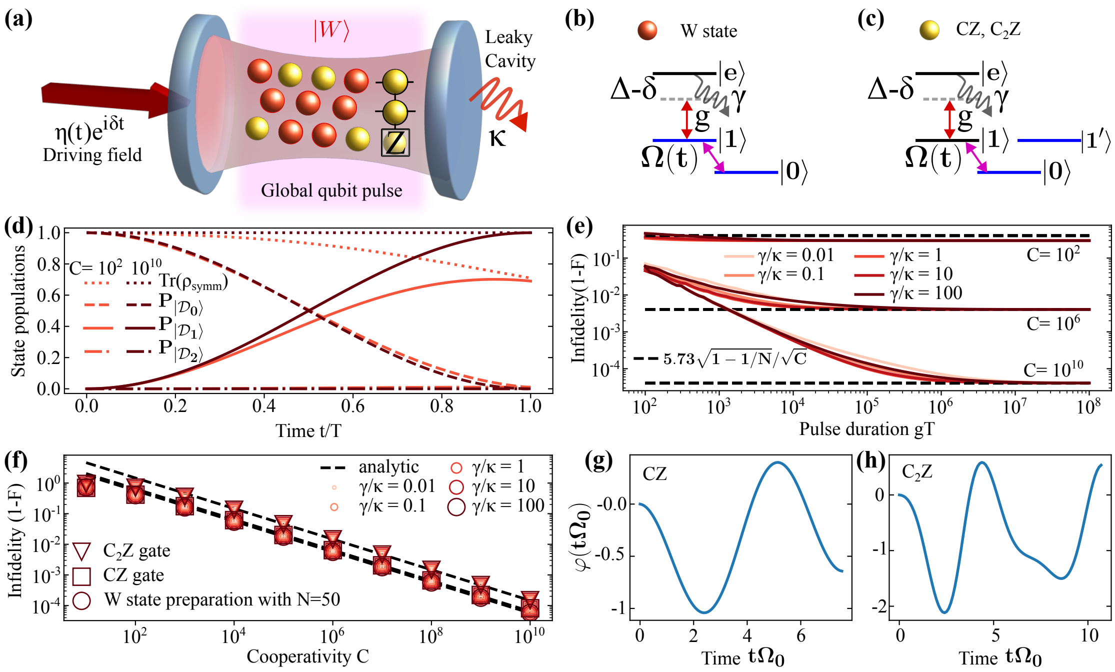

FIGURE 7.1: (a) Schematic of atoms trapped inside a cavity and coupled to a common cavity mode, which is externally driven by a classical field $\eta(t)$. An additional global pulse addresses all the qubits. A multi-qubit entangled W state can be prepared with arbitrarily selected atoms atoms(in red) modeled as three-level systems (as shown in (b)) and a C_2Z gate can be implemented with atoms (in yellow) modeled as four-level systems(as shown in (c)). (b,c) Level schematic for atoms implementing W state preparation and CZ or C_2Z gate. The $|1\rangle \leftrightarrow |e\rangle$ coupling is mediated by the cavity with coupling strength g. An additional (global) laser drive couples the states $|0\rangle$ and $|1\rangle$ with Rabi frequency $\Omega(t)$. The computational qubit states are highlighted in blue. (d) State population dynamics obtained numerically by simulating the dynamics under the full Hamiltonian in Eq. (7.3), plotted for states $|\mathcal{D}_0\rangle, |\mathcal{D}_1\rangle$, and $|\mathcal{D}_2\rangle$ denoted by $P_{|\mathcal{D}_0\rangle}, P_{|\mathcal{D}_1\rangle}$ and $P_{|\mathcal{D}_2\rangle}$ respectively for a system with $N = 2$. The populations $P_{|\mathcal{D}_0\rangle}$ (dashed lines), $P_{|\mathcal{D}_1\rangle}$ (solid lines), and $P_{|\mathcal{D}_2\rangle}$ (dash-dot lines) at each time add up to the trace of the reduced atomic density matrix (dotted lines) $\mathrm{Tr}(\rho_{\mathrm{symm}}) \leq 1$ where ρ_{symm} corresponds to the subspace spanned by states $\{|\mathcal{D}_n\rangle \forall n = 0, 1, \dots N\}$. (e) Infidelity $(1-F)$ as a function of the total pulse duration gT for W state preparation with $N = 2$ for $C = 10^2, 10^6, 10^{10}$ and $\gamma/\kappa = 0.01, 0.1, 1, 10, 100$. The infidelity converges to the analytical estimate(dashed lines) $5.73\sqrt{1 - 1/N}/\sqrt{C}$ (See text Sec. 7.3.1) obtained in the limit $T \to \infty$. (f) Infidelity $(1-F)$ as a function of single particle cooperativity for W state preparation with $N = 50$, CZ gate and C_2Z gate. The dashed lines represent the analytically calculated errors, and numerical points obtained by simulating the dynamics with the full Hamiltonian (Eq. (7.3)) are plotted for $\gamma/\kappa = 0.01, 0.1, 1, 10, 100$ for a fixed pulse duration of $gT = 10^8$. (g,h) Time optimal pulses for implementing CZ gate and C_2Z gate from [63, 64]

The full Hamiltonian $\hat{H}_{\mathrm{full}}$ reads

$$\begin{aligned}
\hat{H}_{\mathrm{full}} &= \omega_0 \hat{n}_0 + \omega_1 \hat{n}_1 + (\omega_e - i\gamma/2)\hat{n}_e + (\omega_c - i\kappa/2)\hat{a}^\dagger \hat{a} \qquad (7.1)\\
&+ g \sum_{j=1}^{N} \left(|e_j\rangle\langle 1_j| + |1_j\rangle\langle e_j|\right)\left(\hat{a}^\dagger + \hat{a}\right)\\
&+ 2|\eta(t)| \sin(\omega_L t + \arg[\eta(t)])(\hat{a}^\dagger + \hat{a})\\
&+ \sum_{j=1}^{N} \left(\Omega(t)\cos(\omega_{\mathrm{gl}} t)|1_j\rangle\langle 0_j| + \mathrm{h.c.}\right).
\end{aligned}$$

We define the detuning between the frequency of the cavity drive laser and of the $|1\rangle \leftrightarrow |e\rangle$ transition as $\Delta = (\omega_e - \omega_1) - \omega_L$, the detuning between the laser and the cavity mode frequency as $\delta = \omega_c - \omega_L$, and the detuning of the $|0\rangle \leftrightarrow |1\rangle$ qubit transition and the global laser as $\delta_{gl} = (\omega_1 - \omega_0) - \omega_{gl}$.

We proceed by defining the following unitary operator

$$\hat{U}(t) = \exp\Big\{\Big[i(\omega_L(\hat{a}^\dagger\hat{a} + \hat{n}_e) + \omega_1(\hat{n}_1 + \hat{n}_e) + \omega_0\hat{n}_0)t\Big]\Big\}. \tag{7.2}$$

In the rotating frame given by $\hat{U}(t)$, $\hat{H}_{\text{full}}$ is transformed as $\hat{H} = \hat{U}\hat{H}_{\text{full}}\hat{U}^\dagger + i\frac{d\hat{U}}{dt}\hat{U}^\dagger$. In the rotating wave-approximation valid for $g, |\eta| \ll \omega_L$, $|\Omega| \ll \omega_{\text{gl}}$, we then obtain the following non-Hermitian Hamiltonian for the system given by,

$$\begin{aligned}
\hat{H} &= \hat{H}^{(\Delta,\delta,g)} + \hat{H}^{(\kappa,\gamma,\eta)} + \hat{H}^{(\Omega)} \\
\hat{H}^{(\Delta,\delta,g)} &= \delta\hat{a}^\dagger\hat{a} + \Delta\hat{n}_e + g(\hat{S}^-\hat{a}^\dagger + \hat{S}^+\hat{a}) \\
\hat{H}^{(\kappa,\gamma,\eta)} &= -\frac{i}{2}\kappa\hat{a}^\dagger\hat{a} - \frac{i}{2}\gamma\hat{n}_e + i\eta(t)\left(\hat{a}^\dagger - \hat{a}\right) \\
\hat{H}^{(\Omega)} &= \sum_{j=1}^{N}\left(\frac{\Omega(t)}{2}|1_j\rangle\langle 0_j| + \frac{\Omega^*(t)}{2}|0_j\rangle\langle 1_j|\right),
\end{aligned} \tag{7.3}$$

where $\hat{S}^- = \sum_{j=1}^{N}|1_j\rangle\langle e_j|$ and $\hat{S}^+ = \sum_{j=1}^{N}|e_j\rangle\langle 1_j|$ are collective operators. The Hamiltonian $\hat{H}$ in Eq. (7.3) consists of three components that represent distinct physical processes. The first component, $\hat{H}^{(\Delta,\delta,g)}$, includes the Tavis-Cummings interaction Hamiltonian, which describes the coupling of atoms to the shared cavity mode [206]. The second component $\hat{H}^{(\kappa,\gamma,\eta)}$, describes the cavity drive and the loss mechanisms, with non-Hermitian contributions from cavity decay (rate κ) and spontaneous emission from the excited state $|e\rangle$ (rate γ). The third component, $\hat{H}^{(\Omega)}$, represents the free-space laser coupling (transversal drive) between the qubit states $|0\rangle$ and $|1\rangle$, driven by a time-dependent Rabi frequency $\Omega(t)$. In Eq. (7.3) we define $\Omega(t) = \Omega_0\exp[i(\varphi(t\Omega_0) + \delta_{gl}t)]$, where Ω_0 is the Rabi-frequency of the laser coupling the qubit transition and $\varphi(t\Omega_0)$ is a phase depending on the dimensionless time $t\Omega_0$. Both photon loss from the cavity and the decay of population from the state $|e\rangle$ are treated as non-Hermitian terms in Eq. (7.3), corresponding to $(-i\kappa/2)\hat{a}^\dagger\hat{a}$ and $(-i\gamma/2)\hat{n}_e$, respectively. For the cavity decay, this corresponds to a conditional evolution under the condition that no photon is lost. For the latter term, this implies the assumption that all population decays outside the computational basis states. We come back to this point in Sec. 7.3.

7.1.1 Cavity polariton states

Cavity polariton states refer to the eigenstates of the atoms-cavity coupling Hamiltonian $\hat{H}^{(\Delta,\delta,g)}$, which are the hybrid atom-photon states.

To diagonalise $\hat{H}^{(\Delta,\delta,g)}$, we identify the operators $\hat{n} = \sum_{j=1}^{N}(|1_j\rangle\langle 1_j| + |e_j\rangle\langle e_j|)$ and $\hat{k} = \sum_{j=1}^{N} |e_j\rangle\langle e_j| + \hat{a}^\dagger\hat{a}$ such that $\left[\hat{H}^{(\Delta,\delta,g)}, \hat{n}\right] = \left[\hat{H}^{(\Delta,\delta,g)}, \hat{k}\right] = 0$. This suggests that $\hat{H}^{(\Delta,\delta,g)}$ is block-diagonal in eigenstates of $\hat{n}$ and $\hat{k}$. Also, with $\left[\hat{n}, \hat{k}\right] = 0$, both $\hat{n}$ and $\hat{k}$ can be diagonalised simultaneously. We define a convenient symmetric basis defined by the states $|a_1 b_e m_{\text{ph}}\rangle$ with $0 \leq a + b \leq N$, $m_{ph} = 0, 1, \ldots \infty$. The state $|a_1 b_e m_{\text{ph}}\rangle$ corresponds to a symmetric superposition of all states with a atoms in state $|1\rangle$, b atoms in state $|e\rangle$ and m photons in the cavity. Thus, $\hat{n}\,|a_1 b_e m_{\text{ph}}\rangle = (a + b)\,|a_1 b_e m_{\text{ph}}\rangle$, $\hat{k}\,|a_1 b_e m_{\text{ph}}\rangle = (b+m)\,|a_1 b_e m_{\text{ph}}\rangle$ with $a+b = n = 0, 1, \ldots, N$, and $b+m = k = 0, 1, \ldots \infty$.

Here and in the remainder of the section, we restrict our analysis to the subspace of $\hat{H}^{(\Delta,\delta,g)}$ spanned by the basis states $\left\{|\psi\rangle : \hat{n}|\psi\rangle = n|\psi\rangle; \hat{k}|\psi\rangle = k|\psi\rangle\right\}$ with $n = 0, 1, 2$ and $k = 0, 1$, which suffices for the discussion of the intended blockade mechanism. In the $k = 0$ subspace of $\hat{H}^{(\Delta,\delta,g)}$, we have the eigenstates $|n_1 0_e 0_{\text{ph}}\rangle \equiv |\mathcal{D}_n\rangle \otimes |0\rangle_{\text{cav}}$ with zero energy. Here $|\mathcal{D}_n\rangle$ refers to the qubit state which is a symmetric superposition of computational states with n qubits in $|1\rangle$ and the rest in $|0\rangle$.

The $k = 1$ subspace of $\hat{H}^{(\Delta,\delta,g)}$ is written as

$$\hat{H}^{(\Delta,\delta,g)}_{n,k=1} = \begin{bmatrix} \delta & \sqrt{n}g \\ \sqrt{n}g & \Delta \end{bmatrix} \tag{7.4}$$

in the basis spanned by $\{|n_1 0_e 1_{\text{ph}}\rangle, |n-1_1 1_e 0_{\text{ph}}\rangle\}$. As a reminder, $|n_1 0_e 1_{\text{ph}}\rangle$ corresponds to the state with equal superposition of all basis states with n atoms in state $|1\rangle$, no atoms in state $|e\rangle$, and one cavity photon. The state $|n-1_1 1_e 0_{\text{ph}}\rangle$ refers to the equal superposition of all states with $n-1$ atoms in state $|1\rangle$, one atom in state $|e\rangle$, and cavity in vacuum state. The eigenstates of $\hat{H}^{(\Delta,\delta,g)}_{n,k=1}$ are then the polariton states $|p_n^\pm\rangle$ (superposition of states $|n_1 0_e 1_{\text{ph}}\rangle$ and $|n-1_1 1_e 0_{\text{ph}}\rangle$) with eigenenergies $\epsilon_n^\pm$, given by

$$\begin{aligned} |p_n^+\rangle &= \cos(\theta/2)\,|n_1 0_e 1_{\text{ph}}\rangle + \sin(\theta/2)\,|n-1_1 1_e 0_{\text{ph}}\rangle\,, & (7.5) \\ |p_n^-\rangle &= -\sin(\theta/2)\,|n_1 0_e 1_{\text{ph}}\rangle + \cos(\theta/2)\,|n-1_1 1_e 0_{\text{ph}}\rangle], & (7.6) \end{aligned}$$

where $\cos(\theta) = (\delta - \Delta)/(\sqrt{(\delta-\Delta)^2 + 4ng^2})$. The eigenenergies are given by

$$\epsilon_n^\pm = \frac{1}{2}(\delta + \Delta) \pm \frac{1}{2}\sqrt{(\delta-\Delta)^2 + 4ng^2}. \tag{7.7}$$

We hence obtain

$$\hat{H}^{(\Delta,\delta,g)}_{n,k=1} = \epsilon_n^+ |p_n^+\rangle\langle p_n^+| + \epsilon_n^- |p_n^-\rangle\langle p_n^-|. \tag{7.8}$$

Note that for $n = 0$, we have only the $|p_0^+\rangle = |n_1 0_e 1_{\text{ph}}\rangle$ state with $\epsilon_0^+ = \delta$. Figure 7.2(a) visualizes the energy spectrum of $\hat{H}^{(\Delta,\delta,g)}$ with eigenstates $|n_1 0_e 0_{\text{ph}}\rangle$ in the $k = 0$ subspace and states $|p_n^\pm\rangle$ in the $k = 1$ subspace.

In the following Sec. 7.2 we derive an effective blockade Hamiltonian, with Eq. (7.3) as the starting point and by assuming the three components of the Hamiltonian $\hat{H}$ in Eq. (7.3) as being associated with different timescales in the system. We start in the diagonalized basis of $\hat{H}^{(\Delta,\delta,g)}$ formed by cavity polariton states introduced in Sec. 7.1.1, then add $\hat{H}^{(\kappa,\gamma,\eta)}$ and $\hat{H}^{(\Omega)}$ as perturbative couplings by assuming a hierarchy of timescales: $\mathbb{T}(\hat{H}^{(\Delta,\delta,g)}) \ll \mathbb{T}(\hat{H}^{(\kappa,\gamma,\eta)}) \ll \mathbb{T}(\hat{H}^{(\Omega)})$.

7.2 Effective Blockade Hamiltonian

In this section, we detail the cavity polariton blockade mechanism which prevents two qubits to be simultaneously excited to the $|1\rangle$ state. We demonstrate this blockade mechanism by first deriving the blockade condition which sets the cavity probe resonant with the N-atom-cavity system when exactly two atoms are in the state $|1\rangle$. Second, we describe the dynamics under the blockade mechanism by deriving an effective non-Hermitian Hamiltonian $\hat{H}_{\text{eff}}$ restricted to the subspace with states $|\mathcal{D}_0\rangle$, initial state with all qubits in $|0\rangle$ and $\overline{|\mathcal{D}_1\rangle}$ (see Eq. (7.9) below), which is a state close to the W state $|\mathcal{D}_1\rangle$ – resulting from the blockade condition – from the total Hamiltonian $\hat{H} = \hat{H}^{(\Delta,\delta,g)} + \hat{H}^{(\kappa,\gamma,\eta)} + \hat{H}^{(\Omega)}$ of Sec. 7.1.

We work in the regime $\Delta, \delta, g \gg \eta, \kappa, \gamma$ and $\Omega_0 \ll \eta$ to derive the blockade condition and the effective Hamiltonian. In this regime, the cavity mode, driven with strength η, is excited much more slowly than the atom-cavity coupling dynamics, with timescales comparable to the losses characterized by κ and γ. Meanwhile, the qubit transition occurs even more slowly than the dynamics governed by the cavity drive. This separation of timescales allows us to treat $\hat{H}^{(\kappa,\gamma,\eta)}$ as a perturbation to $\hat{H}^{(\Delta,\delta,g)}$, with $\hat{H}^{(\Omega)}$ serving as an additional perturbation to the effective system.

The derivation has the following three steps: (i) We establish the blockade condition which results in the cavity polariton state with two qubits in $|1\rangle$ to resonantly interact with the cavity drive. More precisely, this condition leads to the transition between two cavity polariton states in the $n = 2$ subspace resonant with the cavity drive. (ii) Next, we add the Hamiltonian term with the cavity drive $\hat{H}^{(\kappa,\gamma,\eta)}$. This has two effects - a) In the $n = 2$ subspace, owing to the resonance condition set by the blockade condition, the cavity drive further dresses the resonant cavity polariton states into new dressed states. And (b) in other n subspaces ($n \neq 2$), this coupling can be treated perturbatively because of the limit $\Delta, \delta, g \gg \eta, \kappa, \gamma$, which results in effective energy shifts on the cavity polariton states. We calculate the dressed state energies for the former states, and calculate the energy shifts to the latter polariton states. (iii) Finally, we add the coupling term $\hat{H}^{(\Omega)}$ and obtain the effective Hamiltonian. Steps (i), (ii) and (iii) are detailed in Secs. 7.2.1, 7.2.2 and 7.2.3 below, respectively.

The resulting effective Hamiltonian $\hat{H}_{\text{eff}}$ defined on the qubit subspace has the form given by

$$\begin{aligned}\hat{H}_{\text{eff}} = \left(E_0 - i\frac{\Gamma_0}{2}\right)|\mathcal{D}_0\rangle\langle\mathcal{D}_0| + \left(E_1 - i\frac{\Gamma_1}{2}\right)\overline{|\mathcal{D}_1\rangle}\,\overline{\langle\mathcal{D}_1|} \\ + \frac{\sqrt{N}\Omega(t)}{2}\overline{|\mathcal{D}_1\rangle}\langle\mathcal{D}_0| + \frac{\sqrt{N}\Omega^*(t)}{2}|\mathcal{D}_0\rangle\overline{|\mathcal{D}_1\rangle},\end{aligned} \tag{7.9}$$

where E_0, E_1 and Γ_0, Γ_1 are the effective energies and the linewidths corresponding to the states $|\mathcal{D}_0\rangle$ and $\overline{|\mathcal{D}_1\rangle}$, respectively. In Eq. (7.9), $|\mathcal{D}_0\rangle = |00\ldots 0\rangle$ corresponds to all qubits in the $|0\rangle$ state. The state

$$\overline{|\mathcal{D}_1\rangle} = |\mathcal{D}_1\rangle + \mathcal{O}(\kappa, \gamma)|\mathcal{D}_2\rangle \tag{7.10}$$

is our target state – a many-particle (and possibly non-local) W state in the presence of atom and photon losses. For $\kappa, \gamma = 0$, it corresponds to the W state, $|W\rangle = |\mathcal{D}_1\rangle = \left(\frac{1}{\sqrt{N}}\sum_{j=1}^{N}|100\ldots\rangle + |010\ldots\rangle + \ldots|00\ldots 1\rangle\right)$, which is a symmetric Dicke state with one atom in state $|1\rangle$. Similarly, the state $|\mathcal{D}_2\rangle$ corresponds to a symmetric Dicke state with two atoms in state $|1\rangle$, and thus the second term in the r.h.s. of Eq. (7.10) represents the first order corrections to $|\mathcal{D}_1\rangle$ in the presence of finite losses with rates $\kappa, \gamma \neq 0$.

An explicit form for the state $\overline{|\mathcal{D}_1\rangle}$ is obtained by evolving the state $|\mathcal{D}_0\rangle$ with Hamiltonian $\hat{H}_{\text{eff}}$, with $\Omega(t)$ chosen such that the $|\mathcal{D}_0\rangle \leftrightarrow |\mathcal{D}_1\rangle$ transition is driven resonantly for a time $T = \pi/(\sqrt{N}\Omega_0)$. We find that the final state $|\psi(T)\rangle$ after the time evolution T is given by

$$\begin{aligned}|\psi(T)\rangle = -i\sin\left(\frac{\pi\Omega'}{2\Omega_0}\right)\frac{\Omega_0}{\Omega'}\overline{|\mathcal{D}_1\rangle} \\ + \left(\cos\left(\frac{\pi\Omega'}{2\Omega_0}\right) - \sin\left(\frac{\pi\Omega'}{2\Omega}\right)\frac{(\Gamma_0 - \Gamma_1)}{2\sqrt{N}\Omega'}\right)|\mathcal{D}_0\rangle\end{aligned} \tag{7.11}$$

where $\Omega' = \Omega_0\sqrt{1 - (\Gamma_0 - \Gamma_1)^2/(4N\Omega_0^2)}$. The final state $|\psi(T)\rangle$ obtained above has a non-vanishing component along $|\mathcal{D}_0\rangle$ because $\Gamma_0 \neq \Gamma_1 \neq 0$. However as $\kappa, \gamma \to 0$, $|\psi(T)\rangle \to |\mathcal{D}_1\rangle$. We take $T \propto \Omega_0^{-1}$ and as we will see in the following, the blockade regime is set in the limit $\Omega_0 \to 0$ and hence the effective Hamiltonian is derived in the limit $T \to \infty$.

In the following Secs. 7.2.1-7.2.3, we discuss in detail the steps (i)-(iii) above leading to the effective blockade dynamics. We then use the effective dynamics to illustrate the W state preparation and the realization of the CZ and $\mathrm{C_2Z}$ gates in Secs. 7.3 and 7.4, respectively.

7.2.1 Cavity polariton blockade condition

In this section we start with the diagonalised Hamiltonian $\hat{H}^{(\Delta,\delta,g)}$ discussed in Sec. 7.1.1 and establish the cavity polariton blockade condition.

Consider first the energy spectrum of the Hamiltonian $\hat{H}^{(\Delta,\delta,g)}$ in the $n = 0, 1, 2$ and $k = 0, 1$ subspace as shown in Fig. 7.2(a). Note that $\hat{H}^{(\kappa,\gamma,\eta)}$ couples the states in k with states in $k + 1$ within the same n subspace. The state $|n_1 0_e 0_{\mathrm{ph}}\rangle$ is hence coupled to the states $|p_n^{\pm}\rangle$ via $\hat{H}^{(\kappa,\gamma,\eta)}$ (See Fig. 7.2(b)).

The cavity polariton blockade condition makes the η coupling mediated by cavity drive term $i\eta(t)(\hat{a}^\dagger - \hat{a})$ from $\hat{H}^{(\kappa,\gamma,\eta)}$ resonant with the atom-cavity system with two qubits in $|1\rangle$ state. That is, the transition between the cavity polariton states $|2_1 0_e 0_{\mathrm{ph}}\rangle \equiv |\mathcal{D}_2\rangle \otimes |0\rangle_{\mathrm{cav}}$ and $|p_2^-\rangle$ in the $n = 2$ subspace is made resonant with the cavity drive. This is achieved by tuning the cavity drive detuning δ such that

$$\delta = 2g^2/\Delta. \tag{7.12}$$

This is similar to setting $\epsilon_2^- = 0$ in Eq. (7.7). As a result, light enters the cavity and is transmitted when δ is chosen according to Eq. (7.12).

In the following Sec. 7.2.2, we discuss the implications of this condition when the Hamiltonian $\hat{H}^{(\kappa,\gamma,\eta)}$ is introduced.

7.2.2 Dressed states and energy shifts due to perturbative couplings from $\hat{H}^{(\kappa,\gamma,\eta)}$

In this section, we add couplings from the Hamiltonian $\hat{H}^{(\kappa,\gamma,\eta)}$ consisting of the cavity drive term and the loss rates. This coupling is treated perturbatively in the $n \neq 2$ subspaces and non-perturbatively in the $n = 2$ subspace because of a resonant coupling introduced by the cavity polariton blockade condition set by Eq. (7.12). We start first

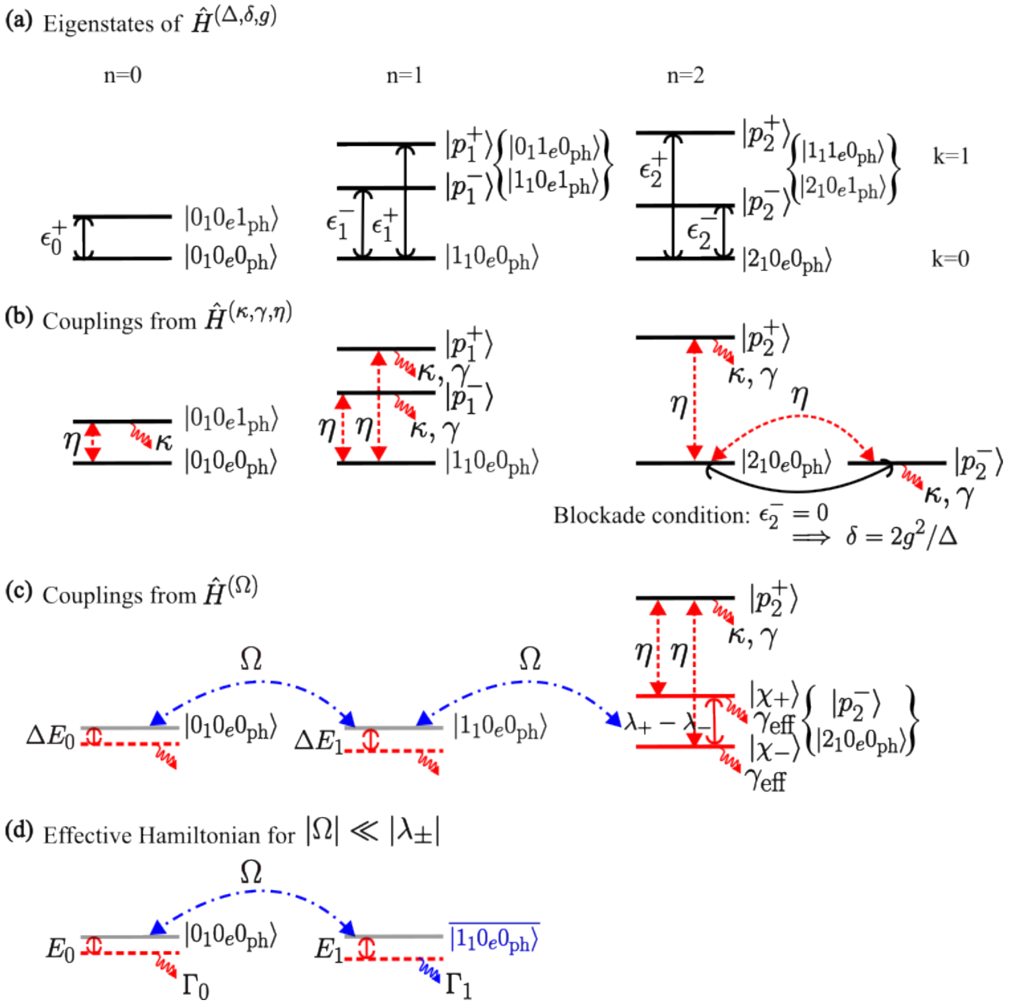

FIGURE 7.2: Level schematic overview of the blockade mechanism. (a) Eigenstates and eigenenergies of $\hat{H}^{(\Delta,\delta,g)}$ truncated to the subspace spanned by states in $n = 0, 1, 2$, $k = 0, 1$ (See text Sec. 7.1.1). (b) Couplings from $\hat{H}^{(\kappa,\gamma,\eta)}$ corresponding to the cavity drive with strength η are denoted by red arrows. The blockade condition is achieved by setting $\epsilon_2^- = 0$, which makes the cavity drive resonant to the $|2_1 0_e 0_{\text{ph}}\rangle \leftrightarrow |p_2^-\rangle$ transition. (c) In the $n = 0$ and $n = 1$ subspaces, weak η coupling shifts the respective states $|0_1 0_e 0_{\text{ph}}\rangle$ and $|1_1 0_e 0_{\text{ph}}\rangle$ in energy (red dashed lines) which also acquire linewidths to the first order in κ, γ. In the $n = 2$ subspace, the states $|2_1 0_e 0_{\text{ph}}\rangle$ and $|p_2^-\rangle$ are dressed by the η interaction into new states $|\chi_\pm\rangle$ (red solid lines) with eigenvalues $\lambda_\pm$ (See text Sec. 7.2.2). The couplings from $\hat{H}^{(\Omega)}$ are shown by blue dash-dot arrows. (d) The effective Hamiltonian restricted to the states $|0_1 0_e 0_{\text{ph}}\rangle$ and $\overline{|1_1 0_e 0_{\text{ph}}\rangle}$ (dressed state due to coupling to $n = 2$ subspace via $\hat{H}^{(\Omega)}$) is obtained in the limit $|\Omega| \ll |\lambda_\pm|$(See text Sec. 7.2.3).

by calculating the energies and linewidths of the dressed polaritons states in the $n = 2$ subspace. We then calculate the energy shifts on the polariton states in the $n = 0$ and $n = 1$ subspaces.

Let the dressed polariton states formed by the η coupling between $|2_1 0_e 0_{\mathrm{ph}}\rangle$ and $|p_2^-\rangle$ in the $n = 2$ subspace be denoted by $|\chi_\pm\rangle$ (See Fig. 7.2(c)). These states correspond to the eigenstates of the Hamiltonian $\hat{H}^{(\Delta,\delta,g)} + \hat{H}^{(\kappa,\gamma,\eta)}$ in the $n = 2$ subspace. The corresponding eigenvalues $\lambda_\pm$ are obtained as the eigenvalues of the matrix

$$\begin{aligned}&\begin{bmatrix} \langle 2_1 0_e 0_{\mathrm{ph}}|\, \hat{H}^{(\kappa,\gamma,\eta)}\, |2_1 0_e 0_{\mathrm{ph}}\rangle & \langle 2_1 0_e 0_{\mathrm{ph}}|\, \hat{H}^{(\kappa,\gamma,\eta)} |p_2^-\rangle \\ \langle p_2^-|\hat{H}^{(\kappa,\gamma,\eta)}\, |2_1 0_e 0_{\mathrm{ph}}\rangle & \langle p_2^-|\hat{H}^{(\kappa,\gamma,\eta)} |p_2^-\rangle \end{bmatrix} \\ &= \begin{bmatrix} 0 & i\eta\Delta/\sqrt{\Delta^2 + 2g^2} \\ -i\eta\Delta/\sqrt{\Delta^2 + 2g^2} & -i(\kappa\Delta^2 + 2\gamma g^2)/(2(\Delta^2 + 2g^2)) \end{bmatrix}.\end{aligned} \tag{7.13}$$

In Eq. (7.13), we have used $|p_2^-\rangle$ obtained by setting $n = 2$ and $\delta = 2g^2/\Delta$ in Eq. (7.6). It is obtained as

$$|p_2^-\rangle = \frac{-\Delta\, |2_1 0_e 1_{\mathrm{ph}}\rangle + \sqrt{2}g\, |1_1 1_e 0_{\mathrm{ph}}\rangle}{\sqrt{\Delta^2 + 2g^2}}. \tag{7.14}$$

Defining $\eta_{\mathrm{eff}} = \eta/(\sqrt{\Delta + 2g^2/\Delta})$ and $\gamma_{\mathrm{eff}} = (\kappa\Delta + 2\gamma g^2)/(\Delta + 2g^2/\Delta)$, we obtain,

$$\lambda_\pm = \pm\sqrt{\eta_{\mathrm{eff}}^2 - \frac{\gamma_{\mathrm{eff}}^2}{16}} - i\frac{\gamma_{\mathrm{eff}}}{4}. \tag{7.15}$$

We will analyse these eigenvalues in the next section.

In the $n = 0$ and $n = 1$ subspaces, $|\eta| \ll |\epsilon^\pm_{n=0,1}|$ results in weak couplings mediated by $\hat{H}^{(\kappa,\gamma,\eta)}$ between the states $|0_1 0_e 0_{\mathrm{ph}}\rangle$ and $|1_1 0_e 0_{\mathrm{ph}}\rangle$ in $k = 0$ to the corresponding polariton states $|p_0^+\rangle$ and $|p_1^\pm\rangle$ in $k = 1$ respectively. These perturbative couplings shift the states $|0_1 0_e 0_{\mathrm{ph}}\rangle$ and $|1_1 0_e 0_{\mathrm{ph}}\rangle$ downward in energy, which up to third order in $\hat{H}^{(\kappa,\gamma,\eta)}$ are calculated as ΔE_0 and ΔE_1 respectively. They are given by (see Appendix C.1)

$$\Delta E_0 = -\frac{\eta^2}{\delta} - i\frac{\kappa\eta^2}{2\delta^2} \tag{7.16}$$

$$\Delta E_1 = -\frac{\eta^2}{\delta - g^2/\Delta} - \frac{i}{2}\left(\frac{\eta^2(\kappa\Delta^2 + \gamma g^2)}{\Delta^2(\delta - g^2/\Delta)^2}\right). \tag{7.17}$$

The energy corrections are obtained up to the first order in κ, γ. Note from Eqs. (7.16) and (7.17) that the states $|0_1 0_e 0_{\mathrm{ph}}\rangle$ and $|1_1 0_e 0_{\mathrm{ph}}\rangle$ also acquire a linewidth owing to the weak coupling to decaying states $|p_0^+\rangle$ and $|p_1^\pm\rangle$ respectively. The corrections to the states can be neglected as the energy contributions of the residual states are in second order of κ, γ. We will consider these energy shifts in the next section to write down the effective Hamiltonian.

7.2.3 Coupling from $\hat{H}^{(\Omega)}$ and effective Hamiltonian

In this section, we add the qubit coupling term $\hat{H}^{(\Omega)}$ which couples the states among different n subspaces. As shown in Fig. 7.2(c), $\hat{H}^{(\Omega)}$ couples the state $|0_1 0_e 0_{\text{ph}}\rangle$ with state $|1_1 0_e 0_{\text{ph}}\rangle$, and the state $|1_1 0_e 0_{\text{ph}}\rangle$ is further coupled to the states $|\chi_\pm\rangle$ in $n = 2$ subspace (recall from Eq. (7.15) the corresponding eigenvalues $\lambda_\pm$).

The goal of this section is to obtain the effective Hamiltonian as in Eq. (7.9), which is done in the following steps. (i) First we establish the limit $\Omega_0 \ll |\lambda_\pm|$ such that the coupling between $|1_1 0_e 0_{\text{ph}}\rangle$ and $|\chi_\pm\rangle$ is either strongly detuned or the states $|\chi_\pm\rangle$ are strongly decaying, preventing excitation of the system from $|1_1 0_e 0_{\text{ph}}\rangle$ to $|\chi_\pm\rangle$. We have from Eq. (7.15) the following two cases.

$$\eta_{\text{eff}} \begin{cases} (\text{case 1}) \ \geq \gamma_{\text{eff}}/4 \\ \implies |\lambda_-| = |\lambda_+| = \eta_{\text{eff}} \propto \sqrt{\Omega_0} \\ (\text{case 2}) \ < \gamma_{\text{eff}}/4 \\ \implies |\lambda_-| > |\lambda_+| = \gamma_{\text{eff}}/4 - \sqrt{\gamma_{\text{eff}}^2/16 - \eta_{\text{eff}}^2} \\ \implies |\lambda_+| \geq \frac{\gamma_{\text{eff}}}{4}\left(1 - \left(1 - \frac{8\eta_{\text{eff}}^2}{\gamma_{\text{eff}}^2}\right)\right) = \frac{2\eta_{\text{eff}}^2}{\gamma_{\text{eff}}} \propto \frac{\Omega_0}{\gamma_{\text{eff}}}. \end{cases} \tag{7.18}$$

In writing the proportionality in the two cases above, we assumed $\eta \propto \sqrt{\Omega_0}$. Later in Sec. 7.3 and Sec. 7.4, we show that an optimal choice of η^2/Ω_0 results in a minimum operational infidelity of W state preparation and CZ, C_2Z gates, respectively. Hence from Eq. (7.15) and Eq. (7.18) $\Omega_0/|\lambda_\pm| \to 0$ as $\Omega_0, \kappa, \gamma \to 0$. Note here that in the case of $\eta_{\text{eff}} \leq \gamma_{\text{eff}}/4$, $\lambda_\pm$ are purely imaginary and hence correspond to only the broadening of the states $|\chi_\pm\rangle$. In this limit, the blockade effect can be seen to be arising from a decay induced QZD-like effect instead of that arising from far-detuned transitions.

(ii) Secondly, in this limit, that is when $\Omega_0 \ll |\lambda_\pm|$, we have a weak coupling between $|1_1 0_e 0_{\text{ph}}\rangle$ and $|\chi_\pm\rangle$ in $n = 2$ subspace mediated by $\hat{H}^{(\Omega)}$, and as a result $|1_1 0_e 0_{\text{ph}}\rangle$ experiences an additional energy correction $\Delta E_1'$, and is weakly dressed giving state corrections which are first order in κ, γ. Let the dressed state be denoted by $\overline{|1_1 0_e 0_{\text{ph}}\rangle}$ (See Figs. 7.2(c)-(d)).

To obtain the energy and state corrections, we define the Hamiltonian in $n = 2$ subspace as $\hat{H}_{n=2}$ given by

$$\hat{H}_{n=2} = \hat{H}_{n=2}^{(\Delta,\delta,g)} + \hat{H}_{n=2}^{(\kappa,\gamma,\eta)} = \begin{bmatrix} 0 & -i\eta & 0 \\ i\eta & \delta - i\kappa/2 & \sqrt{2}g \\ 0 & \sqrt{2}g & \Delta - i\gamma/2 \end{bmatrix}. \tag{7.19}$$

The Hamiltonian matrix in Eq. (7.19) is written in the basis $\{|2_1 0_e 0_{\text{ph}}\rangle, |2_1 0_e 1_{\text{ph}}\rangle, |1_1 1_e 0_{\text{ph}}\rangle\}$. The energy corrections to state $|1_1 0_e 0_{\text{ph}}\rangle$ and the dressed state $\overline{|1_1 0_e 0_{\text{ph}}\rangle}$ are then obtained as

$$\begin{aligned} \Delta E_1' &= \langle 1_1 0_e 0_{\text{ph}}| \hat{H}^{(\Omega)} \left(\hat{H}_{n=2}\right)^{-1} \hat{H}^{(\Omega)} |1_1 0_e 0_{\text{ph}}\rangle \\ &= -\frac{\Omega_0^2}{2}(N-1) \langle 2_1 0_e 0_{\text{ph}}| \left(\hat{H}_{n=2}\right)^{-1} |2_1 0_e 0_{\text{ph}}\rangle \\ &= \frac{-i\Omega_0^2(N-1)}{2\eta^2} \left(\frac{\kappa}{2} + \frac{\gamma g^2}{\Delta^2}\right), \end{aligned} \tag{7.20}$$

$$\begin{aligned} \overline{|1_1 0_e 0_{\text{ph}}\rangle} &= |1_1 0_e 0_{\text{ph}}\rangle - \left(\hat{H}_{n=2}\right)^{-1} \hat{H}^{(\Omega)} |1_1 0_e 0_{\text{ph}}\rangle \\ &= |1_1 0_e 0_{\text{ph}}\rangle - \frac{i\sqrt{2(N-1)}\Omega^*}{4\eta^2} \left(\kappa + \frac{2g^2\gamma}{\Delta^2}\right) |2_1 0_e 0_{\text{ph}}\rangle. \end{aligned} \tag{7.21}$$

In evaluating Eqs. (7.20) and (7.21), we have used $\delta = 2g^2/\Delta$ from Eq. (7.12) and $\hat{H}^{(\Omega)} |1_1 0_e 0_{\text{ph}}\rangle = (\Omega^* \sqrt{N-1}/\sqrt{2}) |2_1 0_e 0_{\text{ph}}\rangle$. Note that $\hat{H}^{(\Omega)} |1_1 0_e 0_{\text{ph}}\rangle$ also has a component along $|0_1 0_e 0_{\text{ph}}\rangle$, which is not relevant for the calculation of $\Delta E_1'$.

Finally by combining the energy shifts ΔE_1 from Eq. (7.17) obtained from perturbative couplings mediated by $\hat{H}^{(\kappa,\gamma,\eta)}$, and $\Delta E_1'$ from Eq.(7.20) obtained from perturbative couplings mediated by $\hat{H}^{(\Omega)}$, we can write the energy of state $\overline{|1_1 0_e 0_{\text{ph}}\rangle}$ as

$$\begin{aligned} E_1 - \frac{i}{2}\Gamma_1 &= \Delta E_1 + \Delta E_1' \\ &= -\frac{\eta^2\Delta}{g^2} - \frac{i}{2}\left(\frac{\eta^2\Delta^2\kappa}{g^4} + \frac{\eta^2\gamma}{g^2} + \frac{(N-1)\Omega_0^2}{\eta^2}\left(\frac{\kappa}{2} + \frac{\gamma g^2}{\Delta^2}\right)\right) \end{aligned} \tag{7.22}$$

We obtain the energy of $|0_1 0_e 0_{\text{ph}}\rangle$ state as obtained in Eq. (7.16) as

$$E_0 - \frac{i}{2}\Gamma_0 = \Delta E_0 = -\frac{\eta^2\Delta}{2g^2} - \frac{i}{2}\left(\frac{\eta^2\Delta^2\kappa}{4g^4}\right) \tag{7.23}$$

Equation (7.22) and Eq. (7.23) summarize the main results of this section, providing the energies E_0 and E_1 of the effective two level system with states $|\mathcal{D}_0\rangle$ and $\overline{|\mathcal{D}_1\rangle}$, respectively, which scale as $\frac{\eta^2\Delta}{g^2}$. These equations also describe the corresponding effective linewidths Γ_0 and Γ_1, which depend on the loss rates κ and γ. Using the obtained values, we can now write the effective Hamiltonian restricted to the states $|0_1 0_e 0_{\mathrm{ph}}\rangle$ and $\overline{|1_1 0_e 0_{\mathrm{ph}}\rangle}$ as

$$\begin{aligned}\hat{H}'_{\mathrm{eff}} &= \left(E_0 - i\frac{\Gamma_0}{2}\right)|0_1 0_e 0_{\mathrm{ph}}\rangle\,\langle 0_1 0_e 0_{\mathrm{ph}}| \\ &+ \left(E_1 - i\frac{\Gamma_1}{2}\right)\overline{|1_1 0_e 0_{\mathrm{ph}}\rangle}\,\overline{|1_1 0_e 0_{\mathrm{ph}}\rangle} \\ &+ \frac{\sqrt{N}\Omega(t)}{2}\overline{|1_1 0_e 0_{\mathrm{ph}}\rangle}\,\langle 0_1 0_e 0_{\mathrm{ph}}| + \mathrm{h.c.}\end{aligned} \tag{7.24}$$

By tracing out the cavity field, which remains in the vacuum state $|0\rangle_{\mathrm{cav}}$ throughout the effective dynamics, and using the definitions $|0_1 0_e 0_{\mathrm{ph}}\rangle = |\mathcal{D}_0\rangle \otimes |0\rangle_{\mathrm{cav}}$ and $\overline{|1_1 0_e 0_{\mathrm{ph}}\rangle} = \overline{|\mathcal{D}_1\rangle} \otimes |0\rangle_{\mathrm{cav}}$, we obtain the effective Hamiltonian $\hat{H}_{\mathrm{eff}}$ in Eq. (7.9). This Hamiltonian describes a driven two-level system with states $|0_1 0_e 0_{\mathrm{ph}}\rangle$ and $\overline{|1_1 0_e 0_{\mathrm{ph}}\rangle}$.

7.3 Non-local W state preparation

In this section, we exploit the effective blockade dynamics to deterministically prepare the state $\overline{|\mathcal{D}_1\rangle}$, which approaches the W state $|\mathcal{D}_1\rangle$ in the limit $\kappa/g, \gamma/g \to 0$ (see Eq. (7.10)). Additionally, we derive an analytical expression for the state-preparation infidelity when $\kappa, \gamma \neq 0$. We recall the effective Hamiltonian $\hat{H}_{\mathrm{eff}}$ from Eq. (7.9) and Eqs. (7.23), (7.22) as

$$\begin{aligned}\hat{H}_{\mathrm{eff}} = &\left(-\frac{\eta^2\Delta}{2g^2} - \frac{i}{2}\Gamma_0\right)|\mathcal{D}_0\rangle\langle\mathcal{D}_0| + \left(-\frac{\eta^2\Delta}{g^2} - \frac{i}{2}\Gamma_1\right)\overline{|\mathcal{D}_1\rangle}\,\overline{\langle\mathcal{D}_1|} \\ &+ \frac{\sqrt{N}\Omega(t)}{2}\overline{|\mathcal{D}_1\rangle}\langle\mathcal{D}_0| + \frac{\sqrt{N}\Omega^*(t)}{2}|\mathcal{D}_0\rangle\overline{\langle\mathcal{D}_1|},\end{aligned} \tag{7.25}$$

where

$$\Gamma_0 = \frac{\kappa\eta^2\Delta^2}{4g^4} \tag{7.26}$$

$$\Gamma_1 = \eta^2\left(\frac{\kappa\Delta^2}{g^4} + \frac{\gamma}{g^2}\right) + \frac{(N-1)\Omega_0^2}{\eta^2}\left(\frac{\kappa}{2} + \frac{\gamma g^2}{\Delta^2}\right). \tag{7.27}$$

By going into a rotating frame given by $\hat{U} = \exp\left[i\left(-\frac{\eta^2\Delta}{2g^2}(|\mathcal{D}_0\rangle\langle\mathcal{D}_0| + \overline{|\mathcal{D}_1\rangle}\,\overline{|\mathcal{D}_1\rangle}) - \delta_{gl}\overline{|\mathcal{D}_1\rangle}\,\overline{\langle\mathcal{D}_1|}\right)t\right]$ and by choosing $\eta^2\Delta/(2g^2) = \delta_{gl}$ for resonant transfer, with $\Omega(t) = \Omega_0 e^{i\delta_{\mathrm{gl}}t}$ (with $\varphi(\Omega_0 t) = 0$), we obtain

$$
\begin{aligned}
\hat{H}_{\mathrm{eff}} = &-\frac{i}{2}\Gamma_0|\mathcal{D}_0\rangle\langle\mathcal{D}_0| + -\frac{i}{2}\Gamma_1\overline{|\mathcal{D}_1\rangle}\,\overline{\langle\mathcal{D}_1|} \\
&+ \frac{\sqrt{N}\Omega_0}{2}\overline{|\mathcal{D}_1\rangle}\langle\mathcal{D}_0| + \frac{\sqrt{N}\Omega_0}{2}|\mathcal{D}_0\rangle\overline{\langle\mathcal{D}_1|}.
\end{aligned}
\tag{7.28}
$$

In the absence of loss ($\Gamma_0 = \Gamma_1 = 0$), starting with initial state $|\mathcal{D}_0\rangle$ and by choosing a pulse of duration $T = \pi/(\sqrt{N}\Omega_0)$, the state $\overline{|\mathcal{D}_1\rangle} = |\mathcal{D}_1\rangle$ is prepared with unit fidelity. In the following, we obtain an analytical expression for the state preparation error in the presence of loss ($\Gamma_0, \Gamma_1 \neq 0$).

7.3.1 W state preparation fidelity calculation

In this section, we obtain the state-preparation error $1 - F$ of state $\overline{|\mathcal{D}_1\rangle}$ as

$$
1 - F = \frac{\pi}{2\sqrt{N}\Omega_0}\left(\Gamma_0 + \Gamma_1\right) \tag{7.29}
$$

$$
= \frac{\pi}{2\sqrt{N}}\left[\frac{\eta^2}{\Omega_0}\left(\frac{5\kappa\Delta^2}{4g^4} + \frac{\gamma}{g^2}\right) + \frac{(N-1)\Omega_0}{\eta^2}\left(\frac{\kappa}{2} + \frac{\gamma g^2}{\Delta^2}\right)\right]. \tag{7.30}
$$

In writing Eq. (7.30), the values of Γ_0 and Γ_1 are substituted from Eq. (7.26) and Eq. (7.27) respectively. Note that since we consider the population decay from the $|e\rangle$ state decaying outside of the computational subspace in our model, the fidelity estimate that we obtain here corresponds to a lower bound on the actual fidelity.

To derive Eq. (7.29), we rewrite $\hat{H}_{\mathrm{eff}} = \hat{H}_0 + \hat{H}_{\mathrm{nh}}$ with $\hat{H}_0 = (\sqrt{N}\Omega_0/2)\overline{|\mathcal{D}_1\rangle}\langle\mathcal{D}_0| + \mathrm{h.c.}$ and $\hat{H}_{\mathrm{nh}} = -i(\Gamma_0/2)|\mathcal{D}_0\rangle\langle\mathcal{D}_0| - i(\Gamma_1/2)\overline{|\mathcal{D}_1\rangle}\,\overline{\langle\mathcal{D}_1|}$. Let $\hat{U}_0(t)$ and $\hat{U}(t)$ be the time-evolution operators for time t under $\hat{H}_0$ and $\hat{H}_{\mathrm{eff}}$ respectively. For a duration T, up to first order in Γ_0, Γ_1, we have

$$
\hat{U}(T) = \hat{U}_0(T) - i\int_0^T \hat{U}_0(T)\hat{U}_0^\dagger(t)\hat{H}_{\mathrm{nh}}\hat{U}_0(t)dt. \tag{7.31}
$$

We define the fidelity F of the $\overline{|\mathcal{D}_1\rangle}$ state preparation as the squared overlap between the final state $|\psi(T)\rangle = \hat{U}(T)|\mathcal{D}_0\rangle$ and the target state $\overline{|\mathcal{D}_1\rangle}$. The infidelity $1 - F$ is given by

$$
1 - F = 1 - \left|\overline{\langle\mathcal{D}_1|}\hat{U}(T)|\mathcal{D}_0\rangle\right|^2. \tag{7.32}
$$

Using $\hat{U}(T)$ from Eq. (7.31) and defining $|\psi_0(t)\rangle = \hat{U}_0(t)|\mathcal{D}_0\rangle$, $1-F$ in Eq. (7.32) is obtained as

$$1 - F = \Gamma_0 \int_0^T dt\, |\langle \mathcal{D}_0|\psi_0(t)\rangle|^2 + \Gamma_1 \int_0^T dt \left|\overline{\langle \mathcal{D}_1|}\psi_0(t)\rangle\right|^2 . \tag{7.33}$$

The integrals $\int_0^T dt\, |\langle s|\psi_0(t)|^2$ in Eq. (7.33) denote the time spent in state $|s\rangle \in \{|\mathcal{D}_0\rangle, \overline{|\mathcal{D}_1\rangle}\}$ during the unitary evolution $\hat{U}_0$ under $\hat{H}_0$ of initial state $|\mathcal{D}_0\rangle$ for time T. In this case, both states $|\mathcal{D}_0\rangle$ and $\overline{|\mathcal{D}_1\rangle}$ are occupied for equal times $T/2$. Hence, with $T = \pi/(\sqrt{N}\Omega_0)$, we obtain $1-F$ as in Eq. (7.29).

The optimal values of η^2/Ω_0 and Δ that minimize $1-F$ in Eq. (7.30) are derived analytically as follows. First, $1-F$ is expressed as a function of the variable $x = \Delta^2$, such that $1 - F = f(x) = ax + x/b + c$. By setting its derivative $\dot{f} = 0$, the minimum value of $f(x)$ is found to be $(1-F)_{\min} = 2\sqrt{ab} + c$, occurring at $x = \sqrt{b/a} = (\Delta^2)_{\text{opt}}$. This result allows $(1-F)_{\min}$ to be further expressed in terms of η^2/Ω_0 as $(1-F)_{\min} = a'(\eta^2/\Omega_0) + b'/(\eta^2/\Omega_0) + c'$. Following a similar procedure, minimizing $(1-F)_{\min}$ with respect to η^2/Ω_0 yields the optimal value $1 - F_{\text{opt.}} = 2\sqrt{a'b'} + c'$ at $\left(\eta^2/\Omega_0\right)_{\text{opt.}} = \sqrt{b'/a'}$. These steps provide the optimal parameters

$$\Delta^W_{\text{opt.}} = \left(\frac{8}{5}\right)^{1/4} \sqrt{\frac{\gamma}{\kappa}} g, \tag{7.34}$$

$$\left(\frac{\eta^2}{\Omega_0}\right)^W_{\text{opt.}} = \sqrt{\frac{N-1}{2}\frac{\kappa}{\gamma}} g. \tag{7.35}$$

With the optimal values from Eq. (7.34) and Eq. (7.35), and by defining cooperativity $C = g^2/(\kappa\gamma)$, we finally obtain the state preparation error from Eq. (7.30) as

$$1 - F^W_{\text{opt.}} = \pi\sqrt{(1-1/N)(\sqrt{5/8} + 7/8)}/\sqrt{C} \approx \frac{5.73\sqrt{1-1/N}}{\sqrt{C}}. \tag{7.36}$$

In order to verify our effective model (Eq. (7.28)) and the analytic expression for the state preparation error (Eq. (7.36)), in Fig. 7.1(d), we numerically simulate the Schrödinger evolution under the full Hamiltonian (Eq. (7.3)), starting from the initial state $|0_1 0_e 0_{\text{ph}}\rangle = |\mathcal{D}_0\rangle \otimes |0\rangle_{\text{cav}}$. We plot the state populations dynamics of the states $|\mathcal{D}_0\rangle$, $|\mathcal{D}_1\rangle$ and $|\mathcal{D}_2\rangle$ along with the trace of density operator in the symmetric subspace (after tracing out the cavity mode) given by $\text{Tr}(\rho_{\text{symm.}}) = \sum_{n=0}^{N} |\langle \mathcal{D}_n|\mathcal{D}_n\rangle|^2$. These results are computed for $N = 2$ with single particle cooperativities $C = 10^2, 10^{10}$, keeping $\gamma/\kappa = 1$. Our results show that the state preparation infidelity - quantified by the final state population in $|\mathcal{D}_1\rangle$ (Eq. (7.32)) is primarily due to $\text{Tr}\,(\rho_{\text{symm}}) < 1$. This leakage out of the symmetric subspace, arising from non-zero decay rates Γ_0 and Γ_1 (due to non-zero κ, γ), is as predicted by our effective model in Eq. (7.28). Furthermore, in Fig. 7.1(e), we plot the state preparation infidelity $1 - F$ as a function of the total pulse duration T for $N = 2$ for different values of cooperativities C and different γ/κ ratios. These numerical results are compared against the analytical infidelity obtained in Eq. (7.36). In the limit $T \to \infty$, the numerical infidelity converges to the analytical estimate, scaling as $\propto 1/\sqrt{C}$ and independent of γ/κ for large C. Finally, in Fig. 7.1(f) we extend this analysis to a larger system with $N = 50$. Here we compare the analytic infidelity (Eq. (7.36)) in the $T \to \infty$ limit and compare it against the CZ ($N = 2$) and $\mathrm{C_2Z}$ ($N = 3$) gate errors which are discussed in Sec. 7.4. We find an excellent agreement between the numerical results from with the full Hamiltonian dynamics (Eq. (7.3)) and the analytic errors derived for large single-particle cooperativities C, which further validates our effective blockade dynamics.

Next, in order to show that our model accurately captures all error sources and correctly predicts the final state populations, we compute separately the contributions from decay of the $|e\rangle$ state (non-zero spontaneous emission rate γ), cavity decay rate (non-zero κ) and non-adiabatic drive effects, and then verify that their sum agrees with the total infidelity computed numerically. In Fig. 7.3(a), we show the error distribution as a function of T for $N = 2$, where the error due to decay of $|e\rangle$ state is computed as $\gamma \int_0^T \langle\psi(t)|\hat{n}_e|\psi(t)\rangle dt$ and the cavity decay error as $\kappa \int_0^T \langle\psi(t)|\hat{a}^\dagger\hat{a}|\psi(t)\rangle dt$; an additional error, due to non-adiabatic effects at short times, is obtained by setting $C \to \infty$. The sum of these three errors is in excellent agreement with the independently computed infidelity (indicated by the dashed-dotted line), confirming that our model accounts accurately for all the error sources for over finite T and as $T \to \infty$. The inset of Fig. 7.3(a) shows the final population $|\langle\psi_s|\psi(T)\rangle|^2$ in different states $|\psi_s\rangle$ for a range of total pulse duration gT for $N = 2$. The final population in all states $\to 0$ as $T \to \infty$ except for the target state $|1_1 0_e 0_{\mathrm{ph}}\rangle \equiv |\mathcal{D}_1\rangle \otimes |0\rangle_{\mathrm{cav.}}$ and states $|0_1 0_e 0_{\mathrm{ph}}\rangle, |2_1 0_e 0_{\mathrm{ph}}\rangle$ which have order one correction of amplitude in κ, γ in the final state $|\psi(T)\rangle$. Fig. 7.3(b) shows the final state populations in all the atomic-symmetric Dicke states $|\mathcal{D}_n\rangle \forall n = 0, \ldots N$ completing the atomic symmetric subspace with density operator $\rho_{\mathrm{symm.}} = \mathrm{Tr}_{\mathrm{cav.}}(|\psi(T)\rangle\langle\psi(T)|)$, for $N = 2$ and $N = 10$. The final population in $|\mathcal{D}_n\rangle$ then corresponds to $\langle\mathcal{D}_n|\rho_{\mathrm{symm.}}|\mathcal{D}_n\rangle$. The population leak into the states $|\mathcal{D}_0\rangle$ and $|\mathcal{D}_2\rangle$ is consistent with our analysis, being proportional to terms that are second order in κ and γ.

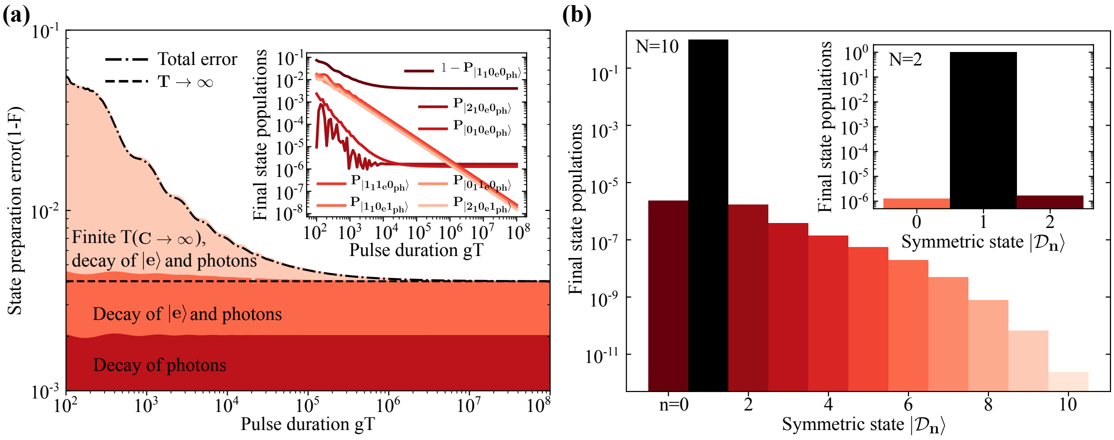

FIGURE 7.3: (a) W state preparation error for $N = 2$ as a function of the total operation time for $\kappa/g = 10^{-3}$, $\gamma/g = 10^{-3}$. The error due to the decay from $|e\rangle$ state, the error due to loss of photons and the error due to finite time (calculated in the limit $C \to \infty$) adds up to give the total error (dash-dot line). The dashed line is the analytical error given by $4.05/\sqrt{C}$ calculated in the limit $T \to \infty$. (a, inset) Final state population (in log-scale) in relevant states $|a_1 b_e m_{\mathrm{ph}}\rangle$ as a function of the pulse duration gT for the same parameters as in (a). The final state as $T \to \infty$ has non-vanishing components along the state $|0_1 0_e 0_{\mathrm{ph}}\rangle$ and $|2_1 0_e 0_{\mathrm{ph}}\rangle$ apart from the near-unity population in the target $|1_1 0_e 0_{\mathrm{ph}}\rangle$ state. (b) Final state populations (in log-scale) in the atomic symmetric Dicke states $|\mathcal{D}_n\rangle$ for $N = 10$ and $N = 2$ (inset) for $\kappa/g = 10^{-3}$, $\gamma/g = 10^{-3}$.

7.4 Non-local CZ and C_2Z gate implementation

In this section, we exploit the effective Hamiltonian derived in Eq. (7.9) to implement a CZ and a C_2Z gate with $N = 2$ and $N = 3$ distant atoms respectively. For this, each atom is modeled as a four-level system with states $\{|0\rangle, |1'\rangle, |1\rangle, |e\rangle\}$. We introduce an additional state $|1'\rangle$ with energy ω_1' such that the computational subspace is now spanned by the states $\{|0\rangle, |1'\rangle\}$ (See Fig. 7.1(c)). All other energies and couplings remain the same as described in Sec. 7.1.

We obtain the full Hamiltonian with the $|1'\rangle$ state as

$$\begin{aligned}\hat{H}_{\text{full}} &= \omega_1'\hat{n}_{1'} + \omega_0\hat{n}_0 + \omega_1\hat{n}_1 + (\omega_e - i\gamma/2)\hat{n}_e \\ &\quad + g\sum_{j=1}^{N}\left(|e_j\rangle\langle 1_j| + |1_j\rangle\langle e_j|\right)\left(\hat{a}^\dagger + \hat{a}\right) + \hat{H}_{\text{drive}} \\ &\quad + \sum_{j=1}^{N}\left(\Omega(t)\cos(\omega_{\text{gl}}t)|1_j\rangle\langle 0_j| + \text{h.c.}\right),\end{aligned} \tag{7.37}$$

with $\hat{n}_{1'} = \sum_{j=1}^{N}|1_j'\rangle\langle 1_j'|$. Transforming $\hat{H}_{\text{full}}$ under the rotating frame given by

$$\hat{U}(t) = \exp\Big\{\Big[i(\omega_L(\hat{a}^\dagger\hat{a} + \hat{n}_e) + \omega_1(\hat{n}_1 + \hat{n}_e) + \omega_0\hat{n}_0 + \omega_1'\hat{n}_{1'})t\Big]\Big\} \tag{7.38}$$

and in the rotating-wave approximation, we obtain the same starting Hamiltonian as in Eq. (7.3), and hence the same approach can be followed to arrive at an effective Blockade Hamiltonian as derived in Sec. 7.2. All additional eigenstates of $\hat{H}^{(\Delta,\delta,g)}$ with atoms in states $|0\rangle, |1'\rangle$- with no atoms in $|1\rangle$- acquire an energy shift similar to that for $|0_1 0_e 0_{\rm ph}\rangle$.

In Sections 7.4.1 and 7.4.2 below, we write down the effective Hamiltonians for implementing a CZ and C_2Z gate respectively. We simulate the gates using the time-optimal pulses found in Refs. [63, 64], and obtain optimal gate parameters for minimizing infidelity for both CZ and C_2Z gates. We also show that gate errors scale as $1/\sqrt{C}$ for both gates. We would like to note here that other optimal solutions for this gate protocol can be obtained more formally, for example by directly finding optimal pulses with the full Hamiltonian, which could in principle perform better for this system than the pulses from Refs. [63, 64].

7.4.1 CZ gate

In this section, we exploit the effective blockade hamiltonian obtained in Section 7.2 to implement a controlled-Z (CZ) gate between two distant atoms. For CZ gate, we consider the two- atom computational basis states $\{|1'1'\rangle, |1'0\rangle, |00\rangle\}$. For initial atom states $\{|1'1'\rangle, |1'0\rangle, |00\rangle\}$, the effective Hamiltonian acts in the subspace spanned by $\{|1'1'\rangle\}$, $\{|1'0\rangle, |1'1\rangle\}$ and $\{|00\rangle, |W\rangle\}$, respectively where $|W\rangle = (|01\rangle + |10\rangle)/\sqrt{2}$. In each of the three decoupled subspaces, we can write the effective Hamiltonian in the same way as in Eq. (7.9), but with N replaced by N_0, the number of atoms initialized in state $|0\rangle$. We denote the effective Hamiltonians in each of these subspaces as $\hat{H}_{1'1'}$, $\hat{H}_{1'0}$, and $\hat{H}_{00}$. Let the effective decay of the state with N_0 atoms initialized in state $|0\rangle$ be $\Gamma_1^{(N_0)}$ with

$$\Gamma_1^{(N_0)} = \frac{\eta^2\Delta^2\kappa}{g^4} + \frac{\eta^2\gamma}{g^2} + (N_0-1)\Omega_0^2\left(\frac{\kappa}{2\eta^2} + \frac{g^2\gamma}{\eta^2\Delta^2}\right). \tag{7.39}$$

We obtain up to single-qubit operations,

$$\begin{aligned}
\hat{H}_{1'1'} &= -\frac{i\Gamma_0}{2}|1'1'\rangle\langle 1'1'| \\
\hat{H}_{1'0} &= \left(\frac{\Omega(t)}{2}|1'1\rangle\langle 1'0| + \text{h.c}\right) + \frac{-i\Gamma_0}{2}|1'0\rangle\langle 1'0| \\
&\quad + -\frac{i\Gamma_1^{(1)}}{2}|1'1\rangle\langle 1'1| \\
\hat{H}_{00} &= \left(\frac{\sqrt{2}\Omega(t)}{2}|W\rangle\langle 00| + \text{h.c}\right) + -\frac{i\Gamma_0}{2}|00\rangle\langle 00| \\
&\quad + -\frac{i\Gamma_1^{(2)}}{2}|W\rangle\langle W|
\end{aligned} \tag{7.40}$$

Let $e^{i\xi_{N_0}}$ be the phases acquired from the evolution of each of the computational basis states $\{|1'1'\rangle, |1'0\rangle, |00\rangle\}$ with $N_0 = 0, 1, 2$ respectively. The evolution implements a CZ gate when $\xi_0 = 0$, $\xi_1 = \theta$ and $\xi_2 = 2\theta + \pi$ for a single-qubit phase θ. Hence up to single qubit phase gates acting on $|0\rangle$ state, a CZ operation can be realized exactly for $\Gamma_0, \Gamma_1 = 0$ by evolving the qubits under the effective Hamiltonian. We note that approach is similar to that used in Ref. [63] to implement a time-optimal CZ gate. In the presence of losses, by following a similar treatment as in Sec. 7.3.1, we can write the error of the CZ gate operation as

$$1 - F = \frac{1}{4\Omega}(\Gamma_0(\tau_{1'1'} + 2\tau_{1'0} + \tau_{00}) + 2\Gamma_1^{(1)}\tau_{1'1} + \Gamma_1^{(2)}\tau_W), \tag{7.41}$$

where τ_q is the dimensionless time spent in the state $|q\rangle$. The prefactor 2 with $\tau_{1'0}$ and $\tau_{1'1}$ is to take into account all states $|1'0\rangle, |01'\rangle$ and $|1'1\rangle, |11'\rangle$, respectively. By inserting the Γ values from Eq. (7.26) and Eq. (7.39), we find optimal values of Δ and Ω_0/η^2 which minimize the gate error for fixed g, γ, κ. The optimal values are given by

$$(\Delta)^{CZ}_{\text{opt.}} = \left(\frac{8(\tau_{1'1} + \tau_{1'0})}{\tau_{1'1'} + 2\tau_{1'0} + \tau_{00} + 4\tau_{1'1} + 4\tau_W}\right)^{1/4}\sqrt{\frac{\gamma}{\kappa}}g \tag{7.42}$$

$$\left(\frac{\Omega_0}{\eta^2}\right)^{CZ}_{\text{opt.}} = \sqrt{\frac{\frac{1}{16}(\tau_{1'1'} + 2\tau_{1'0} + \tau_{00} + 4\tau_{1'1} + 4\tau_W)\frac{\Delta^2\kappa}{g^4} + \frac{1}{4}(\tau_{1'1} + \tau_{1'0})\frac{\gamma}{g^2}}{\tau_W(\frac{\kappa}{2} + \frac{\gamma g^2}{\Delta^2})}} \tag{7.43}$$

The optimal values $(\Delta)^{CZ}_{\text{opt.}}$ and $\left(\frac{\Omega_0}{\eta^2}\right)^{CZ}_{\text{opt.}}$ can be computed by numerically obtaining the values of τ_q. For this, we solve the Schrodinger dynamics for the effective Hamiltonians $\hat{H}_{1'1'}, \hat{H}_{1',0}, \hat{H}_{00}$ with $\Gamma_0 = \Gamma_1^{(N_0)} = 0$ for total pulse duration T. We use $\Omega(t) = \Omega_0 \exp[i(\varphi(t\Omega_0)]$ with $\Omega_0 T = 7.612$, corresponding to the time-optimal solution for the blockade CZ gate for Rydberg qubits [63]. The phase $\varphi(t\Omega_0)$ is taken from the time-optimal pulse plotted in Fig. 7.1(g). We obtain $\tau_q = \Omega_0 \int_0^T |\langle q|\psi_s(t)\rangle|^2 dt$ where $|\psi_s(t)\rangle$ is the state at time t for initial state $|s\rangle$ in a given subspace. That is, $|s\rangle$ corresponds to the states $|1'1'\rangle, |1'0\rangle, |00\rangle$ for $|q\rangle$ associated with $\hat{H}_{1'1'}, \hat{H}_{1'0}, \hat{H}_{00}$ respectively.

By substituting the obtained optimal parameters, we get the gate error for $\Gamma_0 \neq \Gamma_1 \neq 0$ from Eq. (7.41) as

$$1 - F^{CZ}_{\text{opt.}} = 6.45\frac{1}{\sqrt{C}} \tag{7.44}$$

In Fig. 7.1(f) and Fig. 7.4(a), we numerically obtain the gate error by simulating the dynamics of the state $|\psi_{in}\rangle = (|1'1'\rangle + |1'0\rangle + |01'\rangle + |00\rangle)/2$ under the full Hamiltonian (Eq. (7.3)) for time T using the time-optimal pulse to obtain the final state $|\psi(T)\rangle$. We use $\Omega(t) = \Omega_0 \exp[i(\varphi(t\Omega_0) + \delta_{gl}t)]$ with $\delta_{gl} = \eta^2\Delta/(2g^2)$ (as discussed in Sec. 7.3), $\Omega_0 T = 7.612$ and the laser phase $\varphi(\Omega_0 t)$ corresponding to the time-optimal pulse as shown in Fig. 7.1(g). The expected final state under a CZ gate is $|\psi_f\rangle = (|1'1'\rangle +$

$e^{i\theta}|1'0\rangle + e^{i\theta}|01'\rangle + e^{i(2\theta+\pi)}|00\rangle)/2$ where θ is the single qubit phase. The single-qubit phase θ is optimized to minimize the gate error computed as $1 - F = |\langle\psi_f|\psi(T)\rangle|^2$. In Fig. 7.1(d), the obtained gate error is plotted as a function of cooperativity C for $gT = 10^8$. The numerical results (square markers) are independent of γ/κ ratio and for large C match excellently with the analytical estimate (dashed line) as obtained in Eq.(7.44). In Fig. 7.4(a), the gate error is plotted as a function of the total pulse duration gT for different values of cooperativities and linewidth ratios γ/κ. The dashed lines corresponds to the analytical error obtained in Eq. (7.44). We see that for large cooperativities, in the limit $T \to \infty$, the gate error converges to our analytical estimate which depends only on $C = g^2/(\kappa\gamma)$ and is independent of the ratio γ/κ.

In the next section, we naturally extend the application of the effective blockade Hamiltonian to implement a non-local C_2Z gate which acts on arbitrarily initialized $N = 3$ atoms.

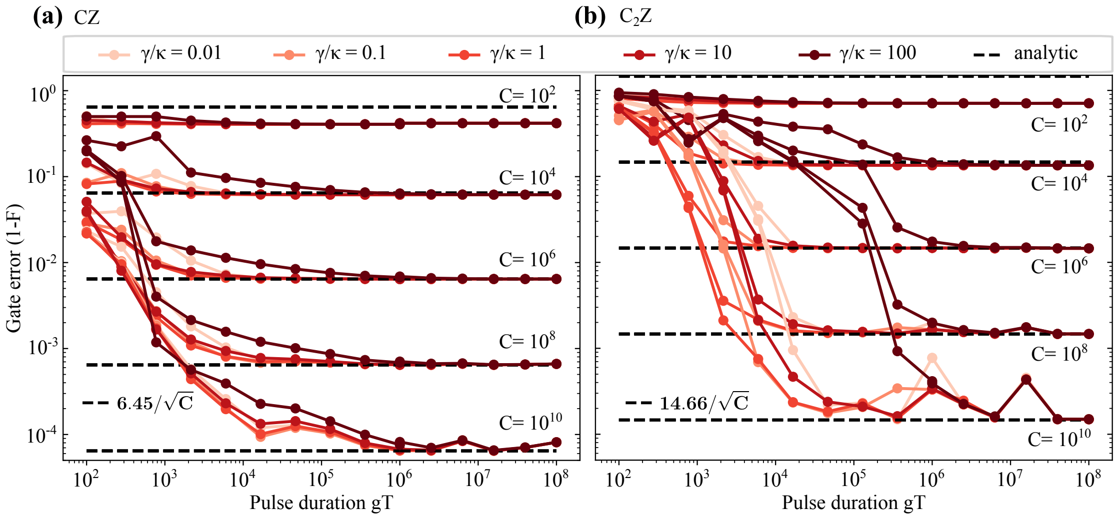

Figure 7.4: Gate error for as a function of the total operation time for (a) CZ gate and (b) C_2Z gate for $C = 10^2, 10^4, 10^6, 10^8, 10^{10}$ and $\gamma/\kappa = 0.01, 0.1, 1, 10, 100$. The infidelity converges to the analytical estimate (dashed lines) $1 - F \propto 1/\sqrt{C}$ (See text Sec. 7.4.1, 7.4.2) obtained in the limit $T \to \infty$.

7.4.2 C_2Z gate

In this section, similar to the CZ gate, we show the implementation of a C_2Z gate in the blockade regime with the time-optimal pulse shown in Fig. 7.1(h). Here, we consider three-atom computational states $\{|1'1'1'\rangle, |1'1'0\rangle, |1'00\rangle, |000\rangle\}$. The effective blockade Hamiltonians (up to single qubit gates) are obtained in each of the decoupled subspaces corresponding to these states respectively as

$$\begin{aligned}
\hat{H}_{1'1'1'} &= -\frac{i\Gamma_0}{2}|1'1'1'\rangle\langle 1'1'1'| \\
\hat{H}_{1'1'0} &= \frac{\Omega(t)}{2}\left(|1'1'0\rangle\langle 1'1'1| + \text{h.c}\right) - \frac{i\Gamma_0}{2}|1'1'0\rangle\langle 1'1'0| \\
&- \frac{i\Gamma_1^{(1)}}{2}|1'1'1\rangle\langle 1'1'1| \\
\hat{H}_{1'00} &= \frac{\sqrt{2}\Omega(t)}{2}\left(|1'00\rangle\langle 1'W| + \text{h.c}\right) - \frac{i\Gamma_0}{2}|1'00\rangle\langle 1'00| \\
&- \frac{i\Gamma_1^{(2)}}{2}|1'W\rangle\langle 1'W| \\
\hat{H}_{000} &= \frac{\sqrt{3}\Omega(t)}{2}\left(|000\rangle\langle W1| + \text{h.c}\right) - \frac{i\Gamma_0}{2}|000\rangle\langle 000| \\
&- \frac{i\Gamma_1^{(3)}}{2}|W1\rangle\langle W1|
\end{aligned} \tag{7.45}$$

where $|1'W\rangle = |1'\rangle \otimes |W\rangle$ and $|W1\rangle = (|001\rangle + |010\rangle + |100\rangle)/\sqrt{3}$.

Following a similar treatment as in Sec. 7.3.1, we can write the C_2Z gate error and the optimal parameters as

$$1 - F^{C_2Z}_{\text{opt.}} = \frac{1}{8\Omega_0}\left((\tau_{1'1'1'} + 3\tau_{1'1'0} + 3\tau_{1'00} + \tau_{1'1'1'})\Gamma_0 + 3\tau_{1'1'1}\Gamma_1^{(1)} + 3\tau_{1'W}\Gamma_1^{(2)} + \tau_{W1}\Gamma_1^{(3)}\right) \tag{7.46}$$

$$(\Delta)^{C_2Z}_{\text{opt.}} = \left(\frac{8t_B}{t_A}\right)^{1/4}\sqrt{\frac{\gamma}{\kappa}}g \tag{7.47}$$

$$\left(\frac{\eta^2}{\Omega_0}\right)^{C_2Z}_{\text{opt.}} = \sqrt{\frac{\frac{1}{8}(3\tau_{1'W} + 2\tau_{W1})(\frac{\kappa}{2} + \frac{\gamma g^2}{\Delta^2})}{\frac{1}{32}\frac{\Delta^2\kappa}{g^4}t_A + \frac{1}{8}\frac{\gamma}{g^2}t_B}}, \tag{7.48}$$

where $t_A = \tau_{1'1'1'} + 3\tau_{1'1'0} + 3\tau_{1'00} + \tau_{000} + 12\tau_{1'1'1} + 12\tau_{1'W} + 4\tau_{W1}$ and $t_B = 3\tau_{1'1'1} + 3\tau_{1'W} + \tau_{W1}$. We obtain the numerically calculated values τ_q as described in Sec. 7.4.1, here by using $\Omega(t) = \Omega_0 \exp[i(\varphi(t\Omega_0) + \delta_{gl}t)]$ with $\delta_{gl} = 0$, $\Omega_0 T = 10.809$ and $\varphi(t\Omega_0)$ corresponding to the time-optimal pulse for C_2Z gate as shown in Fig. 7.1(h). On substituting the τ_q values, we obtain

$$1 - F^{C_2Z}_{\text{opt.}} = 14.66\frac{1}{\sqrt{C}}. \tag{7.49}$$

In Figs 7.1(d) and 7.4(b), we numerically obtain the C_2Z gate error by simulating the dynamics of the state $|\psi_{in}\rangle = (|1'1'1'\rangle + |1'1'0\rangle + |01'1'\rangle + |1'01'\rangle + |1'00\rangle + |01'0\rangle + |001'\rangle + |000\rangle)/\sqrt{8}$ under the full Hamiltonian (Eq. (7.3)) for time T using the time-optimal pulse for C_2Z gate. That is, we use $\Omega(t) = \Omega_0 \exp[i(\varphi(t\Omega_0) + \delta_{gl}t)]$ with $\delta_{gl} = \eta^2\Delta/(2g^2)$ (as discussed in Sec. 7.3), $\Omega_0 T = 10.809$, and $\varphi(t\Omega_0)$ from the time-optimal pulse plotted in Fig. 7.1(h). Note that here the time-optimal pulse is designed such that the conditional phase is acquired by the state $|1'1'1'\rangle$, i.e. the expected final state under the C_2Z gate operation is $|\psi_f\rangle = (e^{i(3\theta+\pi)}|1'1'1'\rangle + e^{i2\theta}\left(|1'1'0\rangle + |01'1'\rangle + |1'01'\rangle\right) + e^{i\theta}\left(|1'00\rangle + |01'0\rangle + |001'\rangle\right) + |000\rangle)/\sqrt{8}$ [64], where θ is a single-qubit phase. For the final state $|\psi(T)\rangle$, the gate error or infidelity is calculated as $1 - F = |\langle\psi_f|\psi(T)\rangle|^2$.

Figure. 7.1(f) verifies the gate error scaling as a function of cooperativity C. The numerical points (triangles) obtained for different values of γ/κ have a good match with the analytical estimate (dashed line) obtained in Eq. (7.49) for large cooperativities which is independent of γ/κ. In Fig. 7.4(b), the gate error is plotted as a function of different total pulse duration gT for different ratios γ/κ and different cooperativities C. We see a general trend of the error decreasing with increasing T for all γ/κ ratios, and converging close to the analytical estimate (dashed line) depending only on C and independent of γ/κ.

In this section, we have seen the application of the blockade mechanism in implementing a non-local CZ and C_2Z gate between distant physical qubits. The effective blockade dynamics result in a differential evolution of the states with different number of atoms initialized in the $|0\rangle$ state corresponding to different initial computational qubit states with qubit subspace spanned by $\{|0\rangle, |1'\rangle\}$. In the next section, we give fidelity estimates for some realistic cavity QED parameters for neutral atom and molecular qubits.

7.5 Realistic fidelities for experiments with neutral atoms and molecules

In this section, we present some examples of experimental quantum computing platforms where the non-local excitation blockade can be implemented.

As a first example, we consider neutral atom systems of ^{87}Rb atoms coupled to a fiber Fabry-Perot optical cavity [198, 207, 208] similar to the cavity in Ref. [193]. We consider the states $|0\rangle = |5S_{1/2}\, F = 1\, m_F = 0\rangle$, $|1\rangle = 5^2S_{1/2}\, F = 2\, m_F = 0\rangle$, $|1'\rangle = |5^2S_{1/2}\, F = 2\, m_F = 1\rangle$ and $|e\rangle = |5^2P_{3/2}\, F = 3\, m_F = 0\rangle$ such that the D_2 transition line in ^{87}Rb with wavelength $\lambda = 780\,\text{nm}$ and $\gamma = 2\pi \times 6\,\text{MHz}$ corresponds to the cavity-coupled $|1\rangle \leftrightarrow |e\rangle$ transition. We consider a Fabry-Perot fiber cavity with finesse $\mathcal{F} \approx 2 \times 10^5$, waist radius $\omega_r \approx 2\,\mu\text{m}$, and $L = 40\,\mu\text{m}$ which gives $C = 3\lambda^2\mathcal{F}/(2\pi^3\omega_r^2) \approx 1500$, $g = \sqrt{3\lambda^2 c\gamma/(2\pi^2 w_r^2 L)} \approx 2\pi \times 400$ MHz and $\kappa = \pi C/L\mathcal{F} \approx 2\pi \times 20\,\text{MHz}$. With this system, the W state preparation with $N = 10$ atoms is achieved with fidelity $F = 86\%$ in time $T \approx 10^4/g = 4\,\mu\text{s}$. A CZ, C_2Z gate is realized in with fidelities $\approx 80\%, 69\%$ respectively in time $T = 10^4/g \approx 4\mu\text{s}$.

Secondly, we consider the case of achieving strong coupling by coupling Rydberg-Rydberg transitions with large electric dipole moments to a microwave on-chip resonator [209, 210]. Here we assume both $|1\rangle$ and $|e\rangle$ states as Rydberg states $|90^2P_{3/2}\rangle$ and $|90^2S_{1/2}\rangle$ in Cs respectively. We have $1/\gamma = 820\,\mu$s and also a non-negligible decay rate γ_1 of the $|1\rangle$ state given by $1/\gamma_1 = 2\,$ms. We have the transition frequency $\omega_e - \omega_1 = \omega_{1e} = 2\pi \times 5.03$ GHz and coupling strength $g \approx 2\pi \times 4\,$MHz[210]. Assuming an achievable quality factor of microwave resonator of $Q \approx 3\times 10^8$ [211], we have $\kappa = \omega_{1e}/Q = 2\pi \times 17\,$Hz corresponding to cavity photon lifetime $1/\kappa \approx 9.3\,$ms. With this system, we can hence achieve a cooperativity of $C \approx 5\times 10^9$. Incorporating the additional decay γ_1 of state $|1\rangle$, the effective decay of the target W state is modified as $\Gamma_1' = \Gamma_1 + \left(1 + \frac{\eta^2\Delta^2}{g^4} + \frac{(N-1)\Omega_0^2(1+g^2/\Delta^2)}{\eta^2}\right)\gamma_1$. The W-state preparation infidelity hence has an extra contribution proportional to $\gamma_1 T/2$, and diverges in the limit $T \to \infty$ after an initial decrease for finite T. With this system, a maximum fidelity of $F = 98.3\%$ is obtained for a pulse duration of $T \approx 930/g \approx 37\,\mu$s for $N = 10$ atoms. A CZ gate with infidelity $1 - F = 4.5 \times 10^{-3}$, is realized in time $T = 280/g \approx 11\,\mu$s, and a C_2Z gate with infidelity $1 - F = 7 \times 10^{-3}$ is realized in time $T = 530/g \approx 21\,\mu$s.

We note that the use of Rydberg states can be further leveraged by exciting them to maximal angular momentum states known as circular Rydberg states which have inherently long lifetimes of several seconds. It is possible to similarly couple transitions within circular Rydberg states (with principal quantum numbers of the order 50) to a high-quality Fabry-Perot microwave resonator with superconducting mirrors [212, 213]. The Rydberg atoms can be further trapped inside a micro structure such that the spontaneous emission from circular states is inhibited [214, 215] giving an increased lifetime of $\approx 100s$.

Another platform of interest is a system of cold polar molecules coupled to a superconducting high-Q stripline cavity. Here, we show the example of CaF molecules. We choose the states in the basis $|N, S, J, I, F, m_F\rangle$ as $|0\rangle = |0, 1/2, 1/2, 1/2, 0, 0\rangle$, $|1\rangle = |0, 1/2, 1/2, 1/2, 1, 0\rangle$ and $|e\rangle = |1, 1/2, 1/2, 1/2, 1, 0\rangle$. Here $\omega_e - \omega_1 = \omega_{1e} \approx 2\pi \times 21$ GHz and $\gamma < 10^{-2}\,$Hz [216] is negligible. A coupling strength of $g \approx 2\pi \times 10$ kHz for the $|1\rangle \leftrightarrow |e\rangle$ is achievable [217]. With a quality factor $Q \approx 3 \times 10^8$, $\kappa = \omega_{1e}/Q = 2\pi \times 70Hz$ corresponding to cavity-photon lifetime $1/\kappa \approx 2.3\,$ms. With this system, choosing $\Delta = 2\pi \times 50\,$kHz, a W state with $N = 10$ atoms can be prepared with 91% fidelity in time $T \approx 1.9\,$ms.

7.6 Conclusion and Outlook

We have presented a cavity polariton blockade mechanism in a cavity QED setup which is exploited for generation of a non-local multi-atom W-state and non-local CZ and C_2Z gates. The latter are obtained just by driving the cavity externally with a probe laser along with an additional global pulse acting on the atoms. A complete quantum mechanical treatment of the system, including the effects of spontaneous emission and cavity decay, allows to characterize the W-state preparation fidelity and the CZ, C_2Z gate errors as a function of the single particle cooperativity C. The errors are found to scale as $\mathcal{O}(C^{-1/2})$, moreover the error of N-atom W-state preparation saturates with N. We present the protocol results with example setups of neutral atoms coupled to a common optical cavity mode, and Rydberg atoms and cold polar molecules coupled to a common microwave mode. The former achieve the W state preparation for moderately sized systems of $N = 10$ in fast operation times of a few microseconds; while the latter achieve high state preparation fidelities.

Moreover, a cavity-QED setup with minimal control knobs- the cavity probe and global qubit pulse- supported by the current experimental progress with neutral atoms in optical cavities [198], can be used as a toolbox to prepare arbitrary many-qubit entangled states by employing optimal control techniques. These techniques can be tailored to prepare optimal states for quantum sensing [218], or increasingly complex entangled states optimized for quantum Fisher information, which is a subject of future work.

Chapter 8

Conclusion and outlook

In this thesis, we introduced a suite of novel protocols designed to implement a broad spectrum of non-local multi-qubit quantum gates and entanglement generation in systems where multiple quantum emitters couple to a shared bosonic mode, making our approach widely applicable to general cavity QED setups. The first two key protocols are the Geometric Phase Gate (GPG) and the Adiabatic Phase Gate (APG) protocols [54], for which we derived closed-form expressions for operation infidelities scaling as $\sim N/\sqrt{C}$ – as a function of qubit number N and cooperativity C – a key parameter characterizing any cavity QED system in the presence of losses from both emitters and cavity photons to the environment. These exact solutions are the first of their kind, and using them, we demonstrated the efficacy of one class of these protocols by achieving entanglement-enhanced quantum sensing. Specifically, we developed a noise-informed state preparation protocol to optimize entangled probe states for quantum sensing in noisy environments [173]. We also presented a cavity-polariton blockade protocol that facilitates W-state entanglement generation and holds promise for realizing time-optimal CZ and C_2Z gates within cavity QED frameworks [192]. All protocols rely on simple classical drives applied to the cavity mode, with some also utilizing global qubit pulses, eliminating the need for individual qubit drives. These approaches are designed for immediate implementation in state-of-the-art experiments, particularly those using cold atoms in tweezer arrays within cavities [55]. Importantly, the versatility of our protocols extends their applicability to a range of quantum systems, including Rydberg atoms, trapped ion chains, polar molecules, and superconducting qubits, as well as to various noise models in our noise-informed sensing protocol. This work provides a strong foundation for advancing both quantum information processing and entanglement-enhanced sensing across a range of experimental platforms, with significant implications for the NISQ era [219] and for quantum error correction (QEC) in the future.

There are several main implications of the GPG and APG protocols. While there are proposals for N-qubit Toffoli gates on qubits coupled via a cavity [35, 37], our protocols give the first native implementation for a large family of other multi-qubit gates. In particular, the GPG protocol introduces for the first time a way to implement geometric phase gates for more than two qubits on these systems, while APG protocol even allows for the implementation of native *arbitrary* phase gates without decomposing them into single- and two-qubit gates. This significantly enhances the prospect of realizing non-local stabilizers and quantum error correction schemes such as LDPC codes [108, 109] with reduced qubit overheads compared to current leading schemes, in particular if our protocols are parallelized in architectures that exploit multiple modes (e.g. frequency, polarization, spatial modes for overlapping cavities) as necessary for parallel operations to support QEC (see below). For near term applications, the GPG protocol enhances the toolbox for the generation of large high-fidelity entangled states such as GHZ states, while the arbitrary phase gates implementable by APG protocol are of significant interest for quantum simulation. All of these tasks can for the first time be accomplished without the need of an external drive of the qubits. Additionally, both protocols applied to just two qubits form, together with single qubit gates, a universal gate set for quantum computation. For Rydberg atoms or polar molecules coupled via a microwave cavity, we anticipate that our protocols can achieve two-qubit gate infidelities below 10^{-3} with realistic parameters. In the case of neutral atoms coupled via optical cavities, infidelities on the order of a few percent can be achieved, but with remarkably fast timescales – on the order of 10 ns for the GPG protocol and hundreds of nanoseconds for the APG protocol. These protocols may in principle also be applied to other leading qubit platforms for quantum computing that exploit delocalized boson modes, such as trapped ions coupled via a motional mode.

We expect that our protocols may significantly benefit from optimization of the time-dependent pulse-shape $\eta(t)$. In particular, while the infidelity for the various gates in the limit $T \to \infty$ is independent of the exact choice of η, we expect that the infidelity at finite T could be improved by applying quantum optimal control techniques to optimize the pulse-shape of $\eta(t)$ [171, 172], making our protocols both higher-fidelity and faster.

In a quantum computing architecture, our protocols could be applied in several manners, either as the only entangling gate of the architecture, or in conjunction with other, local, entangling protocols. For example, in an array of Rydberg atoms, entangling operations between nearby atoms could be performed using the Rydberg blockade mechanism, while entangling atoms further apart could be done with our protocols. It is also possible to use our protocols only for certain error correction tasks, while other entangling operations are done by local gates. Finally, our protocols could also be extended to overlapping cavities [59] to connect even more atoms.

The protocols, together with fast and reliable near neighbour gates may be integrated into an architecture to support fault tolerant quantum computation. For an application of non-local entangled states prepared using GPG protocol, consider a setup where each register qubit has one or more neighbouring ancillary qubits that are addressable. A useful primitive gate is the non-local measurement of a Pauli operator with support on a set of distantly separated register qubits $\{q_k\}$. This could be used for stabilizer measurements or a non-destructive Pauli measurement gate in an LDPC code for example, which has already been demonstrated in a recent work in Ref. [111]. Such measurements are proposed to be performed à la Shor [220] using a $|\mathrm{GHZ}\rangle$ on the set of ancilla $\{a_k\}$ neighbouring the $\{q_k\}$ and prepared via GPG protocol, so that the ancilla controlled gates targeting the register qubits would be spatially near neighbour. The usual $|\mathrm{GHZ}\rangle$ verification steps before the controlled operations would themselves be non-local, but they can be obviated using the Aliferis-DiVincenzo method [221]. In this procedure, errors in the $|\mathrm{GHZ}\rangle$ preparation (encoding) are be accounted for by unpreparing (decoding) the state, which is achievable non-locally since our method is unitary, and measuring the ancilla to infer errors which can be accounted for by adapting the Pauli frame of the computation.

The method above is particularly advantageous when measurements are slow and can be made fault tolerant by performing a second level repetition code on the ancilla. That is achievable via near neighbour controlled operations between the $\{a_k\}$ and a second set of neighbouring ancilla $\{b_k\}$ after the controlled operations acting on the $\{q_k\}$. A syndrome measurement compatible with a bit flip error in both ancilla sub-blocks implies a fault in the non-local encoding that propagated to the data register and can be accounted for in subsequent gates. Otherwise the error likely occured during the non-local decoding and the process can be repeated. Note an alternative method for non-local stabilizer measurments is to use flag qubits [222]. This uses fewer ancilla (as few as 2) but would require faster resets and k non-local CZ gates to measure a weight k non-local stabilizer. Using GPG protocol, for $C \gg 1$ the fidelity for preparing a $|\mathrm{GHZ}_k\rangle$ state vs. a circuit of k CZ gates are comparable but the time to prepare the former for a fixed fidelity is shorter, essentially independent of k, potentially favoring the former approach in this context.

An application of APG protocol is to perform non-local $\mathrm{C}_{N-1}\mathrm{Z}$ gates, which are locally equivalent to multi-controlled Toffoli gates, for majority voting circuits. These are frequently used e.g. in measurement free quantum error correction [189–191]. Even though for $N > 2$ the gate is not Clifford and our implementation is not fault tolerant, the gate *can* be used for fault tolerant quantum error correction when it involves controls that are ancilla that carry error syndrome data that is classical [189].

The GPG protocol, along with its exact solution of quantum dynamics in the presence of noise, combined with optimal control methods, opens the door to the preparation of metrologically useful optimal probe states that achieve a significant entanglement-enhanced advantage in quantum sensing beyond the standard quantum limit, even in the presence of noise [173]. This work introduces the first deterministic protocol for preparing entangled states in the symmetric Dicke subspace of N spins that are not only useful for sensing but also optimally robust in noisy environments, without introducing significant overhead in control complexity. Through this protocol, we demonstrate that a substantial quantum advantage in sensing—specifically in the measurement precision of weak external fields (quantified by the variance in estimated field strength)—can be achieved. The prepared optimal entangled probe states significantly surpass the standard quantum limit, and this advantage is realizable in near-term cold atom experiments in a deterministic, noise-robust manner with the application of just one or a few control pulses. While the results presented in this thesis are directly applicable to cutting-edge experiments with cold atoms trapped in tweezer arrays within cavities [55], we also anticipate that our noise-informed protocols can be extended to a variety of physical setups and noise models.

Lastly, a cavity polariton blockade mechanism in a cavity QED setup is exploited for the generation of a non-local multi-atom W-state, as well as non-local CZ and C_2Z gates [192]. These applications are realized by externally driving the cavity with a probe laser, along with an additional global pulse acting on the initialized atoms. A complete quantum mechanical treatment of the system, including the effects of spontaneous emission and cavity decay, allows for the characterization of the W-state preparation fidelity and the CZ, C_2Z gate errors as a function of cooperativity C. The errors are found to scale as $\mathcal{O}(C^{-1/2})$, and moreover, the error in N-atom W-state preparation saturates with N. With the availability of suitable energy levels, the applications can be generalized to any physical platform where a single common bosonic mode can couple the relevant transition. Furthermore, a cavity-QED setup with minimal control parameters – the cavity probe and global qubit pulse – can serve as a toolbox to prepare arbitrary many-qubit entangled states by employing optimal control techniques. These techniques can be tailored to prepare optimal states for quantum sensing [173], or increasingly complex entangled states optimized for quantum Fisher information.

For all protocol proposals throughout this thesis, we modeled each qubit as a three-level system and the cavity as a single bosonic mode. We expect that our protocols can be generalized to more complex models, such as those involving several excited states, a nonzero coupling from $|0\rangle$ to $|e\rangle$, or multiple bosonic modes (e.g., light modes of different polarizations) supported in the cavity. For instance, the derivations of both protocols can be extended in a straightforward manner to include the coupling of $|1\rangle$ to a second excited state, $|e'\rangle$. Such an additional coupling would only affect the phase θ in the GPG protocol, which implements $\hat{U}_A = e^{i\theta\hat{n}_1^2}$, where $\hat{n}_1$ represents the number operator counting the number of qubits in the $|1\rangle$ state. Additionally, it would modify the dependence of $\varphi(\hat{n}_1)$ on $\hat{n}_1$ in the APG protocol, which implements $\hat{U}_B = e^{i\varphi(\hat{n}_1)}$. Finding the optimal gate parameters and achievable fidelities for more general models of the qubit and cavity will be a subject of future work.

To conclude, cavity QED provides a critical quantum interface between light and matter, forming essential quantum interconnects that enable the reversible conversion of quantum states between physical systems. As such, these interconnects are fundamental to the realization of the quantum internet [223]. Therefore, the protocols proposed in this thesis make significant contributions to this endeavor, representing one of the key future directions stemming from this work.

Moreover, it is evident that the field of quantum computing – particularly with neutral atom-based systems – holds great promise. Atoms trapped in reconfigurable 2D or 3D arrays are at the forefront of this progress [185, 224–226]. Current advancements are focused on integrating these neutral atom architectures with cavity-based systems, enhancing their capabilities and paving the way for the realization of distributed quantum processors capable of scaling quantum computation beyond 10,000 physical qubits [227]. This modular approach would rely on high-fidelity remote entanglement distribution, enabling quantum computation to be spread across processors linked by fast, high-fidelity quantum network channels. Recent pioneering work has demonstrated the trapping of atoms in optical tweezers inside fiber-based optical cavities [55, 228, 229], facilitating direct coupling to photons in a well-defined mode.

The advancements presented in this thesis not only lay a foundation for the progress of quantum computing and entanglement-enhanced sensing across various experimental platforms, but also highlight the potential of leading quantum computing architectures based on neutral atom systems, by proposing the seamless integration of our simple protocols for multi-qubit operations. Most importantly, this work establishes the groundwork for realizing scalable and reliable quantum computing applications and sets the stage for the future quantum internet.

Appendix A

Appendix A: Supporting calculations for the Geometric Phase Gate protocol

A.1 First basis transformation on the cavity

Here we discuss the first time-dependent basis transformation on the subsystem of the cavity. For a function $\alpha(t)$ consider the displacement operator $D(\alpha(t)) = \exp\bigl(\alpha(t)\hat{a}^\dagger - \alpha^*(t)\hat{a}\bigr)$. Recall that it satisfies $D(\alpha)\hat{a}D(\alpha)^\dagger = \hat{a} - \alpha$ and $D(\alpha)\hat{a}^\dagger D(\alpha)^\dagger = \hat{a}^\dagger - \alpha^*$, and furthermore

$$\begin{aligned} \tfrac{\mathrm{d}}{\mathrm{d}t}D(\alpha) &= [\dot{\alpha}\hat{a}^\dagger - \dot{\alpha}^*\hat{a} + i\mathrm{Im}(\dot{\alpha}^*\alpha)]D(\alpha) \\ &= D(\alpha)[\dot{\alpha}\hat{a}^\dagger - \dot{\alpha}^*\hat{a} - i\mathrm{Im}(\dot{\alpha}^*\alpha)]. \end{aligned} \tag{A.1}$$

Now we define $\tilde{\rho} = D(\alpha)\rho D(\alpha)^\dagger$. It satisfies

$$\begin{aligned} \dot{\tilde{\rho}} &= -i(H'\tilde{\rho} - \rho(H')^\dagger) + L'\tilde{\rho}(L')^\dagger - \tfrac{1}{2}\{(L')^\dagger L', \tilde{\rho}\} \\ &+ \left(\tfrac{\mathrm{d}}{\mathrm{d}t}D(\alpha)\right) D(\alpha)^\dagger\tilde{\rho} + \tilde{\rho}D(\alpha)\left(\tfrac{\mathrm{d}}{\mathrm{d}t}D(\alpha)^\dagger\right) \end{aligned} \tag{A.2}$$

where $H' = D(\alpha)HD(\alpha)^\dagger$ and $L' = D(\alpha)LD(\alpha)^\dagger$.

We calculate

$$\begin{aligned} H' &= \delta\hat{a}^\dagger\hat{a} + (\Delta - i\gamma/2)\hat{n}_e + g(\hat{a}^\dagger\hat{S}^- + \hat{a}\hat{S}^+) \\ &+ (i\eta - \delta\alpha)\hat{a}^\dagger - (i\eta^* + \delta\alpha^*)\hat{a} + -g\alpha^*\hat{S}^- \\ &- g\alpha\hat{S}^+ + \delta|\alpha|^2 + i(\eta\alpha^* - \eta^*\alpha) \end{aligned} \tag{A.3}$$

$$\begin{aligned} L'\tilde{\rho}(L')^\dagger \quad & -\tfrac{1}{2}\{(L')^\dagger L, \tilde{\rho}\} = L\tilde{\rho}L^\dagger - \tfrac{1}{2}\{L^\dagger L, \tilde{\rho}\} + \\ & \tfrac{\kappa}{2}(-\alpha^*\hat{a}\rho - \alpha\rho\hat{a}^\dagger + \alpha^*\rho\hat{a} + \alpha\hat{a}^\dagger\rho) \end{aligned} \tag{A.4}$$

and

$$\left(\frac{\mathrm{d}}{\mathrm{d}t}D(\alpha)\right)D(\alpha)^\dagger\tilde{\rho}+\tilde{\rho}D(\alpha)\left(\frac{\mathrm{d}}{\mathrm{d}t}D(\alpha)^\dagger\right)=[\dot{\alpha}\hat{a}^\dagger-\dot{\alpha}^*\hat{a},\tilde{\rho}] \tag{A.5}$$

Plugging this into Eq. (A.2) gives

$$\dot{\tilde{\rho}}=-i\tilde{H}\tilde{\rho}+i\tilde{\rho}\tilde{H}^\dagger+L\rho L^\dagger-\frac{1}{2}\{L^\dagger L,\rho\} \tag{A.6}$$

with

$$\begin{aligned}\tilde{H} &= \delta\hat{a}^\dagger\hat{a}+(\Delta-i\gamma/2)\hat{n}_e+g(\hat{a}^\dagger\hat{S}^-+\hat{a}\hat{S}^+) \\ &- g\alpha^*\hat{S}^--g\alpha\hat{S}^++\Big[(i\eta-(\delta-i\kappa/2)\alpha+i\dot{\alpha})\hat{a}^\dagger+\text{h.c.}\Big]\end{aligned} \tag{A.7}$$

Now we take $\alpha(t)$ such that

$$\dot{\alpha}=-\eta-(i\delta+\kappa/2)\alpha \tag{A.8}$$

which is satisfied by

$$\alpha(t)=\int_0^t \mathrm{d}t'\eta(t')e^{-(i\delta+\kappa/2)(t-t')}. \tag{A.9}$$

With this choice, $\tilde{H}$ becomes simply

$$\tilde{H}=\delta\hat{a}^\dagger\hat{a}+(\Delta-i\gamma/2)\hat{n}_e+g(\hat{a}^\dagger\hat{S}^-+\hat{a}\hat{S}^+)-g\alpha^*\hat{S}^--g\alpha\hat{S}^+ \tag{A.10}$$

A.2 Second basis transformation on the qubits

We perform the time dependent basis transformation $\bar{H}=U\tilde{H}U^\dagger+i\dot{U}U^\dagger$ for

$$U=\exp\left[\frac{\lambda}{2}\left(-e^{i\mu}\hat{S}^++e^{-i\mu}\hat{S}^-\right)\right] \tag{A.11}$$

and

$$\tilde{H}=\delta\hat{a}^\dagger\hat{a}+(\Delta-i\gamma/2)\hat{n}_e+g\hat{a}^\dagger\hat{S}^-+g\hat{a}\hat{S}^+-g\alpha\hat{S}^+-g\alpha^*\hat{S}^-. \tag{A.12}$$

We calculate

$$\begin{aligned}U &= \Big[|0\rangle\langle 0|+\cos\left(\tfrac{\lambda}{2}\right)(|1\rangle\langle 1|+|e\rangle\langle e|) \\ &+ \sin\left(\tfrac{\lambda}{2}\right)\left(-e^{i\mu}|e\rangle\langle 1|+e^{-i\mu}|1\rangle\langle e|\right)\Big]^{\otimes N}\end{aligned} \tag{A.13}$$

which gives

$$\begin{aligned}U\hat{S}^+U^\dagger &= \left(U\hat{S}^-U^\dagger\right)^\dagger=\cos^2\left(\frac{\lambda}{2}\right)\hat{S}^+-e^{-2i\mu}\sin^2\left(\frac{\lambda}{2}\right)\hat{S}^- \\ &+ e^{-i\mu}\sin\left(\frac{\lambda}{2}\right)\cos\left(\frac{\lambda}{2}\right)(\hat{n}_1-\hat{n}_e),\end{aligned} \tag{A.14}$$

and

$$\begin{aligned} U\hat{n}_e U^\dagger &= \cos^2\left(\frac{\lambda}{2}\right)\hat{n}_e + \sin^2\left(\frac{\lambda}{2}\right)\hat{n}_1 \\ &+ \sin\left(\frac{\lambda}{2}\right)\cos\left(\frac{\lambda}{2}\right)\left(e^{-i\mu}\hat{S}^- + e^{i\mu}\hat{S}^+\right) \end{aligned} \tag{A.15}$$

Now first consider $H^{(0)} = \Delta\hat{n}_e - g\alpha\hat{S}^+ - g\alpha^*\hat{S}^-$, the part of $\tilde{H}$ that scales with Δ. We choose λ and μ so that $UH^{(0)}U^\dagger$ is diagonal. We find

$$\begin{aligned} U \quad H^{(0)}U^\dagger &= \left[\Delta\cos^2\left(\frac{\lambda}{2}\right) + \frac{g}{2}\left(\alpha e^{-i\mu} + \text{c.c.}\right)\sin\left(\lambda\right)\right]\hat{n}_e \\ + &\left[\Delta\sin^2\left(\frac{\lambda}{2}\right) - \frac{g}{2}\left(\alpha e^{-i\mu} + \text{c.c.}\right)\sin\left(\lambda\right)\right]\hat{n}_1 \\ + &\left[\frac{\Delta}{2}e^{i\mu}\sin\left(\lambda\right) + e^{2i\mu}\sin^2\left(\frac{\lambda}{2}\right)g\alpha^* - g\alpha\cos^2\left(\frac{\lambda}{2}\right)\right]\hat{S}^+ \\ + &\left[\frac{\Delta}{2}e^{-i\mu}\left(\lambda\right) + e^{-2i\mu}\sin^2\left(\frac{\lambda}{2}\right)g\alpha - g\alpha^*\cos^2\left(\frac{\lambda}{2}\right)\right]\hat{S}^- \end{aligned} \tag{A.16}$$

The coefficients of $\hat{S}^+$ and $\hat{S}^-$ vanish for $\mu = \arg(\alpha)$ and λ such that $\Delta\sin\left(\frac{\lambda}{2}\right)\cos\left(\frac{\lambda}{2}\right) = g\alpha(\cos^2\left(\frac{\lambda}{2}\right) - \sin^2\left(\frac{\lambda}{2}\right))$, which is satisfied for $\cos\lambda = \Delta/\sqrt{\Delta^2 + 4g^2|\alpha|^2}$. We denote by ε_- and ε_+ the coefficients of $\hat{n}$ and $\hat{n}_e$, respectively, and find

$$\begin{aligned} \varepsilon_- &= \Delta\sin^2\left(\frac{\lambda}{2}\right) - 2g|\alpha|\sin\left(\frac{\lambda}{2}\right)\cos\left(\frac{\lambda}{2}\right) \\ &= \frac{1}{2}\left(\Delta - \sqrt{\Delta^2 + 4g^2|\alpha|^2}\right) \end{aligned} \tag{A.17}$$

$$\begin{aligned} \varepsilon_+ &= \Delta\cos^2\left(\frac{\lambda}{2}\right) + 2g|\alpha|\sin\left(\frac{\lambda}{2}\right)\cos\left(\frac{\lambda}{2}\right) \\ &= \frac{1}{2}\left(\Delta + \sqrt{\Delta^2 + 4g^2|\alpha|^2}\right) \end{aligned} \tag{A.18}$$

Now we consider $\tilde{H} - H^{(0)} = \delta\hat{a}^\dagger\hat{a} - i\frac{\gamma}{2}\hat{n}_e + g\hat{a}\hat{S}^+ + g\hat{a}^\dagger\hat{S}^-$ and calculate $U(\tilde{H} - H^{(0)})U^\dagger$ term by term (the notation $\mathcal{O}(g)$ refers to the limit $\Delta/g \to \infty$).

$$U\hat{a}^\dagger\hat{a}U^\dagger = \hat{a}^\dagger\hat{a} \tag{A.19}$$

$$\begin{aligned} U \quad \hat{n}_e U^\dagger &= \frac{1 - \cos\lambda}{2}\hat{n}_1 + \frac{1 + \cos\lambda}{2}\hat{n}_e + \mathcal{O}(g)\hat{S}^+ + \mathcal{O}(g)\hat{S}^- \\ = \quad &\frac{\hat{n}_1 + \hat{n}_e}{2} - \frac{\Delta\left(\hat{n}_1 - \hat{n}_e\right)}{2\sqrt{\Delta^2 + 4g^2|\alpha|^2}} + \mathcal{O}(g)\hat{S}^+ + \mathcal{O}(g)\hat{S}^- \end{aligned} \tag{A.20}$$

$$U\hat{S}^+U^\dagger = \frac{\alpha^*}{\sqrt{\Delta^2 + 4g^2|\alpha|^2}}(\hat{n}_1 - \hat{n}_e) + \mathcal{O}(g)\hat{S}^+ + \mathcal{O}(g)\hat{S}^- \tag{A.21}$$

so that in total we find

$$\begin{aligned} U\tilde{H}U^\dagger &= \delta\hat{a}^\dagger\hat{a} + (\varepsilon_1 - i\gamma_1/2)\hat{n}_1 + (\varepsilon_e - i\gamma_e/2)\hat{n}_e \\ &+ (\zeta\hat{a}^\dagger + \zeta^*\hat{a})(\hat{n} - \hat{n}_e) + \mathcal{O}(g)\hat{S}^+ + \mathcal{O}(g)\hat{S}^- \end{aligned} \tag{A.22}$$

where

$$\gamma_\pm = \frac{\gamma}{2}\left(1 \pm \frac{\Delta}{\sqrt{\Delta^2 + 4g^2|\alpha|^2}}\right), \tag{A.23}$$

$$\zeta = \frac{g^2\alpha}{\sqrt{\Delta^2 + 4g^2|\alpha|^2}}. \tag{A.24}$$

Now using the fact that $i\dot{U}U^\dagger$ is $\mathcal{O}(g)$ and acts on the qubits only (i.e. contains no a or $a^\dagger$ terms) we obtain the expression (5) from the main text for $\bar{H}$.

A.3 Analytic solution of time evolution under $\hat{H}_{\text{eff}}$

In this section we find the analytic solution of the Lindblad equation $\dot{\rho} = -i\hat{H}\rho + i\rho\hat{H}^\dagger + L\rho\hat{L}^\dagger - \frac{1}{2}\{\hat{L}^\dagger\hat{L}, \rho\}$ under $\hat{H} = \delta\hat{a}^\dagger\hat{a} + (-i\gamma_1(t)/2 + \zeta(t)\hat{a}^\dagger + \zeta(t)^*\hat{a})\hat{n}_1$ and $\hat{L} = \sqrt{\kappa}\hat{a}$ for an arbitrary drive $\zeta(t)$ and time dependent decay rate $\gamma_1(t)$. For this, we assume an initial state $\rho(0) = |\beta_n(0)\rangle\langle\beta_m(0)| \otimes |q\rangle\langle q'|$, where β_n and β_m are coherent states and $|q\rangle(|q'\rangle)$ are computational basis states with $n(m)$ qubits in state $|1\rangle$. Note that initial states of this form are a basis of space of all possible initial density matrices, so solving the Lindblad equation for the initial state $\rho(0)$ suffices to solve it for an arbitrary initial state.

In the following we show that the solution to the Lindblad equation is given by

$$\rho(t) = e^{i\varphi_{nm}(t)}\frac{|\beta_n(t)\rangle\langle\beta_m(t)| \otimes |q\rangle\langle q'|}{\langle\beta_m(t)|\beta_n(t)\rangle} \tag{A.25}$$

where $\dot{\beta}_n = -(i\delta + \kappa/2)\beta_n - in\zeta$, i.e.

$$\beta_n(t) = \beta_n(0)e^{-(i\delta+\kappa/2)t} - in\int_0^t \mathrm{d}t'\zeta(t')e^{-(i\delta+\kappa/2)(t-t')} \tag{A.26}$$

and

$$\begin{aligned} \varphi_{nm}(t) &= \int_0^t \mathrm{d}t'\left[(m-n)(\zeta(t')\beta_m(t')^*\right. \\ &+ \left.\zeta(t')^*\beta_n(t')) + i(m+n)\gamma_1(t')/2\right]. \end{aligned} \tag{A.27}$$

Tracing out the cavity then gives the reduced density matrix $\rho_{\text{eff}} = e^{i\varphi_{nm}(t)} \left|q\right\rangle \left\langle q'\right|$ discussed in the main text.

To show Eq. (A.25), we make the Ansatz $\rho = \rho_{nm} \otimes \left|q\right\rangle \left\langle q'\right|$ with $\rho_{nm}(t) = c_{nm}(t) \left|\beta_n(t)\right\rangle \left\langle \beta_m(t)\right|$. The Lindblad equation gives

$$\dot{\rho}_{nm} = -i\hat{H}_n \rho_{nm} + i\rho \hat{H}_m^\dagger + \hat{L}\rho_{nm}\hat{L}^\dagger - \frac{1}{2}\{\hat{L}^\dagger L, \rho_{nm}\}, \tag{A.28}$$

with $\hat{H}_n = \delta \hat{a}^\dagger \hat{a} + (-i\gamma_1/2 + \zeta \hat{a}^\dagger + \zeta^* \hat{a})n$.

We start by calculating the left side of Eq. (A.28). It is a property of coherent states that

$$\frac{\mathrm{d}}{\mathrm{d}t} \left|\beta_n(t)\right\rangle = \dot{\beta}_n \hat{a}^\dagger \left|\beta_n\right\rangle - \frac{1}{2}\frac{\mathrm{d}|\beta_n|^2}{\mathrm{d}t} \left|\beta_n\right\rangle \tag{A.29}$$

so that

$$\begin{aligned} \dot{\rho}_{nm} &= c_{nm}\dot{\beta}_n \hat{a}^\dagger \left|\beta_n\right\rangle \left\langle \beta_m\right| + c_{nm}\dot{\beta}_m^* \left|\beta_n\right\rangle \left\langle \beta_m\right| \hat{a} \\ &+ \left(\dot{c}_{nm} - \frac{c_{nm}}{2}\frac{\mathrm{d}(|\beta_n|^2 + |\beta_m|^2)}{\mathrm{d}t}\right) \left|\beta_n\right\rangle \left\langle \beta_m\right| \end{aligned} \tag{A.30}$$

Now we evaluate the right side of Eq. (A.28):

$$\begin{aligned} \hat{H}_n \rho_{nm}/c_{nm} &= \Big[(\delta\beta_n + n\zeta)\, \hat{a}^\dagger \\ &+ n\zeta^*\beta_n - in\gamma_1/2] \left|\beta_n\right\rangle \left\langle \beta_m\right| \end{aligned} \tag{A.31}$$

$$\begin{aligned} \rho_{nm}\hat{H}_m^\dagger/c_{nm} &= [(\delta\beta_m^* + m\zeta^*)\, \hat{a} \\ &+ m\zeta\beta_m^* + im\gamma_1/2] \left|\beta_n\right\rangle \left\langle \beta_m\right| \end{aligned} \tag{A.32}$$

$$\hat{L}\rho_{nm}\hat{L}^\dagger/c_{nm} = \kappa\beta_n\beta_m^* \left|\beta_n\right\rangle \left\langle \beta_m\right| \tag{A.33}$$

$$\left\{\hat{L}^\dagger\hat{L}, \rho_{nm}\right\}/c_{nm} = \left[\kappa\beta_n\hat{a}^\dagger + \kappa\beta_m^*\hat{a}\right] \left|\beta_n\right\rangle \left\langle \beta_m\right| \tag{A.34}$$

Together, Eq. (A.32)-(A.34) give

$$\begin{aligned} & -i\hat{H}_n\rho_{nm} + i\rho_{nm}\hat{H}_m^\dagger + \hat{L}\rho_{nm}\hat{L}^\dagger - \frac{1}{2}\{\hat{L}_{nm}^\dagger\hat{L}, \rho_{nm}\} \\ = \;& c_{nm}(-i\delta\beta_n - in\zeta - \kappa\beta_n/2)\hat{a}^\dagger \left|\beta_n\right\rangle \left\langle \beta_m\right| \\ + \;& c_{nm}(i\delta\beta_m^* + im\zeta^* - \kappa\beta_m^*/2) \left|\beta_n\right\rangle \left\langle \beta_m\right| \hat{a} \\ + \;& c_{nm}(-in\zeta^*\beta_n + im\zeta\beta_m^* + \kappa\beta_n\beta_m^* \\ - \;& (n+m)\gamma_1/2) \left|\beta_n\right\rangle \left\langle \beta_m\right| \end{aligned} \tag{A.35}$$

Equating Eq. (A.31) and Eq. (A.35) gives Eq. (A.26), as well as

$$\begin{aligned} \dot{c}_{nm}/c_{nm} &= \frac{1}{2}\frac{\mathrm{d}(|\beta_n|^2 + |\beta_m|^2)}{\mathrm{d}t} \\ &- in\zeta^*\beta_n + im\zeta\beta_m^* + \kappa\beta_n\beta_m^* - (n+m)\gamma_1/2 \end{aligned} \tag{A.36}$$

Now we take $c_{nm} = e^{i\varphi_{nm}} / \langle \beta_m | \beta_n \rangle$. Using $\langle \beta_m | \beta_n \rangle = \exp\left(-\frac{1}{2}(|\beta_n|^2 + |\beta_m|^2) + \beta_m^* \beta_n\right)$ we obtain

$$\begin{aligned} i\dot{\varphi}_{nm} &= \frac{\dot{c}_{nm}}{c_{nm}} + \frac{\mathrm{d}}{\mathrm{d}t}\left(-\frac{1}{2}(|\beta_n|^2 + |\beta_m|^2) + \beta_m^* \beta_n\right) \\ &= -in\zeta^* \beta_n + im\zeta \beta_m^* + \kappa \beta_n \beta_m^* \\ &- (n+m)\gamma_1/2 + \dot{\beta}_m^* \beta_n + \beta_m^* \dot{\beta}_n \\ &= i(m-n)\zeta^* \beta_n + i(m-n)\zeta \beta_m^* - (n+m)\gamma_1/2 \end{aligned} \tag{A.37}$$

where in the last equality we inserted $\dot{\beta}_n = -(i\delta + \kappa/2)\beta_n - in\zeta$. Integrating Eq. (A.37) gives Eq. (A.28).

A.3.1 Calculation of the Fidelity in the limit $T \to \infty$

In the following we show that in the limit $T \to \infty$ and to first order in γ and κ the infidelity of the GPG protocol is given by

$$1 - F = \left(\frac{\kappa}{4(1+2^{-N})\delta} + \frac{\gamma\delta}{2g^2}\right) N\theta. \tag{A.38}$$

In the limit $T \to \infty$ the solution to $\dot{\beta}_n = -(i\delta + \kappa/2)\beta_n - in\zeta$ can be obtained by an adiabatic approximation. For this, we insert $\dot{\beta}_n = 0$ and obtain

$$\beta_n = \frac{-in\zeta}{i\delta + \kappa/2} \approx -\frac{n\zeta}{\delta}\left(1 + i\frac{\kappa}{2\delta}\right). \tag{A.39}$$

With Eq. (7) and (10) (main text) we obtain

$$\varphi_{nm} = (n^2 - m^2)\theta + (m-n)^2 \frac{i\kappa}{2\delta}\theta + i(m+n)\int_0^T \mathrm{d}t \gamma_1(t)/2 \tag{A.40}$$

where $\theta = \frac{1}{\delta}\int_0^T \mathrm{d}t |\zeta(t)|^2$. Since in the limit $T \to \infty$ we have $\zeta \to 0$ we approximate

$$\gamma_1 = \frac{\gamma}{2}\left(1 - \sqrt{1 - 4|\zeta|^2/g^2}\right) \approx \frac{\gamma|\zeta|^2}{g^2} \tag{A.41}$$

so that

$$\frac{\varphi_{nm}}{\theta} = n^2 - m^2 + (m-n)^2 \frac{i\kappa}{2\delta} + (m+n)\frac{i\gamma\delta}{2g^2} \tag{A.42}$$

Inserting this into Eq. (22) (main text) and using that

$$\sum_{n,m=0}^{N} \binom{N}{n}\binom{N}{m}(m-n)^2 = 4^N \frac{N}{2} \tag{A.43}$$

and

$$\sum_{n=0}^{N} \binom{N}{n} (n+n) = 2^N N, \tag{A.44}$$

$$\sum_{n,m=0}^{N} \binom{N}{n}\binom{N}{m} (n+m) = 4^N N, \tag{A.45}$$

we obtain Eq. (A.38).

A.4 Effects of coupling inhomogeneities on the fidelity

In this section we calculate the effect different couplings $g_1, ..., g_N$ of each qubit to the cavity on the gate fidelity. We assume that the $g_1, ..., g_N$ are independent and identically distributed random variables and have the quadratic mean $\bar{g} = \sqrt{\mathbb{E}[g_j^2]}$. Furthermore assume that the drive $\eta(t)$, and thus $\alpha(t)$, is chosen as given in the main text, with the homogeneous coupling g replaced by $\bar{g}$.

To be able to obtain analytical solutions we restrict ourselves to the case $T \to \infty$, but expect a similar scaling for finite T.

Following the same steps as in the main text, an effective Hamiltonian can be found as

$$\hat{H}_{\text{eff}} = \delta a^\dagger a + \sum_{q \in \{0,1\}^N} (\zeta_q a^\dagger + \zeta_q^* a) \left|q\right\rangle \left\langle q\right| \tag{A.46}$$

where

$$\zeta_q = \sum_{j=1}^{N} q_j \frac{g_j^2 \alpha}{\sqrt{4 g_j^2 |\alpha|^2 + \Delta^2}} \approx \frac{\alpha}{\Delta} \sum_{j=1}^{N} q_j g_j^2 \tag{A.47}$$

where the last approximation holds in the $T \to \infty$ limit, where $|\alpha| \ll \Delta$.

Starting in the initial state $|\psi(0)\rangle = |0\rangle \otimes |q\rangle$ for a computational basis state $q \in \{0,1\}^N$, the state at the final time T is given by $|\psi(T)\rangle = e^{i\varphi_q(T)} |\beta_q\rangle \otimes |q\rangle$, where $\dot{\beta}_q = -i\delta\beta_q - i\zeta_q$ and $\dot{\varphi}_q = -\mathrm{Re}(\zeta_q^* \beta_q)$. In the limit $T \to \infty$ we obtain $\beta_q(t) = -\zeta_q(t)/\delta$ and

$$\begin{aligned}
\varphi_q(T) &= \left(\sum_j q_j g_j^2\right)^2 \int_0^T \mathrm{d}t \frac{|\alpha(t)|^2}{\Delta\delta} \qquad (A.48)\\
&= \left(\sum_j q_j g_j^2\right)^2 \frac{\theta}{\bar{g}^4}\\
&\approx n\theta^2 + \frac{2n\theta}{\bar{g}^2} \sum_j q_j (g_j^2 - g^2)
\end{aligned}$$

where $n = \sum_j q_j$ is the number of qubits in state $|1\rangle$. Crucially, $\beta_q(T) = 0$, so that the action of the gate can still be described by a unitary operation, given by $U = \sum_q e^{i\varphi_q(T)} |q\rangle \langle q|$. In the following, we will evaluate the averaged fidelity for the difference $U_A^\dagger U$ between the gate U_A which we aim to implement, and the gate U which is actually implemented.

The averaged fidelity can be evaluated as [168]

$$\begin{aligned} 1 - F &= \frac{1}{2^N(2^N+1)} \left(2^N + \left| \sum_{q \in \{0,1\}^N} e^{i(\varphi_q(T) - n\theta^2)} \right|^2 \right) \\ &\approx 1 + \frac{1}{2^N(2^N+1)} \left[\left(\sum_q (\varphi_q - n^2\theta) \right)^2 \right. \\ &- \left. 2^N \sum_q (\varphi_q - n^2\theta)^2 \right] \end{aligned} \tag{A.49}$$

We obtain the upper bounds

$$1 - F \le \frac{1}{2^N} \sum_q (\varphi_q - n^2\theta)^2 \tag{A.50}$$

$$= \frac{4\theta^2}{\bar{g}^4} \frac{1}{2^N} \sum_{q \in \{0,1\}^N} \left(n \sum_j q_j (g_j^2 - \bar{g}^2) \right)^2$$

The expected value of the infidelity can be upper bounded, using the independence of the g_j, as

$$\mathbb{E}[1 - F] \le \frac{4\theta^2}{\bar{g}^4} \sum_q n^2 \sum_j q_j^2 \mathbb{E}[(g_j^2 - \bar{g}_j^2)^2] \tag{A.51}$$

$$= \frac{4\theta^2}{\bar{g}^4} \mathrm{Var}[g_1^2] \frac{1}{2^N} \sum_{n=0}^{N} \binom{N}{n} n^3 \tag{A.52}$$

$$= N^2(N+3) \frac{\theta^2}{2\bar{g}^4} \mathrm{Var}[g_1^2]. \tag{A.53}$$

Note that since we assume that the g_j are independent and indetically distributed, the $\mathrm{Var}[g_1^2]$ can be replace by $\mathrm{Var}[g_j^2]$ for any j.

A.5 Generation of GHZ states

In the following, we show that a GHZ state can be generated by applying $\hat{U}_A$ with $\theta = \pi/2$ to $|+\rangle^{\otimes N}$, followed by the three single qubit gates $\hat{U}_1 = \exp(i\pi\sigma_z/4)$, $\hat{U}_2 =$

$(\sigma_x+\sigma_z)/\sqrt{2}$ and $\hat{U}_3 = \exp(i\pi(N+1)\sigma_z/(4N))$. For this, we proceed in two steps. First, we show that $|\psi\rangle = \hat{U}_1^{\otimes N}\hat{U}_A\,|+\rangle^{\otimes N}$ is the graph state of the complete graph with N vertices. Then we employ the known result that this graph state is equivalent to a GHZ state up to global single qubit gates [166, 167] to explicitly find $\hat{U}_2$ and $\hat{U}_3$ to convert the graph state to the GHZ state.

To see that $|\psi\rangle$ is this graph state, we calculate that (up to an irrelevant global phase)

$$\begin{aligned}\hat{U}_1^{\otimes N}\hat{U}_A &= \exp(-i\pi\hat{n}_1/2)\exp\bigl(i\pi\hat{n}_1^2/2\bigr) \\ &= \exp\left(i\pi\sum_{j<k}\hat{n}_1^{(j)}\hat{n}_1^{(k)}\right)\end{aligned} \tag{A.54}$$

where $\hat{n}_1^{(j)}$ is the single qubit operator $|1\rangle\langle 1|$ on qubit j, so that $\hat{n}_1 = \sum_{j=1}^{N}\hat{n}_1^{(j)}$. Thus, $\hat{U}_1^{\otimes N}\hat{U}_A$ applies a CZ gate simultaneously on each qubit pair. Hence, the state $|\psi\rangle$ is indeed the graph state of the complete graph with N vertices

To convert $|\psi\rangle$ into a GHZ state, we use that $|\psi\rangle$ is stabilized by the N independent stabilizers

$$\hat{S}_1 = \sigma_x\otimes\sigma_z\otimes\ldots\otimes\sigma_z \tag{A.55}$$

$$\hat{S}_2 = \sigma_z\otimes\sigma_x\otimes\sigma_z\otimes\ldots\otimes\sigma_z \tag{A.56}$$

$$\vdots$$

$$\hat{S}_N = \sigma_z\otimes\ldots\otimes\sigma_z\otimes\sigma_x \tag{A.57}$$

i.e. it satisfies $\hat{S}_k\,|\psi\rangle = |\psi\rangle$ for each k. Thus, $\hat{U}_2^{\otimes N}\,|\psi\rangle$ is stabilized by $\hat{U}_2^{\otimes N}\hat{S}_k U_2^{\otimes N}$ (note that $\hat{U}_2^\dagger = \hat{U}_2$). A direct calculation shows that also the state

$$|\mathrm{GHZ}_\alpha\rangle = (|0...0\rangle + e^{i\alpha}\,|1...1\rangle)/\sqrt{2} \tag{A.58}$$

with $\alpha = \pi(N+1)/2$ is stabilized by the $\hat{U}_2^{\otimes N}\hat{S}_k\hat{U}_2^{\otimes N}$. Hence, we conclude $\hat{U}_2^{\otimes N}\,|\psi\rangle = |\mathrm{GHZ}_\alpha\rangle$, up to an irrelevant global phase. A GHZ state can now be generated by applying $\hat{U}_3^{\otimes N}$ to $\hat{U}_2^{\otimes N}\,|\psi\rangle$ to convert $|\mathrm{GHZ}_\alpha\rangle$ to the GHZ state.

Another way to see this is to write $\hat{U}_A = e^{i\frac{\pi}{2}\hat{n}_1^2} = e^{i\frac{\pi}{2}(N\hat{S}^z + (\hat{S}^z)^2)}$. Since $\hat{U}_A$ is permutation symmetric, if we start in the symmetric state $|+\rangle^{\otimes N}$ then we stay in the maximally symmetric subspace of the spins with total spin $S = N/2$ spanned by the Dicke states $\{|M\rangle\}$ for $M = -N/2,\ldots,N/2$. The action of $\hat{U}_A$ on this space is $\hat{U}_A\,|M\rangle = e^{i\frac{\pi}{2}M(N+M)}\,|M\rangle$. For $N = 2\ell$ (even), then up to a global phase the action on this space is $\hat{U} = e^{(-1)^{\ell+1}i\frac{\pi}{4}(\hat{P}^+-\hat{P}^-)}$, where $\hat{P}^\pm$ is the projector onto states with even(odd) Hamming weight. Writing the parity operator $\sigma_z^{\otimes N} = \hat{P}^+ - \hat{P}^-$ we have

$\hat{U}_A = e^{(-1)^{\ell+1} i \frac{\pi}{4} \sigma_z^{\otimes N}}$. We see that applying the uniform Hadamard gate afterward prepares the GHZ state up to a local phase gate

$$\begin{aligned} \hat{H}^{\otimes N} \hat{U}_A \left|+\right\rangle^{\otimes N} &= H^{\otimes N} \hat{U}_A \hat{H}^{\otimes N} \left|0\right\rangle^{\otimes N} \\ &= e^{(-1)^{\ell+1} i \frac{\pi}{4} \sigma_x^{\otimes N}} \left|0\right\rangle^{\otimes N} \\ &= (\left|0 \dots 0\right\rangle - i^{N+1} \left|1 \dots 1\right\rangle)/\sqrt{2}. \end{aligned} \tag{A.59}$$

A similar argument follows for N odd.

Appendix B

Appendix B: Supporting calculations for the Adiabatic Phase Gate protocol

B.1 Eigenenergies of $\hat{H}$ in perturbation theory

In this section we calculate perturbations of the eigenenergies of $\hat{H}$ in the limit $\eta \to 0$. To find the eigenenergy for a computational basis state $|q\rangle$ with n qubits in state $|1\rangle$ it is sufficient to consider the three states $|0,q\rangle$, $|1,q\rangle$ and $|\chi\rangle = \hat{S}^{+}|0,q\rangle/\sqrt{n}$, where the first entry in a ket vector denotes the number of excitations in the cavity mode, and the second entry denotes the state of the qubits. Projected onto these three states, $\hat{H}$ is given by

$$\begin{aligned} \hat{H} &= \underbrace{\delta\,|1,q\rangle\langle 1,q| + \Delta\,|\chi\rangle\langle\chi| + g\sqrt{N}(|1,q\rangle\langle\chi| + |\chi\rangle\langle 1,q|)}_{\hat{H}_0} \\ &+ \underbrace{i\eta\,|1,q\rangle\langle 0,q| - i\eta^{*}\,|0,q\rangle\langle 1,q|}_{\hat{V}} \end{aligned} \tag{B.1}$$

Denote by $|p_\pm\rangle$ the eigenstates of $\hat{H}_0$ and by $E_\pm$ their corresponding energies. The second order perturbation of the eigenenergy of $|0,q\rangle$ is

$$\begin{aligned} \varepsilon_n &= -\sum_j \frac{|\langle 0,q|\,\hat{V}\,|p_j\rangle|^2}{E_j} \\ &= -\eta^2\,\langle 1,q|\,H_0^{-1}\,|1,q\rangle \\ &= -\frac{|\eta|^2\Delta}{\Delta\delta - ng^2} \end{aligned} \tag{B.2}$$

The corresponding eigenstate is

$$|\psi_q(t)\rangle = |0,q\rangle - i\frac{\eta(t)\left(\Delta\,|1,q\rangle - g\sqrt{n}\,|\chi\rangle\right)}{\Delta\delta - ng^2} \tag{B.3}$$

B.2 Effect of losses

In this section we calculate process $\mathcal{E}$ of the adiabatic phase gate protocol to first order in γ and κ in the adiabatic limit. We assume an initial state $\rho(0) = |0,q\rangle\langle 0,q'|$. Let $U(t)$ be unitary evolution in the absence of noise, and let $\tilde{\rho}(t) = \hat{U}(t)^\dagger \rho(t)(t)$. Then

$$\begin{array}{rcl} \dot{\tilde{\rho}} & = & -\frac{\gamma}{2}\hat{U}^\dagger \hat{n}_e \hat{U}\tilde{\rho} - \frac{\gamma}{2}\tilde{\rho}\hat{U}^\dagger \hat{n}_e \hat{U} + \kappa \hat{U}^\dagger \hat{a}\hat{U}\tilde{\rho}\hat{U}^\dagger \hat{a}^\dagger U \\ & - & \frac{\kappa}{2}\hat{U}^\dagger \hat{a}^\dagger \hat{a}\hat{U}\tilde{\rho} - \frac{\kappa}{2}\tilde{\rho}\hat{U}^\dagger \hat{a}^\dagger \hat{a}\hat{U} \end{array} \tag{B.4}$$

To first order in γ and κ we thus find using the adiabatic approximation $\hat{U}(t)\,|0,q\rangle = e^{-i\varphi_n(t)}\,|\psi_q(t)\rangle$ with $\varphi_n(t) = \int_0^t \mathrm{d}t' \varepsilon_n(t')$ that

$$\begin{array}{rcl} \tilde{\rho}(T) & = & |0,q\rangle\langle 0,q'| \\ & + & \displaystyle\int_0^T \mathrm{d}t\Big[-\frac{1}{2}e^{-i\varphi_n(t)}\hat{U}^\dagger(t)(\gamma\hat{n}_e + \kappa\hat{a}^\dagger\hat{a})\,|\psi_q(t)\rangle\langle 0,q'| \\ & - & \displaystyle\frac{1}{2}e^{i\varphi_m(t)}\,|0,q\rangle\langle\psi_{q'}(t)|\,(\gamma\hat{n}_e + \kappa\hat{a}^\dagger\hat{a})\hat{U}(t) \\ & + & \kappa e^{-i(\varphi_n(t)-\varphi_m(t))}\hat{U}^\dagger(t)\hat{a}\,|\psi_q(t)\rangle\langle\psi_{q'}(t)|\,\hat{a}^\dagger\hat{U}(t)\Big] \end{array} \tag{B.5}$$

We obtain

$$\begin{array}{rcl} c_{nm} & := & e^{i(\varphi_n(t)-\varphi_m(t))}\,\langle q|\,\mathcal{E}(|q\rangle\langle q'|)\,|q'\rangle \\ & = & \displaystyle\sum_{k=0}^{\infty}\langle k,q|\,\tilde{\rho}(T)\,|k,q'\rangle \end{array} \tag{B.6}$$

Up to second order in η only terms with $k = 0$ contribute, so we obtain

$$\begin{array}{rcl} c_{nm} & = & 1 + \int_0^T \mathrm{d}t - [\frac{1}{2}\langle\psi_q(t)|\,(\gamma\hat{n}_e + \kappa\hat{a}^\dagger\hat{a})\,|\psi_q(t)\rangle \\ & - & \frac{1}{2}\langle\psi_q'(t)|\,(\gamma\hat{n}_e + \kappa\hat{a}^\dagger\hat{a})\,|\psi_q'(t)\rangle \\ & + & \kappa\,\langle\psi_q(t)|\,\hat{a}\,|\psi_q(t)\rangle\langle\psi_q'(t)|\,\hat{a}^\dagger\,|\psi_q'(t)\rangle\Big]. \end{array} \tag{B.7}$$

Using that $\langle\psi_q|\,\hat{n}_e\,|\psi_q\rangle = |\eta|^2 g^2 n/(\Delta\delta - ng^2)^2$, $\langle\psi_q|\,\hat{a}^\dagger\hat{a}\,|\psi_q\rangle = |\eta|^2\Delta^2/(\Delta\delta - ng^2)^2$ and $\langle\psi_q(t)|\,\hat{a}\,|\psi_q(t)\rangle = -i\eta\Delta/(\Delta\delta - ng^2)$ we find

$$c_{nm} = 1 - \frac{\gamma_n + \gamma_m}{2} - \frac{s_n^2 + s_m^2 - 2s_n s_m}{2} \tag{B.8}$$

with

$$\gamma_n = \frac{\gamma n g^2}{(\Delta\delta - ng^2)^2} I \qquad s_n = \frac{\sqrt{\kappa}\Delta}{\Delta\delta - ng^2}\sqrt{I}. \tag{B.9}$$

B.3 Effects of coupling inhomogeneities on the fidelity

Analogously to Sec. B.3 we now calculate the effect of inhomogeneities in the coupling strength in APG protocol. We assume again that the $g_1, ..., g_N$ are independent and identically distributed random variables and have the quadratic mean $\bar{g} = \sqrt{\mathbb{E}[g_j^2]}$.

Repeating the derivation in the main text with couplings $g_1, ..., g_N$ which are different for each qubit gives a phase

$$\begin{aligned} \varphi_q &= -\tfrac{I}{\delta - \frac{1}{\Delta}\sum_{j=1}^N q_j g_j^2} \\ &\approx -\tfrac{I}{\delta - n\bar{g}^2/\Delta} - \tfrac{I\Delta}{(\delta\Delta - n\bar{g}^2)^2}\sum_j q_j (g_j^2 - \bar{g}^2) \end{aligned} \tag{B.10}$$

which is accumulated when starting with the qubits in state $|q\rangle$ (for $q \in \{0,1\}^N$. Here, as in Sec. B.3, we use $n = \sum_j q_j$. Analogously to Eq. (A.51) we obtain

$$1 - F \leq \frac{1}{2^N} \sum_{q\in\{0,1\}^N} \left[\frac{I\Delta}{(\delta\Delta - n\bar{g}^2)^2} \sum_j q_j (g_j^2 - \bar{g}^2) \right]^2 \tag{B.11}$$

so that

$$\mathbb{E}[1-F] \leq \mathrm{Var}[g_1^2] \frac{1}{2^N} \sum_{n=0}^N \binom{N}{n} n \left[\frac{I\Delta}{(\delta\Delta - n\bar{g}^2)^2} \right]^2 \tag{B.12}$$

B.4 Using the adiabatic phase gate for arbitrary phase gates

In this section we discuss how the APG protocol can be used to implement phase gates $\exp(i\varphi(\hat{n}))$ for arbitrary $\boldsymbol{\varphi} = (\varphi(0), ..., \varphi(N))$ (Here and in the following a bold font is used to indicate vector quantities). We aim to do this by applying K pulses with detunings $\delta_1, ..., \delta_K$ and $\Delta_1, ..., \Delta_K$, as well as driving fields $\eta_1(t), ..., \eta_K(t)$ and corresponding pulse energies $\boldsymbol{I} = (I_1, ..., I_K)$ with $I_k = \int_0^{T_k} |\eta_k(t)|^2 \mathrm{dt}$. With this, we implement a phase gate with $\boldsymbol{\varphi} = A\boldsymbol{I}$, where A is a $(N+1)\times K$ matrix with

$$A_{nk} = -\frac{1}{\delta_k - ng^2/\Delta_k}. \tag{B.13}$$

By adding the infidelities of the individual pulses we obtain an average gate infidelity $\boldsymbol{b} \cdot \boldsymbol{I}$, where

$$b_k = \frac{1}{2^N(2^{N+1})} \left(\sum_{n=0}^{N} \binom{N}{n} \epsilon_k^{(n,n)} + \sum_{n,m=0}^{N} \binom{N}{n} \binom{N}{m} \epsilon_k^{(n,m)} \right) \tag{B.14}$$

with

$$\begin{aligned} \epsilon_k^{(n,m)} &= \gamma g^2 \left(\tfrac{n}{(\Delta_k \delta_k - n g^2)^2} + \tfrac{m}{(\Delta_k \delta_k - m g^2)^2} \right) \\ &+ \kappa \Delta^2 \left(\tfrac{1}{\Delta_k \delta_k - n g^2} - \tfrac{1}{\Delta_k \delta_k - n g^2} \right)^2 . \end{aligned} \tag{B.15}$$

Thus, for a fixed set of detunings $\delta_1, ..., \delta_K$ and $\Delta_1, ..., \Delta_K$, finding the optimal values of $\boldsymbol{I}$ becomes a linear programming problem:

$$\begin{aligned} \text{Find} \quad & \boldsymbol{I} \\ \text{that minimizes} \quad & \boldsymbol{b} \cdot \boldsymbol{I} \\ \text{subject to} \quad & A\boldsymbol{I} = \boldsymbol{\varphi} \\ \text{and} \quad & \boldsymbol{I} \geq 0 \end{aligned}$$

The solution to this linear program can be readily found using the simplex method, which is implemented in various software packages.

Since the solution of the given linear program is always on an extremal point of the simplex given by $A\boldsymbol{I} = \boldsymbol{\varphi}$ and $\boldsymbol{I} \geq 0$, there are exactly $N+1$ indices k such that $I_k \neq 0$. To find the optimal pulse detunings one can thus take the following approach: First take $K \gg N$ and take the $\delta_1, ..., \delta_K$ to form a uniformly spaced grid. Take $\Delta_k - \delta_k$ some constant independent of k to ensure that the different pulses can be implemented by only changing the pulse frequency, not the frequency of the cavity or the $|1\rangle \leftrightarrow |e\rangle$ transition. Now the linear program given above is solved, giving $N+1$ indices k_1,..., k_{N+1} at which $I_k \neq 0$. To implement the phase gate given by $\boldsymbol{\varphi}$, $N+1$ pulses with detunings δ_{k_1},...,$\delta_{k_{N+1}}$ and Δ_{k_1},...,$\Delta_{k_{N+1}}$ as well as pulse energies $I_{k_1}, ..., I_{k_{N+1}}$ have to be applied.

A reduction to $N-1$ instead of $N+1$ required pulses is obtained if one only aims to implement the phase gate $\exp(i\varphi(\hat{n}))$ up to a global phase and single qubit gates. Formally, this means replacing the constraint $A\boldsymbol{I} = \boldsymbol{\varphi}$ by

$$\forall n \geq 2 \qquad (A\boldsymbol{I})_n - n(A\boldsymbol{I})_1 + (n-1)(A\boldsymbol{I})_0 = \varphi_n \tag{B.16}$$

Since this condition is still linear in $\boldsymbol{I}$, the optimal $\boldsymbol{I}$ can be found as before through a linear program.

With the procedure outlined above, $\boldsymbol{I}$ is chosen to maximize the average gate fidelity. For implementing a $\mathrm{C}_{N-1}\mathrm{Z}$ gate, our goal is instead to maximize the minimal fidelity. This is not possible with our linear programming approach in a straight forward manner, so we resort to a heuristic approach. For this, we replace the b_k (Eq. (B.14)) by

$$b_k = \frac{1}{(N+1)^2} \sum_{n,m=0}^{N} \epsilon_k^{(n,n)} \tag{B.17}$$

and solve the corresponding linear program. Compared to Eq. (B.14) this approach has the advantage that it weights the performance of the gate for all n and m equally, while Eq. (B.14) weights terms with $n, m \sim N/2$ higher than terms with extreme n and m. The resulting $\boldsymbol{I}$ are then used to evaluate the minimal fidelity.

Appendix C

Appendix C: Supporting calculations for cavity polariton blockade protocol

C.1 Energy shifts due to perturbative couplings from cavity drive

In this section, we present the calculation of the perturbative energy shifts on the states $|0_1 0_e 0_{\mathrm{ph}}\rangle$ and $|1_1 0_e 0_{\mathrm{ph}}\rangle$, due to the couplings governed by the non-Hermitian Hamiltonian $\hat{H}^{(\kappa,\gamma,\eta)}$ in the $k=0$ and $k=1$ subspaces of $\hat{H}^{(\Delta,\delta,g)}$.

Using time-independent perturbation theory, we calculate the energy shifts up to third order in $\hat{H}^{(\kappa,\gamma,\eta)}$, which also correspond to effective linewidths up to first order in κ and γ. The shifts on states $|0_1 0_e 0_{\mathrm{ph}}\rangle$ and $|1_1 0_e 0_{\mathrm{ph}}\rangle$ are denoted as ΔE_0 and ΔE_1 respectively, which are obtained as

$$\begin{aligned}
\Delta E_0 &= \langle 0_1 0_e 0_{\mathrm{ph}}| \hat{H}^{(\kappa,\gamma,\eta)} |0_1 0_e 0_{\mathrm{ph}}\rangle + \frac{\langle 0_1 0_e 0_{\mathrm{ph}}| \hat{H}^{(\kappa,\gamma,\eta)} |p_0^+\rangle\langle p_0^+| \hat{H}^{(\kappa,\gamma,\eta)} |0_1 0_e 0_{\mathrm{ph}}\rangle}{-\epsilon_0^+} \\
&\quad + \frac{\langle 0_1 0_e 0_{\mathrm{ph}}| \hat{H}^{(\kappa,\gamma,\eta)} |0_1 0_e 0_{\mathrm{ph}}\rangle \langle p_0^+| \hat{H}^{(\kappa,\gamma,\eta)} |p_0^+\rangle\langle p_0^+| \hat{H}^{(\kappa,\gamma,\eta)} |0_1 0_e 0_{\mathrm{ph}}\rangle}{(-\epsilon_0^+)^2} \\
\Delta E_1 &= \langle 1_1 0_e 0_{\mathrm{ph}}| \hat{H}^{(\kappa,\gamma,\eta)} |1_1 0_e 0_{\mathrm{ph}}\rangle + \langle 1_1 0_e 0_{\mathrm{ph}}| \hat{H}^{(\kappa,\gamma,\eta)} \left(\frac{|p_1^+\rangle\langle p_1^+|}{-\epsilon_1^+} + \frac{|p_1^-\rangle\langle p_1^-|}{-\epsilon_1^-} \right) \hat{H}^{(\kappa,\gamma,\eta)} |1_1 0_e 0_{\mathrm{ph}}\rangle \\
&\quad + \langle 1_1 0_e 0_{\mathrm{ph}}| \hat{H}^{(\kappa,\gamma,\eta)} \left(\frac{|p_1^+\rangle\langle p_1^+|}{-\epsilon_1^+} + \frac{|p_1^-\rangle\langle p_1^-|}{-\epsilon_1^-} \right) \hat{H}^{(\kappa,\gamma,\eta)} \left(\frac{|p_1^+\rangle\langle p_1^+|}{-\epsilon_1^+} + \frac{|p_1^-\rangle\langle p_1^-|}{-\epsilon_1^-} \right) \hat{H}^{(\kappa,\gamma,\eta)} |1_1 0_e 0_{\mathrm{ph}}\rangle .
\end{aligned} \tag{C.1}$$

To simplify Eq. (C.1), we use

$$\left(\frac{|p_1^+\rangle\langle p_1^+|}{\epsilon_1^+}+\frac{|p_1^-\rangle\langle p_1^-|}{\epsilon_1^-}\right)=\left(\hat{H}^{(\Delta,\delta,g)}_{n=1,k=1}\right)^{-1}, \tag{C.2}$$

$$\text{with } \hat{H}^{(\Delta,\delta,g)}_{n=1,k=1}=\begin{bmatrix}\delta & g\\ g & \Delta\end{bmatrix}, \tag{C.3}$$

$$\text{and } \hat{H}^{(\kappa,\gamma,\eta)}_{n=1,k=1}=\begin{bmatrix}-i\frac{\kappa}{2} & 0\\ 0 & -i\frac{\gamma}{2}\end{bmatrix}, \tag{C.4}$$

where the matrices are written in the basis $\{|1_1 0_e 1_{ph}\rangle, |0_1 1_e 0_{ph}\rangle\}$. On calculating Eq. (C.1) using the above matrices, one obtains the energy shifts as in Eq. (7.16) and Eq. (7.17).

Bibliography

[1] A. Einstein, B. Podolsky, and N. Rosen. Can quantum-mechanical description of physical reality be considered complete? *Phys. Rev.*, 47:777–780, May 1935.

[2] Menas Kafatos et al. Bell's theorem, quantum theory and conceptions of the universe [electronic resource].

[3] Daniel M Greenberger, Michael A Horne, Abner Shimony, and Anton Zeilinger. Bell's theorem without inequalities. *American Journal of Physics*, 58(12):1131–1143, 1990.

[4] N. David Mermin. What's Wrong with these Elements of Reality? *Physics Today*, 43(6):9–11, 06 1990.

[5] J. M. Raimond, M. Brune, and S. Haroche. Manipulating quantum entanglement with atoms and photons in a cavity. *Rev. Mod. Phys.*, 73:565–582, Aug 2001.

[6] D. Leibfried, R. Blatt, C. Monroe, and D. Wineland. Quantum dynamics of single trapped ions. *Rev. Mod. Phys.*, 75:281–324, Mar 2003.

[7] Helmut Ritsch, Peter Domokos, Ferdinand Brennecke, and Tilman Esslinger. Cold atoms in cavity-generated dynamical optical potentials. *Rev. Mod. Phys.*, 85:553–601, Apr 2013.

[8] Christian Gross and Immanuel Bloch. Quantum simulations with ultracold atoms in optical lattices. *Science*, 357(6355):995–1001, 2017.

[9] Florian Schäfer, Takeshi Fukuhara, Seiji Sugawa, Yosuke Takasu, and Yoshiro Takahashi. Tools for quantum simulation with ultracold atoms in optical lattices. *Nature Reviews Physics*, 2(8):411–425, 2020.

[10] Andreas J. Heinrich, William D. Oliver, Lieven M. K. Vandersypen, Arzhang Ardavan, Roberta Sessoli, Daniel Loss, Ania Bleszynski Jayich, Joaquin Fernandez-Rossier, Arne Laucht, and Andrea Morello. Quantum-coherent nanoscience. *Nature Nanotechnology*, 16(12):1318–1329, 2021.

[11] Andrew J. Daley, Immanuel Bloch, Christian Kokail, Stuart Flannigan, Natalie Pearson, Matthias Troyer, and Peter Zoller. Practical quantum advantage in quantum simulation. *Nature*, 607(7920):667–676, 2022.

[12] Frank Arute, Kunal Arya, Ryan Babbush, Dave Bacon, Joseph C. Bardin, Rami Barends, Rupak Biswas, Sergio Boixo, Fernando G. S. L. Brandao, David A. Buell, Brian Burkett, Yu Chen, Zijun Chen, Ben Chiaro, Roberto Collins, William Courtney, Andrew Dunsworth, Edward Farhi, Brooks Foxen, Austin Fowler, Craig Gidney, Marissa Giustina, Rob Graff, Keith Guerin, Steve Habegger, Matthew P. Harrigan, Michael J. Hartmann, Alan Ho, Markus Hoffmann, Trent Huang, Travis S. Humble, Sergei V. Isakov, Evan Jeffrey, Zhang Jiang, Dvir Kafri, Kostyantyn Kechedzhi, Julian Kelly, Paul V. Klimov, Sergey Knysh, Alexander Korotkov, Fedor Kostritsa, David Landhuis, Mike Lindmark, Erik Lucero, Dmitry Lyakh, Salvatore Mandrà, Jarrod R. McClean, Matthew McEwen, Anthony Megrant, Xiao Mi, Kristel Michielsen, Masoud Mohseni, Josh Mutus, Ofer Naaman, Matthew Neeley, Charles Neill, Murphy Yuezhen Niu, Eric Ostby, Andre Petukhov, John C. Platt, Chris Quintana, Eleanor G. Rieffel, Pedram Roushan, Nicholas C. Rubin, Daniel Sank, Kevin J. Satzinger, Vadim Smelyanskiy, Kevin J. Sung, Matthew D. Trevithick, Amit Vainsencher, Benjamin Villalonga, Theodore White, Z. Jamie Yao, Ping Yeh, Adam Zalcman, Hartmut Neven, and John M. Martinis. Quantum supremacy using a programmable superconducting processor. *Nature*, 574(7779):505–510, 2019.

[13] Mohsin Iqbal, Nathanan Tantivasadakarn, Ruben Verresen, Sara L. Campbell, Joan M. Dreiling, Caroline Figgatt, John P. Gaebler, Jacob Johansen, Michael Mills, Steven A. Moses, Juan M. Pino, Anthony Ransford, Mary Rowe, Peter Siegfried, Russell P. Stutz, Michael Foss-Feig, Ashvin Vishwanath, and Henrik Dreyer. Non-abelian topological order and anyons on a trapped-ion processor. *Nature*, 626(7999):505–511, 2024.

[14] Dolev Bluvstein, Simon J. Evered, Alexandra A. Geim, Sophie H. Li, Hengyun Zhou, Tom Manovitz, Sepehr Ebadi, Madelyn Cain, Marcin Kalinowski, Dominik Hangleiter, J. Pablo Bonilla Ataides, Nishad Maskara, Iris Cong, Xun Gao, Pedro Sales Rodriguez, Thomas Karolyshyn, Giulia Semeghini, Michael J. Gullans, Markus Greiner, Vladan Vuletić, and Mikhail D. Lukin. Logical quantum processor based on reconfigurable atom arrays. *Nature*, 626(7997):58–65, 2024.

[15] Carl W. Helstrom. Quantum detection and estimation theory. *Journal of Statistical Physics*, 1(2):231–252, 1969.

[16] Alexander S Holevo. *Probabilistic and statistical aspects of quantum theory*, volume 1. Springer Science & Business Media, 2011.

[17] Vittorio Giovannetti, Seth Lloyd, and Lorenzo Maccone. Quantum-enhanced measurements: Beating the standard quantum limit. *Science*, 306(5700):1330–1336, 2004.

[18] Sergio Boixo, Animesh Datta, Matthew J. Davis, Steven T. Flammia, Anil Shaji, and Carlton M. Caves. Quantum metrology: Dynamics versus entanglement. *Phys. Rev. Lett.*, 101:040403, Jul 2008.

[19] MATTEO G. A. PARIS. Quantum estimation for quantum technology. *International Journal of Quantum Information*, 07(supp01):125–137, 2009.

[20] C. L. Degen, F. Reinhard, and P. Cappellaro. Quantum sensing. *Reviews of Modern Physics*, 89:035002, 2017.

[21] Luca Pezzè, Augusto Smerzi, Markus K Oberthaler, Roman Schmied, and Philipp Treutlein. Quantum metrology with nonclassical states of atomic ensembles. *Reviews of Modern Physics*, 90(3):035005, 2018.

[22] Jérôme Beugnon, Charles Tuchendler, Harold Marion, Alpha Gaëtan, Yevhen Miroshnychenko, Yvan R. P. Sortais, Andrew M. Lance, Matthew P. A. Jones, Gaétan Messin, Antoine Browaeys, and Philippe Grangier. Two-dimensional transport and transfer of a single atomic qubit in optical tweezers. *Nature Physics*, 3:696–699, 2007.

[23] Dolev Bluvstein, Harry Levine, Giulia Semeghini, Tout T. Wang, Sepehr Ebadi, Marcin Kalinowski, Alexander Keesling, Nishad Maskara, Hannes Pichler, Markus Greiner, Vladan Vuletić, and Mikhail D. Lukin. A quantum processor based on coherent transport of entangled atom arrays. *Nature*, 604:451–456, 2022.

[24] Rolf Landauer. Is quantum mechanics useful? *Philosophical Transactions of the Royal Society of London. Series A: Physical and Engineering Sciences*, 353(1703):367–376, 1995.

[25] W. G. Unruh. Maintaining coherence in quantum computers. *Phys. Rev. A*, 51:992–997, Feb 1995.

[26] Michael A Nielsen and Isaac L Chuang. *Quantum computation and quantum information.* Cambridge university press, 2010.

[27] G Massimo Palma, Kalle-Antti Suominen, and Artur Ekert. Quantum computers and dissipation. *Proceedings of the Royal Society of London. Series A: Mathematical, Physical and Engineering Sciences*, 452(1946):567–584, 1996.

[28] Claude Cohen-Tannoudji, Jacques Dupont-Roc, and Gilbert Grynberg. *Atom-photon interactions: basic processes and applications.* John Wiley & Sons, 1998.

[29] Serge Haroche and J-M Raimond. *Exploring the quantum: atoms, cavities, and photons*. Oxford university press, 2006.

[30] T. Pellizzari, S. A. Gardiner, J. I. Cirac, and P. Zoller. Decoherence, Continuous Observation, and Quantum Computing: A Cavity QED Model. *Physical Review Letters*, 75:3788–3791, 1995.

[31] J. I. Cirac and P. Zoller. Quantum Computations with Cold Trapped Ions. *Physical Review Letters*, 74:4091–4094, 1995.

[32] Klaus Mølmer and Anders Sørensen. Multiparticle Entanglement of Hot Trapped Ions. *Physical Review Letters*, 82:1835–1838, 1999.

[33] C. A. Sackett, D. Kielpinski, B. E. King, C. Langer, V. Meyer, C. J. Myatt, M. Rowe, Q. A. Turchette, W. M. Itano, D. J. Wineland, and C. Monroe. Experimental entanglement of four particles. *Nature*, 404:256–259, 2000.

[34] J. J. García-Ripoll, P. Zoller, and J. I. Cirac. Speed Optimized Two-Qubit Gates with Laser Coherent Control Techniques for Ion Trap Quantum Computing. *Physical Review Letters*, 91:157901, 2003.

[35] J. Borregaard, P. Kómár, E. M. Kessler, A. S. Sørensen, and M. D. Lukin. Heralded Quantum Gates with Integrated Error Detection in Optical Cavities. *Physical Review Letters*, 114:110502, 2015.

[36] L.-M. Duan and H. J. Kimble. Efficient Engineering of Multiatom Entanglement through Single-Photon Detections. *Physical Review Letters*, 90:253601, 2003.

[37] Philippe Lewalle, Leigh S. Martin, Emmanuel Flurin, Song Zhang, Eliya Blumenthal, Shay Hacohen-Gourgy, Daniel Burgarth, and K. Birgitta Whaley. A Multi-Qubit Quantum Gate Using the Zeno Effect. *arXiv:2211.05988*, 2022.

[38] Giovanni Barontini, Leander Hohmann, Florian Haas, Jérôme Estève, and Jakob Reichel. Deterministic generation of multiparticle entanglement by quantum zeno dynamics. *Science*, 349(6254):1317–1321, 2015.

[39] Jürgen Volz, Roger Gehr, Guilhem Dubois, Jérôme Estève, and Jakob Reichel. Measurement of the internal state of a single atom without energy exchange. *Nature*, 475(7355):210–213, 2011.

[40] Panagiotis Kl. Barkoutsos, Jerome F. Gonthier, Igor Sokolov, Nikolaj Moll, Gian Salis, Andreas Fuhrer, Marc Ganzhorn, Daniel J. Egger, Matthias Troyer, Antonio Mezzacapo, Stefan Filipp, and Ivano Tavernelli. Quantum algorithms for electronic structure calculations: Particle-hole Hamiltonian and optimized wavefunction expansions. *Physical Review A*, 98:022322, 2018.

[41] Stefan Balauca and Andreea Arusoaie. Efficient Constructions for Simulating Multi Controlled Quantum Gates. In Derek Groen, Clélia de Mulatier, Maciej Paszynski, Valeria V. Krzhizhanovskaya, Jack J. Dongarra, and Peter M. A. Sloot, editors, *Computational Science – ICCS 2022*, volume 13353, pages 179–194. Springer International Publishing, Cham, 2022.

[42] J. D. Pritchard, J. A. Isaacs, M. A. Beck, R. McDermott, and M. Saffman. Hybrid atom-photon quantum gate in a superconducting microwave resonator. *Physical Review A*, 89:010301, 2014.

[43] Chan U Lei, Lev Krayzman, Suhas Ganjam, Luigi Frunzio, and Robert J. Schoelkopf. High coherence superconducting microwave cavities with indium bump bonding. *Applied Physics Letters*, 116:154002, 2020.

[44] D Hunger, T Steinmetz, Y Colombe, C Deutsch, T W Hänsch, and J Reichel. A fiber Fabry–Perot cavity with high finesse. *New Journal of Physics*, 12:065038, 2010.

[45] Manuel Uphoff, Manuel Brekenfeld, Gerhard Rempe, and Stephan Ritter. Frequency splitting of polarization eigenmodes in microscopic Fabry–Perot cavities. *New Journal of Physics*, 17:013053, 2015.

[46] Giovanni Barontini, Leander Hohmann, Florian Haas, Jérôme Estève, and Jakob Reichel. Deterministic generation of multiparticle entanglement by quantum Zeno dynamics. *Science*, 349:1317–1321, 2015.

[47] Guntram Scheithauer. Jorge nocedal and stephen j. wright: Numerical optimization, springer series in operations research, 1999, isbn 0-387-98793-2.

[48] Eric Jones, Travis Oliphant, Pearu Peterson, and others. SciPy: Open source scientific tools for Python, 2001.

[49] Dietrich Leibfried, Murray D Barrett, T Schaetz, Joseph Britton, J Chiaverini, Wayne M Itano, John D Jost, Christopher Langer, and David J Wineland. Toward heisenberg-limited spectroscopy with multiparticle entangled states. *Science*, 304(5676):1476–1478, 2004.

[50] Monika H Schleier-Smith, Ian D Leroux, and Vladan Vuletić. States of an ensemble of two-level atoms with reduced quantum uncertainty. *Physical review letters*, 104(7):073604, 2010.

[51] Bernd Lücke, Manuel Scherer, Jens Kruse, Luca Pezzé, Frank Deuretzbacher, Phillip Hyllus, Oliver Topic, Jan Peise, Wolfgang Ertmer, Jan Arlt, et al. Twin

matter waves for interferometry beyond the classical limit. *Science*, 334(6057):773–776, 2011.

[52] Géza Tóth and Iagoba Apellaniz. Quantum metrology from a quantum information science perspective. *Journal of Physics A: Mathematical and Theoretical*, 47:424006, 2014.

[53] Iagoba Apellaniz, Bernd Lücke, Jan Peise, Carsten Klempt, and Géza Tóth. Detecting metrologically useful entanglement in the vicinity of dicke states. *New Journal of Physics*, 17(8):083027, 2015.

[54] Sven Jandura, Vineesha Srivastava, Laura Pecorari, Gavin K. Brennen, and Guido Pupillo. Nonlocal multiqubit quantum gates via a driven cavity. *Physical Review A*, 110(6):062610, December 2024.

[55] Brandon Grinkemeyer, Elmer Guardado-Sanchez, Ivana Dimitrova, Danilo Shchepanovich, G Eirini Mandopoulou, Johannes Borregaard, Vladan Vuletić, and Mikhail D Lukin. Error-detected quantum operations with neutral atoms mediated by an optical cavity. *arXiv preprint arXiv:2410.10787*, 2024.

[56] R. J. Thompson, G. Rempe, and H. J. Kimble. Observation of normal-mode splitting for an atom in an optical cavity. *Phys. Rev. Lett.*, 68:1132–1135, Feb 1992.

[57] Anton Öttl, Stephan Ritter, Michael Köhl, and Tilman Esslinger. Correlations and counting statistics of an atom laser. *Phys. Rev. Lett.*, 95:090404, Aug 2005.

[58] Adam Holmes, Sonika Johri, Gian Giacomo Guerreschi, James S. Clarke, and A. Y. Matsuura. Impact of qubit connectivity on quantum algorithm performance. *Quantum Science and Technology*, 5:025009, 2020.

[59] Joshua Ramette, Josiah Sinclair, Zachary Vendeiro, Alyssa Rudelis, Marko Cetina, and Vladan Vuletić. Any-to-any connected cavity-mediated architecture for quantum computing with trapped ions or Rydberg arrays. *arXiv:2109.11551 [physics, physics:quant-ph]*, 2021.

[60] Nathan Shammah, Shahnawaz Ahmed, Neill Lambert, Simone De Liberato, and Franco Nori. Open quantum systems with local and collective incoherent processes: Efficient numerical simulations using permutational invariance. *Physical Review A*, 98(6):063815, 2018.

[61] M. Abdelhafez, B. Baker, A. Gyenis, P. Mundada, A. A. Houck, D. Schuster, and J. Koch. Universal gates for protected superconducting qubits using optimal control. *Physical Review A*, 101(2), 2020.

[62] The cavity drive pulse $\eta(t)$ in the original frame is obtained by inverting the pulse $\zeta(t)$ in Eq. (4.14) with a finite value of $\Delta \gg g$ which is set by a choice of $\max_t|\eta(t)| \gg g$: $\eta(t) = -\frac{\Delta}{S(t)}(\dot{\zeta}(t) + (i\delta + \frac{\kappa}{2})\zeta(t)) - \frac{2\Delta g^2}{S(t)^3}\zeta(t)\frac{d}{dt}|\zeta(t)|^2$, where $S(t) = g^2\sqrt{1 - 4|\zeta(t)|^2/g^2}$. Here, we make a choice of $\max_t(|\eta(t)|) = 30g$.

[63] Sven Jandura and Guido Pupillo. Time-Optimal Two- and Three-Qubit Gates for Rydberg Atoms. *Quantum*, 6:712, May 2022.

[64] Simon J. Evered, Dolev Bluvstein, Marcin Kalinowski, Sepehr Ebadi, Tom Manovitz, Hengyun Zhou, Sophie H. Li, Alexandra A. Geim, Tout T. Wang, Nishad Maskara, Harry Levine, Giulia Semeghini, Markus Greiner, Vladan Vuletić, and Mikhail D. Lukin. High-fidelity parallel entangling gates on a neutral-atom quantum computer. *Nature*, 622(7982):268–272, October 2023.

[65] M. Brune, P. Nussenzveig, F. Schmidt-Kaler, F. Bernardot, A. Maali, J. M. Raimond, and S. Haroche. From lamb shift to light shifts: Vacuum and subphoton cavity fields measured by atomic phase sensitive detection. *Phys. Rev. Lett.*, 72:3339–3342, May 1994.

[66] S. D. Hogan, J. A. Agner, F. Merkt, T. Thiele, S. Filipp, and A. Wallraff. Driving rydberg-rydberg transitions from a coplanar microwave waveguide. *Phys. Rev. Lett.*, 108:063004, Feb 2012.

[67] M. Brune, J. M. Raimond, P. Goy, L. Davidovich, and S. Haroche. Realization of a two-photon maser oscillator. *Phys. Rev. Lett.*, 59:1899–1902, Oct 1987.

[68] M. Brune, F. Schmidt-Kaler, A. Maali, J. Dreyer, E. Hagley, J. M. Raimond, and S. Haroche. Quantum rabi oscillation: A direct test of field quantization in a cavity. *Phys. Rev. Lett.*, 76:1800–1803, Mar 1996.

[69] E. Hagley, X. Maître, G. Nogues, C. Wunderlich, M. Brune, J. M. Raimond, and S. Haroche. Generation of einstein-podolsky-rosen pairs of atoms. *Phys. Rev. Lett.*, 79:1–5, Jul 1997.

[70] X. Maître, E. Hagley, G. Nogues, C. Wunderlich, P. Goy, M. Brune, J. M. Raimond, and S. Haroche. Quantum memory with a single photon in a cavity. *Phys. Rev. Lett.*, 79:769–772, Jul 1997.

[71] G. Nogues, A. Rauschenbeutel, S. Osnaghi, M. Brune, J. M. Raimond, and S. Haroche. Seeing a single photon without destroying it. *Nature*, 400(6741):239–242, 1999.

[72] Arno Rauschenbeutel, Gilles Nogues, Stefano Osnaghi, Patrice Bertet, Michel Brune, Jean-Michel Raimond, and Serge Haroche. Step-by-step engineered multiparticle entanglement. *Science*, 288(5473):2024–2028, 2000.

[73] A. Auffeves, P. Maioli, T. Meunier, S. Gleyzes, G. Nogues, M. Brune, J. M. Raimond, and S. Haroche. Entanglement of a mesoscopic field with an atom induced by photon graininess in a cavity. *Phys. Rev. Lett.*, 91:230405, Dec 2003.

[74] P. Maioli, T. Meunier, S. Gleyzes, A. Auffeves, G. Nogues, M. Brune, J. M. Raimond, and S. Haroche. Nondestructive rydberg atom counting with mesoscopic fields in a cavity. *Phys. Rev. Lett.*, 94:113601, Mar 2005.

[75] Sébastien Gleyzes, Stefan Kuhr, Christine Guerlin, Julien Bernu, Samuel Deléglise, Ulrich Busk Hoff, Michel Brune, Jean-Michel Raimond, and Serge Haroche. Quantum jumps of light recording the birth and death of a photon in a cavity. *Nature*, 446(7133):297–300, 2007.

[76] Ian D Leroux, Monika H Schleier-Smith, and Vladan Vuletić. Implementation of cavity squeezing of a collective atomic spin. *Physical Review Letters*, 104(7):073602, 2010.

[77] Kevin C Cox, Graham P Greve, Joshua M Weiner, and James K Thompson. Deterministic squeezed states with collective measurements and feedback. *Physical review letters*, 116(9):093602, 2016.

[78] Justin G Bohnet, Brian C Sawyer, Joseph W Britton, Michael L Wall, Ana Maria Rey, Michael Foss-Feig, and John J Bollinger. Quantum spin dynamics and entanglement generation with hundreds of trapped ions. *Science*, 352(6291):1297–1301, 2016.

[79] Edwin Pedrozo-Peñafiel, Simone Colombo, Chi Shu, Albert F Adiyatullin, Zeyang Li, Enrique Mendez, Boris Braverman, Akio Kawasaki, Daisuke Akamatsu, Yanhong Xiao, et al. Entanglement on an optical atomic-clock transition. *Nature*, 588(7838):414–418, 2020.

[80] A. André, D. DeMille, J. M. Doyle, M. D. Lukin, S. E. Maxwell, P. Rabl, R. J. Schoelkopf, and P. Zoller. A coherent all-electrical interface between polar molecules and mesoscopic superconducting resonators. *Nature Physics*, 2:636–642, 2006.

[81] P. Rabl, D. DeMille, J. M. Doyle, M. D. Lukin, R. J. Schoelkopf, and P. Zoller. Hybrid Quantum Processors: Molecular Ensembles as Quantum Memory for Solid State Circuits. *Physical Review Letters*, 97:033003, 2006.

[82] Rahul Sawant, Jacob A Blackmore, Philip D Gregory, Jordi Mur-Petit, Dieter Jaksch, Jesús Aldegunde, Jeremy M Hutson, M R Tarbutt, and Simon L Cornish. Ultracold polar molecules as qudits. *New Journal of Physics*, 22:013027, 2020.

[83] L.-M. Duan. Geometric Manipulation of Trapped Ions for Quantum Computation. *Science*, 292:1695–1697, 2001.

[84] Michel H. Devoret and John M. Martinis. Implementing Qubits with Superconducting Integrated Circuits. In *Experimental Aspects of Quantum Computing*, pages 163–203. Springer, Boston, MA, 2005.

[85] John M. Martinis, Michel H. Devoret, and John Clarke. Quantum Josephson junction circuits and the dawn of artificial atoms. *Nature Physics*, 16(3):234–237, March 2020.

[86] V. E. Manucharyan, J. Koch, L. I. Glazman, and M. H. Devoret. Fluxonium: Single cooper-pair circuit free of charge offsets. *Science*, 326:113–116, 2009.

[87] Emma L. Rosenfeld, Connor T. Hann, David I. Schuster, Matthew H. Matheny, and Aashish A. Clerk. High-fidelity two-qubit gates between fluxonium qubits with a resonator coupler. *PRX Quantum*, 5:040317, Nov 2024.

[88] Long B. Nguyen, Gerwin Koolstra, Yosep Kim, Alexis Morvan, Trevor Chistolini, Shraddha Singh, Konstantin N. Nesterov, Christian Jünger, Larry Chen, Zahra Pedramrazi, Bradley K. Mitchell, John Mark Kreikebaum, Shruti Puri, David I. Santiago, and Irfan Siddiqi. Blueprint for a high-performance fluxonium quantum processor. *PRX Quantum*, 3:037001, Aug 2022.

[89] Helin Zhang, Chunyang Ding, D.K. Weiss, Ziwen Huang, Yuwei Ma, Charles Guinn, Sara Sussman, Sai Pavan Chitta, Danyang Chen, Andrew A. Houck, Jens Koch, and David I. Schuster. Tunable inductive coupler for high-fidelity gates between fluxonium qubits. *PRX Quantum*, 5:020326, May 2024.

[90] Leon Ding, Max Hays, Youngkyu Sung, Bharath Kannan, Junyoung An, Agustin Di Paolo, Amir H. Karamlou, Thomas M. Hazard, Kate Azar, David K. Kim, Bethany M. Niedzielski, Alexander Melville, Mollie E. Schwartz, Jonilyn L. Yoder, Terry P. Orlando, Simon Gustavsson, Jeffrey A. Grover, Kyle Serniak, and William D. Oliver. High-fidelity, frequency-flexible two-qubit fluxonium gates with a transmon coupler. *Phys. Rev. X*, 13:031035, Sep 2023.

[91] Ebru Dogan, Dario Rosenstock, Loïck Le Guevel, Haonan Xiong, Raymond A. Mencia, Aaron Somoroff, Konstantin N. Nesterov, Maxim G. Vavilov, Vladimir E. Manucharyan, and Chen Wang. Two-fluxonium cross-resonance gate. *Phys. Rev. Appl.*, 20:024011, Aug 2023.

[92] Erika Janitz, Mihir Bhaskar, and Lilian Childress. Cavity quantum electrodynamics with color centers in diamond. *Optica*, 7, 09 2020.

[93] Xiaoze Liu, Tal Galfsky, Zheng Sun, Fengnian Xia, Erh-chen Lin, Yi-Hsien Lee, Stéphane Kéna-Cohen, and Vinod M Menon. Strong light–matter coupling in two-dimensional atomic crystals. *Nature Photonics*, 9(1):30–34, 2015.

[94] Shaojun Wang, Songlin Li, Thibault Chervy, Atef Shalabney, Stefano Azzini, Emanuele Orgiu, James A Hutchison, Cyriaque Genet, Paolo Samorì, and Thomas W Ebbesen. Coherent coupling of ws2 monolayers with metallic photonic nanostructures at room temperature. *Nano letters*, 16(7):4368–4374, 2016.

[95] Serge Haroche. A short history of cavity quantum electrodynamics. In *Conference on Coherence and Quantum Optics*, page CTuF2. Optica Publishing Group, 2007.

[96] E. M. Purcell, H. C. Torrey, and R. V. Pound. Resonance absorption by nuclear magnetic moments in a solid. *Phys. Rev.*, 69:37–38, Jan 1946.

[97] Beili Hu, Josiah Sinclair, Edita Bytyqi, Michelle Chong, Alyssa Rudelis, Joshua Ramette, Zachary Vendeiro, and Vladan Vuletić. Site-selective cavity readout and classical error correction of a 5-bit atomic register. *arXiv preprint arXiv:2408.15329*, 2024.

[98] T. M. Graham, L. Phuttitarn, R. Chinnarasu, Y. Song, C. Poole, K. Jooya, J. Scott, A. Scott, P. Eichler, and M. Saffman. Midcircuit measurements on a single-species neutral alkali atom quantum processor. *Phys. Rev. X*, 13:041051, Dec 2023.

[99] David Petrosyan and Michael Fleischhauer. Quantum information processing with single photons and atomic ensembles in microwave coplanar waveguide resonators. *Phys. Rev. Lett.*, 100:170501, Apr 2008.

[100] Serge Haroche. Nobel lecture: Controlling photons in a box and exploring the quantum to classical boundary. *Rev. Mod. Phys.*, 85:1083–1102, Jul 2013.

[101] T. Brecht, M. Reagor, Y. Chu, W. Pfaff, C. Wang, L. Frunzio, M. H. Devoret, and R. J. Schoelkopf. Demonstration of superconducting micromachined cavities. *Applied Physics Letters*, 107(19):192603, 11 2015.

[102] Teresa Brecht, Wolfgang Pfaff, Chen Wang, Yiwen Chu, Luigi Frunzio, Michel H Devoret, and Robert J Schoelkopf. Multilayer microwave integrated quantum circuits for scalable quantum computing. *npj Quantum Information*, 2(1):16002, 2016.

[103] Alexandre Blais, Arne L. Grimsmo, S. M. Girvin, and Andreas Wallraff. Circuit quantum electrodynamics. *Rev. Mod. Phys.*, 93:025005, May 2021.

[104] Alex Krasnok, Pashupati Dhakal, Arkady Fedorov, Pedro Frigola, Michael Kelly, and Sergey Kutsaev. Superconducting microwave cavities and qubits for quantum information systems. *Applied Physics Reviews*, 11(1):011302, 01 2024.

[105] Ziyi Zhao, Eva Gurra, Eric I. Rosenthal, Leila R. Vale, Gene C. Hilton, and K. W. Lehnert. Integrating planar circuits with superconducting 3D microwave cavities using tunable low-loss couplers. *Applied Physics Letters*, 123(1):014001, 07 2023.

[106] Iivari Pietikäinen, Ond řej Černotík, Alec Eickbusch, Aniket Maiti, John W.O. Garmon, Radim Filip, and Steven M. Girvin. Strategies and trade-offs for controllability and memory time of ultra-high-quality microwave cavities in circuit quantum electrodynamics. *PRX Quantum*, 5:040307, Oct 2024.

[107] Daniel Gottesman. Fault-Tolerant quantum computation with constant overhead. *Quantum Information and Computation*, 14:1339–1371, 2014.

[108] Nikolas P. Breuckmann and Jens Niklas Eberhardt. Quantum Low-Density Parity-Check Codes. *PRX Quantum*, 2:040101, 2021.

[109] Lawrence Z. Cohen, Isaac H. Kim, Stephen D. Bartlett, and Benjamin J. Brown. Low-overhead fault-tolerant quantum computing using long-range connectivity. *Science Advances*, 8:eabn1717, 2022.

[110] Sergey Bravyi, Andrew W. Cross, Jay M. Gambetta, Dmitri Maslov, Patrick Rall, and Theodore J. Yoder. High-threshold and low-overhead fault-tolerant quantum memory, 2023.

[111] Omprakash Chandra, Gopikrishnan Muraleedharan, and Gavin K Brennen. Non-local resources for error correction in quantum ldpc codes. *arXiv preprint arXiv:2409.05818*, 2024.

[112] Austin G. Fowler, Matteo Mariantoni, John M. Martinis, and Andrew N. Cleland. Surface codes: Towards practical large-scale quantum computation. *Physical Review A*, 86:032324, 2012.

[113] Shi-Biao Zheng and Guang-Can Guo. Efficient Scheme for Two-Atom Entanglement and Quantum Information Processing in Cavity QED. *Physical Review Letters*, 85:2392–2395, 2000.

[114] Almut Beige, Daniel Braun, Ben Tregenna, and Peter L. Knight. Quantum Computing Using Dissipation to Remain in a Decoherence-Free Subspace. *Physical Review Letters*, 85:1762–1765, 2000.

[115] Anders S. Sørensen and Klaus Mølmer. Measurement Induced Entanglement and Quantum Computation with Atoms in Optical Cavities. *Physical Review Letters*, 91:097905, 2003.

[116] Shi-Biao Zheng. Unconventional geometric quantum phase gates with a cavity QED system. *Physical Review A*, 70:052320, 2004.

[117] M. B. Plenio, S. F. Huelga, A. Beige, and P. L. Knight. Cavity-loss-induced generation of entangled atoms. *Physical Review A*, 59:2468–2475, 1999.

[118] S Bose, P L Knight, M B Plenio, and V Vedral. Proposal for Teleportation of an Atomic State via Cavity Decay. *PHYSICAL REVIEW LETTERS*, 83:4, 1999.

[119] Jongcheol Hong and Hai-Woong Lee. Quasideterministic Generation of Entangled Atoms in a Cavity. *Physical Review Letters*, 89:237901, 2002.

[120] L. M. Duan, M. D. Lukin, J. I. Cirac, and P. Zoller. Long-distance quantum communication with atomic ensembles and linear optics. *Nature*, 414(6862):413–418, 2001.

[121] L.-M. Duan. Entangling many atomic ensembles through laser manipulation. *Phys. Rev. Lett.*, 88:170402, Apr 2002.

[122] P. Domokos, J. M. Raimond, M. Brune, and S. Haroche. Simple cavity-qed two-bit universal quantum logic gate: The principle and expected performances. *Phys. Rev. A*, 52:3554–3559, Nov 1995.

[123] M. J. Kastoryano, F. Reiter, and A. S. Sørensen. Dissipative Preparation of Entanglement in Optical Cavities. *Physical Review Letters*, 106:090502, 2011.

[124] Sisi Zhou, Mengzhen Zhang, John Preskill, and Liang Jiang. Achieving the heisenberg limit in quantum metrology using quantum error correction. *Nature Communications*, 9(1):78, 2018.

[125] Rafał Demkowicz-Dobrzański, Jan Czajkowski, and Pavel Sekatski. Adaptive quantum metrology under general markovian noise. *Phys. Rev. X*, 7:041009, Oct 2017.

[126] Yingkai Ouyang and Gavin K. Brennen. Finite-round quantum error correction on symmetric quantum sensors, 2024.

[127] Boris Braverman, Akio Kawasaki, Edwin Pedrozo-Peñafiel, Simone Colombo, Chi Shu, Zeyang Li, Enrique Mendez, Megan Yamoah, Leonardo Salvi, Daisuke Akamatsu, Yanhong Xiao, and Vladan Vuletić. Near-unitary spin squeezing in ^{171}Yb. *Phys. Rev. Lett.*, 122:223203, Jun 2019.

[128] H. Ritsch, P. Domokos, F. Brennecke, and T. Esslinger. Cold atoms in cavity-generated dynamical optical potentials. *Reviews of Modern Physics*, 85:553, 2013.

[129] M. H. Schleier-Smith, I. D. Leroux, and V. Vuletić. States of an ensemble of two-level atoms with reduced quantum uncertainty. *Physical Review Letters*, 104:073604, 2010.

[130] K. C. Cox, G. P. Greve, J. M. Weiner, and J. K. Thompson. Deterministic squeezed states with collective measurements and feedback. *Physical Review Letters*, 116:093602, 2016.

[131] B. Braverman, A. Kawasaki, E. Pedrozo-Peñafiel, S. Colombo, C. Shu, Z. Li, E. Mendez, M. Yamoah, L. Salvi, D. Akamatsu, Y. Xiao, and V. Vuletić. Near-unitary spin squeezing in ^{171}yb optical lattice clocks. *Physical Review Letters*, 122:223203, 2019.

[132] O. Hosten, R. Krishnakumar, N. J. Engelsen, and M. A. Kasevich. Measurement noise 100 times lower than the quantum-projection limit using entangled atoms. *Science*, 352:1552, 2016.

[133] M. Penasa, S. Gerlich, T. Rybarczyk, V. Métillon, M. Brune, J. M. Raimond, S. Haroche, L. Davidovich, and I. Dotsenko. Measurement of the decoherence of photon number superpositions in a cavity. *Physical Review A*, 94:022313, 2016.

[134] A. Facon, E.-K. Dietsche, D. Grosso, S. Haroche, J.-M. Raimond, M. Brune, and S. Gleyzes. A sensitive electrometer based on a rydberg atom in a schrödinger-cat state. *Nature (London)*, 535:262, 2016.

[135] G. Grynberg, A. Aspect, C. Fabre, and C. Cohen-Tannoudji. *Introduction to Quantum Optics: From the Semi-classical Approach to Quantized Light*. Cambridge University Press, 2010.

[136] Serge Haroche and Jean-Michel Raimond. *Exploring the Quantum: Atoms, Cavities, and Photons*. Oxford University Press, 08 2006.

[137] Roy J. Glauber. Coherent and incoherent states of the radiation field. *Phys. Rev.*, 131:2766–2788, Sep 1963.

[138] E.T. Jaynes and F.W. Cummings. Comparison of quantum and semiclassical radiation theories with application to the beam maser. *Proceedings of the IEEE*, 51(1):89–109, 1963.

[139] Michael Tavis and Frederick W Cummings. Exact solution for an n-molecule—radiation-field hamiltonian. *Physical Review*, 170(2):379, 1968.

[140] R. H. Dicke. Coherence in spontaneous radiation processes. *Phys. Rev.*, 93:99–110, Jan 1954.

[141] Crispin Gardiner and Peter Zoller. *Quantum noise: a handbook of Markovian and non-Markovian quantum stochastic methods with applications to quantum optics.* Springer Science & Business Media, 2004.

[142] Heinz-Peter Breuer and Francesco Petruccione. *The theory of open quantum systems.* Oxford University Press, USA, 2002.

[143] Goran Lindblad. On the generators of quantum dynamical semigroups. *Communications in mathematical physics*, 48:119–130, 1976.

[144] Steffen J Glaser, Ugo Boscain, Tommaso Calarco, Christiane P Koch, Walter Köckenberger, Ronnie Kosloff, Ilya Kuprov, Burkhard Luy, Sophie Schirmer, Thomas Schulte-Herbrüggen, et al. Training schrödinger's cat: Quantum optimal control: Strategic report on current status, visions and goals for research in europe. *The European Physical Journal D*, 69:1–24, 2015.

[145] Frank K Wilhelm, Susanna Kirchhoff, Shai Machnes, Nicolas Wittler, and Dominique Sugny. An introduction into optimal control for quantum technologies. *arXiv preprint arXiv:2003.10132*, 2020.

[146] Navin Khaneja, Timo Reiss, Calle Kehlet, Thomas Schulte-Herbrüggen, and Steffen J Glaser. Optimal control of coupled spin dynamics: Design of nmr pulse sequences by gradient ascent algorithms. *Journal of Magnetic Resonance*, 172(2):296–305, 2005.

[147] Bradley A. Chase and J. M. Geremia. Collective processes of an ensemble of spin-1/2 particles. *Phys. Rev. A*, 78:052101, Nov 2008.

[148] Henning Labuhn, Sylvain Ravets, Daniel Barredo, Lucas Béguin, Florence Nogrette, Thierry Lahaye, and Antoine Browaeys. Single-atom addressing in microtraps for quantum-state engineering using Rydberg atoms. *Physical Review A*, 90:023415, 2014.

[149] Yang Wang, Aishwarya Kumar, Tsung-Yao Wu, and David S. Weiss. Single-qubit gates based on targeted phase shifts in a 3D neutral atom array. *Science*, 352:1562–1565, 2016.

[150] Thomas F Gallagher. Rydberg atoms. *Reports on Progress in Physics*, 51(2):143, 1988.

[151] Antoine Browaeys and Thierry Lahaye. Interacting cold rydberg atoms: A toy many-body system. In *Niels Bohr, 1913-2013: Poincaré Seminar 2013*, pages 177–198. Springer, 2016.

[152] M. Saffman, T. G. Walker, and K. Mølmer. Quantum information with rydberg atoms. *Rev. Mod. Phys.*, 82:2313–2363, Aug 2010.

[153] Randall G. Hulet and Daniel Kleppner. Rydberg atoms in "circular" states. *Phys. Rev. Lett.*, 51:1430–1433, Oct 1983.

[154] Sam R. Cohen and Jeff D. Thompson. Quantum computing with circular rydberg atoms. *PRX Quantum*, 2:030322, Aug 2021.

[155] Paul Méhaignerie, Yohann Machu, Andrés Durán Hernández, Gautier Creutzer, David J Papoular, Jean-Michel Raimond, Clément Sayrin, and Michel Brune. Interacting circular rydberg atoms trapped in optical tweezers. *arXiv preprint arXiv:2407.04109*, 2024.

[156] T. Xia, X. L. Zhang, and M. Saffman. Analysis of a controlled phase gate using circular rydberg states. *Phys. Rev. A*, 88:062337, Dec 2013.

[157] R. C. Teixeira, A. Larrouy, A. Muni, L. Lachaud, J.-M. Raimond, S. Gleyzes, and M. Brune. Preparation of long-lived, non-autoionizing circular rydberg states of strontium. *Phys. Rev. Lett.*, 125:263001, Dec 2020.

[158] Arthur Larrouy, Sabrina Patsch, Rémi Richaud, Jean-Michel Raimond, Michel Brune, Christiane P. Koch, and Sébastien Gleyzes. Fast navigation in a large hilbert space using quantum optimal control. *Phys. Rev. X*, 10:021058, Jun 2020.

[159] T. L. Nguyen, J. M. Raimond, C. Sayrin, R. Cortiñas, T. Cantat-Moltrecht, F. Assemat, I. Dotsenko, S. Gleyzes, S. Haroche, G. Roux, Th. Jolicoeur, and M. Brune. Towards quantum simulation with circular rydberg atoms. *Phys. Rev. X*, 8:011032, Feb 2018.

[160] W. J. Childs, David R. Cok, G. L. Goodman, and L. S. Goodman. Hyperfine and spin–rotational structure of CaBr X $^2\Sigma$ (v = 0) by molecular-beam laser-rf double resonance. *The Journal of Chemical Physics*, 75:501–507, 1981.

[161] Stefan Yoshi Buhmann, M. R. Tarbutt, Stefan Scheel, and E. A. Hinds. Surface-induced heating of cold polar molecules. *Physical Review A*, 78:052901, 2008.

[162] A. Somoroff, Q. Ficheux, Raymond A. Mencia, H. Xiong, R. Kuzmin, and V. E. Manucharyan. Millisecond coherence in a superconducting qubit. *Phys. Rev. Lett.*, 130:267001, Jun 2023.

[163] Peter Groszkowski and Jens Koch. Scqubits: a python package for superconducting qubits. *Quantum*, 5:583, 2021.

[164] Sai Pavan Chitta, Tianpu Zhao, Ziwen Huang, Ian Mondragon-Shem, and Jens Koch. Computer-aided quantization and numerical analysis of superconducting circuits, 2022.

[165] Long B. Nguyen, Yen-Hsiang Lin, Aaron Somoroff, Raymond Mencia, Nicholas Grabon, and Vladimir E. Manucharyan. High-coherence fluxonium qubit. *Phys. Rev. X*, 9:041041, 2019.

[166] M. Hein, J. Eisert, and H. J. Briegel. Multi-party entanglement in graph states. *Physical Review A*, 69:062311, 2004.

[167] D. Leibfried, M. D. Barrett, T. Schaetz, J. Britton, J. Chiaverini, W. M. Itano, J. D. Jost, C. Langer, and D. J. Wineland. Toward Heisenberg-Limited Spectroscopy with Multiparticle Entangled States. *Science*, 304:1476–1478, 2004.

[168] Line Hjortshøj Pedersen, Niels Martin Møller, and Klaus Mølmer. Fidelity of quantum operations. *Physics Letters A*, 367:47–51, 2007.

[169] Ilya N. Moskalenko, Ilya A. Simakov, Nikolay N. Abramov, Alexander A. Grigorev, Dmitry O. Moskalev, Anastasiya A. Pishchimova, Nikita S. Smirnov, Evgeniy V. Zikiy, Ilya A. Rodionov, and Ilya S. Besedin. High fidelity two-qubit gates on fluxoniums using a tunable coupler. *npj Quantum Information*, 8(1):130, Nov 2022.

[170] J.-M. Cheng, Y. Zhang, X.-F. Zhou, and Z.-W. Zhou. Enhancing quantum coherence of a fluxonium qubit by employing flux modulation with tunable-complex-amplitude. *New Journal of Physics*, 24, 12 2022.

[171] Steffen J. Glaser, Ugo Boscain, Tommaso Calarco, Christiane P. Koch, Walter Köckenberger, Ronnie Kosloff, Ilya Kuprov, Burkhard Luy, Sophie Schirmer, Thomas Schulte-Herbrüggen, Dominique Sugny, and Frank K. Wilhelm. Training Schrödinger's cat: Quantum optimal control: Strategic report on current status, visions and goals for research in Europe. *The European Physical Journal D*, 69:279, 2015.

[172] Frank K. Wilhelm, Susanna Kirchhoff, Shai Machnes, Nicolas Wittler, and Dominique Sugny. An introduction into optimal control for quantum technologies. *arXiv:2003.10132*, 2020.

[173] Vineesha Srivastava, Sven Jandura, Gavin K Brennen, and Guido Pupillo. Entanglement-enhanced quantum sensing via optimal global control. *arXiv preprint arXiv:2409.12932*, 2024.

[174] Samuel L Braunstein and Carlton M Caves. Geometry of quantum states. In *Quantum Communications and Measurement*, pages 21–30. Springer, 1995.

[175] Samuel L Braunstein, Carlton M Caves, and Gerard J Milburn. Generalized uncertainty relations: theory, examples, and lorentz invariance. *annals of physics*, 247(1):135–173, 1996.

[176] Mattias T. Johnsson, Nabomita Roy Mukty, Daniel Burgarth, Thomas Volz, and Gavin K. Brennen. Geometric pathway to scalable quantum sensing. *Phys. Rev. Lett.*, 125:190403, Nov 2020.

[177] Nir Gutman, Alexey Gorlach, Offek Tziperman, Ron Ruimy, and Ido Kaminer. Universal control of symmetric states using spin squeezing. *Physical Review Letters*, 132(15):153601, 2024.

[178] Liam J Bond, Matthew J Davis, Jiří Minář, Rene Gerritsma, Gavin K Brennen, and Arghavan Safavi-Naini. Efficient state preparation for metrology and quantum error correction with global control. *arXiv preprint arXiv:2312.05060*, 2023.

[179] Samuel L Braunstein and Carlton M Caves. Statistical distance and the geometry of quantum states. *Physical Review Letters*, 72(22):3439, 1994.

[180] Without loss of generality, we set $\beta_{\text{opt}} = 0$ by adding a step in the protocol corresponding to global qubit rotation by the found β_{opt} along the field-axis $\vec{n}$ (known).

[181] Thomas Monz, Philipp Schindler, Julio T Barreiro, Michael Chwalla, Daniel Nigg, William A Coish, Maximilian Harlander, Wolfgang Hänsel, Markus Hennrich, and Rainer Blatt. 14-qubit entanglement: Creation and coherence. *Physical Review Letters*, 106(13):130506, 2011.

[182] S. Kuhr, W. Alt, D. Schrader, I. Dotsenko, Y. Miroshnychenko, A. Rauschenbeutel, and D. Meschede. Analysis of dephasing mechanisms in a standing-wave dipole trap. *Physical Review A*, 72:023406, 2005.

[183] Anil Shaji and Carlton M Caves. Qubit metrology and decoherence. *Physical Review A—Atomic, Molecular, and Optical Physics*, 76(3):032111, 2007.

[184] Jian Li, Mika A Sillanpää, GS Paraoanu, and Pertti J Hakonen. Pure dephasing in a superconducting three-level system. In *Journal of Physics: Conference Series*, volume 400, page 042039. IOP Publishing, 2012.

[185] Hannah J Manetsch, Gyohei Nomura, Elie Bataille, Kon H Leung, Xudong Lv, and Manuel Endres. A tweezer array with 6100 highly coherent atomic qubits. *arXiv preprint arXiv:2403.12021*, 2024.

[186] Tyler Keating, Charles H Baldwin, Yuan-Yu Jau, Jongmin Lee, Grant W Biedermann, and Ivan H Deutsch. Arbitrary dicke-state control of symmetric rydberg ensembles. *Physical Review Letters*, 117(21):213601, 2016.

[187] S. Merkel. *Quantum control of d-dimensional quantum systems with application to alkali atomic spins*. PhD thesis, University of New Mexico, 2009.

[188] Harper R. Grimsley, Sophia E. Economou, Edwin Barnes, and Nicholas J. Mayhall. An adaptive variational algorithm for exact molecular simulations on a quantum computer. *Nature Communications*, 10:3007, 2019.

[189] Gerardo A. Paz-Silva, Gavin K. Brennen, and Jason Twamley. Fault Tolerance with Noisy and Slow Measurements and Preparation. *Physical Review Letters*, 105:100501, 2010.

[190] Daniel Crow, Robert Joynt, and M. Saffman. Improved Error Thresholds for Measurement-Free Error Correction. *Physical Review Letters*, 117:130503, 2016.

[191] H. Ekmel Ercan, Joydip Ghosh, Daniel Crow, Vickram N. Premakumar, Robert Joynt, Mark Friesen, and S. N. Coppersmith. Measurement-free implementations of small-scale surface codes for quantum-dot qubits. *Physical Review A*, 97:012318, 2018.

[192] Vineesha Srivastava, Sven Jandura, Gavin K. Brennen, and Guido Pupillo. Cavity polariton blockade for non-local entangling gates with trapped atoms, 2025.

[193] Giovanni Barontini, Leander Hohmann, Florian Haas, Jérôme Estève, and Jakob Reichel. Deterministic generation of multiparticle entanglement by quantum Zeno dynamics. *Science*, 349(6254):1317–1321, September 2015.

[194] Almut Beige, Daniel Braun, Ben Tregenna, and Peter L. Knight. Quantum Computing Using Dissipation to Remain in a Decoherence-Free Subspace. *Physical Review Letters*, 85(8):1762–1765, August 2000.

[195] Guido Pupillo, Ana Maria Rey, Gavin Brennen, Carl J. Williams, and Charles W. Clark. Scalable quantum computation in systems with Bose-Hubbard dynamics. *Journal of Modern Optics*, 51(16-18):2395–2404, November 2004.

[196] Jürgen Volz, Roger Gehr, Guilhem Dubois, Jérôme Estève, and Jakob Reichel. Measurement of the internal state of a single atom without energy exchange. *Nature*, 475(7355):210–213, July 2011.

[197] Daniel Gottesman, Thomas Jennewein, and Sarah Croke. Longer-Baseline Telescopes Using Quantum Repeaters. *Physical Review Letters*, 109(7):070503, August 2012.

[198] Brandon Grinkemeyer, Elmer Guardado-Sanchez, Ivana Dimitrova, Danilo Shchepanovich, G. Eirini Mandopoulou, Johannes Borregaard, Vladan Vuletić, and Mikhail D. Lukin. Error-Detected Quantum Operations with Neutral Atoms Mediated by an Optical Cavity, October 2024.

[199] D. Main, P. Drmota, D. P. Nadlinger, E. M. Ainley, A. Agrawal, B. C. Nichol, R. Srinivas, G. Araneda, and D. M. Lucas. Distributed quantum computing across an optical network link. *Nature*, 638(8050):383–388, February 2025.

[200] Peter P. Rohde, Zixin Huang, Yingkai Ouyang, He-Liang Huang, Zu-En Su, Simon Devitt, Rohit Ramakrishnan, Atul Mantri, Si-Hui Tan, Nana Liu, Scott Harrison, Chandrashekar Radhakrishnan, Gavin K. Brennen, Ben Q. Baragiola, Jonathan P. Dowling, Tim Byrnes, and William J. Munro. The quantum internet (technical version), 2025.

[201] Zheshen Zhang and Quntao Zhuang. Distributed quantum sensing. *Quantum Science and Technology*, 6(4):043001, July 2021.

[202] Thomas Boulier, Maxime J. Jacquet, Anne Maître, Giovanni Lerario, Ferdinand Claude, Simon Pigeon, Quentin Glorieux, Alberto Amo, Jacqueline Bloch, Alberto Bramati, and Elisabeth Giacobino. Microcavity polaritons for quantum simulation. *Advanced Quantum Technologies*, 3(11):2000052, 2020.

[203] Jacqueline Bloch, Andrea Cavalleri, Victor Galitski, Mohammad Hafezi, and Angel Rubio. Strongly correlated electron–photon systems. *Nature*, 606(7912):41–48, June 2022.

[204] J. Bellessa, J. Bloch, E. Deleporte, V. M. Menon, H. S. Nguyen, H. Ohadi, S. Ravets, and T. Boulier. Materials for excitons–polaritons: Exploiting the diversity of semiconductors. *MRS Bulletin*, 49(9):932–947, September 2024.

[205] Anders S. Sørensen and Klaus Mølmer. Measurement Induced Entanglement and Quantum Computation with Atoms in Optical Cavities. *Physical Review Letters*, 91(9):097905, August 2003.

[206] Michael Tavis and Frederick W. Cummings. Exact Solution for an N-Molecule—Radiation-Field Hamiltonian. *Physical Review*, 170(2):379–384, June 1968.

[207] D Hunger, T Steinmetz, Y Colombe, C Deutsch, T W Hänsch, and J Reichel. A fiber Fabry–Perot cavity with high finesse. *New Journal of Physics*, 12(6):065038, June 2010.

[208] Manuel Uphoff, Manuel Brekenfeld, Gerhard Rempe, and Stephan Ritter. Frequency splitting of polarization eigenmodes in microscopic Fabry–Perot cavities. *New Journal of Physics*, 17(1):013053, January 2015.

[209] Manuel Kaiser, Conny Glaser, Li Yuan Ley, Jens Grimmel, Helge Hattermann, Daniel Bothner, Dieter Koelle, Reinhold Kleiner, David Petrosyan, Andreas Günther, and József Fortágh. Cavity-driven Rabi oscillations between Rydberg states of atoms trapped on a superconducting atom chip. *Physical Review Research*, 4(1):013207, March 2022.

[210] J. D. Pritchard, J. A. Isaacs, M. A. Beck, R. McDermott, and M. Saffman. Hybrid atom-photon quantum gate in a superconducting microwave resonator. *Physical Review A*, 89(1):010301, January 2014.

[211] Chan U Lei, Lev Krayzman, Suhas Ganjam, Luigi Frunzio, and Robert J. Schoelkopf. High coherence superconducting microwave cavities with indium bump bonding. *Applied Physics Letters*, 116(15):154002, April 2020.

[212] M. Brune, E. Hagley, J. Dreyer, X. Maître, A. Maali, C. Wunderlich, J. M. Raimond, and S. Haroche. Observing the Progressive Decoherence of the “Meter” in a Quantum Measurement. *Physical Review Letters*, 77(24):4887–4890, December 1996.

[213] A. Signoles, E. K. Dietsche, A. Facon, D. Grosso, S. Haroche, J. M. Raimond, M. Brune, and S. Gleyzes. Coherent Transfer between Low-Angular-Momentum and Circular Rydberg States. *Physical Review Letters*, 118(25):253603, June 2017.

[214] J. Mozley, P. Hyafil, G. Nogues, M. Brune, J.-M. Raimond, and S. Haroche. Trapping and coherent manipulation of a Rydberg atom on a microfabricated device: A proposal. *The European Physical Journal D*, 35(1):43–57, August 2005.

[215] Sam R. Cohen and Jeff D. Thompson. Quantum Computing with Circular Rydberg Atoms. *PRX Quantum*, 2(3):030322, August 2021.

[216] Stefan Yoshi Buhmann, M. R. Tarbutt, Stefan Scheel, and E. A. Hinds. Surface-induced heating of cold polar molecules. *Physical Review A*, 78(5):052901, November 2008.

[217] P. Rabl, D. DeMille, J. M. Doyle, M. D. Lukin, R. J. Schoelkopf, and P. Zoller. Hybrid Quantum Processors: Molecular Ensembles as Quantum Memory for Solid State Circuits. *Physical Review Letters*, 97(3):033003, July 2006.

[218] Vineesha Srivastava, Sven Jandura, Gavin K. Brennen, and Guido Pupillo. Entanglement-enhanced quantum sensing via optimal global control, October 2024.

[219] John Preskill. Quantum Computing in the NISQ era and beyond. *Quantum*, 2:79, 2018.

[220] David P. DiVincenzo and Peter W. Shor. Fault-tolerant error correction with efficient quantum codes. *Phys. Rev. Lett.*, 77:3260–3263, Oct 1996.

[221] David P. DiVincenzo and Panos Aliferis. Effective Fault-Tolerant Quantum Computation with Slow Measurements. *Physical Review Letters*, 98:020501, 2007.

[222] Rui Chao and Ben W. Reichardt. Quantum error correction with only two extra qubits. *Phys. Rev. Lett.*, 121:050502, Aug 2018.

[223] H. J. Kimble. The quantum internet. *Nature*, 453(7198):1023–1030, 2008.

[224] Dolev Bluvstein, Harry Levine, Giulia Semeghini, Tout T. Wang, Sepehr Ebadi, Marcin Kalinowski, Alexander Keesling, Nishad Maskara, Hannes Pichler, Markus Greiner, Vladan Vuletić, and Mikhail D. Lukin. A quantum processor based on coherent transport of entangled atom arrays. *Nature*, 604(7906):451–456, 2022.

[225] Daniel Barredo, Vincent Lienhard, Sylvain de Léséleuc, Thierry Lahaye, and Antoine Browaeys. Synthetic three-dimensional atomic structures assembled atom by atom. *Nature*, 561(7721):79–82, 2018.

[226] Lars Pause, Lukas Sturm, Marcel Mittenbühler, Stephan Amann, Tilman Preuschoff, Dominik Schäffner, Malte Schlosser, and Gerhard Birkl. Supercharged two-dimensional tweezer array with more than 1000 atomic qubits. *Optica*, 11(2):222–226, Feb 2024.

[227] The technology of microlens-generated tweezer arrays [226] however forsees a potential for further propelling atomic quantum arrays to qubit numbers of 10^5 by exploiting more laser sources.

[228] Lukas Hartung, Matthias Seubert, Stephan Welte, Emanuele Distante, and Gerhard Rempe. A quantum-network register assembled with optical tweezers in an optical cavity. *Science*, 385(6705):179–183, 2024.

[229] Tamara orđević, Polnop Samutpraphoot, Paloma L. Ocola, Hannes Bernien, Brandon Grinkemeyer, Ivana Dimitrova, Vladan Vuletić, and Mikhail D. Lukin. Entanglement transport and a nanophotonic interface for atoms in optical tweezers. *Science*, 373(6562):1511–1514, 2021.